

**UNIVERSIDADE DE LISBOA**  
**INSTITUTO SUPERIOR TÉCNICO**

**Spatio-temporal characterization of high harmonic  
generation for plasma diagnostics**

**Jayanath Chalappurath Payyan Koliyadu**

Supervisor: Doctor Marta Leitão Mota Fajardo

Co-supervisors: Doctor Philippe Zeitoun

Doctor Gonçalo Nuno Marmelo Foito Figueira

Thesis approved in public session to obtain the PhD Degree in

**Physics**

**Jury final classification: Pass with Distinction**

**2018**



**UNIVERSIDADE DE LISBOA**  
**INSTITUTO SUPERIOR TÉCNICO**

**Spatio-temporal characterization of high harmonic  
generation for plasma diagnostics**

**Jayanath Chalappurath Payyan Koliyadu**

**Supervisor:** Doctor Marta Leitão Mota Fajardo  
**Co-supervisors:** Doctor Philippe Zeitoun  
Doctor Gonçalo Nuno Marmelo Foito Figueira

Thesis approved in public session to obtain the PhD Degree in

**Physics**

**Jury final classification: Pass with Distinction**

**Jury**

**Chairperson:** Doctor Luís Paulo da Mota Capitão Lemos Alves  
Instituto Superior Técnico - Universidade de Lisboa

**Members of the Committee:**

Doctor Elke Christina Plönjes-Palm  
Deutsches Elektronen-Synchrotron (DESY), Germany

Doctor Helder Manuel Paiva Rebelo Cerejo Crespo  
Faculdade de Ciências - Universidade do Porto

Doctor João Alberto dos Santos Mendanha Dias  
Instituto Superior Técnico - Universidade de Lisboa

Doctor Marta Leitão Mota Fajardo  
Instituto Superior Técnico - Universidade de Lisboa

**Funding Institutions**

Fundação para a Ciência e Tecnologia - FCT, Portugal under grant -  
SFRH/BH/52419\_2013 (PDF APPLAuSE), VOXEL (Horizon2020 RIA-FET-OPEN  
project, Grant Number: 665207), LASERLAB Europe.



## Abstract

The extreme ultra-violet (XUV) spectral region of the electromagnetic spectrum is characterized by shorter wavelengths, higher photon energies and a possibility to support lower pulse duration compared to visible or infrared radiation. These properties make XUV pulses an apt tool for applications like imaging, probing and lithography with a spatial resolution reaching up to tens of nanometers and temporal resolution on the order of femtoseconds to attoseconds. The available sources of coherent XUV radiation are high harmonic generation (HHG), X-ray lasers (XRL) and free electron lasers (FEL). Work done in this thesis is focused on XUV pulses from HHG.

In order to use XUV pulses from HHG for different applications, it is important to optimize its photon number and to characterize the stability in terms of energy, pointing, spatial as well as temporal properties. For experiments like plasma probing, holography, coherent diffraction imaging and XRL seeding it is necessary to have spatially characterized, and energy optimized XUV pulses with stability in pointing and energy. For spatial characterization of XUV pulses and XUV optics, mainly the spatial phase characterization is considered. Knowing the spatial phase of the XUV pulse helps to optimize the wavefront of the pulses and thereby improving the focusing of XUV pulses. The XUV wavefront is characterized mostly using Hartmann wavefront sensors (WFS) for XUV radiation. For temporal characterization of XUV pulses from HHG, different ex-situ and in-situ methods have been proposed and used. An in-situ method called spatially encoded arrangement - spectral phase interferometry for direct electric field reconstruction (SEA-SPIDER) can be used to efficiently characterize pulse duration of XUV pulses from HHG.

XUV sources by HHG from gases were set up at the laboratory of intense laser (L2I), IST, Lisbon, Portugal using the in-house built diode pumped terawatt level laser and, at the Laboratoire d'Optique Appliquée (LOA), Paris, France using a commercially available Ti:Sapphire laser and also at the VOXEL lab, IST, using commercially available Ti:Sapphire lasers. The high harmonic sources were optimized in photon count and characterized in energy stability, spatial intensity distribution, pointing and spectrum. An experiment on HHG in solids was performed at JETI200, Helmholtz Institute, Jena, Germany using a 200 terawatt Ti:Sa laser. The solid HHG conditions were optimized to generate high harmonics under coherent wake emission and relativistic oscillating mirror mechanisms. The solid high harmonics were characterized in spectrum.

The spatial metrology of the XUV pulses includes design and calibration of XUV wavefront sensors, wavefront characterization of XUV optics and XUV sources. The XUV wavefront sensors are calibrated using HHG as the XUV source. An XUV Hartmann WFS and a novel high-NA XUV Hartmann WFS were calibrated in collaboration with Imagine Optic, France. XUV multilayer mirrors with three different central wavelengths were calibrated for wavefront aberrations introduced on reflection. The wavefront of a toroidal mirror at grazing incidence was measured after the focus using the high-NA XUV WFS and a preliminary optimization was carried out. The wavefront of XUV pulses from HHG in gases was measured and optimized for XUV sources at L2I and LOA. The wavefront of high harmonics from solids was measured using the calibrated high-NA XUV WFS for the first time at JETI200.

A SPIDER code was developed and later modified into a SEA-SPIDER code. Numerical simulations were carried out using this code to determine the experimental parameters required. The SPIDER and SEA-SPIDER code developed could retrieve the pulse duration even under simulated noisy conditions. SEA-SPIDER experimental setups were designed and carried out at the LOA and VOXEL lab, IST, Lisbon. First results from the experiments are also presented. An all-optical temporal metrology method based on autocorrelation using four-wave mixing in the XUV was carried out at the seeded FERMI FEL 2, Trieste, Italy. The coherence time of XUV pulses from FERMI FEL 2 was measured using this method.

The possible applications with the characterized XUV pulses is discussed. The use of an XUV wavefront sensor for measuring plasma parameters in laser-produced plasma at L2I is discussed. The calibrated high-NA XUV WFS and wavefront characterized XUV sources can be used in the proposed wavefront corrected in-line holography experiment in the XUV for achieving better resolution in the reconstruction.

**Keywords:** High harmonic generation, XUV spatial metrology, high-NA XUV WFS, XUV temporal metrology, SEA-SPIDER, FEL.

## Resumo

A região do espectro electromagnético correspondente à radiação ultravioleta extrema (XUV) é caracterizada por comprimentos de onda mais curtos e energias de fótons mais elevadas, e pela capacidade de suportar durações de impulsos mais baixas, relativamente às regiões espectrais do visível e do infravermelho. Estas propriedades fazem dos impulsos de XUV ferramentas adequadas para aplicações como a litografia, a imagiologia e o diagnóstico de amostras onde são necessárias resoluções espaciais e temporais extremamente elevadas (respectivamente, de poucas dezenas de nanómetros e de poucos femtosegundos a attosegundos). As principais fontes de XUV coerente são a geração de harmónicas elevadas (HHG), os lasers de raios-X (XRL) e os lasers de electrões livres (FEL). O trabalho descrito nesta tese é focado na geração de impulsos de XUV a partir de HHG.

De forma a utilizar uma fonte de HHG para diferentes fins (diagnóstico em plasmas, holografia, imagiologia e como fonte de impulsos para XRL) é necessário fazer a sua optimização e caracterização em termos de energia, de estabilidade, e das propriedades espaciais e temporais. Entre estas, uma das principais propriedades a ter em conta é a fase espacial do feixe de XUV. O conhecimento da fase espacial pode ajudar a optimizar a frente de onda do feixe de forma a melhorar a focagem dos impulsos de XUV. A medição e caracterização desta propriedade é conseguida sobretudo através da utilização de sensores de frente de onda Hartmann (WFS). Para a caracterização temporal dos impulsos, diferentes procedimentos, “ex-situ” e “in-situ”, estão a ser propostos e realizados. Um procedimento “in-situ” designado por arranjo codificado espacialmente de interferometria de fase espectral para a reconstrução directa do campo eléctrico (SEA-SPIDER) pode ser usado para caracterizar eficientemente o perfil temporal dos impulsos de produzidos pelas fontes HHGs.

Neste trabalho duas fontes de impulsos de XUV do tipo HHG obtidas a partir de gases foram implementadas, uma no Laboratório de Lasers Intensos (L2I) do Instituto Superior Técnico (IST), Lisboa, Portugal, para a qual foi usada um laser sub-Terawatt bombeado por díodos, e outra no Laboratoire d’Optique Appliquée (LOA), Paris, França, onde foi empregue um laser comercial de Ti:safira. Em ambas as fontes de XUV, o número de fótons foi optimizado, a estabilidade da energia e a posição no alvo foram medidos, assim como, o perfil espacial do feixe e o espectro gerado. Uma outra experiência de HHG em sólidos foi efectuada no JETI200, Helmholtz Institute Jena, Alemanha, utilizando um laser de 200 TW de Ti:safira. As condições para geração de impulsos de XUV em sólidos foram optimizadas de forma a gerar harmónicas elevadas sob a influência dos mecanismos de “coherent wake emission” e “relativistic oscillating mirror”. Durante a experiência, os seus espectros foram adquiridos.

A metrologia espacial dos impulsos XUV inclui o design e a calibração dos respectivos WFS, e a caracterização das frentes-de-onda das ópticas e das fontes de XUV. Os sensores de frente de onda XUV são calibrados através de fontes HHG. Neste trabalho, dois Hartmann WFS, um deles uma nova versão de WFS para aberturas numéricas elevadas (high-NA XUV WFS), foram caracterizados e calibrados em colaboração com Imagine Optic em França.

Espelhos de multicamadas com três comprimentos de onda centrais diferentes foram calibrados para introduzirem aberrações em reflexão. A frente de onda de um espelho toroidal com um ângulo

de incidência rasante foi medida após o foco usando o high-NA XUV WFS, sendo posteriormente otimizada de forma a aumentar a intensidade no foco. As frentes de onda dos impulsos de HHG em gases foram medidas e otimizadas para utilização em experiências nos laboratórios L2I e LOA. As frentes de onda de HHG em sólidos foram medidas pela primeira vez no novo high-NA XUV WFS calibrado no JETI200. Um código para o SPIDER foi desenvolvido e posteriormente modificado para o SEA-SPIDER. Foram realizadas simulações numéricas utilizando este código de forma a determinar os parâmetros experimentais necessários. O código desenvolvido para ambos os SPIDERS consegue calcular a duração dos impulsos mesmo em condições em que é introduzido ruído. As montagens experimentais do SEA-SPIDER foram desenhadas e implementadas nos laboratórios LOA e VOXEL no IST. Os primeiros resultados experimentais são apresentados neste trabalho.

Um método de metrologia temporal puramente óptico, baseado na autocorrelação usando o processo de mistura de quatro ondas (“fourwave mixing”), foi realizado no FERMI FEL 2 em Trieste, Itália. Com este método foi medida a coerência temporal dos impulsos de XUV.

As possíveis aplicações com os impulsos XUV caracterizados são discutidas neste trabalho. É discutido o uso de um WFS para medir os parâmetros de um plasma produzido no L2I. O high-NA XUV WFS calibrado e as fontes de XUV devidamente caracterizadas podem ser usadas em experiências de holografia “in-line” com frente de onda de XUV corrigida de forma a serem atingidas resoluções mais elevadas na reconstrução das imagens.

**Palavras-chave:** Geração de harmônicas elevadas (HHG), XUV metrologia espacial, high-NA XUV WFS, XUV metrologia temporal, SEA-SPIDER, FEL.

## Acknowledgments

My thesis would not have been complete without the support of my supervisors, colleagues, friends, and family. Here I acknowledge their contributions.

First, I would like to thank my supervisor Prof. Dr. Marta Fajardo for her support, guidance, and motivation during the thesis. I also thank her for helping with realizing collaborations, experiments, and meetings in different countries across Europe. I thankfully acknowledge the support and guidance from my co-supervisors Dr. Philippe Zeitoun during the year at LOA and also during the whole thesis. I also acknowledge the support and guidance from my co-supervisor prof. Dr. Gonçalo Figueira.

I am grateful to Dr. Swen Kunzel for his patience in guiding and supporting me during the thesis. I thank Swen for the long discussions, for the times during the experiments, and for being a good friend.

I would like to thank Dr. Celso Joao for his support during the time in the Laboratory of Intense Lasers (L2I) at IST. I acknowledge and thank the support from Dr. Li Lu during the various experiments at the Laboratoire d'Optique Appliquée (LOA), France and Helmholtz Institute, Jena, Germany.

The collaboration with Imagine optic, Orsay, France was an important part in the thesis. I would like to thank Guillaume Dovillaire and Dr. Dietmark Korn from Imagine Optic, for providing technical support for the XUV wavefront sensor calibration experiments.

I thankfully acknowledge the collaboration and support of Prof. Dr. Matt Zepf during the experiments at Helmholtz Institute, Jena.

I would like to thank Prof. Dr. Giovanni de Ninno for his collaboration and support for the experiments at the FERMI free electron laser, Elettra – Synchrotron, Trieste, Italy.

The support from colleagues at the group of lasers and plasmas (GoLP), IST and LOA who created a friendly and creative environment to work and study are thankfully mentioned.

The experiments during the thesis would not have been possible without the help of technicians at GoLP, LOA and JETI 200 Helmholtz Institute, Jena. I appreciate the help from Nuno Gomes from GoLP, Jean-lou Charles and Bernard Allali from LOA, and Georg Schaefer from JETI 200.

I appreciate the help of Carmo Nunes, secretary of IPFN during the early days in Lisbon and the support during entire length of the APPLAuSE PhD program. I am grateful to the secretaries Anabella and Carla from IPFN and Lucie and Patricia from LOA for their kind support in handling various paperwork during the thesis.

The funding from FCT through the APPLAuSE PhD program for the four years of the PhD is thankfully mentioned. I also like to acknowledge the funding from Laserlab, COST and VOXEL for participating in different experiments, meetings and conferences.

I acknowledge the governing committee of APPLAuSE PhD program and all other people involved for their support and effort in the functioning and improvement of the PhD program.

The encouragement and motivation from Dr. Alok Sharan for pursuing a career in research is thankfully mentioned. I would like to thank Dr. Buvanesh Ramakrishna for his support during the PhD and for being a mentor and a good friend. The support, motivation and friendship of Dr. Kalyan Shanthakumari is thankfully acknowledged.

I would like to thank all my friends who, always cheered me up and supported me during the time of the thesis. The company of colleagues from GoLP, LOA and the first cohort of the APPLAuSE PhD program are thankfully mentioned.

Finally, I wholeheartedly thank my family for their unconditional love and support which is always a motivation for me to go forward.

Dedicated to all my teachers and mentors.



# Contents

Abstract . . . . .	iii
Resumo . . . . .	v
Acknowledgement . . . . .	vii
List of Figures . . . . .	xiii
List of Tables . . . . .	xix
List of Acronyms . . . . .	xxi
<b>1 Introduction</b>	<b>1</b>
1.1 Motivation . . . . .	1
1.2 Topic overview . . . . .	3
1.3 Thesis outline . . . . .	4
<b>2 High harmonic generation</b>	<b>7</b>
2.1 Introduction . . . . .	7
2.2 HHG from gases . . . . .	8
2.2.1 Theoretical description of HHG from gases . . . . .	9
2.2.2 Experimental results on HHG and global optimization . . . . .	16
2.3 HHG from solids . . . . .	29
2.3.1 Theoretical description of HHG from solids . . . . .	30
2.3.2 Experimental results on HHG from solids . . . . .	34
2.4 Comparison between different HHG sources . . . . .	39
<b>3 Spatial metrology of HHG and XUV optics</b>	<b>41</b>
3.1 Introduction . . . . .	41
3.1.1 XUV Optics . . . . .	42
3.1.2 Hartmann WFS . . . . .	44
3.2 Experimental results on calibration of XUV WFS . . . . .	47
3.2.1 Calibration of an XUV WFS . . . . .	48
3.2.2 Design and calibration of a high-NA XUV WFS . . . . .	50
3.3 Experimental results on wavefront characterization of XUV optics . . . . .	55
3.3.1 Multilayer mirror calibration . . . . .	55
3.3.2 Toroidal mirror wavefront optimization using high-NA XUV WFS . . . . .	59

---

3.4	Experimental results on wavefront characterization of HHG . . . . .	63
3.4.1	Wavefront characterization of high harmonics from gases . . . . .	63
3.4.2	Wavefront characterization of high harmonics from solids . . . . .	69
3.4.3	A comparison between wavefront of HHG from gases and solids . . . . .	73
<b>4</b>	<b>Temporal metrology of XUV pulses</b>	<b>75</b>
4.1	Introduction . . . . .	75
4.1.1	Temporal characterization techniques for XUV pulses . . . . .	76
4.2	All optical temporal metrology of XUV pulses from HHG . . . . .	82
4.2.1	Introduction to SPIDER and SEA-SPIDER . . . . .	82
4.2.2	Numerical simulations for SPIDER and SEA-SPIDER . . . . .	90
4.2.3	Experimental progress for SEA-SPIDER . . . . .	99
4.3	All optical temporal metrology of XUV free-electron laser . . . . .	111
4.3.1	Introduction to Free electron laser . . . . .	111
4.3.2	Overview of four-wave mixing . . . . .	114
4.3.3	Experimental results . . . . .	117
<b>5</b>	<b>Conclusions and perspectives</b>	<b>123</b>
5.1	Conclusions . . . . .	123
5.1.1	Achievements . . . . .	124
5.2	Perspectives . . . . .	125
5.2.1	Plasma diagnostics with XUV radiation . . . . .	126
5.2.2	XUV imaging with wavefront correction . . . . .	128
5.3	Scientific contributions . . . . .	132
	<b>Bibliography</b>	<b>135</b>

# List of Figures

1.1	Electromagnetic spectrum showing spectral range from infrared to hard X-rays with the XUV spectral region highlighted (in violet). Modified from [1] . . . . .	1
2.1	Schematic of general experimental setup for HHG. . . . .	7
2.2	Schematic of a simple setup for HHG. . . . .	8
2.3	Schematic of a typical spectrum for HHG from gases. The high intensity lower harmonic orders, the plateau region and the cutoff of HH orders are shown in the spectrum. . . . .	9
2.4	Pictorial representation of the three-step model for HHG from gases. The sinusoidal curve in red shows the electric field of the laser. The motion of the electron, shown in the blue circle, under the effect of electric field and emission of XUV radiation on recombination are shown in the picture. . . . .	10
2.5	The trajectory of electron in the electric field of the laser with ionization at different phases of the laser cycle (calculated using the equation 2.3). The red dotted line shows the electric field amplitude and the blue, green and violet lines shows the different electron trajectories. . . . .	11
2.6	HH signal calculated with the equation 2.23 for HH order 25 generated with driving laser of wavelength 800 nm in argon with at 30 mbar of pressure at different coherence lengths. Taken from [86] . . . . .	16
2.7	Block diagram of the experimental setup for HHG with the laser system at L2I, IPFN, IST. . . . .	17
2.8	Experimental setup for HHG at L2I, IPFN, IST. The gas cell used for HHG is shown in the inset. . . . .	18
2.9	Optimized HH cross-section for (a) argon and (b) xenon gases. . . . .	18
2.10	Single-shot energy stability analysis for high-harmonics generated in argon and xenon . . . . .	19
2.11	The optimized HH spectrum for argon at L2I, IPFN. . . . .	20
2.12	The optimized HH spectrum for xenon at L2I, IPFN. The low intense lines in the picture in (a) and low intense peaks in the line-out in (b) are the diffraction pattern of the XUV beam from the supporting grid of the grating. . . . .	20
2.13	The optimized HH spectrum for xenon with fundamental and second harmonic beams at L2I, IPFN . . . . .	20
2.14	Schematic of the HH beamline at Salle Corail, LOA. . . . .	22
2.15	HH beamline at Salle Corail, LOA. . . . .	22

2.16	Optimized HH intensity cross-section at Salle Corail, LOA . . . . .	22
2.17	Schematic of XUV spectrometer at Salle Corail, LOA. . . . .	23
2.18	The optimized HH spectrum for argon at salle corail, LOA. . . . .	24
2.19	The optimized HH spectrum for neon at Salle Corail, LOA. . . . .	24
2.20	The optimized HH spectrum for xenon at Salle Corail, LOA. . . . .	25
2.21	Schematic of lasers and HHG experimental setup at VOXEL lab, IST Lisbon . . . . .	26
2.22	Footprint of HHG from Ar at 13 mbar measured at the VOXEL lab, IST. . . . .	26
2.23	Schematic of XUV spectrometer setup at VOXEL Lab, IST Lisbon. . . . .	27
2.24	The optimized HH spectrum for argon at VOXEL lab, IST. . . . .	27
2.25	The optimized HH spectrum for xenon and neon at VOXEL lab, IST. . . . .	28
2.26	The optimized HH spectrum for argon with fundamental and second harmonic pulses at VOXEL lab, IST. . . . .	29
2.27	Schematics of a simple setup of HHG from solids. . . . .	29
2.28	Schematics of basic idea of the ROM model. Figure taken from [95] . . . . .	31
2.29	A pictorial representation of plasma wave generation under the CWE model for HHG in solids. (a) Electrons are pulled out of the plasma in the electric field of the laser at near critical densities, (b) the electrons accelerated in the electric field of the laser are pushed back into the plasma as field changes sign and (c) propagation of electrons in the over-dense plasma and formation of electron bunches and emission of radiation as attosecond bursts. Figure modified from [104]. . . . .	33
2.30	The JETI200 Laser at Helmholtz Institute in Jena, Germany. In the inset: (a) shows the gratings of the compressor in vacuum, (b) shows the cryo-cooled joule level Ti: Sapphire amplifier crystal (with the pumping on), (c) shows the Ti: Sapphire amplifier crystal (with the pumping on) in another multipass amplifier from the laser system [105] . . . . .	35
2.31	The Schematics of PM alignment and reflectivity at JETI200 . . . . .	35
2.32	Measured contrast of the JETI200 laser system using a Sequoia. . . . .	36
2.33	Schematic of the experimental setup for generation of HH from solids and spectral charac- terization at JETI200, Helmholtz Institute, Jena, Germany. . . . .	37
2.34	The optimized focal spot of the laser at the target position at JETI200. . . . .	37
2.35	Raw image of the solid HH spectrum from Jasný spectrometer . . . . .	37
2.36	HH spectrum from generated under CWE mechanism. . . . .	38
2.37	HH spectrum from generated under the ROM mechanism. . . . .	38
3.1	Reflectivity of mirrors with different substrates at 32 nm for linearly polarized XUV radiation [92]. . . . .	43
3.2	Illustration of reflection of light from different layers of a multilayer mirror. . . . .	43
3.3	Schematic of the working principle of Hartmann WFS. The pattern generated by a reference wavefront (shown in green) on the CCD after the Hartmann plate is compared to the pattern generated by a test wavefront (shown in red) to measure the wavefront aberrations. . . .	44

3.4	Schematic of the wavefront of a spherical wave. . . . .	45
3.5	XUV Hartmann WFS for calibration. . . . .	48
3.6	Schematic of the setup for calibration of XUV wavefront sensor . . . . .	49
3.7	Spatial filtering of XUV with 10 $\mu\text{m}$ pinhole . . . . .	49
3.8	Raw image of spatially filtered XUV signal recorded on XUV Hartmann WFS. . . . .	50
3.9	Reconstructed Intensity and wavefront of the calibration beam after the pinhole, used for XUV WFS calibration . . . . .	51
3.10	The schematic, picture, schematic of Hartmann plate and picture of Hartmann plate of the high-NA XUV WFS. . . . .	52
3.11	Schematic of the setup for calibration of high-NA wavefront sensor . . . . .	52
3.12	The experimental setup for optimizing the pinhole position with HHs and the spatially filtered XUV beam. . . . .	53
3.13	Experimental setup for calibration of the high-NA wavefront sensor. In this picture WFS is placed at a distance of 17 cm from the pinhole. . . . .	53
3.14	Raw image of the spatially filtered XUV signal recorded on the high-NA XUV Hartmann WFS. . . . .	54
3.15	Reconstructed intensity and wavefront of the spatially filtered XUV beam used for high-NA XUV WFS calibration. . . . .	54
3.16	The RMS wavefront of the different calibration images acquired for the high-NA XUV WFS calibration. . . . .	55
3.17	Schematics of multilayer mirror calibration . . . . .	56
3.18	Spatially filtered XUV beam from a 10 $\mu\text{m}$ pinhole. The cut in the intensity pattern at the left side of the figure is due to the clipping of XUV beam by an aluminum filter holder placed before the X-ray CCD. . . . .	57
3.19	Experimental setup for multilayer mirror calibration . . . . .	57
3.20	Raw image of spatially filtered XUV signal recorded on the high-NA XUV Hartmann WFS. . . . .	58
3.21	Reconstructed wavefront of (a) reference beam and (b,c,d) calibrated wavefronts of multilayer mirrors (with different central wavelengths). . . . .	58
3.22	Schematic of the experimental setup for optimization of toroidal mirror focus using high-NA XUV WFS. . . . .	60
3.23	Image of focal spot at different distances from the focus of a toroidal mirror illuminated by a He-Ne laser and recorded using a visible CCD. In (b) the high intense spot size is 25 $\mu\text{m}$ $\times$ 32 $\mu\text{m}$ . . . . .	60
3.24	Experimental setup for optimization of toroidal mirror focus showing the orientation of the toroidal mirror with respect to the WFS. The violet line shows the direction of XUV beam. . . . .	61
3.25	Raw image of XUV beam after the focus of the toroidal mirror recorded on the high-NA XUV Hartmann WFS. . . . .	62
3.26	Reconstructed Intensity and wavefront from the toroidal mirror before (a, b) and after (c, d) optimization, measured at 17 cm from the toroidal mirror focus. . . . .	63
3.27	XUV Hartmann wavefront sensor. . . . .	64

3.28 Schematic of experimental setup for wavefront characterization of high harmonics generated from gases. . . . .	64
3.29 XUV WFS attached to the vacuum chamber for wavefront characterization of high harmonics generated from gases. . . . .	65
3.30 Raw image of spatially filtered XUV signal recorded on an XUV Hartmann WFS. . . . .	65
3.31 The measured wavefront of high harmonics at different gas pressures. (g) and (h) The optimized wavefront errors at 65 mbar. . . . .	66
3.32 XUV Hartmann WFS from DESY, Germany . . . . .	67
3.33 Schematic of the experimental setup for HH wavefront measurement at L2I . . . . .	68
3.34 Experimental setup showing the XUV WFS attached to the HHG beamline at L2I. . . . .	68
3.35 An example of a reconstructed high harmonic wavefront (acquisition 1) measured with the Hartmann type XUV wavefront sensor. . . . .	69
3.36 The evolution of the RMS wavefront error and the Zernike coefficients of the main aberrations. . . . .	69
3.37 Schematic of the experimental setup for wavefront characterization at Helmholtz Institute, Jena, Germany . . . . .	70
3.38 Schematic of the experimental setup of high-NA XUV WFS inside the target chamber for measuring the wavefront of HH from solids (a) and a picture of the high-NA XUV WFS inside a protective aluminum box on a multi-axis stage (b). . . . .	71
3.39 Raw image of spatially filtered XUV signal recorded on an XUV Hartmann WFS. . . . .	71
3.40 Reconstructed intensity and the wavefront of HHG in solids under the CWE mechanism. . . . .	72
3.41 Reconstructed intensity and wavefront of HHG in solids under the ROM mechanism. . . . .	72
4.1 Schematic of an experimental setup for cross-correlation method. The XUV pulses generated by HHG in neon gas. The photoelectrons generated by the XUV pulses in krypton gas in presence of the IR laser is recorded using a time of flight (TOF) electron spectrometer. Figure taken from [150]. . . . .	77
4.2 Schematic of an experimental setup for RABITT. XUV pulses from HHG ionizes argon gas in presence of the IR laser and the electron generated are detected using a TOF electron spectrometer. Taken from [151]. . . . .	78
4.3 Schematic of an experimental setup for streaking. The electrons ionized by the XUV pulses are streaked by the IR lase field present and detected using a TOF electron spectrometer. Figure taken from [154]. . . . .	79
4.4 Schematic of a typical experimental setup for FROG. Photoelectron spectrum generated by the XUV in presence of IR is recorded with respect to the delay between XUV and IR to generate the FROG trace. Figure taken from [56]. . . . .	79
4.5 Schematic of an experimental setup for a double color in-situ method. IR laser and its SH generate HHs and the modulation in the HH spectrum is recorded using an XUV spectrometer. Figure modified from [165]. . . . .	80

4.6	Schematic of an experimental setup for STRAP. Polarized IR laser and its weak second harmonic interact at angle in a gas jet and a spatial modulation is introduced in the XUV intensity distribution. Figure taken from [167]. . . . .	81
4.7	A flow chart of SPIDER Algorithm. Modified from [62]. . . . .	85
4.8	Concept of integration or concatenation of the phase difference extracted from a SPIDER spectrogram. Taken from [62]. . . . .	86
4.9	Schematic of experimental setup for SPIDER. Modified from [60]. . . . .	86
4.10	Pictorial representation of wave-vector difference ( $\mathbf{k}_1 - \mathbf{k}_2$ ). . . . .	88
4.11	Schematic of a basic setup for SEA-SPIDER in XUV. . . . .	88
4.12	Schematic of experimental for generating a pulse and its spectrally sheared replica. . . .	89
4.13	Results from the SPIDER algorithm for SH pulses. . . . .	91
4.14	Results from the SPIDER algorithm for XUV pulses. . . . .	93
4.15	Delay and shear with noise for SPIDER. . . . .	94
4.16	Results from SPIDER algorithm with noise added. . . . .	94
4.17	Results from the SEA-SPIDER algorithm. . . . .	97
4.18	Results from the SEA-SPIDER algorithm with Gaussian noise. . . . .	97
4.19	The SH intensity at different $\theta$ are normalized to the SH intensity at $\theta = 29.02^\circ$ . The dotted lines shows the central wavelength of the SH intensity spectrum at different $\theta$ . . . . .	99
4.20	Schematic of the experimental setup for SEA-SPIDER at Salle Corail, LOA. . . . .	100
4.21	Spectrum and spectral stability of the IR laser measured before the BBO. . . . .	101
4.22	Spectrum showing the contrast in intensity between IR and SH using dichroic mirrors and high reflecting laser line mirrors. . . . .	101
4.23	Experimental setup for generating spectrally sheared HH sources at Salle Corail, LOA . .	102
4.24	Spectrum and spectral stability of the second harmonic measured after BBO. . . . .	102
4.25	Footprint of HHG with wavefront splitting configuration of the tested SEA-SPIDER experimental setup. . . . .	103
4.26	Schematic of the SEA-SPIDER experimental setup at VOXEL Lab, IST. . . . .	103
4.27	Experimental setup for generating the SH and its spectrally sheared replica at the VOXEL lab, IST . . . . .	104
4.28	Spectrum and stability of the IR laser measured before BBO. . . . .	105
4.29	Spectrum and stability of the second harmonic measured after BBO. . . . .	105
4.30	Experimentally measured SH spectrum of the phase matching angle scan for SHG in a BBO crystal. . . . .	106
4.31	Spatial interference obtained between SH and its spectrally sheared replica. . . . .	106
4.32	Footprint of HH beams from the two beamlines. . . . .	107
4.33	Spectrum of the SH pulse and its replica. . . . .	108
4.34	Reconstruction of the electric field of SH pulses using the SPIDER algorithm. . . . .	109
4.35	The spectrum of SH pulses from the SEA-SPIDER experimental setup. . . . .	110
4.36	Schematic of oscillatory motion of an electron in an undulator [190, 86] . . . . .	112

---

4.37 Schematic of a seeded FEL [192] . . . . .	112
4.38 Schematic of the two stage seeded FERMI FEL, Trieste [192] . . . . .	114
4.39 Schematic of a possible FWM geometry [189] . . . . .	115
4.40 Schematic of transient grating generation in XUV at FERMI FEL (Inset: $\vec{k}$ diagram) [189] .	116
4.41 Experimental setup at MiniTIMER delay line, DiPROL, FERMI FEL [204] . . . . .	118
4.42 Schematic of the experimental setup at the MiniTIMER delay line, DiPROL, FERMI FEL. .	118
4.43 Experimental setup at DiPROI, FERMI FEL [204] . . . . .	119
4.44 The averaged spectrum of FERMI FEL 2 measured over 50 acquisitions. . . . .	120
4.45 The transient grating based autocorrelation signal measured for FERMI FEL 2. . . . .	120
5.1 Schematic of basic experimental arrangement used for wavefront sensing of high-density targets. . . . .	127
5.2 Schematic of in-line holography imaging. Modified from [213] . . . . .	129
5.3 Numerical simulations for in-line holography with wavefront correction. Taken from [213] .	130
5.4 Schematic of the concept of wavefront correction in in-line holography using XUV beams.	131

# List of Tables

2.1	Optimized operating conditions for HHG in argon and xenon calculated for the whole HH spectrum . . . . .	19
2.2	Typical operating conditions for HHG in argon and neon and their corresponding XUV beam parameters (calculated for the whole HH spectrum). . . . .	23
2.3	Optimized operating conditions for HHG in argon, xenon and neon, and their corresponding XUV beam parameters (calculated for the whole HH spectrum). . . . .	28
2.4	The typical conditions for generation of solid HH under CWE and ROM mechanisms at JETI200. . . . .	39
2.5	Comparison between different XUV sources generated by the process of HHG in gases and solids. . . . .	40
3.1	The value of major aberrations for the reference wavefront and multilayer mirror (MLM - eV) with different central wavelengths. . . . .	59
3.2	The value of major aberrations for the wavefront from toroidal mirror measured at 17 cm from the focus. . . . .	62
3.3	The value of major wavefront aberrations for high harmonic beam measured at different gas pressures . . . . .	67
3.4	Mean values for the RMS wavefront error and the Zernike coefficients over 13 acquisitions. . . . .	70
3.5	The value of major wavefront aberrations for solid HHG under different mechanisms. . . . .	73
3.6	The value of major wavefront errors for HHG from solids and gases (MLM -multilayer mirror). . . . .	74
4.1	Principle parameters for FERMI FEL [194, 193, 196] . . . . .	114



# List of Acronyms

ADK	-	Ammosov–Delone–Krainov
Al	-	Aluminum
BBO	-	Beta Barium Borate
CCD	-	Charged-Coupled Device
CDI	-	Coherent Diffraction Imaging
CPA	-	Chirped Pulse Amplification
DiProl	-	Diffraction and Projection Imaging
FEL	-	Free Electron Laser
FERMI	-	Free Electron laser Radiation for Multidisciplinary Investigations
FET	-	Future Emerging Technology
FT	-	Fourier Transform
FTH	-	Fourier Transform Holography
FTL	-	Fourier Transform Limit
FWHM	-	Full Width Half Maximum
FWM	-	Four Wave Mixing
GDD	-	Group Delay Dispersion
HGHG	-	High Gain Harmonic Generation
HH	-	High Harmonic
HHG	-	High Harmonic Generation
ICF	-	Inertial Confinement Fusion
IPFN	-	Institute for Plasmas and Nuclear Fusion
IR	-	Infra-Red
IST	-	Instituto Superior Técnico
KB	-	Kirkpatrick - Baez
L2I	-	Laboratory for Intense Lasers
LOA	-	Laboratoire d'Optique Appliquée
OAP	-	Off Axis Parabola
PM	-	Plasma Mirror
RMS	-	Root Mean Square
ROC	-	Radius of Curvature

---

ROI	-	Region of Interest
SASE	-	Self Amplified Spontaneous Emission
SEA	-	Spatially Encoded Arrangement
SFA	-	Strong Field Approximation
SH	-	Second Harmonic
SHG	-	Second Harmonic Generation
SM	-	Spherical Mirror
SPIDER	-	Spectral Phase Interferometry by Direct Electric field Reconstruction
STP	-	Standard Temperature and Pressure
TDSE	-	Time Dependent Schrödinger Equation
TOD	-	Third Order Dispersion
TOF	-	Time Of Flight
UV	-	Ultra-Violet
VOXEL	-	Volumetric medical X-ray imaging at Extremely Low dose
WDM	-	Warm Dense Matter
WFS	-	Wavefront Sensor
XUV	-	Extreme Ultra-Violet

# Chapter 1

## Introduction

The extreme ultraviolet (XUV) radiation in the electromagnetic spectrum spans over a photon energy range of  $\sim 10$  eV to  $\sim 124$  eV and a corresponding wavelength range of  $\sim 121$  nm to  $\sim 10$  nm [1]. Figure 1.1 shows a pictorial representation of the electromagnetic spectrum from far-infrared (IR) to hard X-rays with the XUV spectral region highlighted. Shorter wavelengths, higher photon energies and the possibility to support lower pulse duration make XUV radiation an apt tool for applications like imaging [2], probing [3] and lithography [4], with a spatial resolution going up to tens of nanometers and a temporal resolution on the order of femtoseconds to attoseconds. However, it is difficult to generate, manipulate and use XUV radiation mainly because of the presence of many atomic resonances in this spectral region, which results in high absorption and low reflectance in most of the materials [1].

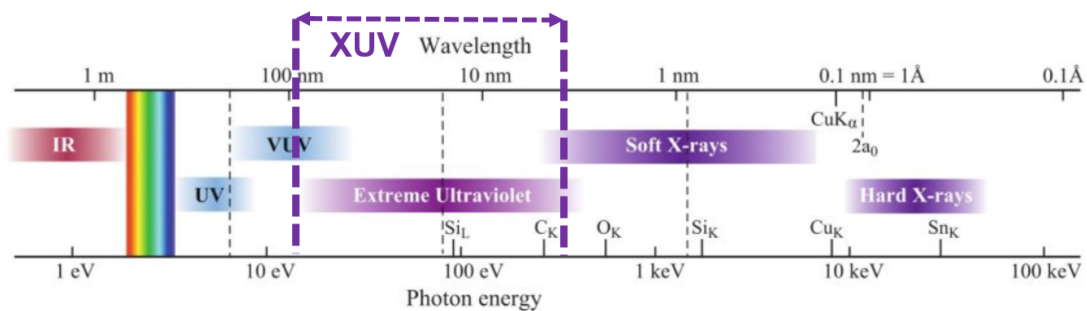


Figure 1.1: Electromagnetic spectrum showing spectral range from infrared to hard X-rays with the XUV spectral region highlighted (in violet). Modified from [1]

This thesis presents the work done towards generation, optimization, characterization and possible applications of XUV pulses generated by the process of high harmonic generation.

In this chapter, an overview of the topic being studied and the outline of the thesis are presented.

### 1.1 Motivation

The main motivation to work with XUV sources are their applications. Coherent XUV sources have exciting applications in different branches of science such as physics, chemistry and biology and also for industries in lithography [4]. Applications in physics are on more fundamental areas such as

plasma physics [3], solid state physics [5], atomic physics [6, 7], study of XUV optics [1], generation of ultrashort attosecond light sources [8], and imaging electronic and molecular processes [6]. Applications in chemistry include study of reactions at ultrashort time scales, study of ultrafast nuclear and electronic dynamics [9]. Applications in biology include mostly imaging biomolecules and cells [2, 10, 11]. For industries working with semiconductors, there is a high interest in sources which can be used in lithography to create next-generation computer chips with structures in the order of few tens of nanometers and coherent XUV sources are potential candidates [4].

The most interesting applications for the work included in this thesis are imaging with XUV sources to achieve nanometer spatial resolution and using XUV sources for plasma probing. In both cases a high temporal resolution in the order of femtoseconds to attoseconds is also desired. These motivations are briefly explained in the following paragraphs. Furthermore, available XUV sources are also presented.

An imaging system consists of a light source and an optical system. The light source can be coherent or incoherent and the optics can be reflective or transmissive. The advent of ultrashort coherent light sources have helped in improving the resolution of the imaging system. The resolution of the imaging systems ultimately depends on the wavelength of the light source. The spatial resolution ( $d$ ) of an imaging system is defined by Abbe's diffraction limit and it is given by [12],

$$d = \frac{\lambda}{2 n \sin(\theta)} \quad (1.1)$$

where  $\lambda$  is the wavelength of the light source,  $n$  is the refractive index and  $\theta$  is the angle made by the light source at the object. The use of optical or IR short pulse lasers has limitations in achievable resolution, since resolution scales with the illuminating wavelength. Although methods like stimulated-emission-depletion fluorescence microscopy [13] and scanning near-field optical microscopy [14] can go around the diffraction limit in-terms of resolution, they need specific sample preparation. Another way to get higher resolution is to image using shorter wavelength radiation. Also, for imaging purposes, it is important to have a source with short pulse duration so that the sample is not destroyed due to long time exposure.

An example of an object that require probing with high spatial and temporal resolution at short wavelength are high energy density plasmas. High energy density plasmas are created in high power laser facilities worldwide. When a high power laser (intensity  $> 10^{14}$  W/cm<sup>2</sup>) interacts with a solid target, the target undergoes a transition from solid to plasma state. With ultra-short laser heating, the plasma passes through an intermediate state, called warm-dense-matter (WDM), in which the density is nearly equal to solid density but the temperature is on the order of  $\sim 10^5$  K. This transient state exists for picoseconds [15, 16]. Knowing how this transition is happening and understanding the dynamics of this intermediate high energy density plasma state is important for modeling how the laser energy is absorbed by solids. This in return helps understanding the laser energy deposition on targets in inertial confinement fusion (ICF) [17] and for modeling the equations of state of astrophysical objects where the main constituent is WDM [18, 16]. For high density plasma states it is important to have a probe which can penetrate the plasma with temporal resolution of sub-picoseconds since the evolution of the plasma states happens in picoseconds. The use of ultrashort high power optical lasers for probing these high

energy density states is limited since the optical lasers cannot penetrate the high energy density states. Optical lasers can provide information from the reflected light [19]. Using shorter wavelength sources in the XUV or X-rays which can penetrate the high energy density states serves as more appropriate probe for these states [16, 20].

Available sources with ultrashort pulse duration and short wavelengths are X-rays produced by free-electron lasers (FEL) [21, 22, 23, 24], XUV pulses produced by the process of high-harmonic generation (HHG) [25, 26, 27] and soft X-ray lasers (XRL) [28, 29]. Although X-rays from FELs can provide spatially coherent XUV pulses with a high photon number ( $2 \times 10^{13}$  photons / shot) and peak intensities  $> 10^{18}$  W/cm<sup>2</sup> [21, 23], its major drawbacks are size, cost and availability. The most widely available source of ultrashort pulse coherent XUV radiation is HHG, which has also a high spatial and temporal coherence [30] and supports additionally pulse durations  $< 100$  attoseconds [31, 32, 33]. Compared to FELs the photon number of HHG is smaller ( $10^9 - 10^{11}$  photons/shot), but it is sufficient to carry out single-shot experiments [34]. Although soft XRLs are sources of coherent XUV radiation, they can be seeded with HHG to get better beam quality and shorter pulse duration [35, 36] and require higher power lasers for generation compared to HHG [37]. We are mainly interested in using XUV pulses from HHG as a source because of its simple setup for the generation, laser-like coherence and pulse properties and availability compared to other XUV sources.

In order to use XUV pulses from HHG for different applications it is important to optimize the photon number and to characterize the stability, spatial and temporal properties. For experiments like plasma probing [3, 38], holography [39], coherent diffraction imaging [34] and X-ray laser seeding [28, 36] it is necessary to have spatially characterized, energy optimized XUV pulses with stability in pointing and energy.

## 1.2 Topic overview

XUV pulses generated by the process of HHG serves as a competent XUV source which has high spatial and temporal coherence compared to other XUV sources. High harmonics (HHs) are generated by focusing a high intensity laser ( $10^{14}$  W/cm<sup>2</sup> -  $10^{15}$  W/cm<sup>2</sup>) on a gas. HHs can also be generated by focusing a higher laser intensity ( $> 10^{16}$  W/cm<sup>2</sup>) on a solid target. HH spectra from gases are typically composed of discrete lines at odd multiples of the incoming laser frequency, with three characteristic intensity ranges. For lowest order harmonics the intensity decreases rapidly, then reaches a plateau of near-constant emission amplitude for orders typically higher than 7 [40] and a sudden intensity drop at the maximum orders, the so-called cut-off. XUV pulses from HHG have already been used in applications like coherent diffraction imaging (CDI) [41], holography [42, 39], plasma diagnostics [3, 43] and for pump-probe studies of ultrafast processes [44, 45]. The use of characterized XUV sources improves the quality of the results in these applications [46].

The major difficulty in the characterization of XUV pulses are that they have high absorption and low reflectivity in most of the materials [1]. Hence, the characterization of the properties of the XUV pulse has to be carried out using detectors sensitive and optimized for the XUV spectral region. Optimization in

photon number and wavefront is achieved by adjusting the phase matching conditions of the different high-harmonic orders [47, 48, 49, 50, 51]. The spatial profile of the XUV beams is measured using XUV sensitive CCDs. The spectral characterization is performed using XUV spectrometers.

In spatial characterization of XUV pulses and XUV optics, mainly the spatial phase characterization is considered. Knowing the spatial phase of the XUV beam helps to optimize the wavefront of the pulses and thereby improving the focusing of XUV pulses [52]. The spatial properties of the XUV wavefront is characterized using wavefront sensors (WFS) in the XUV [53, 54] and diffraction interferometry [55]. The available WFS in the XUV have lower numerical aperture and this limits the characterization to low divergent XUV sources and optics.

Different ex-situ and in-situ methods [56] have been proposed and used for characterizing the temporal structure of XUV pulses from HHG. In ex-situ method the XUV pulses interacts with a gas jet and the photoelectrons produced are recorded using an electron spectrometer and the temporal structure is retrieved by modeling the interaction of XUV pulses with the gas jet [57, 58]. These methods are more like experiments rather than an easy to setup standalone temporal diagnostics. In in-situ method (all optical methods), the pulse duration is obtained by manipulating the XUV generation process in HHG and detecting the XUV pulses directly [56]. One of the most robust all-optical method based on the similar methods for IR laser pulses is called spectral phase interferometry for direct electric field reconstruction (SPIDER) [59]. The extension of this method to the XUV regime relies on the interference of the XUV pulse with its spectrally sheared replica [60]. This technique requires only optical components and does not require an expensive and difficult to operate electron spectrometer. Additionally, single-shot measurements are possible [59, 60]. Although the in-situ methods are comparatively easy to set-up and use, the generation of a chirped replica of the XUV pulse and its interference with the original pulse is a very difficult task [61, 62].

### 1.3 Thesis outline

In this thesis, the main goal was to study the spatio-temporal characterization of XUV pulses from HHG and further study the use of these characterized XUV pulses in applications such as imaging and plasma diagnostics. The thesis is composed of chapters on generation, characterization (spatial and temporal) of XUV pulses, mainly from HHG and finally the conclusions. The plan of this thesis is outlined below.

The work as a part of the thesis is composed of four main chapters:

- ❖ **High harmonic generation:** The second chapter presents HHG in gases and solids and their comparison. The theory of HHG in gases and solids is described. HHG from gases was the focus of the study and HHG in gases has been setup and optimized using different laser system in different laboratories. Experimental results on HHG in solids is also presented. Finally, the different XUV sources based on HHG are compared.
- ❖ **Spatial metrology of HHG and XUV optics:** The third chapter discusses the calibration of XUV WFSs and wavefront characterization of XUV optics and XUV sources. The XUV WFSs are

calibrated using HHG in gases as the XUV source. The spatial properties of XUV optics and XUV pulses from HHG in gases and solid were characterized using the calibrated XUV WFS. The comparison between the wavefront properties of XUV pulses from HHG in gases and solid are also presented.

- ❖ **Temporal metrology of XUV pulses:** The fourth chapter discusses the temporal characterization of XUV pulses from HHG and FEL. An all-optical method for temporal characterization of XUV pulses from HHG based on SPIDER is discussed. The numerical results and first experimental results are also presented. An all-optical temporal characterization method based on autocorrelation using transient gratings is discussed for XUV pulses from a seeded FEL and the experimental result is presented.
- ❖ **Conclusions and perspectives:** The fifth chapter discusses the conclusions and achievements from work carried out during the thesis. It also discusses future perspectives. The perspectives include a brief discussion about the application of characterized XUV pulses. The use of wavefront correction for in-line holography is presented. The possibility of measuring volumetric plasma parameters using an XUV wavefront sensor in laser-produced plasma is also discussed.



# Chapter 2

## High harmonic generation

### 2.1 Introduction

HHG is a highly nonlinear process [63], in which high-intensity ultrashort laser pulses (typical intensity  $> 10^{13}$  W/cm<sup>2</sup>) interact with a medium (gas or solid) generating higher order harmonics of the fundamental laser frequency. A typical setup for HHG is shown in figure 2.1. In the experimental setup, an IR laser is focused onto a medium using a lens and the higher order harmonics of the laser frequency are generated when phase matching conditions [47, 48, 64] are achieved.

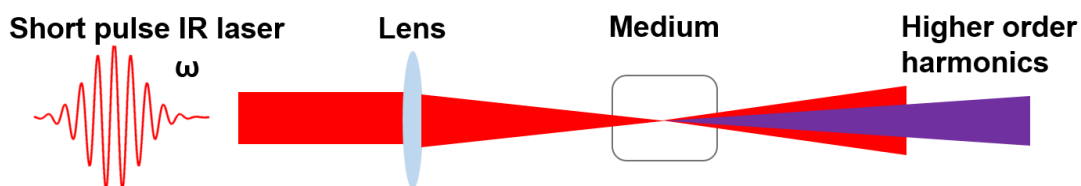


Figure 2.1: Schematic of general experimental setup for HHG.

HHG was first observed in solids using long pulse CO<sub>2</sub> lasers [65] and later in gases during multi-photon emission studies using short pulse IR lasers [40]. HHG was also observed in solids and molecules when interacting with high-intensity ultrashort laser pulses [66, 67]. The study of HHG over the last few decades has enabled generation of sources with never before achievable temporal and spatial resolution [68]. As the process is inherently ultrashort and the naturally produced attosecond timescale pulses [8] of bright coherent X-rays / XUV [69, 70] provides a new tool for ultrafast physics. The process of HHG has been exploited for attosecond imaging of molecular orbitals [6, 7], attosecond studies in spectroscopy [71], to investigate the photo-emission timescales from solids [5], study of ultrafast current switching in solids [72], to study the fundamental timescales of ionization [73], and the real-time observation of electrons tunneling from their atoms for the first time [73]. HHG from gases is the most commonly used source of coherent ultrashort XUV radiation compared to other mediums of HHG. HHG in solids can also be used as a source of XUV radiation as well as to study laser-plasma interactions [74, 70]. In general, HHG from solids is more intense compared to HHG from gases albeit with higher divergence [70, 75]. HHG observed in molecules is mostly used for imaging molecules and the study of

electron dynamics [67].

This chapter presents the theoretical description and the experimental results on HHG from gases and solids. Experimental results were obtained at IST Lisbon - Portugal, LOA - France and Helmholtz Institute Jena - Germany, on HHG and optimization ranging from low intensity gas HHG to relativistic intensity in laser-solid HHG. In the final section, a comparison between different HH sources is presented.

## 2.2 HHG from gases

Coherent XUV sources generated by HHG in gases have undergone significant development in the last few decades. Comparatively low maintenance cost and less complex experimental setups for HHG in gases have helped it to become a widespread complimentary source to XRLs and FELs as a source of high-intensity coherent XUV pulses. Unlike the XRLs and FELs, HHG in gases provides broad spectral bandwidth, spectral tunability, possibility to support attosecond pulses and high coherence. One of the drawbacks with HHG in gases is the comparatively lower photon counts. However single shot imaging applications have been successfully carried out [34, 42]. The availability of high repetition rate tabletop ultrafast laser systems has led to the development of tabletop HHG sources which gained significant attention in the recent years. The HHG in gases provides broadband XUV spectra which have led to the development of ultrashort XUV pulses with pulse duration  $< 100$  attoseconds [33, 32]. This has opened new frontiers in time-resolved studies of ultrafast phenomena [8, 71, 73]. The possibility to achieve spatial resolution in the order of nanometers and temporal resolution in the order of femtoseconds to attoseconds using HHG in gases has resulted in various applications as summarized in the references [27, 68]. The highly coherent XUV pulses from HHG in gases has been used for applications such as monitoring electron motion [6], studying molecular dynamics [7], coherent diffraction imaging [34], plasma probing [3, 76], attosecond pulse generation [77, 8], attosecond spectroscopy [78] and Fourier transform holography [79].

HHG from gases occurs when ultra-short pulse lasers with intensities in the range of  $> 10^{13}$  W/cm<sup>2</sup> to  $< 10^{16}$  W/cm<sup>2</sup> interact with noble gases. Figure 2.2 shows the schematic of a simple setup for HHG. The IR laser is focused using a lens onto a gas cell filled with noble gas and the XUV pulses generated are separated from the lower HH orders and residual IR laser using metallic filters.

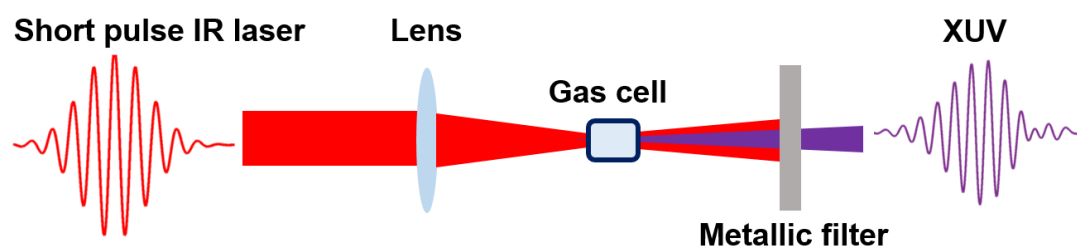


Figure 2.2: Schematic of a simple setup for HHG

HHG from gases has a characteristic spectrum which consists of strong harmonic emission until the first few harmonics and then a plateau of harmonics with a lower efficiency and finally a steep cutoff. The schematic of a typical HHs spectrum is shown figure 2.3. In the plateau region of the spectrum

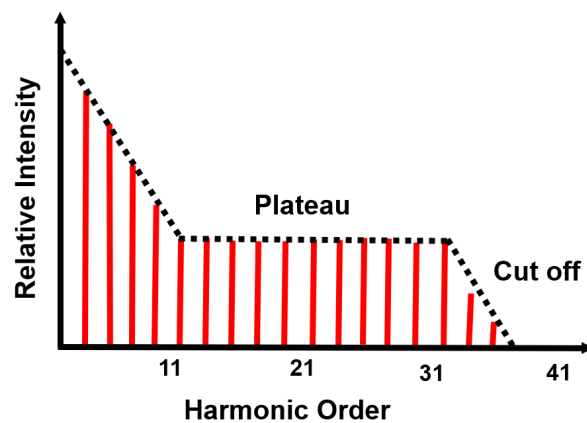


Figure 2.3: Schematic of a typical spectrum for HHG from gases. The high intensity lower harmonic orders, the plateau region and the cutoff of HH orders are shown in the spectrum.

exists several harmonic orders with nearly same intensity and this is contrary to nonlinear optics in the perturbative regime, where the intensity of higher harmonics decreases for higher orders [63]. The plateau region of the HH spectrum falls mostly in the XUV spectral range, when using near IR laser for HHG. Pulses in the water window region of electromagnetic spectrum were also generated by HHG in gases using mid IR lasers [80, 81]. The efficiency of HHG in gases is usually in order of  $10^{-6}$  and for well optimized conditions this may go up to  $10^{-4}$  [47, 51]. With this low efficiency, the HHG produces XUV pulses with single shot energies ranging from few nanojoules to microjoules.

## 2.2.1 Theoretical description of HHG from gases

HHG in gases was first theoretically described using a semi-classical model by Corkum et al. [82]. It is also known as the three-step model or simple man's model. The model considers tunnel ionization of an electron in an atom of a gas medium under the influence of the electric field of a high intensity laser pulse [82] to explain this extreme nonlinearity in HHG unlike the classical nonlinear optics where perturbation of polarization is considered to explain nonlinear behavior under the high intense laser pulse [63]. Later Lewenstein et al. [83] provided a quantum mechanical model for HHG in gases. The theory describes the single atom response under the electric field of an ultrashort laser pulse and for coherent build up of HH signal it is necessary to consider the macroscopic phase matching of the HHs generated.

### 2.2.1.1 Three step model

The model explains the ionization of atoms in the electric field of the ultrashort laser pulse by tunnel ionization, a quantum mechanical concept, and the movement of electrons in the electric field of a laser, which is expressed by the classical Lorentz force [82]. According to the three-step model, HHG in gases involves three steps: tunnel ionization of electron, movement of the electron in the electric field of the laser and then electron recombination with the ion within a certain probability and the energy gained by the electron during its movement in the electric field of the laser is emitted as radiation. Figure 2.4 shows a pictorial representation of the three-step model for HHG from gases. The three-step model is explained below, considering a single atom response. In the first step of the three-step model, the

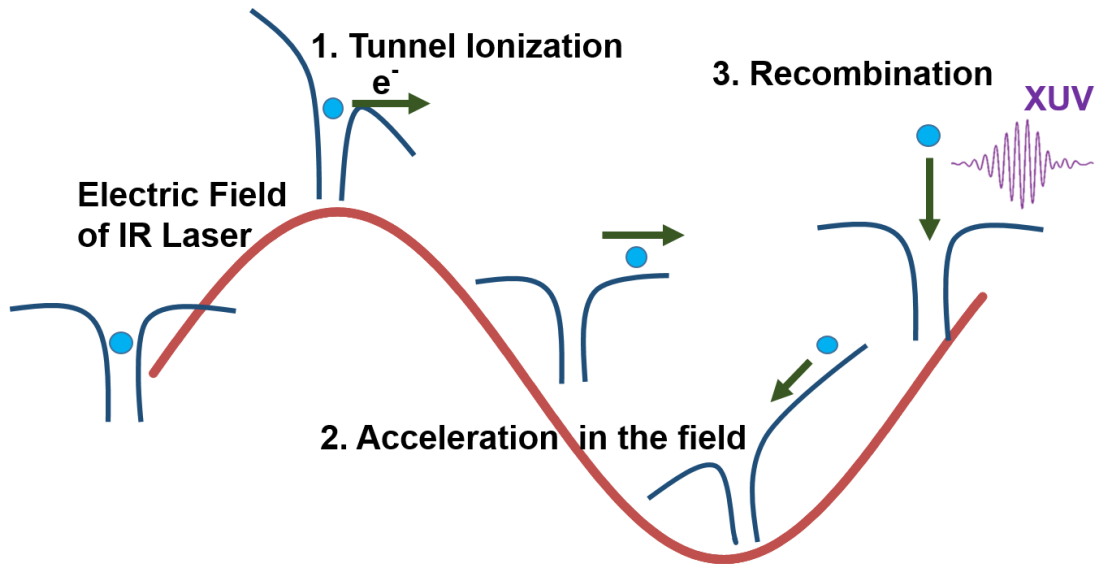


Figure 2.4: Pictorial representation of the three-step model for HHG from gases. The sinusoidal curve in red shows the electric field of the laser. The motion of the electron, shown in the blue circle, under the effect of electric field and emission of XUV radiation on recombination are shown in the picture.

high-intensity laser pulse interacts with the noble gas and depending on the intensity of the laser and the ionization potential of the atom, the ionization can happen in three different regimes: above-threshold ionization, tunnel ionization and multi-photon ionization. The regime of ionization is determined by the Keldysh parameter  $\gamma$  and it is given by [84]

$$\gamma = \sqrt{\frac{I_p}{2 U_p}} \quad (2.1)$$

where  $I_p$  is the ionization potential of the atom and  $U_p$  is the pondermotive force exerted by the laser on the atoms and it is given by [84]

$$U_p = \frac{e^2 E^2}{4 m_e \omega_0^2} \propto I_L \lambda_L^2 \quad (2.2)$$

where  $e$  is the charge of an electron,  $E$  is the amplitude of the electric field of the laser,  $m_e$  is the mass of the electron,  $\omega_0$  is the frequency of the laser,  $I_L$  is the intensity of the laser and  $\lambda_L$  is the wavelength of the laser. In the three-step model, tunnel ionization is considered to explain the HHG from gases and hence,  $\gamma < 1$  [84]. The electric field of the laser causes the lowering of the Coulomb potential for the valence electron in the atom and this gives a higher probability for the electron to move into the continuum states and thus ionizes the atom. The ionization rate, in this case, can be calculated using the ADK (Ammosov-Delone-Krainov) theory [85]. In the second step this electron, which is now in the continuum starts with zero velocity gets accelerated in the electric field of the laser. The trajectory of the electron can be calculated by considering a non-relativistic movement of the electrons in the alternating electric field of the laser [82] and here the magnetic field of the laser is neglected. The position of the electron in the electric field,  $E(t) = E_0 \cos[\omega t]$  can be calculated with the following equation [86],

$$x = \frac{-eE}{\omega_0 m_e} \left( \frac{\cos[\omega t_0]}{\omega} - \frac{\cos[\omega t]}{\omega} + \sin[\omega t_0](t - t_0) \right) \quad (2.3)$$

where  $t$  is the time and  $t_0$  is the time at which the electron tunnels into the continuum. Depending on the phase of the electric field at the point where the electrons are tunneling into the continuum states, the electrons can return to the ion or not. The trajectory of the electron can be short or long with equal kinetic energy depending on the phase at which the electron interacts with the electric field of the laser. Figure 2.5 shows a simulation of electron trajectories using equation 2.3 under the electric field of the laser with ionization happening in different phases in the laser cycle. The calculation was carried-out assuming a central wavelength of 800 nm and a peak intensity of  $1 \times 10^{14}$  W/cm<sup>2</sup> for the laser. The different trajectories of the electrons tunneling into the continuum are shown in blue, green and violet. The electron trajectories shown in green and violet shows the electrons returning to zero position and recombines with the ionized atom and electrons in other trajectories shown in blue does not recombine with the ionized atom. The electron trajectories shown in green are called the short trajectory and the electron trajectories shown in violet are called long electron trajectories. The electrons traveling in the long trajectory spend more time in the continuum and gain energy slower compared to electrons in the short trajectory. Despite having two trajectories, electrons from both long and short trajectories recombine with the ion with same kinetic energy. The divergence of the radiation emitted on recombination of electrons traveled in the short trajectory is smaller compared that from the long trajectory [87].

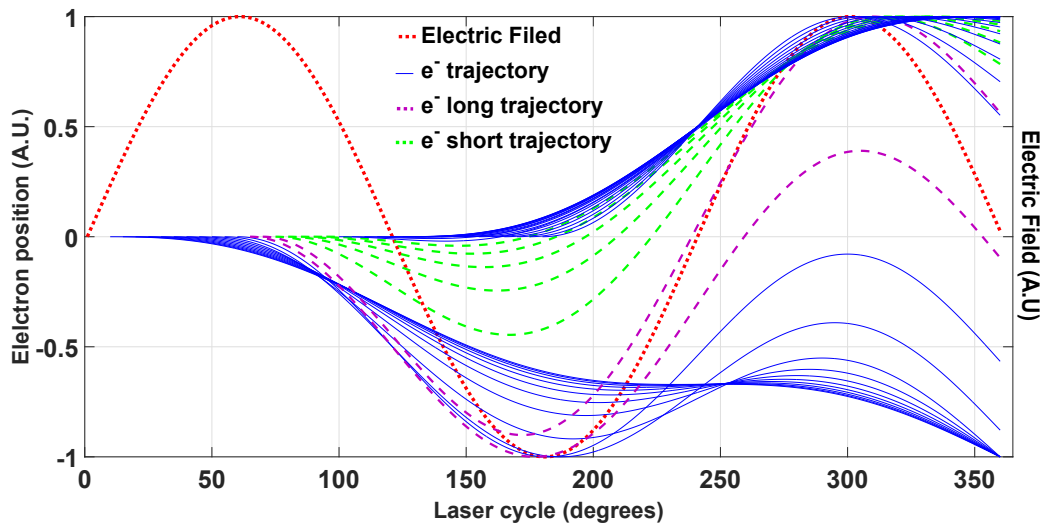


Figure 2.5: The trajectory of electron in the electric field of the laser with ionization at different phases of the laser cycle (calculated using the equation 2.3). The red dotted line shows the electric field amplitude and the blue, green and violet lines shows the different electron trajectories.

In the third step, the electrons which return may recombine with the ion with a certain probability. During the recombination, the kinetic energy, which the electron gained during its travel in the electric field is emitted as radiation. The emitted radiation can be written as

$$\hbar\omega = I_p + E_{kin} \quad (2.4)$$

where  $\hbar$  is the reduced Planks constant,  $\omega$  is the frequency of the emitted radiation and  $E_{kin}$  is the kinetic energy gained by the electron in the electric field of the laser. The maximum kinetic energy ( $E_{max}$ ) that

the electron can gain in the electric field of laser can be written as

$$E_{max} = I_p + 3.17 U_p \quad (2.5)$$

The three step model gives a general understanding of the HHG in gases and also gives an idea of the highest frequency of radiation emitted from HH generation, a cutoff law (from 2.4 and 2.5) in case of a single atom response. However it is still not able to explain the characteristic spectrum of the HHG shown in figure 2.3. For further understanding, a full quantum mechanical study of HHG is required.

### 2.2.1.2 The Lewenstein model

Lewenstein et al., proposed the full quantum mechanical explanation of HHG in gases [83]. The model considers strong field approximation (SFA) for ionization of the atoms and solves the time dependent Schrödinger equation (TDSE) for the system of bound electrons in the atom and the laser electric field [83]. The TDSE considering the dipole approximation in the case of a single electron activity is given by [83]

$$i \frac{\partial}{\partial t} |\psi(\vec{x}t)\rangle = \left[ -\frac{1}{2} \nabla^2 + V(\vec{x}) - E \cos(t)x \right] \frac{\partial}{\partial t} |\psi(\vec{x}t)\rangle \quad (2.6)$$

where  $V(\vec{x})$  is the Coulomb potential which binds the electron with the atom and  $E \cos(t)x$  is polarized electric field of the laser in the  $x$  direction. Atomic units are considered in this equation, where  $\hbar = e = m_e = c = \epsilon_0 = \omega = 1$ . Here  $\epsilon_0$  is the vacuum permittivity and  $\omega$  is the laser field frequency. The assumptions in the three step model, tunnel ionization and neglecting magnetic field of the laser field is also considered in the Lewenstein model. The time dependent wave functions can be written as [83]

$$|\psi(\vec{x}t)\rangle = a(t)|0\rangle + \int d^3 d_x^*(\mathbf{v}) b(\mathbf{v}, t) |\mathbf{v}\rangle \quad (2.7)$$

where  $a(t) \simeq 1$  is the ground state amplitude,  $d_x$  is the dipole matrix elements for bound-free transitions considering a laser with a linear polarization in the  $x$  direction,  $\mathbf{v}$  is the kinetic momentum of the electron which undergoes transition to continuum and  $b(\mathbf{v}, t)$  are the amplitudes of the continuum states. The time dependent dipole moment and therefore the electron position for the  $x$  component is given by [83]

$$x(t) = \langle \psi | x | \psi \rangle \quad (2.8)$$

With the knowledge of the expression for the amplitude of  $b(\mathbf{v}, t)$ , the above equation can be written as [83]

$$x(t) = \int d^3 \mathbf{v} b(\mathbf{v}, t) + c.c \quad (2.9)$$

With the introduction of a new variable which is a canonical moment,  $\mathbf{p} = \mathbf{v} + \mathbf{A}(t)$  with a vector potential  $\mathbf{A}(t) = \int_{-\infty}^t E(t') dt'$ , the equation 2.9 can be written as [83]

$$x(t) = i \int_0^t dt' \int d^3 \mathbf{p} E \cos(t') d_x(\mathbf{p} - \mathbf{A}(t')) \cdot d_x^*(\mathbf{p} - \mathbf{A}(t')) \exp[-iS(\mathbf{p}, t, t')] + c.c., \quad (2.10)$$

where  $iS(\mathbf{p}, t, t')$  is the quasi-classical action and it is given by [83]

$$S(\mathbf{p}, t, t') = \int_{t'}^t dt'' \left( \frac{(\mathbf{p} - \mathbf{A}(t''))^2}{2} + I_p \right) \quad (2.11)$$

The equation 2.10 can be interpreted as the sum of probability amplitudes corresponding to the three different steps of the three steps model (2.2.1.1). The first term,  $d^3\mathbf{p} E \cos(t') d_x(\mathbf{p} - \mathbf{A}(t'))$  gives the probability amplitude for the electron to make a transition from the bound states to the continuum states at a time  $t'$  with a canonical momentum  $\mathbf{p}$ . The electronic wave function is propagated until the time  $t$  and it acquires a phase factor which is given by  $\exp[-iS(\mathbf{p}, t, t')]$ . The probability amplitude for recombination of the electron with the ion is given by the term  $d_x^*(\mathbf{p} - \mathbf{A}(t'))$ . The spectral intensity of harmonic emission  $I(\omega)$  can be then obtained by the Fourier transform of the dipole moment  $x(t)$  and it is given by [83]

$$I(\omega) = \left| \int x(t) \exp[-i\omega t] dt \right|^2 \quad (2.12)$$

The Lewenstein model gives a quantum mechanical explanation for the HHG in gases. However, it only describes the motion of single electron under strong field approximation and considers that the electron is always in the ground state. The model also does not include the propagation effects. Further discussion on propagation effects is required to completely explain the coherent buildup and emission of HHs.

### 2.2.1.3 Phase matching

So far only the single atom response to the laser field has been discussed. For having a considerable amount of HH signal, HHG from many atoms and its coherent addition over the length of the HHG medium needs to be achieved. The incident laser and the different HH orders generated during HHG propagate through the medium of generation with different group velocities because of the wavelength dependent refractive index of the medium. For a coherent build up of the HH signal, different parameters of the laser and the medium have to be controlled and balanced. This process is called phase matching [63]. Analogous to classical nonlinear optics the phase matching is written in terms of the dispersion introduced by the medium on the different HH orders. The phase mismatch  $\Delta k$  for HHG in gases is given by [48]

$$\Delta k = \Delta k_N + \Delta k_P + \Delta k_{Gouy} + \Delta k_{at} \quad (2.13)$$

where

❖  $\Delta k_N$  is the phase mismatch introduced by the neutral gaseous medium for HHG. It is given by

$$\Delta k_N = \frac{2\pi q}{\lambda} (n(\lambda) - n(\lambda_q)) \frac{p}{p_{atm}} (1 - \eta) \quad (2.14)$$

where  $q$  is the HH order,  $\lambda$  is the laser wavelength,  $\lambda_q$  is the HH wavelength,  $n(\lambda)$  is the wavelength dependent refractive index of the medium for the laser,  $n(\lambda_q)$  is the wavelength dependent refractive index of the medium for different HH order,  $p$  is the pressure of the gas medium,  $p_{atm}$  is the atmospheric pressure and  $\eta$  is the ionization fraction and it is given by the ratio of electron number

density to atomic number density ( $\eta = N_e/N_{at}$ ). The phase mismatch caused by the neutral gas can be controlled primarily by controlling the gas pressure and the ionization fraction.

- ❖  $\Delta k_P$  is the phase mismatch introduced by the change in dispersion caused by the electrons which are generated as a result of the ionization of the gaseous medium by the laser. It is also called plasma induced phase mismatch. It is given by

$$\Delta k_P = N_{atm} \frac{p}{\rho_{atm}} \eta \lambda r_e \left( \frac{1 - q^2}{q} \right) \quad (2.15)$$

where  $N_{atm}$  atomic number density at standard temperature and pressure (STP),  $r_e$  is the classical electron radius.  $r_e$  is given by

$$r_e = \frac{1}{4\pi\epsilon_0} \frac{e^2}{m_e c^2} \quad (2.16)$$

where  $\epsilon_0$  is the permittivity of free space and  $c$  is the speed of light. The plasma induced phase mismatch can be controlled primarily by controlling the intensity of the laser at the focus and there by controlling the ionization of the gaseous medium and the gas pressure.

- ❖  $\Delta k_{Gouy}$  is the phase mismatch introduced by focusing of the laser in the gas. It results from the Gouy phase shift of  $\pi$  introduced for a Gaussian beam when focused. It is also called the geometrical phase mismatch since it comes from the focusing geometry. This results in a  $\pi$  phase change in the phase velocity of the laser. The phase mismatch introduced by the Gouy phase from the laser focusing is given by [48]

$$\Delta k_{Gouy}(z) = q \frac{\pi \lambda \omega_0^2}{\pi^2 \omega_0^4 + \lambda^2 z^2} \quad (2.17)$$

where  $\omega_0$  is the beam waist of the driving laser at  $1/e^2$  of the intensity,  $z$  is the propagation distance of the laser with  $z = 0$  at the focus. For  $z = 0$ , i.e when the laser focused at the center of the medium, the phase mismatch introduced can be written as

$$\Delta k_{Gouy}(z) = \frac{q}{z_R} \quad (2.18)$$

where  $z_R$  is the Rayleigh length given by

$$z_R = \frac{\pi \omega_0^2}{\lambda} \quad (2.19)$$

The geometrical phase mismatch can be controlled primarily by changing the focal spot size.

- ❖  $\Delta k_{at}$  is the phase mismatch as a result of the generation of HH from single atom with a phase depending on the intensity of the laser [87]. It is also called the atomic phase mismatch. It is given by

$$\Delta k_{at}(z) = \alpha_i \frac{8 I_0 z}{z_f^2 \left( 1 + \frac{4z^2}{z_R^2} \right)^2} \quad (2.20)$$

where  $\alpha_i$  is a coefficient associated with the electron trajectory ( $i = 1$  for short trajectory and  $i = 2$  is for the long trajectory) with its value is in the order of  $10^{-14}$  cm<sup>2</sup>/W [87] and  $I_0$  is the laser intensity

at the focus.

The different phase mismatch parameters can be controlled in the experiment by scanning the different experimental parameters. In an experiment, the laser parameters which can be controlled are pulse energy, pulse duration, focal spot diameter and focus position with respect to the center of the gas medium, beam diameter and focal length of the lens. The gas the parameters which can be controlled are the gas species, pressure, gas cell geometry or gas jet distribution. For constructive interference of the generated HH orders, the phase mismatch  $\Delta k$  is minimized. The propagation distance over which a HH order constructively interfere is called the coherence length for HHG ( $L_{coh}$ ) and it is given by

$$L_{coh} = \frac{\pi}{\Delta k} \quad (2.21)$$

where  $\Delta k$  is the phase mismatch between the fundamental laser field and the  $q^{th}$  HH order [47]. The intensity of a single HH order after the coherent addition from the HHG can be written as [64],

$$I \propto L_{med}^2 \frac{\sin^2\left[\frac{\Delta k L_{med}}{2}\right]}{\left(\frac{\Delta k L_{med}}{2}\right)^2} \quad (2.22)$$

where  $L_{med}$  is the length of the HHG medium. The equation 2.22 gives a quadratic increase of the HH signal with the increase of the length of the medium without considering the re-absorption. The HH intensity considering the re-absorption along the propagation direction is given by [47]

$$I = \rho^2 A_q^2 \frac{4L_{abs}^2}{1 + 4\pi^2\left(\frac{L_{abs}^2}{L_{coh}^2}\right)} \left( 1 + \exp\left[-\frac{L_{med}}{L_{abs}}\right] - 2\cos\left[\frac{\pi L_{med}}{L_{coh}}\right] \exp\left[\frac{L_{med}}{L_{abs}}\right] \right) \quad (2.23)$$

where  $\rho$  is the gas density,  $A_q$  is the individual HH signal calculated using the Lewenstein Model (2.2.1.2) and  $L_{abs}$  is the absorption length for the HH orders. The  $L_{abs}$  is give by

$$L_{abs} = \frac{1}{\rho\sigma} \quad (2.24)$$

where  $\sigma$  is the ionization cross section for th medium.

For experiments, we need to have a relation on how the HH intensity changes with the use of different gas cell or gas medium length and phase matching. Figure 2.6 shows the variation of HH intensity with respect to the length of the HHG medium  $L_{med}$  at different  $L_{coh}$  and  $L_{abs}$  values. Here the HH intensity saturates after  $L_{med}$  is few times  $L_{abs}$  and when  $L_{coh} \leq L_{abs}$  there is no coherent build up of HH signal. For the optimization of HH signal the condition relating  $L_{abs}$ ,  $L_{med}$  and  $L_{coh}$  is given by [47],

$$L_{med} > 3L_{abs} \text{ and } L_{coh} > 5L_{abs} \quad (2.25)$$

In the experiments,  $L_{med}$  and  $L_{abs}$  are fixed depending on the length of the gas cell used and  $L_{coh}$  depends on the phase matching of HHs. Equation 2.25 gives the limit on how long the gas medium needs to be for maximum HH yield under optimized conditions.

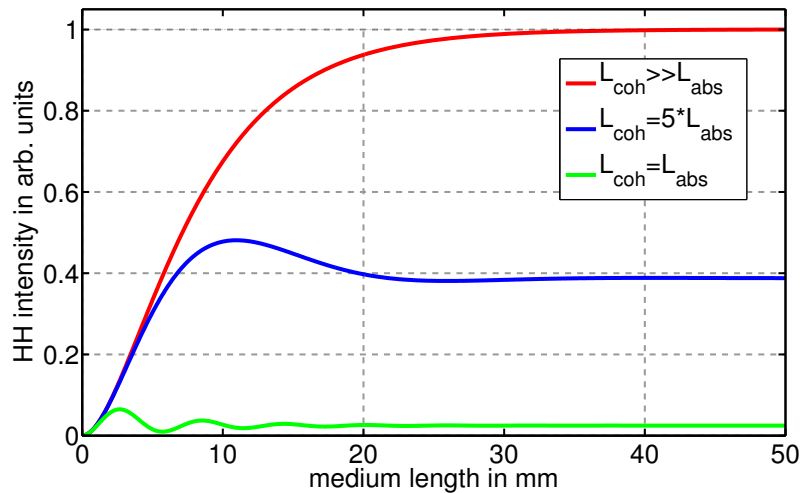


Figure 2.6: HH signal calculated with the equation 2.23 for HH order 25 generated with driving laser of wavelength 800 nm in argon with at 30 mbar of pressure at different coherence lengths. Taken from [86]

## 2.2.2 Experimental results on HHG and global optimization

The generation of XUV pulses by HHG in gases was studied experimentally using different laser systems in different laboratories. The HHG was optimized in terms of photon counts under the available conditions and spectral characterization was also performed. These experimental results are presented in this section.

### 2.2.2.1 L2I, IPFN, IST Lisbon, Portugal

HHG at the Laboratory for Intense Lasers (L2I) in IPFN, IST was performed using an in-house built diode pumped laser system [88]. The laser is a chirped pulse amplification (CPA) system consisting of two stages of amplification. The laser systems start with a Ti:Sapphire Oscillator, MIRA900 from Coherent Inc with a central wavelength of 1030 nm. The nanojoule, 120 fs pulses from the oscillator are stretched using gratings and then it is seeded to the diode-pumped double stage amplifier system. The first stage amplifier is a regenerative amplifier with a Yb:CaF<sub>2</sub> crystal and pumped by diodes. This stage amplifies the seed pulse energy from few nano-joules to few millijoules with an output central wavelength at 1030 nm. The pulses are further amplified by a second amplifier stage which is a multi-pass amplifier with a Yb:YAG crystal as the amplification medium pumped and laser diodes for pumping. The second stage amplifies the pulses to nearly 100 mJ with tens of ps pulse duration. These amplified pulses are temporally compressed using a compressor to generate pulses with energy  $\sim 30$  mJ and a pulse duration of  $\sim 1000$  fs at 1030 nm. The laser has a repetition rate of 1 Hz. Since both amplifications stages are diode pumped, the laser system is compact and easy to operate compared to a glass-based laser system. Figure 2.7 shows the block diagram for the experimental setup for HHG at L2I. It consists of the laser part and the experimental part.

The laser, after compression, is steered into the vacuum chamber using dielectric mirrors. The schematic and picture of HHG experimental part are shown in figure 2.8. The setup can be used to obtain

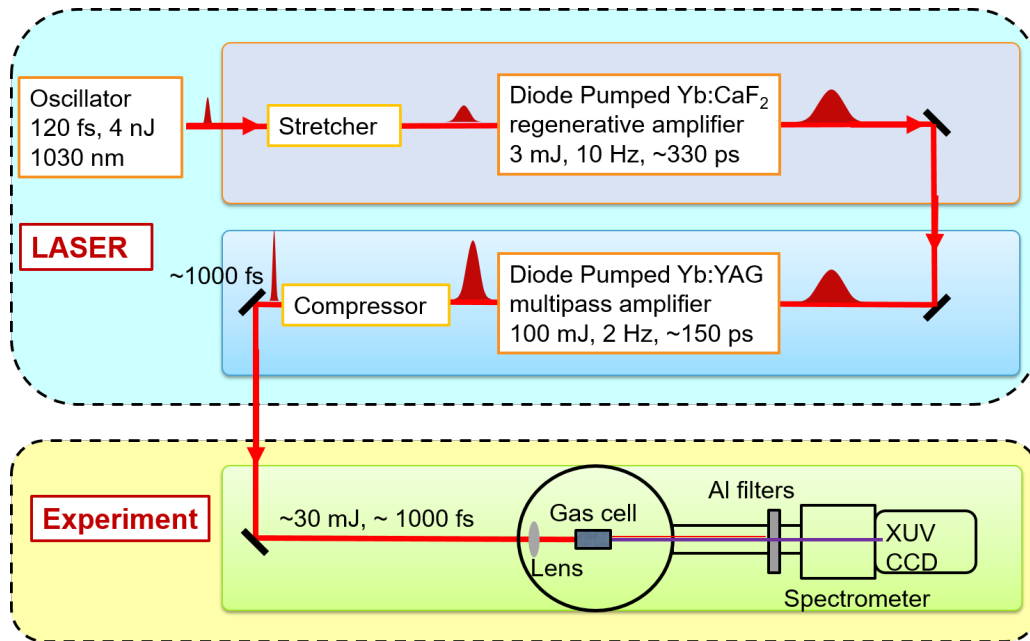


Figure 2.7: Block diagram of the experimental setup for HHG with the laser system at L2I, IPFN, IST.

the HH footprint (cross-section of the spatial intensity distribution) in the far-field or the spectrum. The experimental setup for the HH footprint is shown in figure 2.8a. In the experimental setup, motorized plano-convex lenses with different focal lengths which are placed inside the vacuum chamber were used to focus the IR beam in the gas cell (see the inset in figure 2.8a) with a length of 10 mm. The gas cell was filled with noble gases, argon or xenon separately. XUV pulses generated are filtered from the residual IR pulse using two nickel grid supported aluminum filters of thickness 150 nm for each. After the aluminum filters, an XUV sensitive CCD was placed to record the HH footprint. The CCD used was PIXIS-XO: 1024B back illuminated and thinned imaging X-ray CCD from Princeton Instruments. The CCD has  $1024 \times 1024$  pixels with a pixel size of  $13 \mu\text{m} \times 13 \mu\text{m}$ . The setup for obtaining HH spectrum is shown in figure 2.8b. The spectrometer used is an imaging XUV spectrometer described in reference [86]. The XUV spectrometer consists of a spherical concave focusing mirror with a radius of curvature (ROC) of 8 m placed at a grazing incidence of  $9^\circ$  with respect to incident beam and it is followed by a transmission grating (1000 lines / mm) and an X-ray CCD. The XUV generated at the gas cell was imaged onto the CCD through the transmission grating by the spherical mirror. The spherical mirror was placed at 50 cm from the CCD.

For HHG, the IR laser energy used after compression was  $\sim 30$  mJ with a pulse duration of 1000 fs. The high-harmonic photon count was optimized for two noble gases, argon and xenon. The optimization was carried out by changing the following parameters in the experimental setup the focal length of the lens, gas cell length, the position of focus, gas pressure and laser beam diameter before the lens. The optimized total energy of all harmonic orders was calculated by taking into account the quantum efficiency and gain of the CCD and central frequency of the high-harmonic spectrum. Furthermore, the used Al filter with a thickness of 150 nm on a nickel support grid was cross-calibrated with a second Al filter, which resulted in a transmission of 40%. In the case of both gases, the aperture before the lens was reduced to

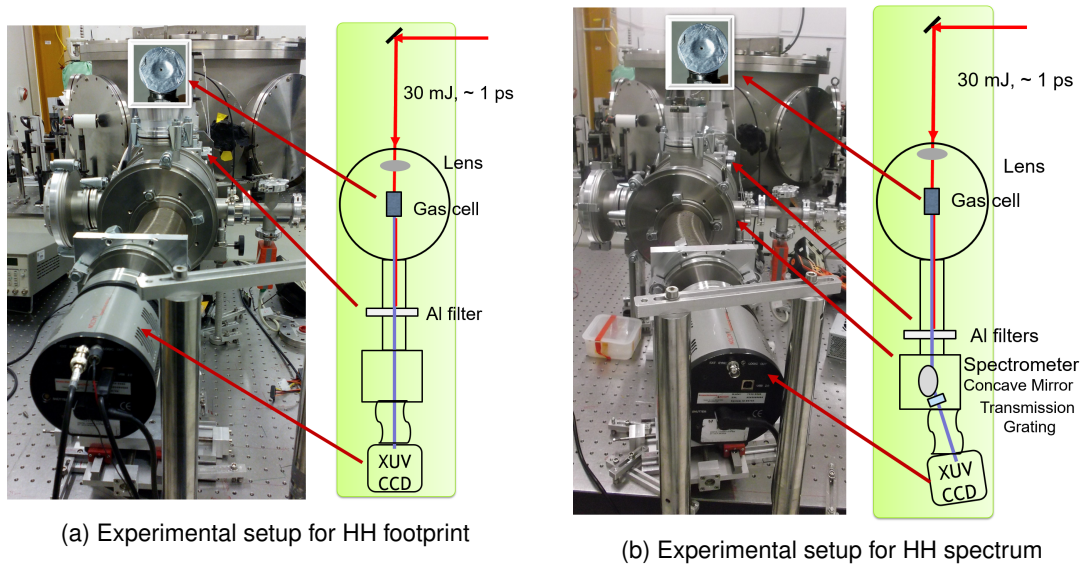


Figure 2.8: Experimental setup for HHG at L2I, IPFN, IST. The gas cell used for HHG is shown in the inset.

9 mm and a pulse energy of  $\sim 10$  mJ measured after the aperture. The focus was placed at the exit of the gas-cell for optimized HHG. The optimization parameters are listed in table 2.1. Figure 2.9 shows the optimized HH beam cross-section and spectrum for argon and xenon. The periodic structure results from a near-field diffraction effect from the nickel support grid of the filter.

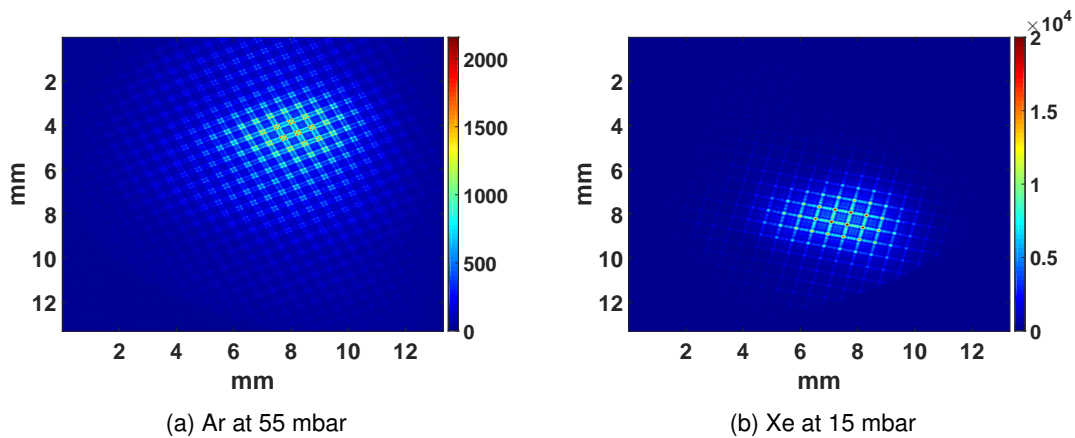


Figure 2.9: Optimized HH cross-section for (a) argon and (b) xenon gases.

The total number of XUV photon ( $N_p$ ) at a particular wavelength ( $\lambda$ ) can be estimated from the images recorded by the CCD using the following equation [16, 86]

$$N_p(\lambda) = \frac{N_c G}{QE(\lambda) (E_{\text{photon}}/3.65)} \quad (2.26)$$

where  $N_c$  is the number of counts in the CCD,  $QE(\lambda)$  is the quantum efficiency of the CCD,  $E_{\text{photon}}$  is the single photon energy in eV and 3.65 eV is the band gap of silicon in eV.  $E_{\text{photon}}/3.65$  is the number of electron generated per photon.  $G$  is the analogue to digital conversion gain of the CCD (PIXIS-XO) and it can be set as 1, 2 and 3, and this corresponds 3.56, 1.84 and 1 electrons per CCD count respectively.

From the photon number, the HH energy is given by

$$E_p(\lambda) = N_p(\lambda) \frac{hc}{\lambda} \quad (2.27)$$

where  $h$  is the Plank's constant,  $c$  is the speed of light and  $\lambda$  is the HH wavelength. The energy is finally calculated considering the aluminum filter transmission. The results after estimating the photon number

Parameters	Units	Argon	Xenon
IR beam size	mm	9	9
Focal length	mm	500	700
Gas pressure	mbar	55	15
HH photon number	per shot	$7.7 \times 10^7$	$3.6 \times 10^8$
Total energy of HHs	nJ	0.44	1.44
Divergence horizontal	mrad	2.48	1.89
Divergence vertical	mrad	2.18	1.25

Table 2.1: Optimized operating conditions for HHG in argon and xenon calculated for the whole HH spectrum

and the energy are listed in table 2.1. The spatial profile and shot-to-shot stability of the HHs beam from argon and xenon was also measured and figure 2.10 shows the shot to shot stability analysis.

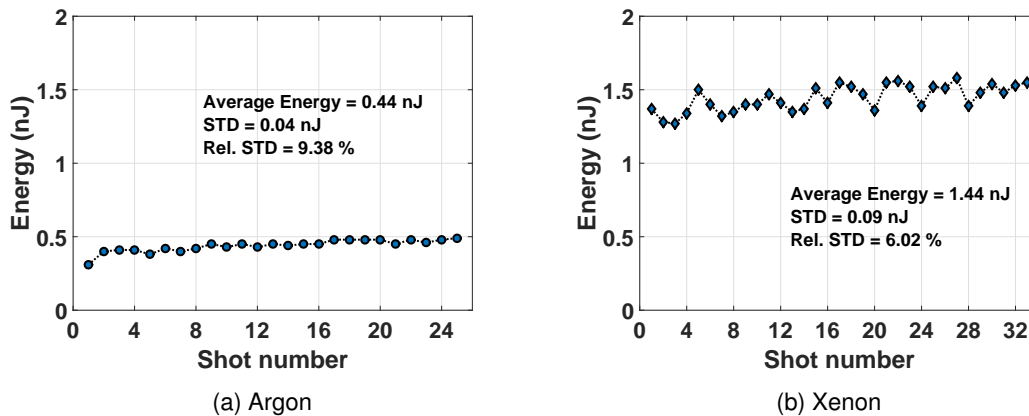


Figure 2.10: Single-shot energy stability analysis for high-harmonics generated in argon and xenon

At the optimized HHG conditions listed in table 2.1, the spectrum of HHG in argon and xenon was recorded. Figure 2.11a and 2.11b shows the image and calibrated line-out of the spectrum for HHG from argon. The XUV spectrum from HHG in argon consists of 9 harmonic orders ranging from 23<sup>rd</sup> harmonic of 1030 nm to 39<sup>th</sup> harmonic. Nearly 70 % of the total energy of the harmonic spectrum is concentrated in three harmonics orders, 31, 33 and 35.

Figure 2.12a and 2.12b shows the image and calibrated line-out of the spectrum for HHG from xenon. The XUV spectrum from HHG in xenon consists of 4 harmonic orders ranging from 17<sup>th</sup> harmonic of 1030 nm to 23<sup>rd</sup> harmonic. Nearly 44 % of the total energy of the harmonic spectrum is concentrated in 21<sup>st</sup> harmonic order.

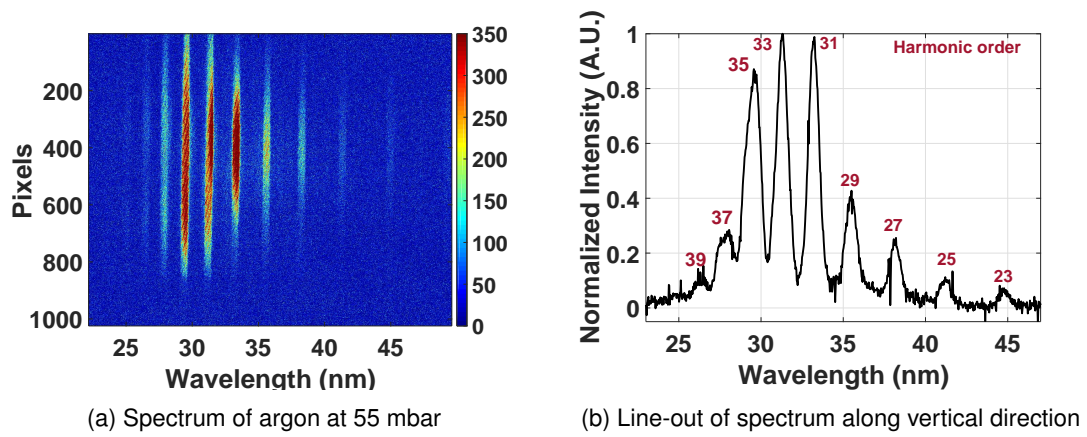


Figure 2.11: The optimized HH spectrum for argon at L2I, IPFN.

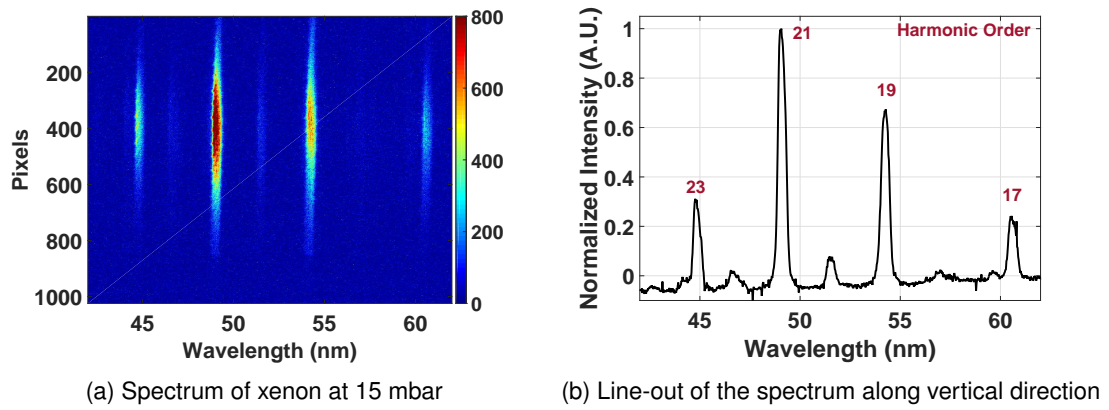


Figure 2.12: The optimized HH spectrum for xenon at L2I, IPFN. The low intense lines in the picture in (a) and low intense peaks in the line-out in (b) are the diffraction pattern of the XUV beam from the supporting grid of the grating.

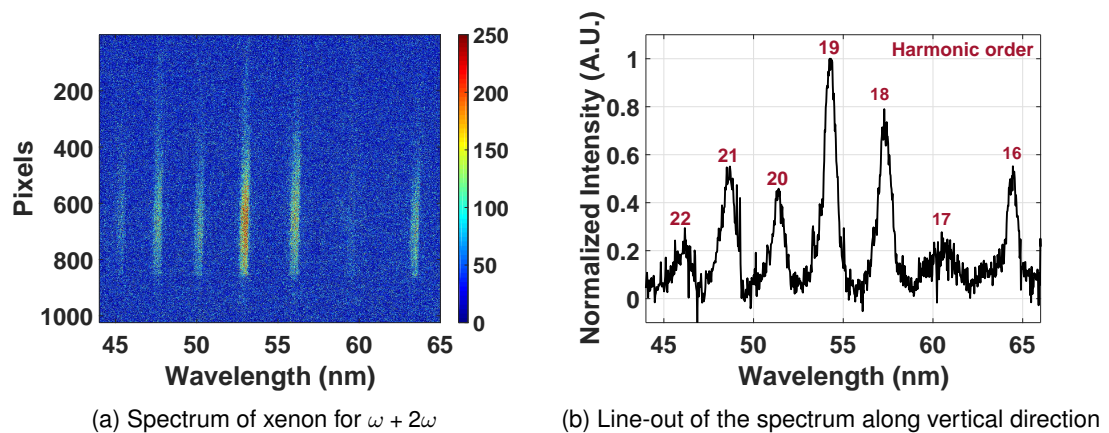


Figure 2.13: The optimized HH spectrum for xenon with fundamental and second harmonic beams at L2I, IPFN

HHG using the IR laser and its second harmonic was also tested at L2I. A KDP crystal was used to generate the second harmonic of the IR laser with 10% efficiency. Because of reduction in the energy after the SHG, the HHG was only observed in xenon which has lower ionization potential compared to argon. The spectral intensity was optimized for HHG in xenon with  $\omega$  and  $2\omega$  fields at the same conditions as that of HHG in xenon with only  $\omega$  field. Figure 2.13a and 2.13b show the image and calibrated line-out of the spectrum for HHG from xenon using IR laser ( $\omega$ ) and its second harmonic ( $2\omega$ ). The spectrum shows both odd and even harmonics as expected for the cases with  $\omega$  and  $2\omega$  [89, 90]. The XUV spectrum consists of 7 harmonic orders ranging from 16<sup>th</sup> harmonic of 1030 nm to 22<sup>nd</sup> harmonic. Compared to the HHG spectrum from xenon with just IR laser in figure 2.12, the spectrum with  $\omega$  and  $2\omega$  has more harmonic orders and also a shift in the spectral energy distribution to lower order harmonics. The shift is due to the presence of  $2\omega$  field which reduces the cutoff of the HHs as the cutoff is proportional to the wavelength as shown in equation 2.5 [90]. The energy of XUV pulses from HHG with  $\omega$  and  $2\omega$  fields was around 0.04 nJ considering the whole spectrum. This is two orders lower in energy compared to the XUV pulse energy for HHG in xenon with only the fundamental laser field. This might be because of the lower pulse energy in  $\omega$  and  $2\omega$  after the SHG and also the fact that the delay between the IR and SH pulses was not controlled.

XUV sources from HHG in argon and xenon were optimized and characterized in pulse energy and spectrum. The XUV sources with a different spectrum of wavelengths can be now used for different applications. HH from xenon gives more energy per shot compared to HH from argon and can be used for single shot experiments. However, HH from argon goes to shorter XUV wavelengths and hence can be used for XUV imaging.

### 2.2.2.2 Salle Corail, LOA, France

HHG in different noble gases was successfully carried out at Salle Corail, Laboratoire d'Optique Appliquée (LOA), France. The HH beamline consists of a high repetition rate laser system, beam transport using dielectric mirrors and vacuum chambers for HHG.

The laser system at the HH beamline in Salle Corail is a commercial laser system from Coherent Inc., called Legend Elite Duo. It is a Ti:Sapphire laser system. It consists of a two-stage amplification system based on Ti:Sapphire crystals. The seed from an oscillator first passes through a regenerative amplifier followed by a single pass amplifier. The output the laser used in the high harmonic beamline has a central wavelength of 800 nm, pulse duration < 40 fs, pulse energy of 3.5 mJ which can be increased up to 5 mJ and a repetition rate of 4 kHz which can be increased up to 5 kHz.

Figure 2.14 shows the schematic of the HH beamline at Salle Corail, LOA. The beamline consists of three vacuum chambers, gas cell chamber, diagnostic chamber and experimental chamber. The gas cell chamber has a gas cell placed in the middle of the chamber and can be pressurized with different gases through a gas feed-through. The diagnostic chamber is mainly used for measuring the spectrum of HHs generated. The experimental chamber is where the different experiments using the XUV pulses are performed. Figure 2.15 shows a picture of the beamline with the three different vacuum chambers.

For HHG, the IR laser is focused on a gas cell of length 15 mm in the gas cell chamber using

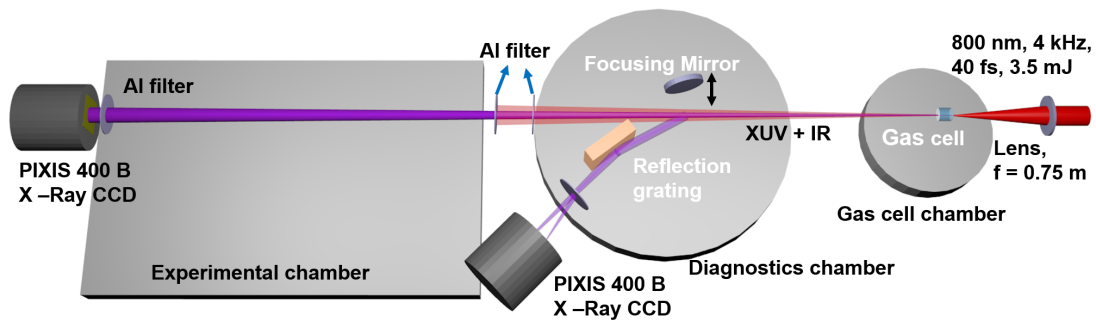


Figure 2.14: Schematic of the HH beamline at Salle Corail, LOA.

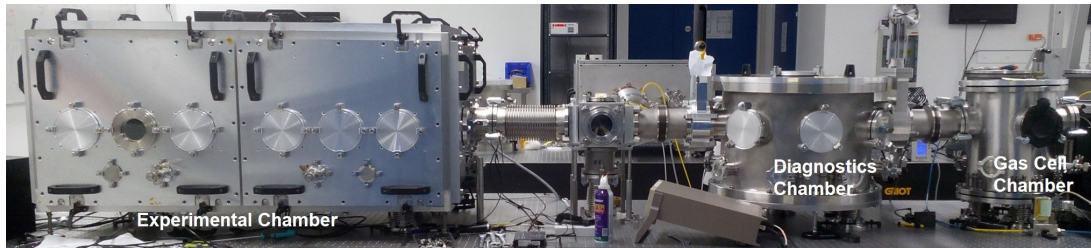


Figure 2.15: HH beamline at Salle Corail, LOA.

a plano-convex lens with a focal length of 750 mm. The XUV beam produced in the gas cell chamber travels through the diagnostic chamber and two free-standing aluminum filters of thicknesses 150 nm, and 300 nm were placed before the experimental chamber to filter-out the residual IR laser. A PIXIS: 400 B X-ray CCD from Princeton instruments with  $1340 \times 400$  square pixels with a pixel size of  $20 \mu\text{m}$  was placed at the end of the experimental chamber to record the high harmonic footprint. The HHG was optimized in argon and neon in terms of photon count. Figure 2.16a and 2.16b shows the footprint of optimized HHG from argon and neon respectively.

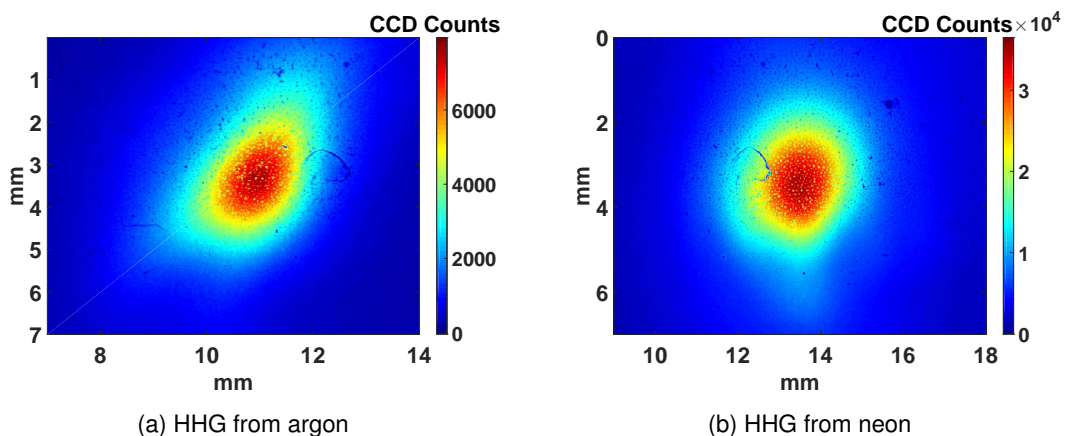


Figure 2.16: Optimized HH intensity cross-section at Salle Corail, LOA

The parameters for typical operating conditions for HHG using argon and neon are listed in table 2.2. From the CCD counts, the HH photon count was estimated using equation 2.26. The two filters used here were not cross calibrated experimentally and hence we used the estimated theoretical filter transmission. The theoretical estimate of transmission of XUV by aluminum filters with thicknesses of 150 nm and 300 nm was done assuming that there was 5 nm thick  $\text{Al}_2\text{O}_3$  formed on both side of the

two filters [91, 92] and the for a central wavelength of 32 nm the filter transmission are 40% and 30% respectively. Using the theoretical filter transmission along with the equation 2.27, the HH energy was estimated for HHG from argon and neon and the values are listed in table 2.2.

Parameters	Units	Argon	Neon	Xenon
IR beam size	mm	12	13	12
Focal length	mm	750	750	750
Gas pressure	mbar	30 - 60	40 - 60	13
HH photon number	per shot	$2.75 \times 10^6$	$1.1 \times 10^6$	$< 1 \times 10^6$
Total energy of HHs	nJ	0.02	0.01	$< 0.01$
Divergence horizontal	mrad	0.7	0.7	
Divergence vertical	mrad	1	0.8	

Table 2.2: Typical operating conditions for HHG in argon and neon and their corresponding XUV beam parameters (calculated for the whole HH spectrum).

For measuring the HH spectra, the spectrometer in the diagnostics chamber was used. Figure 2.17 shows the schematics of the XUV spectrometer in the diagnostics chamber at Salle Corail, LOA. The spectrometer consists of a concave spherical focusing mirror made of silica with a ROC of 2 m followed by a reflective plane diffraction grating. The grating has 450 lines per mm and works at an angle of incidence of  $8.4^\circ$  and it was placed at 25 cm from an XUV detector. The detector used was a PIXIS: 400 B X-ray CCD. The HH spectra were recorded for HHG from argon, neon and xenon.

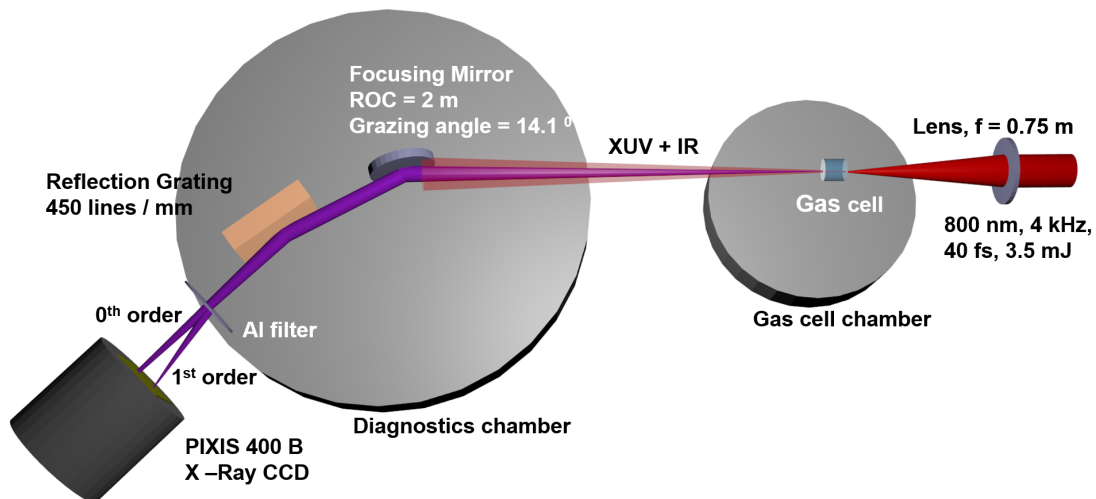


Figure 2.17: Schematic of XUV spectrometer at Salle Corail, LOA.

The HH spectrum from argon was recorded at a pressure of 30 mbar mainly because at this pressure the HH orders around 30 nm are stronger and most of the experiments are planned for an XUV wavelength around 30 nm. Figure 2.18a and 2.18b shows an image and line-out of the calibrated HH spectrum from argon respectively. The line-out of the spectrum shows that most of the energy is concentrated in mainly three harmonic orders from 23 to 27, and 25<sup>th</sup> harmonic order is the strongest. HHG from argon was the main source of XUV in experiments and the central wavelength for XUV was

assumed to be the strong 25<sup>th</sup> harmonic order and this corresponds to a wavelength of 32 nm considering the central wavelength of the laser used for HHG at 800 nm.

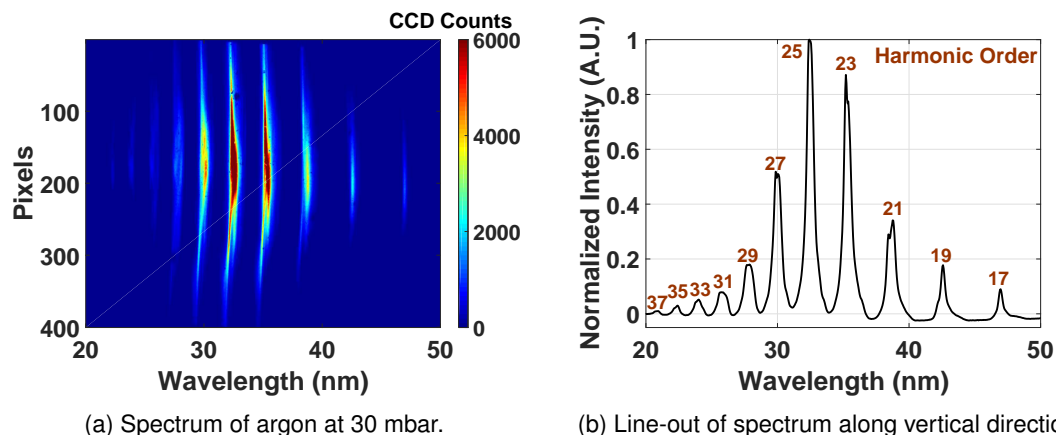


Figure 2.18: The optimized HH spectrum for argon at salle corail, LOA.

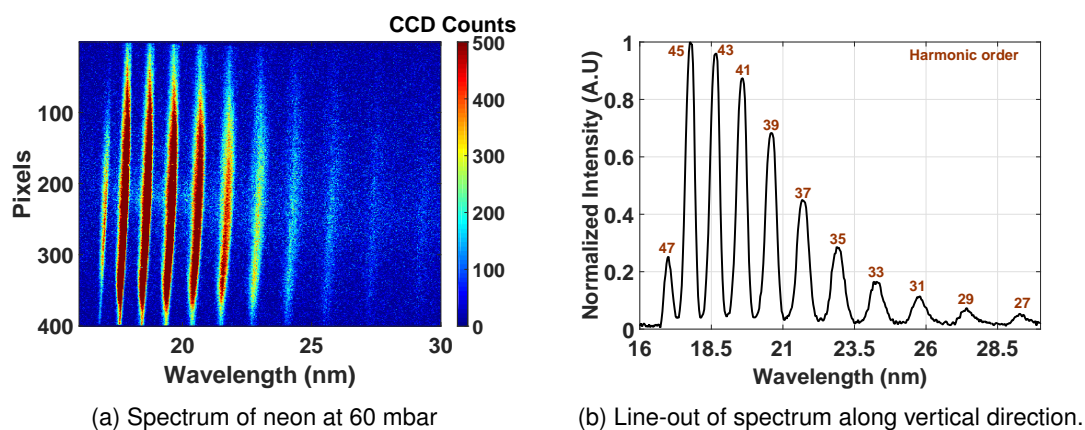


Figure 2.19: The optimized HH spectrum for neon at Salle Corail, LOA.

The HH spectrum from neon was measured at a pressure of 60 mbar. Figure 2.19a and 2.19b shows an image and line-out of the calibrated HH spectrum from neon respectively. With HH from neon, lower wavelengths can be reached compared to HH from argon. Harmonic orders from 27 to 47 was observed with higher intensities at 41, 43 and 45. The spectrum also shows a sharp cutoff at  $\sim 17$  nm and this is due to the cutoff the aluminum filter used to filter out the residual IR.

The HH spectrum from xenon was measured at a pressure of 13 mbar. Figure 2.20a and 2.20b show an image and a line-out of the calibrated HH spectrum from xenon respectively. With HH from xenon, higher wavelengths ( $> 60$  nm) compared to HH from argon can be reached. The strongest harmonic order observed was the 17<sup>th</sup> harmonic order. Xenon is mostly not used in the lab as it was expensive and it causes difficulty for the turbo-molecular pumps to maintain the high vacuum required for the XUV beamline.

XUV source from HHG in argon, and neon was set up and typical operating conditions and XUV beam parameters were obtained. HHs from argon, neon, and xenon were also characterized in the spectrum. The HHs from the three different gases provides XUV wavelengths from  $\sim 60$  nm to  $\sim 17$  nm. However, HHG in argon gives more photons per shot compared to HHG in neon and xenon. Also, the 25<sup>th</sup>

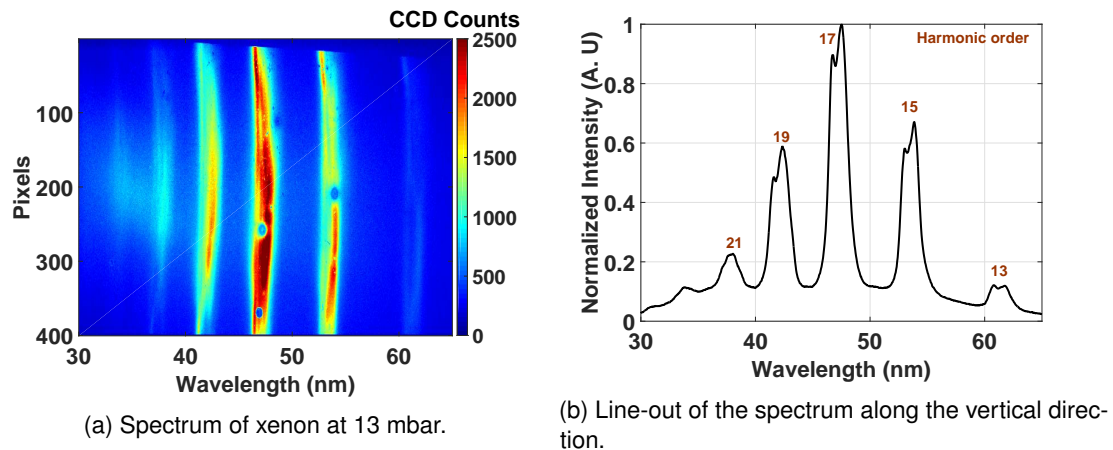


Figure 2.20: The optimized HH spectrum for xenon at Salle Corail, LOA.

harmonics is stronger in the argon spectrum. Hence, for applications like wavefront sensor calibration and imaging, HHG from argon can be used as the XUV source.

### 2.2.2.3 VOXEL Lab, IPFN, IST Lisbon, Portugal

The VOXEL lab was established at IST in early 2017 as part of the VOlumetric medical X-ray Imaging at Extremely Low dose (VOXEL) project, a Future Emerging Technology (FET) project under the Horizon 2020 European Union research and innovation program [93].

The laser system at VOXEL lab consists of two commercial lasers Astrella and Hidra from Coherent, Inc based on amplification using Ti:Sapphire crystals. The Astrella laser system consists of an oscillator followed by a regenerative amplifier. The output of the Astrella laser system has a central wavelength of 800 nm, pulse duration  $< 35$  fs, pulse energy  $\sim 7.5$  mJ and a repetition rate of 1 kHz. The laser is compact and stable in terms of output power, beam profile and beam pointing. The Hidra laser system is seeded from the oscillator of Astrella laser system and the stretched seed is then amplified by a regenerative amplifier followed by a multi-pass amplifier. The output of the Hidra laser system has a central wavelength of 800 nm, pulse duration  $< 40$  fs, pulse energy  $> 25$  mJ and a repetition rate of 10 Hz. Since both lasers are seeded from the same oscillator, they can be optically synchronized which is useful in pump-probe experiments.

The HHG beamline at the VOXEL lab consists of the IR laser, a gas cell chamber where the IR laser is focused onto a gas cell and it is followed by an experimental chamber, where XUV diagnostics are placed and the experiments are performed. Figure 2.21 shows the schematics of the experimental setup for HHG at the VOXEL lab. Both laser systems can be used for HHG at the VOXEL lab. The IR pulses from the lasers are steered onto the gas cell chamber with dielectric mirrors with ultra-broadband coating and anti-reflection coating for the spectral bandwidth of the laser. A plano-convex lens with a focal length of 750 mm is used to focus the laser onto a gas cell of length 15 mm to generate the HHs of the laser. Al filters with different thicknesses are used to filter out the residual IR from the XUV. The intensity cross-section or footprint of the XUV beam generated is detected using an X-ray CCD, PIXIS- XO 1024 B from Princeton Instruments. The CCD used has  $1024 \times 1024$  pixels with a pixel size of  $13 \mu\text{m} \times 13 \mu\text{m}$ .

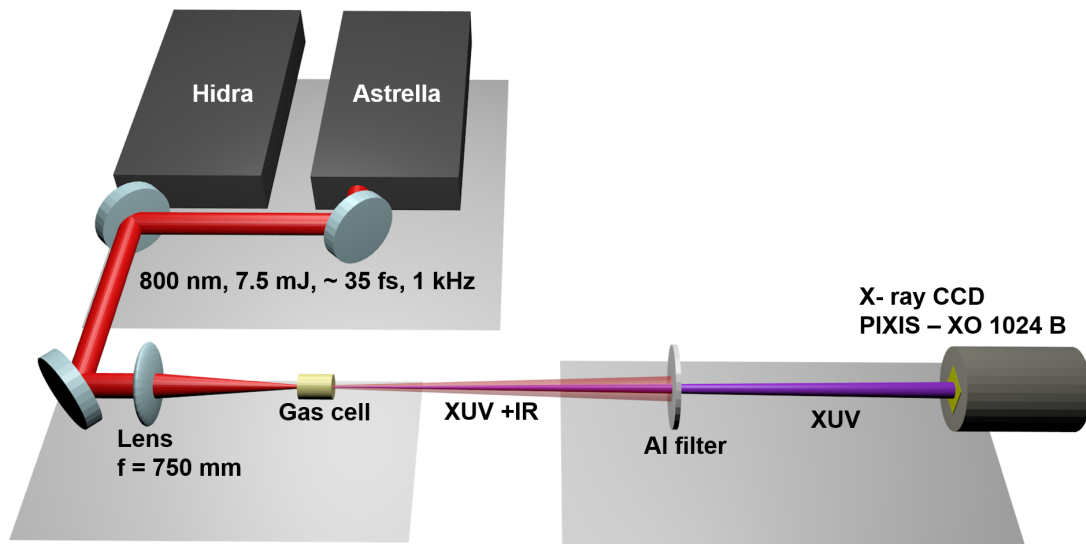


Figure 2.21: Schematic of lasers and HHG experimental setup at VOXEL lab, IST Lisbon

HHG was optimized in argon. The Astrella laser system was used for HHG. For optimization of HHG in argon, a flat uncoated mirror at  $45^\circ$  was used to reflect XUV pulses to the XUV CCD. This was done to avoid the CCD from saturation due to the high photon count. Further, an aluminum filter of 464.5 nm with nickel supporting grids was used to filter out the residual IR and was placed before the gold-coated mirror. Figure 2.22 shows the footprint of HHG optimized for argon at 13 mbar. The optimization parameters and the XUV parameters obtained are listed in table 2.3. Further the spectrum of HHG in argon was studied at the optimized conditions.

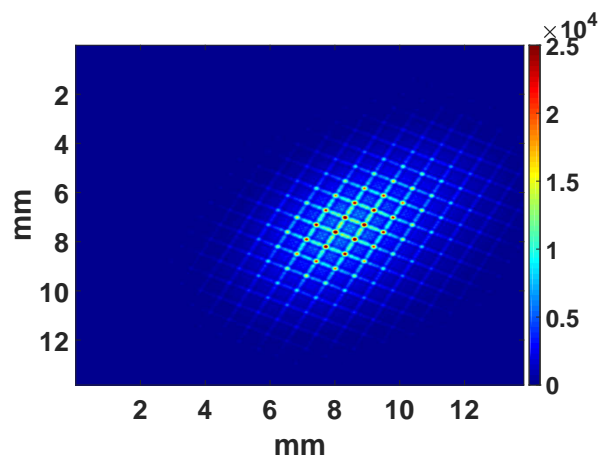


Figure 2.22: Footprint of HHG from Ar at 13 mbar measured at the VOXEL lab, IST.

The XUV spectrometer at VOXEL lab is realized in the experimental chamber. It consists of a spherical mirror, a gold-coated flat mirror, a grating and an XUV sensitive CCD. Figure 2.23 shows the schematic of the experimental setup for the XUV spectrometer in the experimental chamber at VOXEL lab. The focusing spherical mirror is made of silica and has a ROC = 10 m and is placed at a grazing angle of  $8^\circ$  with respect to the incident XUV beam. The XUV beam focused by the spherical mirror is steered on to the grating by a gold-coated flat mirror, which also placed at a grazing angle of  $8^\circ$ . The flat

mirror is placed on a motorized tip/tilt mount for adjusting the position of spectral lines on the CCD. The transmission grating used is a free-standing gold grating with a clear aperture of  $10\text{ mm} \times 10\text{ mm}$  and has a grating constant of  $1000\text{ lines / mm}$ . The grating is placed perpendicular to the incident beam. XUV spectrum is recorded using the PIXIS- XO 1024 B CCD. An aluminum filter of thickness  $464.5\text{ nm}$  with nickel supporting grids were used to filter out the residual IR.

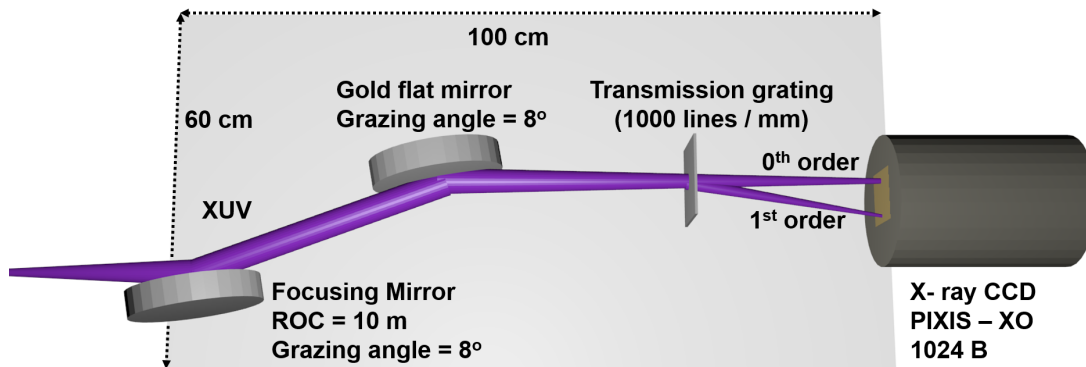
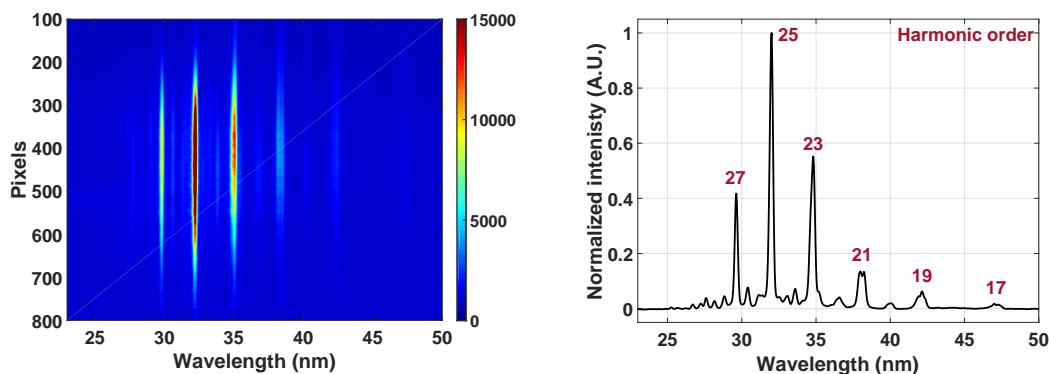


Figure 2.23: Schematic of XUV spectrometer setup at VOXEL Lab, IST Lisbon.

XUV spectrum was recorded for HHG in argon. Figures 2.24a and 2.24 shows the image and line-out of the calibrated spectrum for HHG in argon. The spectrum consists of 6 HH orders and  $25^{\text{th}}$  harmonic whose wavelength corresponds to  $32\text{ nm}$  is the strongest. The low intense lines in between the strong lines in figure 2.24a is due to the diffraction from the supporting grids of the grating and edge diffraction from the spherical mirror.



(a) Spectrum of argon at 13.5 mbar

(b) Line-out of spectrum along vertical direction.

Figure 2.24: The optimized HH spectrum for argon at VOXEL lab, IST.

The HHG in xenon and neon was carried out with the spectrometer setup. HHG in xenon was optimized at a pressure of  $3.8\text{ mbar}$ . Figure 2.25a shows the line-out of the calibrated spectrum for HHG in xenon. The spectrum shows three harmonic orders and they are lower orders compared to the HH spectrum from argon. The different optimization parameters for HHG in xenon and the XUV parameters obtained are listed in table 2.3. HHG in neon was difficult to optimize since it was not possible to maintain the vacuum at pressures higher than  $20\text{ mbar}$ . However, the spectrum of HHG in neon was obtained. Figure 2.25b shows the line-out of the calibrated spectrum for HHG in neon. The spectrum shows eight harmonic orders and higher orders compared to the spectrum for HHG in argon are observed. The

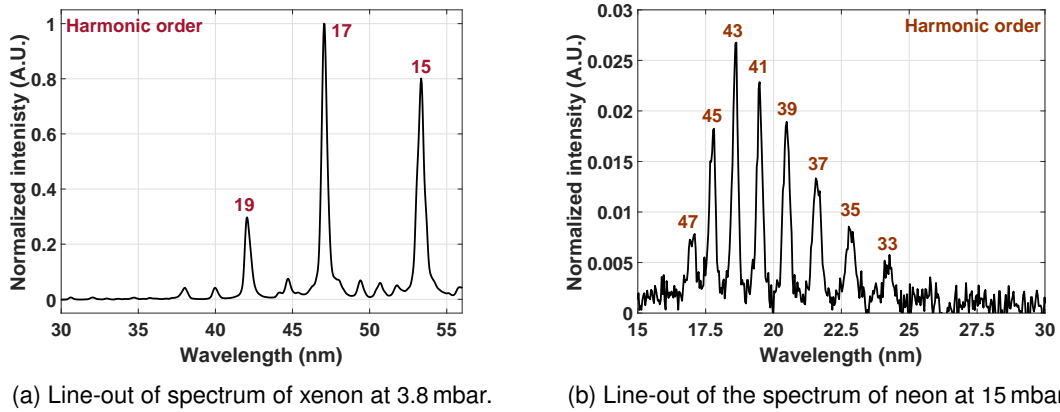


Figure 2.25: The optimized HH spectrum for xenon and neon at VOXEL lab, IST.

conditions for HHG in neon and the obtained XUV parameters are tabulated in table 2.3.

Parameters	Units	Argon	Xenon	Neon
IR beam size	mm	8	13	8
Focal length	mm	750	750	750
Gas pressure	mbar	13	3.8	15
HH photon number	per shot	$3.4 \times 10^8$	$4.9 \times 10^8$	$5 \times 10^5$
Total energy of HHs	nJ	2.1	1.8	0.006
Divergence horizontal	mrad	1.5		
Divergence vertical	mrad	1.5		

Table 2.3: Optimized operating conditions for HHG in argon, xenon and neon, and their corresponding XUV beam parameters (calculated for the whole HH spectrum).

HHG with fundamental and SH pulses was performed at VOXEL lab. A BBO with a thickness of  $100 \mu\text{m}$  was used for generating the SH. The BBO was placed after the lens which focuses the IR laser. The BBO used has an efficiency of  $\sim 10\%$ . The spectrum was recorded with fundamental and SH pulses for HHG in argon. Figures 2.26a and 2.26b shows the image and line-out of the calibrated spectrum for HHG from argon with fundamental and SH pulses. The spectrum shows odd and even harmonics from  $25^{\text{st}}$  to  $17^{\text{th}}$  harmonic orders. The strongest harmonic order is  $21^{\text{st}}$  harmonic order. The spectrum shows a redshift of harmonic orders compared to the spectrum of HHG in argon with fundamental frequency only. This is due to the presence of  $2\omega$  frequency which in turn reduces the cutoff of the harmonics at the same generation conditions [90]. Here also the delay between the IR and SH pulses was not controlled. However, the HHG process using IR and SH pulses was optimized with a total HH energy equal to  $\sim 60\%$  of the total HH energy for the HHG with only IR laser pulses.

A HHG beamline was successfully established and the XUV pulses generated were characterized in energy and spectrum at the VOXEL lab, IST. HHG in xenon has the highest number of photons however high harmonic generation in argon has higher energy. The XUV pulses generated with single shot energy  $\sim 2 \text{ nJ}$  at the high harmonic beamline from argon and xenon can be now used for applications

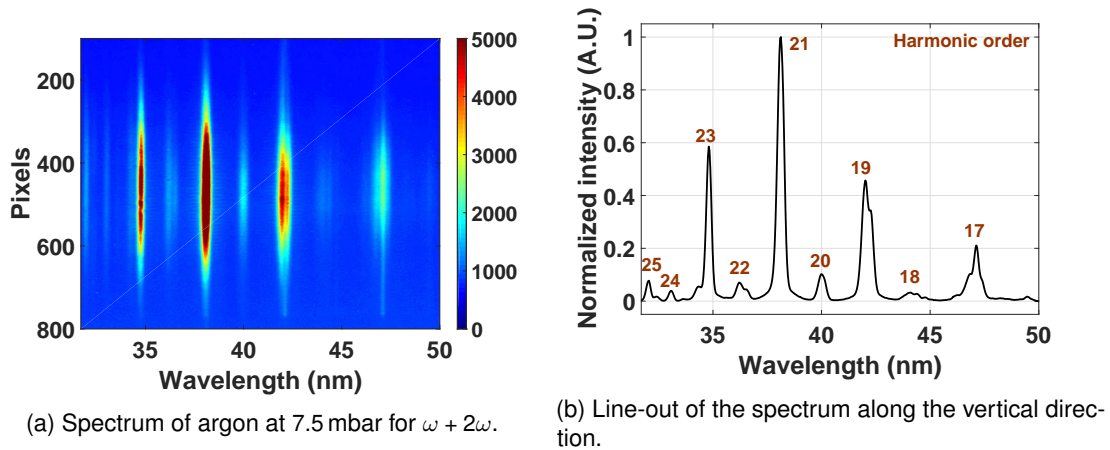


Figure 2.26: The optimized HH spectrum for argon with fundamental and second harmonic pulses at VOXEL lab, IST.

like laser-plasma pump-probe experiments which require high single shot XUV probe energy. The XUV source can be also used for single shot imaging experiments.

## 2.3 HHG from solids

HHG from solids was first observed with CO<sub>2</sub> laser-produced plasma [65]. In our studies, we are mostly interested in HHG from solids with high-intensity ultrashort pulse lasers [66]. HHG from solids can be used as a source of coherent XUV sources and also can be used to study the properties of plasma under high intense laser fields [74, 70]. The HHs are generated from solids when a high-intensity laser pulse (Intensity  $\geq 10^{16}$  W/cm<sup>2</sup>) interacts with a solid, typically optical quality silica glass. The laser-solid interaction creates an over-dense plasma and a coherent beam of higher order harmonics of the incident laser beam are emitted from the solid surface in reflection [66, 94, 95]. Figure 2.27 shows a simple setup for HHG from solids in reflection with metallic filters filtering the XUV beam generated from the residual driving IR laser and lower order harmonics generated.

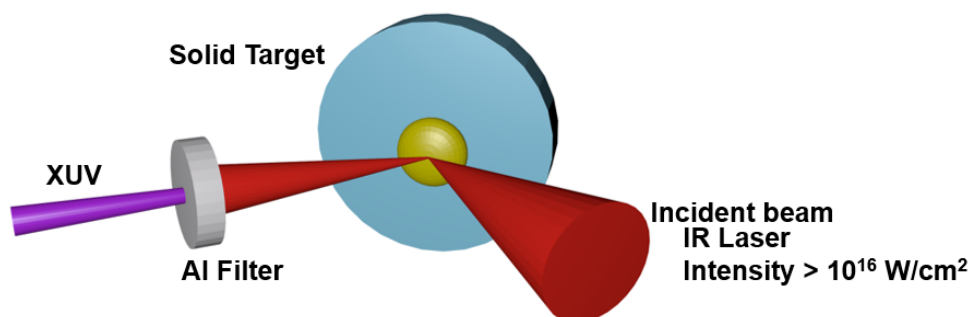


Figure 2.27: Schematics of a simple setup of HHG from solids.

HHG from solids also support short pulse duration from femtosecond up to attosecond [96, 95]. The efficiency of HHG in solids is also in the order of  $10^{-6}$  [70]. However, the intensity of laser used is higher for HHG in solids, hence the intensity of harmonics generated from solids is in general higher compared to harmonics generated from gases [95, 70]. This is an important motivation to proceed with

further study of HHG in solids. However, the filtering of XUV pulses reduces the intensity as the filtering should be stronger since HHG results in generation of debris and also there is strong component of fundamental IR laser along the specular direction. The divergence of the harmonics from solids is higher compared to that from gases [75].

The higher HH intensity from HHG in solids can be effectively utilized in applications if we can characterize the pulse properties both spatially and temporally. One of the motivation of this experiment on HHG from solids is to measure the spatial characteristics of HHs generated and use it to study the evolution of HH source conditions during laser-solid interaction. The spectral and spatial characterization may give insight into the plasma creation mechanisms.

This section discusses briefly about the theory and presents experimental results of HHG from solids.

### 2.3.1 Theoretical description of HHG from solids

The HHG from solids was theoretically described under different formulations. The basic assumption in all the models is that the plasma created by the laser is considered collision-less with fixed ions in the background. The harmonics are generated from the movement of electrons under the incident laser field [94]. HHG from solids under different conditions have been explored [97, 98, 74]. The work in this thesis mainly focuses on HHG from over-dense plasma using high-intensity femtosecond lasers.

The first explanation for harmonic generation from over-dense plasma is based on the concept of resonance absorption [99, 97]. The idea here is that the high intense laser field causes generation of plasma waves, and at critical surface where the laser frequency equals to the plasma frequency ( $\omega_L = \omega_p$ ), the plasma wave interacts with the laser, generating the second harmonic of the laser frequency [99]. The radiation with frequency  $2\omega_L$  is mostly reflected but the transmitted part excites a plasma wave at critical surface for the  $2\omega_L$  frequency which results in oscillation of plasma at  $2\omega_L$  frequency. This resonant oscillation generates the third harmonic,  $3\omega_L$  and this continues to the higher order harmonics. This model is called the linear mode coupling in the plasma density gradient [99]. This model was able to explain the HHG in solids with long pulse lasers. With advent lasers with sub-picosecond pulse duration, which can reach relativistic intensities ( $> 10^{18}$  W/cm<sup>2</sup>), new models were proposed to explain the HHG in solids under sub-relativistic [74] and relativistic conditions [100, 96].

Based on this general model of interaction, the most understood and explored mechanisms for describing solid HHG in reflection with ultrashort short high intensity ( $\geq 10^{16}$  W/cm<sup>2</sup>) laser pulses are relativistically oscillating mirror (ROM) [95, 101, 70] and coherent wake emission (CWE) [74]. In general HHs from CWE is observed for laser intensities  $\sim 10^{16}$  W/cm<sup>2</sup> and ROM mechanism is observed for laser intensities  $\geq 10^{18}$  W/cm<sup>2</sup>.

#### 2.3.1.1 Relativistic oscillating mirror model

The relativistic oscillating mirror model for HHG from solids was first proposed by Bulanov et al. [102] and later expanded by Lichters et al. [100]. The model explains HHG from solid surfaces for laser-solid interaction considering laser intensities  $\geq 10^{18}$  W/cm<sup>2</sup>.

When a high intensity short pulse ( $\leq 100$  fs) laser is focused on a solid target with a density greater than the critical density  $N_c = m_e \epsilon_0 \omega_L^2 / e^2$ , it results in the ionization of the material surface in the rising edge of the pulse and this results in generation of electrons, which move at relativistic velocities in the incident laser field. Here,  $m_e$  is the mass of the electron,  $\epsilon_0$  is the electric permittivity of free space,  $\omega_L^2$  is the angular frequency of the laser and  $e$  is charge of the electron. The oscillations of this relativistic electrons result in the creation of a mirror-like surface from which the laser is reflected with an up-shift in the frequency which corresponds to the harmonics of the laser frequency. The theoretical formulations consider creation of a cold electron fluid with a static background of ions. Here the laser is considered to be incident on the target at an angle. Considering the incident laser field [95]

$$E_{inc}(t) = \sin(\omega_L t) \quad (2.28)$$

where  $\omega_L$  is the laser frequency and  $t$  is the time in the lab frame. The reflected field from the relativistically oscillating mirror target can be written as [95],

$$E_{ref}(t) = \sin(\omega_L t + 2k_L X_m(t')) \quad (2.29)$$

where  $t'$  is the time in the moving mirror frame and  $X_m(t)$  is the coordinate describing the surface of the electron density.  $X_m(t)$  can be described as the effective surface from which the incident laser field is reflected.  $X_m(t)$  becomes  $X_m(t')$  in the moving mirror frame. The time in the moving frame or retarded time is related to the time in lab frame by [95]

$$t' = t + \frac{(R + X_m(t'))}{c} \quad (2.30)$$

where  $R$  is the distance between the observer and the plasma-vacuum interface.  $R/c$  is a time-independent constant phase term and this was omitted in equation 2.29. Figure 2.28 shows the schematics of the basic idea of the ROM model.  $E_{ref}(t)$  can be calculated by calculating the value

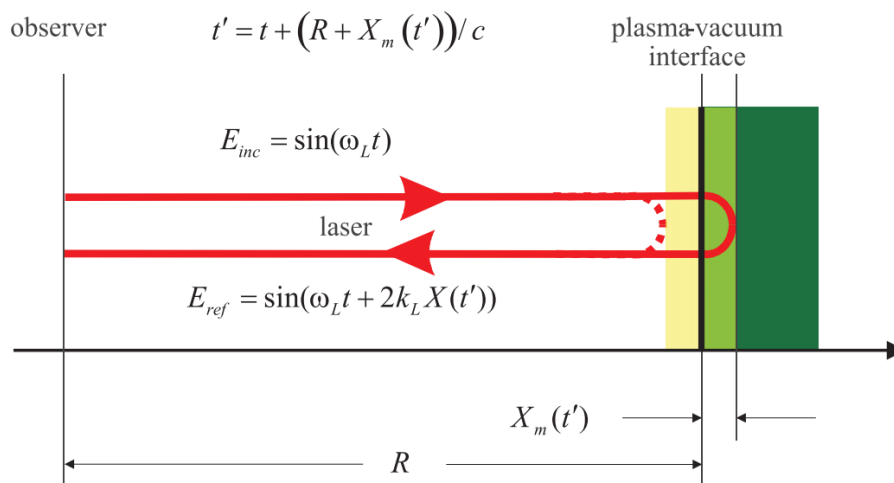


Figure 2.28: Schematics of basic idea of the ROM model. Figure taken from [95]

of  $X_m(t')$ . The first approximation for  $X_m(t')$  is given by [95]

$$X_m(t') = A_m \sin(2\omega_L t' + \phi_m) \quad (2.31)$$

where  $A_m$  is the amplitude of oscillation of the mirror and  $\phi_m$  is the relative phase between the incident wave and the mirror position. For relativistic cases,  $A_m$  can be written as [95]

$$A_m = \frac{\lambda_L}{4\pi} \frac{\sqrt{\gamma_{max}^2 - 1}}{\gamma_{max}} \quad (2.32)$$

where  $\gamma_{max}$  is the relativistic factor and for a maximum oscillating velocity of the mirror,  $v_{max}$  it is given by [95]

$$\gamma_{max} = \frac{1}{\sqrt{1 - \frac{v_{max}^2}{c^2}}} \quad (2.33)$$

Further,  $\gamma_{max}$  can be written in terms of the normalized laser vector potential,  $a_0$  as  $\gamma_{max} = \sqrt{1 + a_0^2}$  where  $a_0$  is given by [95]

$$a_0 = \frac{eE_0}{\omega_L m_e c} = \sqrt{\left( \frac{I \lambda_L^2 (\mu m)}{1.37 \times 10^{18}} \right)} \quad (2.34)$$

where  $E_0$  is the normalized laser electric field. From the above relations equation 2.31 can be written as [95]

$$X_m(t') = \frac{\lambda_L}{4\pi} \frac{a_0}{\sqrt{1 + a_0^2}} \sin(2\omega_L t' + \phi_m) \quad (2.35)$$

The reflected field can be calculated by knowing the values of  $a_0$  and  $\phi_m$  using the equations 2.29 and 2.31. The Fourier transform of the field gives the spectrum of the harmonics predicted by the ROM model [95]. The model gives the cutoff harmonic order as [95]

$$n_{co} = \frac{\sqrt{1 + a_0^2} + a_0}{\sqrt{1 + a_0^2} - a_0} \approx 4\gamma_{max}^2 \text{ for } a_0 \gg 1 \quad (2.36)$$

and also the scaling of harmonic intensity is given by [95]

$$I(\omega) \propto \omega^{-q} \quad (2.37)$$

where  $q \approx \frac{5}{2}$ . The calculations using the ROM model also shows that the laser with p-polarization on an over-dense target gives highly efficient HHs compared to a laser with s-polarization [100, 95, 94] and the same trend was observed in experiments as well [66].

### 2.3.1.2 Coherent wake emission model

The coherent wake emission model for HHG from solids was proposed and experimentally observed by Quere et al., [74]. The CWE model explains HHG from solids at lower laser intensities compared to the ROM model.

The higher efficiency for CWE harmonics was observed when  $p$  polarized laser pulses with peak intensities in the range of  $\approx 10^{16}$  W/cm<sup>2</sup> was used [74]. The  $p$ -polarized laser electric field has an electric

field component normal to the surface of the target. When the laser is incident on the target, it ionizes the surface of the target, creating a plasma. The electrons on the surface of the plasma are pulled in to the plasma-vacuum interface by the electric field component of the laser. The electrons travel in the electric field and are pushed back in to the plasma with a velocity given by [103]

$$v_{osc} = \frac{eE}{m_e\omega_L} \quad (2.38)$$

where  $E$  is the electric field component of the laser perpendicular to the surface of the target. This process results in the absorption of the laser energy and is called Brunel absorption or vacuum heating [103, 74]. The electrons which return from vacuum travels deeper in the plasma when the trajectory it traveled is longer in vacuum. The returned electrons form a bunch and interact with the electrons in the plasma and trigger generation of plasma waves throughout the density gradient ( $n(x)$ ) [104] of the plasma surface. This happens in each laser cycle. Figure 2.29 shows a pictorial representation of the generation of the plasma waves in CWE model for HHG from solids.

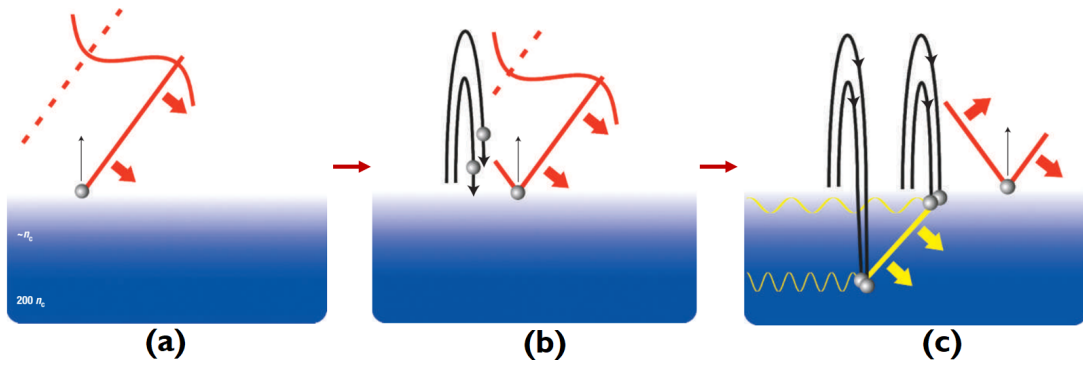


Figure 2.29: A pictorial representation of plasma wave generation under the CWE model for HHG in solids. (a) Electrons are pulled out of the plasma in the electric field of the laser at near critical densities, (b) the electrons accelerated in the electric field of the laser are pushed back into the plasma as field changes sign and (c) propagation of electrons in the over-dense plasma and formation of electron bunches and emission of radiation as attosecond bursts. Figure modified from [104].

The frequency of spatially dependent plasma oscillations can be written as

$$\omega_p(x) = \omega_L \frac{N}{N_c} \quad (2.39)$$

These plasma oscillations are coherently triggered at each cycle of the laser. The wave vector  $k$  of the plasma oscillations, in the beginning, has a direction parallel to the electric field  $E$  and coherent triggering of Brunel electrons results in the generation of a transverse component for this oscillation, which then radiates as the harmonics of the laser frequency [74]. The harmonics are thus generated in the wake of the coherent triggering by the Brunel electrons and the process is called coherent wake emission (CWE). The maximum harmonic order emitted by the CWE is limited by the maximum plasma frequency of the target. The maximum harmonic order  $h_{max}$  is given by [104]

$$h_{max} = \sqrt{N_{max}/N_c} \quad (2.40)$$

where  $N_{max}$  is the maximum plasma density for fully ionized targets and with a  $N_{max}$  in the order of few hundreds of  $N_c$ , the XUV spectral range can be reached [104].

For efficient HHG under CWE mechanism, phase matching conditions have to be fulfilled between the plasma oscillations and the emitted radiation. This is achieved when the wave vector of plasma oscillations are parallel to the target surface. Simulations predict efficiency up to  $10^{-4}$  for CWE [74]. From the simulations and experiments, it has been observed that the typical CWE emission reaches 25 nm - 80 nm in the XUV with divergence in the order of few milliradians [74, 104].

### 2.3.2 Experimental results on HHG from solids

The experiment on HHG in solids was performed at JETI200, Helmholtz Institute (HI), Jena, Germany [105]. The aim of the HHG in solids at JETI200 was to study the wavefront of HH from solids. The HHG from solids was first tested to obtain a stable generation condition for HHs. An introduction to the JETI200 laser system and the experiment on solid HHG are presented in the following sections.

#### 2.3.2.1 JETI200 laser system

The JETI200 - Jenaer Titanium:Sapphire 200 terawatt laser system is a commercial laser from Amplitude Technologies. The laser is based on Ti:Sapphire amplifiers. It consists of five stage amplification. The seed from the oscillator passes through two sets of the regenerative amplifier and multi-pass amplifiers in tandem and finally passes through a cryo-cooled single pass amplifier. After the final amplifier, the laser is compressed using a vacuum compressor. The laser can produce more than 200 terawatt peak power. After compression, the laser has a specified maximum pulse energy of 4 J at a pulse duration of  $\sim 17$  fs with a central wavelength of 800 nm and repetition rates of 1 – 10 Hz. Figure 2.30 shows the JETI200 laser system.

For the operation of a high power laser, it is important to know and reduce the pre-pulse in the laser pulse. The contrast between the pre-pulse and the main pulse should be as high as possible. For achieving a higher contrast for the laser, a plasma mirror (PM) was installed in the laser beam line. The leading edge of the high-intensity laser ionizes the mirror surface creating an over-dense plasma which reflects only the high-intensity part of the pulse [106]. Using a plasma mirror the low energy pre-pulses can be removed and thereby increasing the temporal contrast. Figure 2.31a shows the schematics of the setup of PM at JETI200. The IR laser after the compressor is steered into the PM chamber. The mirrors used in the experimental setups were of  $\sim 150$  mm in diameter with anti-reflection coating for the spectral bandwidth of IR laser. In the PM chamber mirror, M3 directs the beam onto an off-axis parabola (OAP) of f-number,  $f/15$ . The OAP 1 focuses the laser onto the PM. The laser reflected from the PM is re-collimated by OAP 2 and mirror M4 directs the laser back to the beamline. Mirrors M3 and M4 can be moved out of the beamline to bypass the PM. The PM is placed on a 3-axis translation stage to optimize its position after each shot. The position of the PM with respect to the focused laser beam is optimized by checking the reflectivity. Figure 2.31b shows the reflectivity of the PM at different positions along the focus of OAP 1. The zero position corresponds to the focus position of the OAP 1 and the positive values indicate the position after focus. A maximum reflectivity of 80 % is achieved using the plasma mirror. After

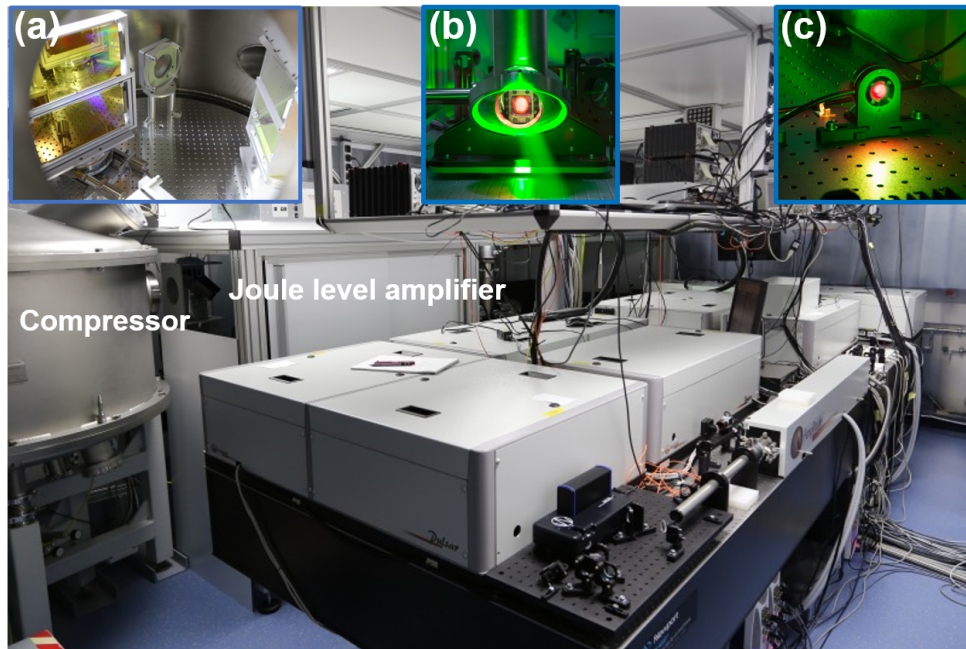


Figure 2.30: The JETI200 Laser at Helmholtz Institute in Jena, Germany. In the inset: (a) shows the gratings of the compressor in vacuum, (b) shows the cryo-cooled joule level Ti: Sapphire amplifier crystal (with the pumping on), (c) shows the Ti: Sapphire amplifier crystal (with the pumping on) in another multipass amplifier from the laser system [105]

the PM, the IR laser beam is steered into the target chamber using dielectric mirrors.

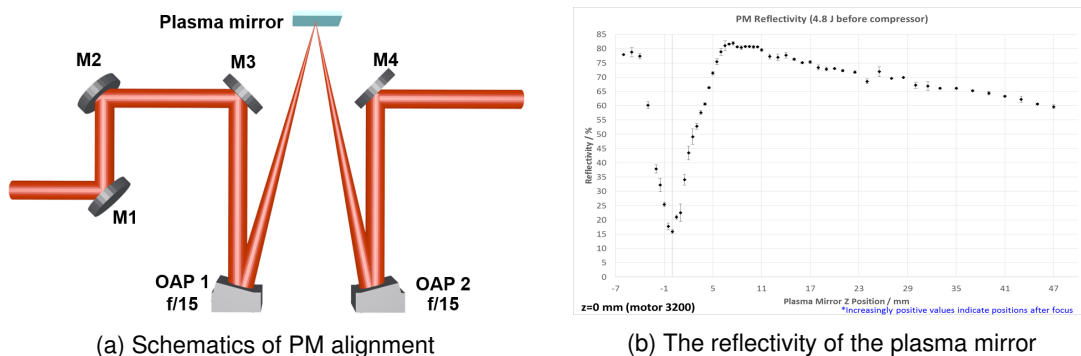


Figure 2.31: The Schematics of PM alignment and reflectivity at JETI200

The pulse contrast was measured using a third order autocorrelation method (Sequoia from Amplitude). Figure 2.32 shows a plot of the pulse contrast measurement without the PM at the target chamber, without PM in the laser lab and with PM in the laser lab. With the PM the contrast improved from  $10^{-5}$  to  $\sim 10^{-8}$  when measured in the laser lab.

### 2.3.2.2 HHG from solids at JETI200

The experimental setup and the results obtained for HHG in solids under CWE and ROM at JETI 200 is presented here.

The schematic of the solid HHG experimental setup at JETI200 is shown in figure 2.33. The target chamber has a dimension of 1900 mm  $\times$  750 mm. In the target chamber mirrors M1, M3 and M4 are

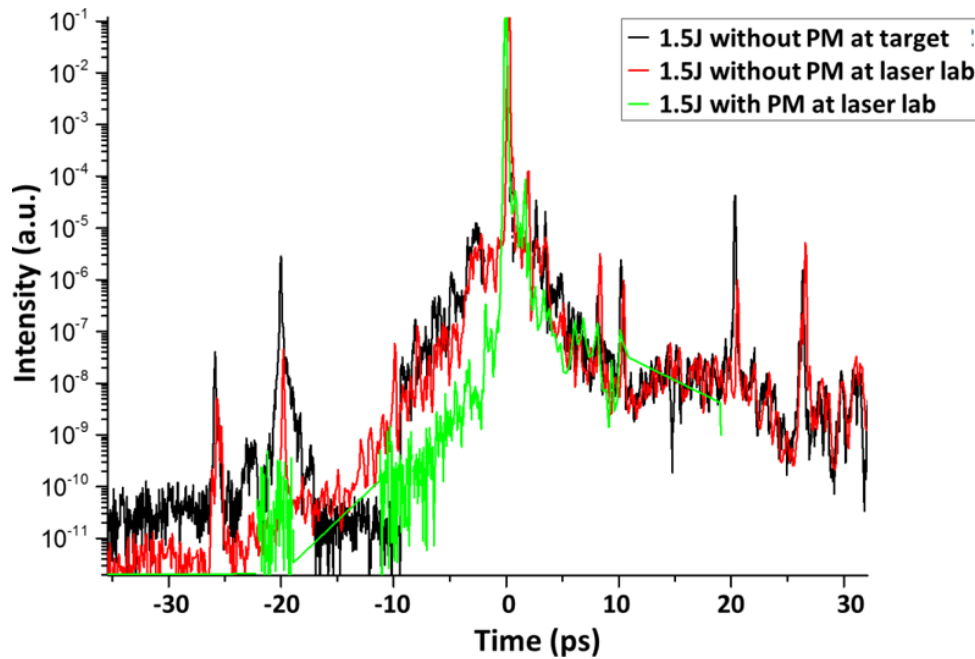


Figure 2.32: Measured contrast of the JETI200 laser system using a Sequoia.

used to steer the IR laser onto the OAP, which has a f-number of  $f/3$ , focusing the IR laser pulses on to a glass target. The mirror M1 has a smaller mirror M2 attached to it to generate the pre-pulses to change the initial state of the target when necessary. The OAP is designed to work at an angle of  $30^\circ$ . The target was placed at  $45^\circ$  with respect to the focused IR laser pulses. This was done to increase the efficiency of HHG from solids. The target used was dielectric silica mirror. After the target, an aluminum filter wheel with filters of different thicknesses was placed in the specular direction of the IR beam to filter out the residual IR beam from XUV beam generated during solid HHG. An XUV spectrometer called Jasny spectrometer [107] was used for diagnostics and was placed after the aluminum filter wheel and is attached to the target chamber. The Jasny spectrometer consists of a toroidal mirror grating and an XUV detector. The detector used was Newton CCD from Andor [108]. The CCD used was back illuminated and thinned. It has  $2048 \times 512$  pixels with a pixel size of  $13.5 \mu\text{m} \times 13.5 \mu\text{m}$ .

The focusing of the IR laser with the OAP at the target chamber was optimized by adjusting the positioning of the OAP with respect to the incoming laser beam. The focus obtained was imaged through an imaging system with a bandpass filter for the IR laser spectrum. The best focus achieved is shown in figure 2.34a. Figure 2.34b shows the vertical line-out of the figure 2.34a and from this, the FWHM of the focal spot is estimated to be in the order of  $\sim 4 \mu\text{m}$ . With this focal spot diameter and the given specifications of the laser at JETI200, a peak intensity of  $\sim 4.5 \times 10^{20} \text{ W/cm}^2$  can be reached.

The spectrum of HHG from solids were recorded using the Jasny spectrometer [107, 109]. Figure 2.35 shows the raw image of the spectrum obtained. The central bright spot shows the zeroth order, the bright spots on the side of the central spot are the first orders and the second orders are seen on the sides [107, 109]. The second order of the spectrum was selected and used for calibration. The spectrum is calibrated using the edge of aluminum filter cutoff for the XUV. The solid HH spectrum under CWE and ROM mechanisms were recorded under different laser conditions as tabulated in table 2.4.

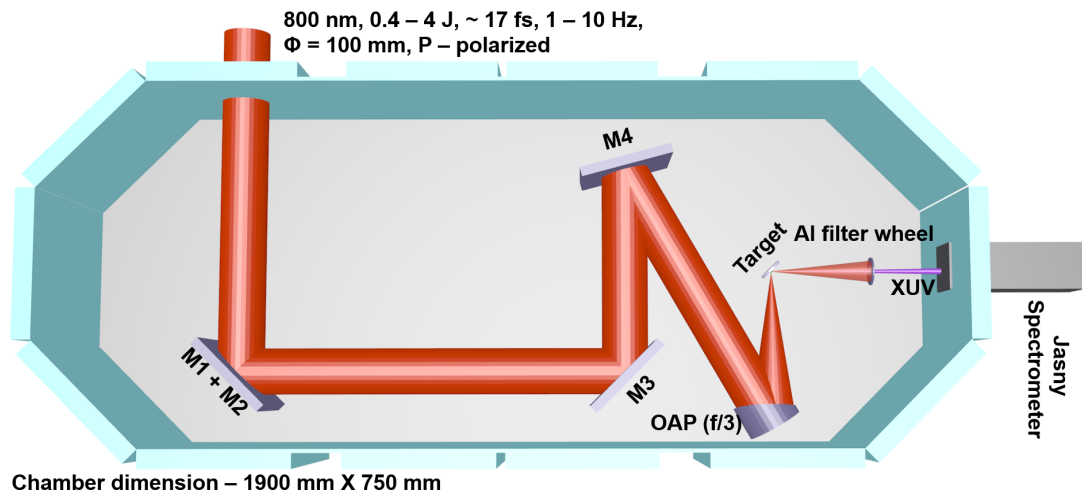


Figure 2.33: Schematic of the experimental setup for generation of HH from solids and spectral characterization at JETI200, Helmholtz Institute, Jena, Germany.

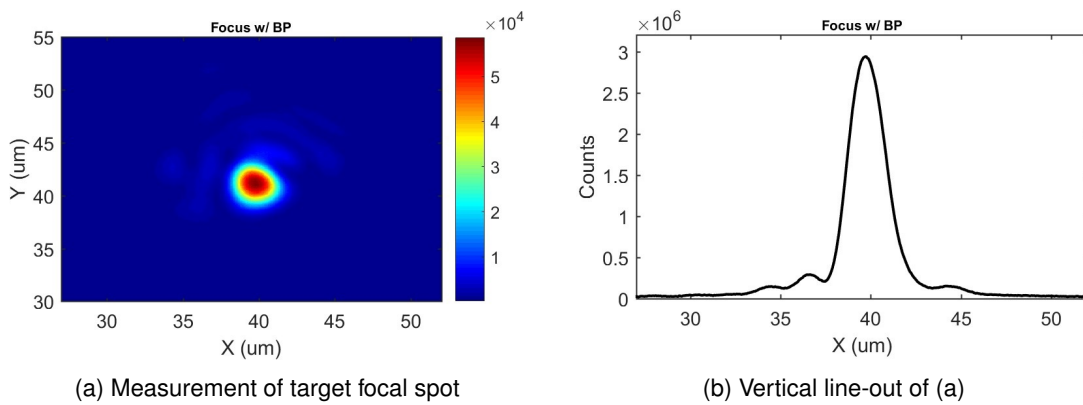


Figure 2.34: The optimized focal spot of the laser at the target position at JETI200.

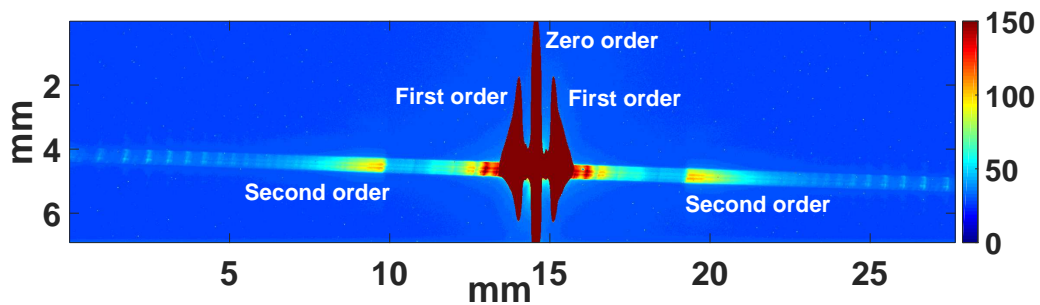


Figure 2.35: Raw image of the solid HH spectrum from Jasnly spectrometer

Figures 2.36a and 2.36b shows an image and a line-out of the calibrated CWE spectrum obtained at JETI200 respectively. In the CWE spectrum, harmonic orders around 30 nm (25<sup>th</sup> harmonic of 800 nm) is seen, although there are stronger higher order harmonics. The strong harmonics around 30 nm compared to other harmonic orders around shows that the harmonic emission in this spectral region is mainly under CWE mechanism. This is similar to the prediction from simulations for solid HHG by CWE mechanism, where the HHs were generated with a lower limit around 25 nm [104]. However, the strong higher order harmonics below 25 nm were generated from ROM mechanism. The generation of harmonics under CWE and ROM mechanism depends on the plasma scale length and in many cases harmonics from both mechanisms can be found in the spectrum [101, 110]. In the current conditions, although the major contribution of harmonic intensity is from ROM mechanism, the lower harmonic orders are mainly generated under the CWE mechanism. The dotted black line in the spectrum shows the aluminum absorption edge.

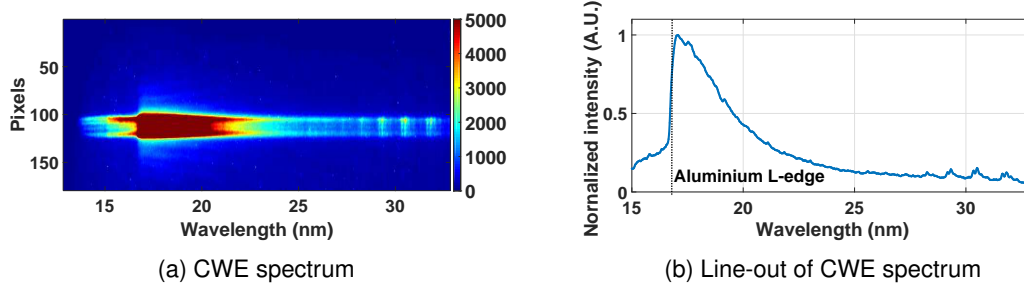


Figure 2.36: HH spectrum from generated under CWE mechanism.

Figures 2.37a and 2.37b shows image and line-out of the calibrated HH spectrum of solid HHG with ROM mechanism respectively. Here all the harmonic orders around 30 nm and below are stronger, unlike in the case of the CWE spectrum. Also, the HH orders are seen until the cutoff of the aluminum filter  $\sim 17$  nm. This shows that most of the harmonic emission is under ROM mechanism. Figure 2.37b shows the vertical line-out of figure 2.37a. From theoretical calculations, considering conditions of HHG, the harmonics can reach below the aluminum cutoff. However, the current experimental setup limits the HHs observed, until the cutoff of the aluminum filter.

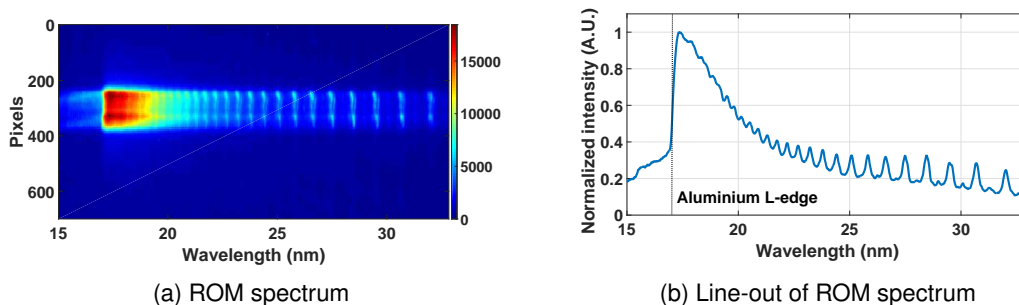


Figure 2.37: HH spectrum from generated under the ROM mechanism.

The laser parameters for generating HHs from solids under CWE and ROM mechanisms, and the obtained XUV properties are listed in table 2.4. The energy and photon numbers are obtained for the whole spectrum assuming a central wavelength of 25 nm, and filter transmission of 16 % and spectrometer

efficiency of 10% for both CWE and ROM mechanisms. The XUV photon number and energy obtained are listed in table 2.4. From the obtained XUV energy, the efficiency of HHG in solids at JETI 200 can be estimated as  $\sim 10^{-10}$ . This is four orders lower than the theoretical efficiency of  $\sim 10^{-6}$  [70].

<b>Mecha- nism</b>	<b>Laser Energy</b> (J)	<b>Pulse duration</b> (fs)	<b>Beam size</b> (mm)	<b>Pre- pulse</b> (ps)	<b>Repetition rate</b> (Hz)	<b>Photon number</b>	<b>En- ergy</b> nJ
CWE	1.8	24	100	0	1	$\sim 4 \times 10^8$	$\sim 3$
ROM	2.4	24	100	-4.5	1	$\sim 6 \times 10^8$	$\sim 4.5$

Table 2.4: The typical conditions for generation of solid HH under CWE and ROM mechanisms at JETI200.

Solid HHG under CWE and ROM mechanisms were successfully established at JETI 200. The conditions obtained are typical operating conditions. Fluctuation was observed in spectrum and photon counts over a number shots. Hence, further analysis and optimization is required for improving the operating conditions. The energy of XUV photons obtained is compared to HHG in gases. This opens ways to use the XUV pulses from solid HHG in applications such as imaging, lithography. However, to use it in applications, the HHs should be stable in energy, spectrum and pointing. Furthermore, HHs should be characterized spatially and temporally.

## 2.4 Comparison between different HHG sources

HHG in gases using different laser systems was optimized in energy and the parameters of the XUV pulses produced are listed in table 2.5. The HHG in solids was successfully carried out for the first time at JETI 200 and HH was generated under CWE and ROM mechanisms. The energy, photon number and spectral range of HHs obtained in solids are listed in table 2.5.

The energy of XUV pulses from HHG in solids is higher than from HHG in gases, at the expense of much higher interaction intensities. However, it was observed that the stability of harmonics in terms of pointing and energy is higher for HHG in gases. Also, HHG using different gases provides a wider spectrum of XUV wavelengths and in optimized cases, a higher efficiency.

The optimized XUV sources at L2I can be now used for imaging in the XUV and using HHG in xenon at L2I can be used for plasma probing as it has higher single shot XUV pulse energy. Although the XUV sources at LOA were operated at lower single shot energies, the source has a repetition rate of 4 kHz and this gives photon number in the order of  $10^9$  photons per second. Among the XUV sources at LOA, the HHG in argon has the highest energy per shot and this source can be used for applications in imaging and characterization of the wavefront of multilayer mirrors and XUV optics, and calibration of wavefront sensors as these experiments require highly stable harmonics with high photon number. The high repetition rate HHG beam line at LOA reduces the acquisition time for imaging and wavefront calibration experiments. The XUV pulses from HHG in gases at the VOXEL lab have higher energy compared to sources at L2I and LOA. Also, this source has a repetition rate of 1 kHz, which can provide XUV pulses with  $\sim 1 \times 10^{12}$  photons per second for HHG in argon and xenon. This source can be hence used for

LAB	Medium	Pressure / mechanism	Photon number per shot	Total HH energy (nJ)	Wavelength Range (nm)	Efficiency
L2I	Argon gas	55 mbar	$7 \times 10^7$	0.44	26.4 - 44.8	$4.4 \times 10^{-8}$
L2I	Xenon gas	15 mbar	$3.6 \times 10^8$	1.44	44.8 - 60.6	$1.4 \times 10^{-7}$
LOA	Argon gas	60 mbar	$2.75 \times 10^6$	0.02	21.6 - 47.0	$8 \times 10^{-9}$
LOA	Neon gas	40 mbar	$1.1 \times 10^6$	0.01	17.1 - 29.6	$4 \times 10^{-9}$
LOA	Xenon gas	13 mbar	$< 1 \times 10^6$	$< 0.01$	38 - 65.1	$< 4 \times 10^{-9}$
VOXEL lab	Argon gas	13.5 mbar	$3.4 \times 10^8$	2.1	29.6 - 42.1	$1.4 \times 10^{-6}$
VOXEL lab	Xenon gas	3.8 mbar	$4.9 \times 10^8$	1.8	42.1 - 53.3	$1.2 \times 10^{-6}$
VOXEL lab	Neon gas	15 mbar	$5 \times 10^5$	0.006	17.02 - 24.2	$4 \times 10^{-9}$
JETI 200	Glass	CWE	$\sim 4 \times 10^8$	$\sim 3$	28.5 - 32	$1.7 \times 10^{-9}$
JETI 200	Glass	ROM	$\sim 6 \times 10^8$	$\sim 4.5$	17.02 - 32	$1.9 \times 10^{-9}$

Table 2.5: Comparison between different XUV sources generated by the process of HHG in gases and solids.

experiments like wavefront sensor calibration, XUV optics characterization, and imaging experiments. Furthermore, the XUV source at VOXEL lab can also be used for single shot experiments.

The XUV source at JETI200 from HHG in solids has energies in the order of few nanojoules, but has low efficiency. Further experiments and analysis are required to optimize the generation process for using it in applications. However, given the limited beam-time available, the achieved efficiency was considered sufficient for the main purpose of the experiment, the characterization of the wavefront of solid HHs for the first time to our knowledge.

## Chapter 3

# Spatial metrology of HHG and XUV optics

### 3.1 Introduction

XUV pulses from HHG have important applications in imaging, probing and lithography. A high spatial quality is required for the XUV pulses in all these applications. A tight and small focus is important for applications like lithography, where a smaller focus can make smaller imprints. Also, a smaller focus increases the fluence at the focus. A higher energy at the focus helps in plasma probing with XUV, as it allows probing plasma with higher spatial resolution. Spatial characterization gives information on how well a pulse can be focused and also its intensity distribution.

Spatial metrology of a pulse consists of characterizing its amplitude (spatial distribution) and its phase (wavefront). For XUV pulses, the spatial amplitude can be determined by using an XUV sensitive CCD [111, 108]. The XUV CCDs can also be used to estimate the photon count and energy of the HHs generated as shown in section 2.2.2. The spatial distribution of XUV pulses, when focused can also be obtained by observing the fluorescence from materials like Ce-YAG [112, 113].

The wavefront of a beam is defined as the positions of different spatial points in the beam with a constant phase relation. The characterization of the wavefront of a beam gives the spatial phase of the beam. Any deviation from a perfect plane wavefront is called a wavefront aberration. The aberrations in the wavefront of a beam diminishes the convergence of energy of the beam to a point image or a spot, thereby degrading the image or reduces the intensity at the spot. Hence, characterizing the wavefront quality of a beam gives us the information on how well the beam can be focused to get better quality images or reach higher peak intensities. This is important for applications which require a higher spatial resolution or a high flux at a target. It is also important to characterize the wavefront of the pulses reflected by optics used to focus the pulses as they also contribute to wavefront aberrations. The XUV optics used are usually reflective optics and they can be multilayer mirrors or optics in grazing incidence (discussed in 3.1.1). In the case of coherent XUV beams and XUV optics, wavefront aberrations can be measured using different methods like XUV interferometers [114] and XUV wavefront sensors (WFS) [53, 54, 115].

The most commonly used WFSs in the XUV are Hartmann WFSs [54]. The Hartmann XUV WFS has advantages over the other type of wavefront measurement since it can measure both intensity and phase of the beam simultaneously, it can work with spatially and temporally partially coherent beams [54] and it is easy to set up and use.

For lithography, using lower wavelengths i.e, in the XUV region of the spectrum is advantageous since the XUV pulses can be focused to smaller spots compared to UV or visible radiations. A smaller focal spot is highly desired for creating smaller features and to have higher throughput. For a smaller focal spot, it requires high numerical aperture (NA)  $> 0.1$  optics to focus the pulses [4]. In order to use these high-NA optics, they need to be characterized and optimized using a high-NA WFS. For XUV radiation, it is difficult to use multiple optics to collimate the highly diverging beam from a high-NA optic. Hence, it is highly desired to have a high-NA XUV WFS. Also, spatial characterization of highly diverging XUV sources, such as HHG from solids [75] requires high-NA XUV WFS.

The optics used in the XUV to manipulate the pulses in different directions or to select a particular wavelength need to be characterized in wavefront at the XUV wavelengths. At-wavelength characterization is important since it will give information about the local changes in the wavefront introduced by the XUV optics.

In this chapter experimental results on the calibration of high-NA XUV WFSs are presented. Furthermore, the characterization of the wavefront of XUV optics and HHG using the XUV WFSs are also discussed.

### 3.1.1 XUV Optics

The optical properties of commonly used optical materials such as silica, gold, and silver are characterized by very low reflectivity at nearly normal incidence and attenuation lengths of  $< \mu\text{m}$  for the XUV spectral range [1]. This makes it difficult to use dispersive optics for XUV radiation. Mostly reflective optics at grazing incidence and multilayer mirrors are used for manipulating XUV radiation [1].

#### 3.1.1.1 Reflective optics at grazing incidence

The reflectivity of optics in grazing incidence geometry for XUV radiation increases with decreasing grazing angle. Figure 3.1 shows the change of reflectivity with the angle of incidence changing from normal incidence to grazing for silica, silver, and gold at a wavelength of 32 nm [92]. The region marked in black dashed lines in the figure 3.1 shows the grazing incidence angle with reflectivity  $> 20\%$  for silica, silver, and gold. Optics for the XUV can be thus made with silica or coating the silica substrate with either silver or gold and can be used at a grazing angle for better reflectivity for XUV. When using focusing optics in grazing incidence, the focal length depends also on the grazing angle and it is given by

$$f_{\text{grazing}} = f \sin(\theta_{\text{grazing}}) \quad (3.1)$$

where  $f$  is the focal length at normal incidence and  $\theta$  is the grazing angle. The most commonly used focusing optics in grazing incidence geometry for XUV pulses are spherical concave mirrors and toroidal

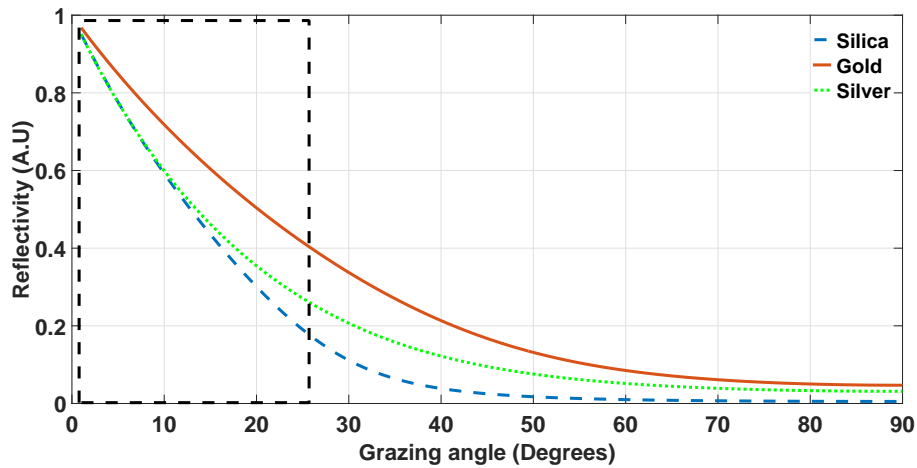


Figure 3.1: Reflectivity of mirrors with different substrates at 32 nm for linearly polarized XUV radiation [92].

mirrors [116]. A combination of these focusing mirrors can also be used in grazing incidence geometry to focus the XUV beam called, Kirkpatrick-Baez geometry [117].

### 3.1.1.2 Multilayer mirrors

One way to use optics in the XUV spectral region at normal incidence or near normal incidence is with a type of mirrors called multilayer mirrors [1]. A multilayer mirror has alternated layers of two or more materials with different refractive indexes. When an XUV beam is incident on a multilayer mirror, the different layers reflect a small part of the beam and finally the beams reflected from different layers interfere to form the reflected XUV beam from the multilayer mirror. The layers of the multilayer mirror follow the Bragg's law ( $m\lambda = 2d \sin(\theta)$ ) with a periodicity,  $d$  equal to one bilayer thickness,  $\lambda$  is the wavelength of the radiation and  $\theta$  is the angle of incidence. The bilayer thickness,  $d = t_A + t_B$  where  $t_A$  and  $t_B$  are the thicknesses of the low  $Z$  ( $Z$  - atomic number) layer and the high  $Z$  layer respectively [1]. Figure 3.2 shows the reflection of an incident beam from different layers of a multilayer mirror. Usually the

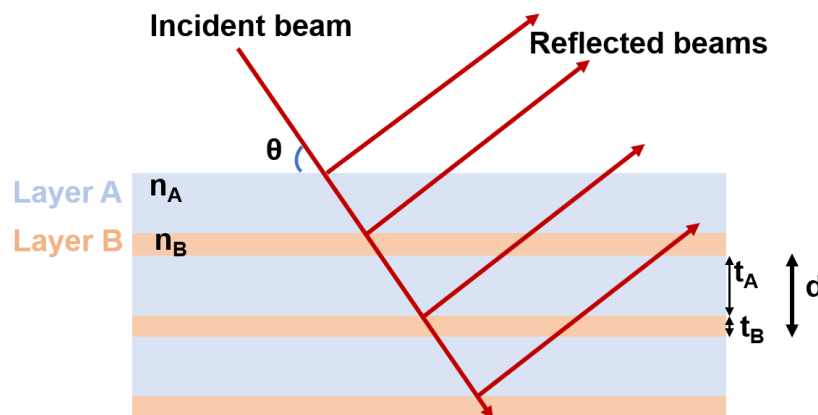


Figure 3.2: Illustration of reflection of light from different layers of a multilayer mirror.

alternating layers have materials with high  $Z$  and low  $Z$ . The idea is that the layer with high  $Z$  elements

acts as the main scattering component and the low Z element one acts as the spacer which provides the interface for the beam to interact with the alternating layers of the high Z material. The beam passes through the low Z material (layer A) and is then reflected at the interface of the low Z material layer and high Z material layer (layer B). These reflected beams constructively interfere at a particular angle to get maximum reflectivity.

### 3.1.2 Hartmann WFS

A Hartmann WFS works on the basis of projecting a beam sampled through a hole array on to a 2D detector. The technique was developed in 1900 by J. Hartmann [118] and it allows to track the directions of individual rays in a beam. The basic working principle of Hartmann WFS is illustrated in figure 3.3. First, a reference beam, usually a near perfect plane or spherical wavefront is allowed to pass

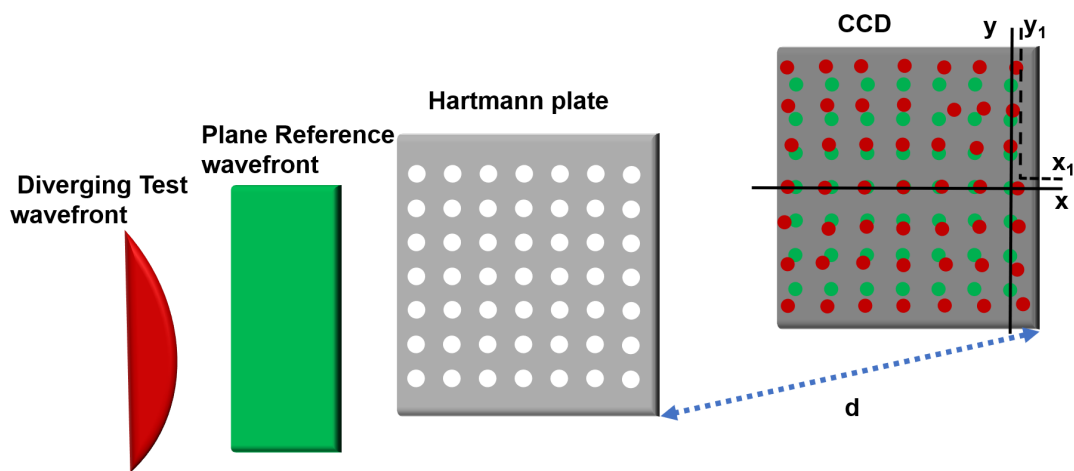


Figure 3.3: Schematic of the working principle of Hartmann WFS. The pattern generated by a reference wavefront (shown in green) on the CCD after the Hartmann plate is compared to the pattern generated by a test wavefront (shown in red) to measure the wavefront aberrations.

through the aperture/hole array, also called Hartmann plate. The holes are also called sub-apertures. The positions of the pattern of the XUV pulses projected onto the detector by the Hartmann plate are recorded. These positions are considered as the reference positions (shown in green) and they are denoted by coordinates  $x_0$  and  $y_0$  in figure 3.3. When a beam with wavefront aberrations (shown in red) is incident on the hole array, the pattern projected deviates from the reference position and these positions are denoted by coordinates  $x_1$  and  $y_1$  in figure 3.3. The wavefront errors hence can be calculated by estimating the change in position for the patterns on the detector for the wavefront with aberration to that of the perfect wavefront. The wavefront is represented by a phase value  $\phi$ . Figure 3.4 describes the wavefront  $\phi$  for a spherical wave originating from the center, O. The wavefront at a distance  $R$  from O can be written as

$$R^2 = r_1^2 + (R^2 - \phi(r_1)^2) \quad (3.2)$$

Solving for  $\phi$  by expanding, we can estimate  $\phi$  as

$$\phi(r) \approx \frac{r^2}{2R} \text{ for } R \gg r \quad (3.3)$$

The slope of the wavefront is given by

$$\frac{\partial\phi(r)}{\partial r} \approx \frac{r}{R} \quad (3.4)$$

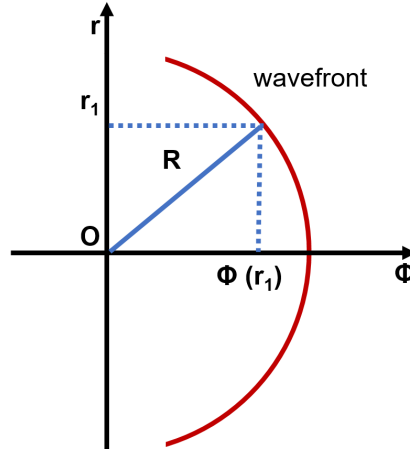


Figure 3.4: Schematic of the wavefront of a spherical wave.

For a Hartmann WFS with a 2 D detector, the slope is calculated by taking the difference between the centroids of the diffraction pattern produced by the test and reference wavefront. For the case shown in figure 3.3, the average slope of the wavefront over a sub-aperture in the hole array plate along the  $x$  direction is written as

$$\frac{d\phi(x, y)}{dx} = \frac{\Delta x}{f} = \frac{x_0 - x_1}{f} \quad (3.5)$$

where  $f$  is the distance between the Hartmann plate and the CCD. An analogous equation holds true for the slope of the wavefront over the sub-aperture along the  $y$ -axis. In a Hartmann WFS, after getting the value of slopes from the sub-apertures, also called the local wavefront slopes, the wavefront of the beam can reconstructed by using mainly two methods: modal reconstruction and zonal reconstruction [119, 120, 121]. Both reconstruction methods are briefly described below.

### 3.1.2.1 Modal wavefront reconstruction

In modal wavefront reconstruction, the wavefront is represented by a polynomial function,  $F_n(x, y)$  with coefficients,  $C_n$ . In wavefront metrology of an optical system mostly the Zernike polynomials are used as the polynomial function [120]. Zernike polynomials are a set of orthogonal polynomials defined over a unit circle. The individual Zernike polynomials can be used to describe the lower and higher order wavefront aberrations. The major aberrations which can be obtained from Zernike polynomials are piston, tilt, defocus, coma and astigmatism [120]. The modal reconstruction of the wavefront and the aberration values can be found by least square fitting of the slopes calculated over the whole wavefront. For  $x$  direction it is given by

$$\frac{d\phi(x, y)}{dx} = \sum_n \frac{d}{dx} C_n F_n(x, y) \quad (3.6)$$

The analog of equation 3.6 gives the wavefront in  $y$ -direction. The modal reconstruction gives a smooth fit over the whole wavefront considering the superposition of different optical aberrations, i.e. lower order and higher order wavefront errors. However, it does not take into account the local fluctuations in the wavefront slopes.

### 3.1.2.2 Zonal wavefront reconstruction

Zonal wavefront reconstruction follows a linear integration of the wavefront gradients along the different sub-apertures. This takes into account the local slope variations. In the linear integration method, the slopes at a sub-aperture  $n$  is calculated as the sum of wavefront height of previous sub-aperture plus slope of the previous sub-aperture  $n - 1$  times the distance between the sub-apertures ( $d$ ). It is given in the  $x$ -direction as [119]

$$\frac{d\phi_n}{dx} = \phi_{n-1} + \frac{d\phi_{n-1}}{dx} d \quad (3.7)$$

where  $n$  is the sub-aperture number. A more advanced and highly accurate zonal reconstruction was introduced by Southwell [122]. In the Southwell reconstruction the wavefront height at a point  $(n, m)$  is calculated by taking the average of wavefront heights predicted by its nearest neighbors. It is given by [121, 119]

$$\phi_{n,m} = \sum_{j=-1}^1 \sum_{i=-1}^1 I_{n+i,m+j} \left[ \phi_{n+i,m+j} + \left( \frac{\frac{\partial \phi}{\partial x_{n,m}} + \frac{\partial \phi}{\partial x_{n+i,m+j}}}{2} \right) d \right] \quad (3.8)$$

where  $\phi_{n,m}$  is the wavefront at grid location  $(n, m)$ ,  $d$  is the separation between the  $(n, m)$  integration area and the  $(n + i, m + j)$  integration area and  $I_{n+i,m+j}$  is the intensity measured in the  $(n + i, m + j)$  integration area [121, 119].

### 3.1.2.3 Hartmann WFS in the XUV

The first XUV WFS was developed by Le Pape et al., in 2002, based on the Shack-Hartmann technique [53]. Later, a XUV WFS based on Hartmann technique was developed by Imagine Optic [123] in collaboration with LOA [124] and SOLEIL synchrotron, France [125] in 2003 [54]. This Hartmann XUV WFS consists of an aperture array made of nickel plate placed at a fixed distance from XUV sensitive CCD [111]. In the XUV Hartmann WFS from Imagine Optic, the holes of the Hartmann plate have a square shape and the square holes are tilted by  $25^\circ$  from the horizontal of the plate [126]. The holes are tilted to avoid cross-talk between consecutive diffraction patterns formed on the CCD [54]. Later, a Hartmann WFS in the XUV was also jointly developed by Laser-Laboratorium Göttingen e.V. (LLG) [127] and Deutsches Elektronen-Synchrotron (DESY) [22] [115]. The currently available XUV WFS are designed to work in the spectral range of 4 nm to 44 nm [128, 129].

For a Hartmann WFS, the numerical aperture (NA) can be estimated considering the size of the Hartmann plate, the size of the detector and the distance between the Hartmann plate and the detector. For the currently available WFS in the XUV region, the estimated numerical aperture is in the order of 0.01 [54, 129]. This limits the use to XUV beams with a divergence of few milliradian and prevents from characterizing XUV beams with larger divergence as encountered on solid high harmonics [75], XUV

lithography [130, 4] and XUV microscopy [131, 132].

#### 3.1.2.4 Calibration of XUV Hartmann WFS

The wavefront aberrations in a Hartmann WFS are calculated by comparing the shift of the projection of a wavefront with aberrations to that of a perfectly known wavefront. Commonly, a known wavefront is obtained by spatially filtering an XUV beam and the filtered beam is assumed to have a near perfect spherical wavefront. The spatial filtering is usually done by placing a pinhole in the XUV beam. The pinhole causes the diffraction of the XUV beam. To have a reference beam with a wavefront quality in the order of  $\lambda_{XUV}/100$ , the useful apertures of the Hartmann plate should be illuminated by half of the airy disk formed by the XUV beam diffracted from a pinhole [133, 54]. The maximum pinhole diameter,  $d_{max}$  that can be used to generate the near perfect spherical wavefront can be calculated using the Airy disk formula given by

$$d_{max} = 1.22 \frac{\lambda_{XUV} L}{D} \quad (3.9)$$

where  $\lambda_{XUV}$  is the XUV wavelength,  $L$  is the distance between pinhole and the Hartmann plate and  $D$  is the size of the Hartmann plate. The spatial filtering reduces the intensity of the XUV beam and thus to get a good signal to noise ratio for calibration data the XUV signal needs to be integrated over time. The integration over time requires the XUV source to be highly stable in energy and pointing. When designing the Hartmann WFS, the Hartmann plate has to be designed and optimized with a grid for a wavelength range for which the wavefront characterization needs to be done. Once calibrated at a given wavelength, the sensor keeps its accuracy on the whole designed spectral range [54].

## 3.2 Experimental results on calibration of XUV WFS

The wavefront characterization of high-NA optics and highly diverging sources, requires a high NA XUV Hartmann WFS. Two XUV WFS's with higher NA compared to the available ones [128, 129] were designed, developed and calibrated in collaboration with Imagine Optic [123], a pioneer in XUV spatial metrology. The XUV WFSs were designed and assembled at Imagine Optic and were calibrated in XUV at the HH beam line in Salle Corail, LOA. The results of XUV WFS calibration are presented in this section.

### Preliminary calibration of XUV WFS @ Imagine Optic

The WFSs designed and assembled by Imagine Optic undergoes a preliminary calibration using a laser beam at Imagine Optics, Orsay, France [134]. This calibration makes use of the Talbot effect [135, 136], in which a diffraction pattern is generated when a diffractive optics is illuminated with a plane wave and the image of the diffractive optics is repeated at fixed distances along the propagation direction of the plane wave. In the preliminary calibration setup for the XUV WFS, the Hartmann plate position is adjusted with respect to the CCD by looking at the Talbot image pattern on the CCD, generated from the Hartmann plate which is illuminated with a laser beam. The parallel alignment of the Hartmann plate with

respect to the CCD is assured using this method. Also the Hartmann plate to CCD distance, size of the holes in the Hartmann plate are calibrated accurately. After this preliminary calibration using Talbot effect, the XUV WFSs are calibrated in using an XUV beam.

### 3.2.1 Calibration of an XUV WFS

#### 3.2.1.1 Design of the XUV WFS ( $NA \approx 0.02$ )

The Hartmann type XUV WFS consists of a Hartmann plate with a grid pitch of  $210\ \mu\text{m}$  and the detector used is a PIXIS XO 1024B X-ray CCD from Princeton instruments. The Hartmann plate is made of nickel and it is square in shape with a size of  $13\ \text{mm} \times 13\ \text{mm}$ . It has  $60 \times 60$  square holes to sample the XUV beam and the holes are rotated by  $25^\circ$  in order to minimize the overlap of diffraction pattern from adjacent holes on the detector [126]. It is placed at a distance of  $43.5\ \text{mm}$  from the CCD. The PIXIS XO 1024B X-ray CCD is thinned back-illuminated with  $1024 \times 1024$  pixels and a pixel size of  $13\ \mu\text{m} \times 13\ \mu\text{m}$ . The total length of the XUV WFS is  $270\ \text{mm}$ . The numerical aperture in case of the WFS is estimated considering size of the Hartmann plate, size of the detector and the distance between the Hartmann plate and the detector. The estimated NA of this WFS is  $\approx 0.02$  and it is double the NA of currently available XUV WFS [128, 129]. Figure 3.5a shows the picture of XUV WFS with a ruler and figure 3.5b gives a direct view of the Hartmann plate inside the XUV WFS.

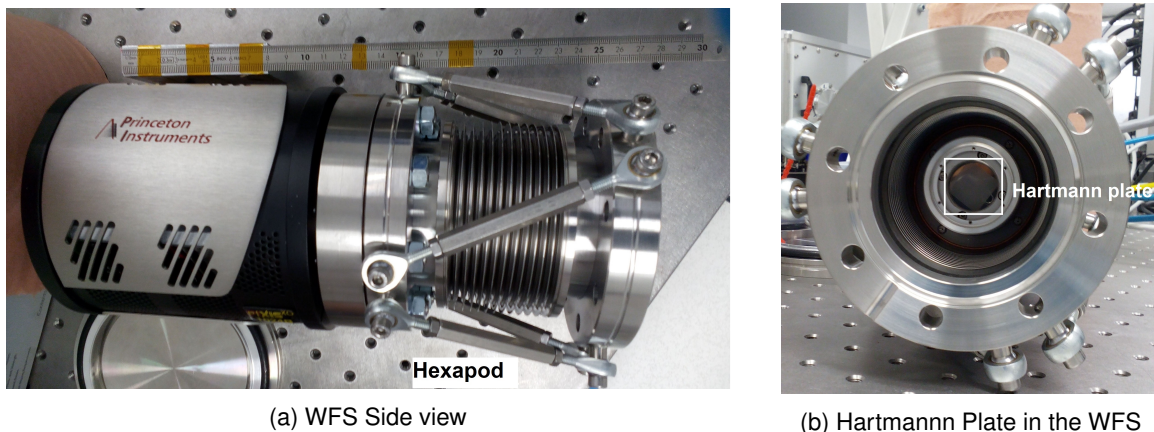


Figure 3.5: XUV Hartmann WFS for calibration.

#### 3.2.1.2 Calibration of XUV WFS

The first part of the calibration is spatial filtering of the XUV beam. For spatial filtering, the pinhole size was estimated using the equation 3.9 considering a distance of  $305\ \text{cm}$  between pinhole and WFS, XUV wavelength of  $32\ \text{nm}$  and a Hartmann plate size of  $13\ \text{mm}$ . The estimated pinhole size (diameter) was  $\sim 9\ \mu\text{m}$ . Because of unavailability of the pinhole of size  $< 9\ \mu\text{m}$  in the lab, we used a  $10\ \mu\text{m}$  pinhole for calibration. The  $10\ \mu\text{m}$  pinhole used was a ceramic pinhole from Edmund optics, which has the specifications to be used with high power lasers.

Figure 3.6 shows the schematics for calibration of Hartmann type XUV WFS. The experimental setup consists of the XUV source, spatial filtering with  $10\ \mu\text{m}$  pinhole and the WFS. HHG in argon was

used as the source of XUV beam. For HHG, the laser (described in section 2.2.2.2) is focused onto the gas cell with a length of 20 mm with argon at 30 mbar of pressure. The central wavelength of the harmonic spectrum is assumed to be at 32 nm considering the earlier spectral characterization of HHs. The XUV beam is then spatially filtered and used for calibration of the WFS. For calibration, the WFS was placed at a distance of 305 cm after the pinhole position.



Figure 3.6: Schematic of the setup for calibration of XUV wavefront sensor

The pinhole was placed at a distance of 15 cm from the gas cell to spatially filter the XUV beam generated by HHG. This placement of pinhole close to the gas cell partially helps in blocking the residual IR laser. Figure 3.7a shows the experimental setup with the gas cell and pinhole. The pinhole was placed on a 3-axis stage to further optimize its position in the XUV beam and hence to optimize the transmission through it. A large chip-size PI-MTE-2048B X-ray in-vacuum CCD from Princeton Instruments was used as detector after the pinholes to optimize the XUV transmission through the pinhole. The CCD was placed at a distance of 165 cm from the pinhole position. The spatially filtered XUV beam had a diameter ( $1/e^2$ ) of  $\sim 10$  mm after 165 mm and it is shown in figure 3.7b. The FWHM of the beam was  $\sim 6$  mm. From this, the FWHM beam size at a distance of 305 mm was estimated to be greater than 13 mm which is the size of the Hartmann plate in the WFS.

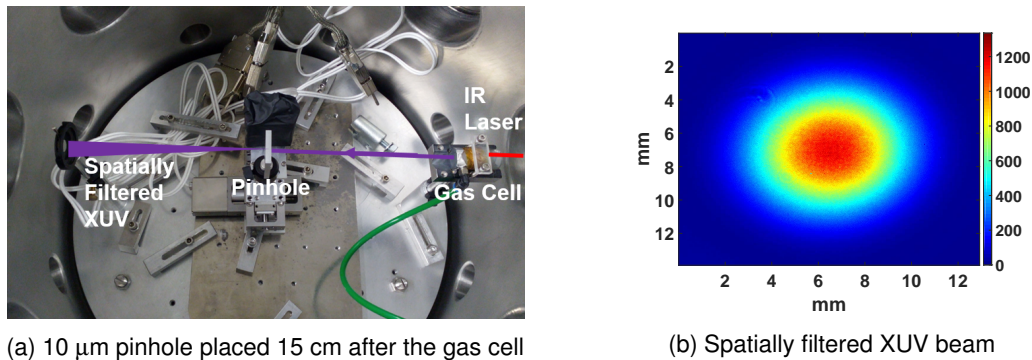
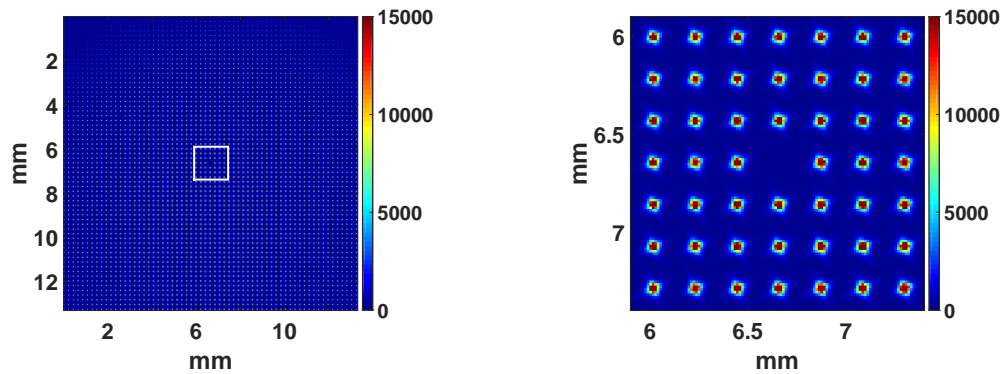


Figure 3.7: Spatial filtering of XUV with 10  $\mu$ m pinhole

For measuring the wavefront, the WFS should be aligned perpendicular to the incident XUV beam. This was done using the hexapod (marked in figure 3.5a) attached onto the CCD of the XUV WFS. The hexapod is a six axis positioner which gives 2-D movement plus tip / tilt motion for the XUV WFS attached to a flange on a vacuum chamber. For aligning the XUV beam perpendicular to the WFS, the central part of the Hartmann plate in the WFS is used. At the center of the Hartmann plate there is a position with no hole (from now on called black-hole) and this does not project any pattern onto the CCD. For XUV beam to be perpendicular to the WFS, the position of black-hole should be at the center of the CCD and in this case, the center of the CCD is at pixels (512, 512). Since we cannot exactly pinpoint the center of

the black-hole, the alignment is carried out by analyzing the pattern on the CCD projected by the nearby holes and aligning the center of these patterns along the vertical and horizontal center pixels in the CCD.

After the XUV beam was aligned perpendicular to the WFS, the calibration images for the XUV WFS were recorded. Figure 3.8a shows the raw image recorded by the XUV WFS with a white square showing the center part with black-hole. Figure 3.8b shows the zoom of the part marked in figure 3.8a and here we can clearly see the position of the black-hole and also the diffraction pattern from the Hartmann plate.



(a) False color map of the raw image from the WFS (b) Zoomed central part shown in white square in (a).

Figure 3.8: Raw image of spatially filtered XUV signal recorded on XUV Hartmann WFS.

Multiple images were acquired with the WFS at the same position and the variation of the slopes at same sub-pupils in different images were compared. This analysis allowed the production of a calibration file at Imagine Optics. The procedure of generation of this calibration file is trade secret of Imagine Optic. This calibration file was used in the HASO software to reconstruct the wavefront and intensity of the calibration beam. The software is from Imagine Optic and it can be used to control the WFS, analyze the wavefront errors and also reconstruct the wavefront and intensity of the XUV beam. Figure 3.9a and 3.9b shows the reconstructed intensity and wavefront of the beam respectively. Analysis using the HASO software with the calibration file gives a wavefront accuracy of  $\lambda/29$  RMS for the calibrated XUV WFS, assuming a central wavelength of  $\lambda = 32$  nm for the XUV beam.

## 3.2.2 Design and calibration of a high-NA XUV WFS

### 3.2.2.1 Design of high-NA XUV WFS ( $NA \approx 0.1$ )

The high-NA XUV Hartmann WFS was designed and assembled at Imagine Optic SA [123]. It is an in-vacuum WFS and consists of a Hartmann plate attached to an in-vacuum detector. The Hartmann plate is made of nickel with a thickness of 40 – 50  $\mu\text{m}$  with a diameter of 32.5 mm and a clear aperture of 20 mm. The Hartmann plate has square holes with a dimension of 50  $\mu\text{m}$  separated by 150  $\mu\text{m}$  and the holes are rotated by 25° in order to minimize the overlap of diffraction pattern from adjacent holes on the detector [126]. The Hartmann plate is placed at a distance of 50 mm from the detector on a cylindrical tube. A large chip-size PI-MTE-2048B X-ray CCD from Princeton Instruments is used as the detector. The CCD is an in-vacuum CCD with water cooling and it is thinned and back-illuminated with 2048  $\times$

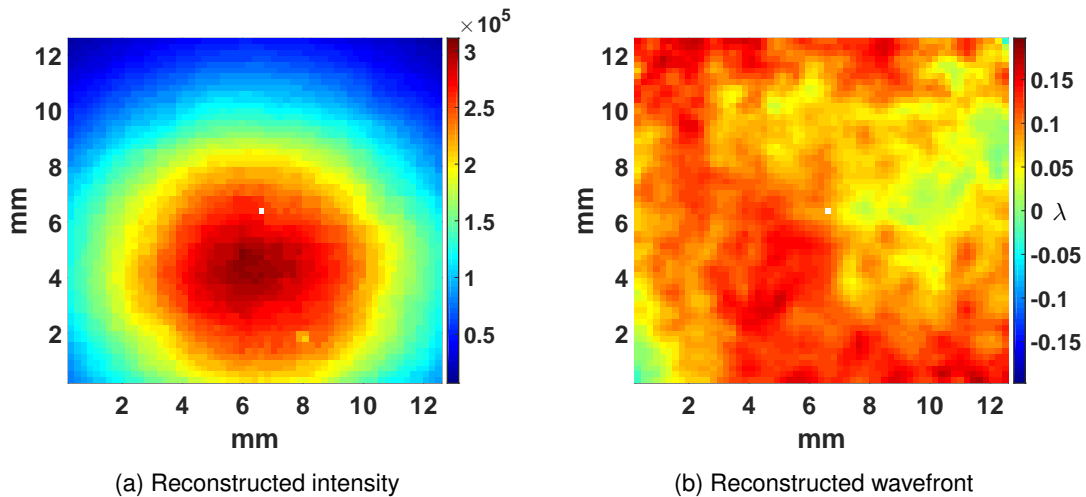


Figure 3.9: Reconstructed Intensity and wavefront of the calibration beam after the pinhole, used for XUV WFS calibration

2048 pixels. The pixel size is  $13.5\ \mu\text{m} \times 13.5\ \mu\text{m}$ . The high-NA XUV WFS is compatible to high vacuum conditions, up to a pressure of  $\sim 10^{-6}$  mbar. Considering the Hartmann plate and CCD configuration, the NA of the high-NA XUV WFS is estimated to be in the order of 0.1 which is an order higher compared to the currently available XUV WFS [128, 129]. The high-NA XUV WFS has a dimension of  $170\ \text{mm} \times 60\ \text{mm} \times 80\ \text{mm}$  which is smaller compared to currently available XUV WFS [128, 129]. However, the high-NA XUV WFS does not have any motorization attached to it. So it has to be attached with necessary translation stages, rotation and tip/tilt stages for optimizing its alignment during experiments. The schematic of the high-NA XUV WFS is shown in figure 3.10a. Figure 3.10b shows the high-NA XUV WFS placed on a rotation and tip/tilt stage. Figure 3.10c and 3.10d shows the schematic and a picture of the Hartmann place used in the high-NA XUV WFS, respectively.

The in-vacuum design of the WFS enables it to be highly maneuverable. It can be used for close-in detection to characterize highly diverging XUV beams. Because of the high-NA of the this WFS, it can be used to characterize the wavefront of XUV focusing optics which can create sub-micron focal spots and also can be used to optimize these focal spots.

### 3.2.2.2 Calibration of high-NA XUV WFS

A perfectly known wavefront for calibrating the high-NA XUV WFS is generated by spatial filtering of XUV beam using a pinhole. The size of the pinhole required to create near spherical wavefront was estimated using the equation 3.9. Since the WFS is an in-vacuum, the distance from the pinhole was limited by the size of the vacuum chamber used. In case of the experimental chamber at Salle Corail, LOA this distance can be safely assumed to be 60 cm (more or less half the chamber length). Considering a maximum distance of 60 cm between pinhole and WFS, XUV wavelength of 32 nm and a Hartmann plate size of 20 mm, the estimated maximum diameter of the pinhole required was  $\sim 1\ \mu\text{m}$ . Since we want to keep the WFS within less than 60 cm, a pinhole of size  $0.5\ \mu\text{m} \pm 0.3\ \mu\text{m}$  was used. The pinhole size is very small compared to the case of the XUV WFS calibration (3.2.1). So in case of the high-NA XUV WFS, the XUV beam was focused to increase the transmission through the  $0.5\ \mu\text{m}$  pinhole.

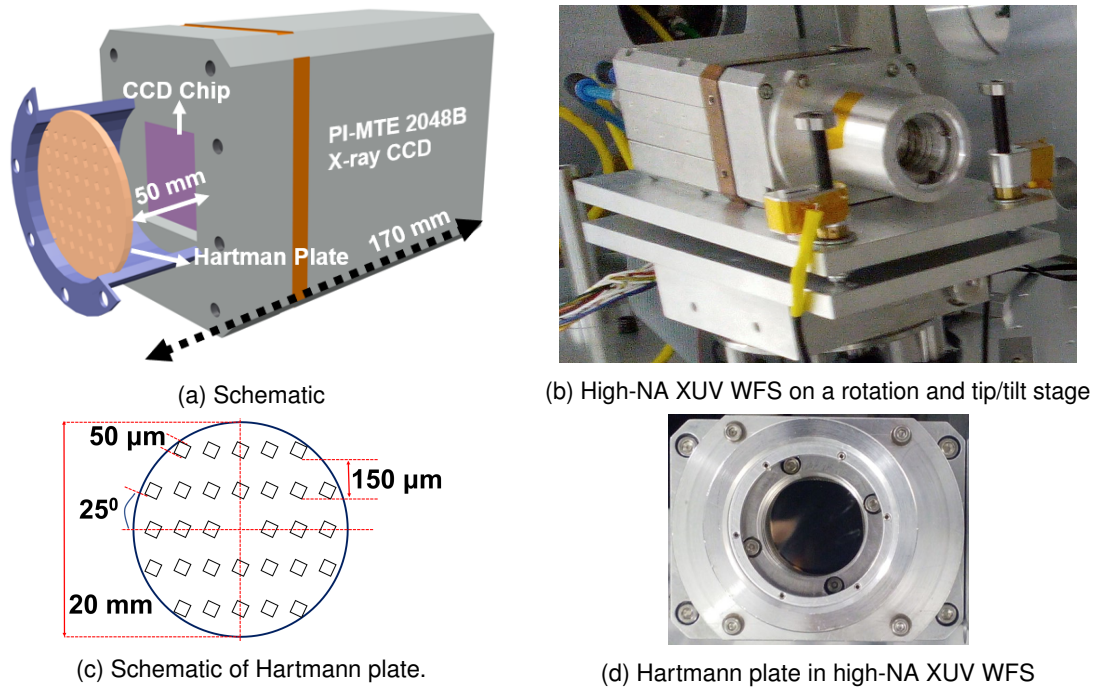


Figure 3.10: The schematic, picture, schematic of Hartmann plate and picture of Hartmann plate of the high-NA XUV WFS.

Figure 3.11 shows the schematic of the experimental setup for high-NA XUV WFS calibration. The laser (described in section 2.2.2.2) was focused onto a gas cell with a length of 20 mm filled with argon gas at a pressure of 30 mbar using a plano-convex lens of focal-length 750 mm. The residual infrared laser was filtered with two aluminum filters of thicknesses 150 nm and 300 nm. A flat silicon plate was used at  $10^\circ$  grazing angle to steer the harmonic beam to the gold-coated toroidal mirror (ROC horizontal = 1500 mm, dimensions = 100 mm  $\times$  30 mm) which was also aligned at  $10^\circ$  grazing incidence. The toroidal mirror was placed in 5-axis stage for aligning it with respect to the incident beam. A set of pinholes was mounted on a 3-axis translation stage and placed at the focal spot of the toroidal mirror to spatially filter the focused high harmonic beam. Among the set of pinholes, a ceramic pinhole of diameter  $0.5 \mu\text{m} \pm 0.3 \mu\text{m}$  was used to spatially filter the high harmonic beam required for calibration of the high-NA XUV WFS.

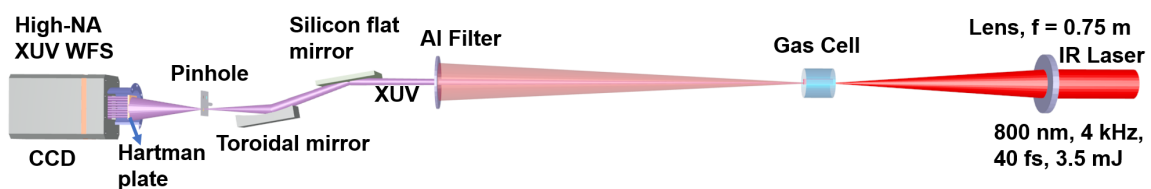
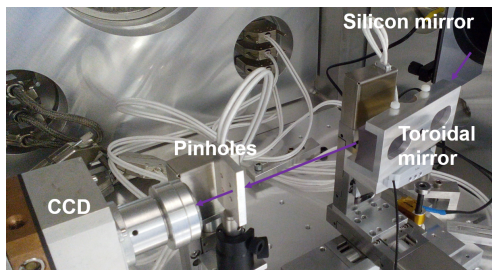


Figure 3.11: Schematic of the setup for calibration of high-NA wavefront sensor

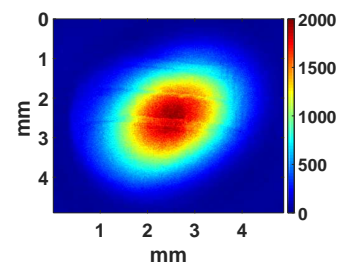
The first part of the calibration is to generate the spatially filtered XUV beam. Once the toroidal mirror was optimized for the best focal spot using a He-Ne laser and visible CCD (which will be described in further details later, see figure 3.23), the pinholes were placed at the focus of the toroidal mirror. After a pre-alignment with the He-Ne laser, the pinhole positions were optimized using XUV beam. For

this, an X-ray PI-MTE 2048B in-vacuum CCD was placed 5 cm after the pinhole. The pinhole position was optimized for maximum transmission of XUV through it. Figure 3.12a shows the picture of the experimental setup for aligning the pinhole with XUV beam. The pinhole position was optimized by moving the pinhole in the 3-axis stage with respect to the incoming beam. The optimized beam was recorded in the CCD and an image was acquired with an integration time over 1 minute.

Figure 3.12b shows a cross-section of the intensity profile of the Airy disk produced by the beam diffracted from the pinhole measured at a distance of 5 cm from the pinhole. The beam was slightly elliptical with FWHM in the horizontal and vertical direction 2.9 mm and 2.8 mm respectively. The estimated FWHM of the Airy disk of the XUV beam diffracted from the pinhole assuming a central wavelength of 32 nm for the harmonics and 0.5  $\mu\text{m}$  as the beam diameter for the pinhole at a distance of 5 cm from the pinhole was 5.8 mm. But the obtained FWHM of the Airy disk was smaller and this might be due to larger pinhole size. From the obtained airy disk pattern the pinhole diameter was estimated to be  $\sim 0.8 \mu\text{m}$ . From the experimentally obtained FWHM of the beam, the position where the FWHM of the beam will be more than the diameter of the Hartmann plate was estimated. At 35 cm from the pinhole, the FWHM of the Airy disk was estimated to be  $\approx 20.6$  mm. This estimated size of the beam was enough to cover the Hartmann plate with the FWHM of Airy disk of the beam diffracted from the pinhole.



(a) Experimental setup



(b) Spatially filtered XUV beam

Figure 3.12: The experimental setup for optimizing the pinhole position with HFs and the spatially filtered XUV beam.

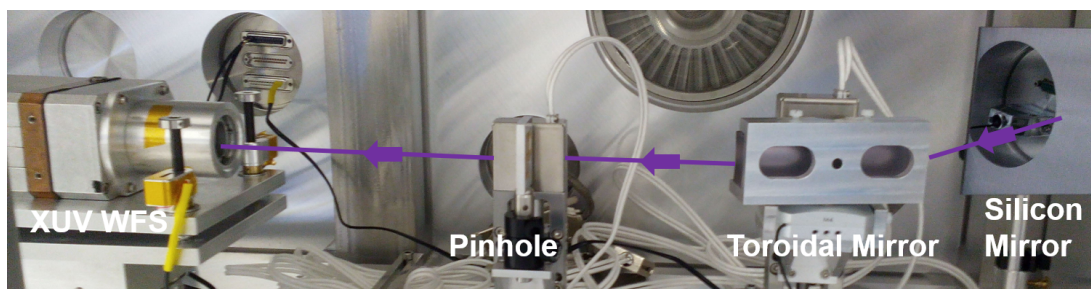
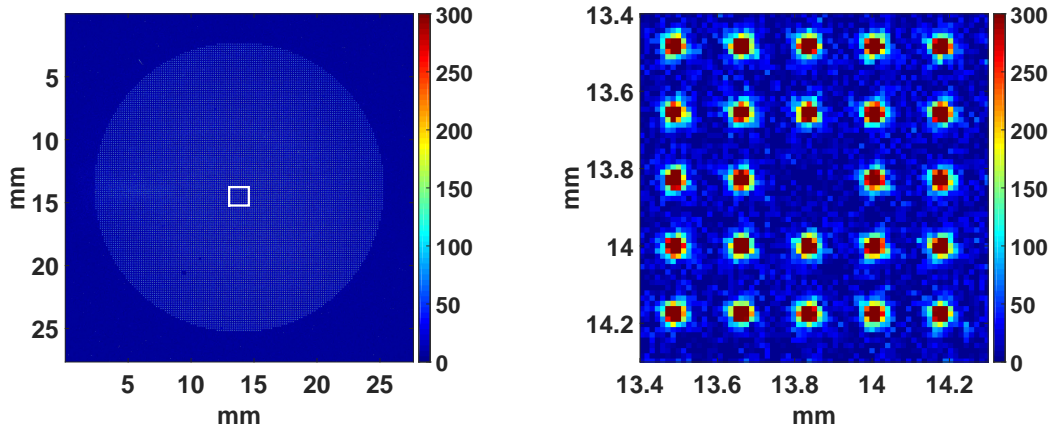


Figure 3.13: Experimental setup for calibration of the high-NA wavefront sensor. In this picture WFS is placed at a distance of 17 cm from the pinhole.

Figure 3.13 shows a picture of the experimental setup for calibration of high-NA XUV WFS in the experimental chamber. The WFS is placed at the estimated distance of 35 cm from the pinhole on a multi-axis stage. The multi-axis stage consists of a translation stage which can move perpendicular to the incident beam direction, a rotation stage which can rotate in the horizontal plane and also a tip/tilt

stage that can be used to adjust the orientation of WFS in the vertical direction with respect to the XUV beam. An aluminum filter of thickness 150 nm was placed in front of the WFS to further filter out the residual IR laser and also to block the light noise in the experimental chamber from the pressure gauge and translation stages. The WFS was aligned perpendicular to the XUV beam by aligning the back-hole to the center of the CCD (described in section 3.2.1.2). In the case of the high-NA XUV WFS, the CCD center is at pixel coordinates (1024,1024).



(a) False color map of the raw image from the WFS (b) Zoomed central part shown in white square in (a).

Figure 3.14: Raw image of the spatially filtered XUV signal recorded on the high-NA XUV Hartmann WFS.

The images of the XUV beam were acquired with the high-NA XUV WFS with an integration time over 30 minutes to get a good signal to noise ratio. The CCD of the WFS was cooled down to  $-30^{\circ}$  during these acquisitions to further reduce the noise. The figure 3.14a shows the raw wavefront sensor image with a white square showing the center part with black-hole. Figure 3.14b shows the zoom of the part marked in figure 3.14a and here we can clearly see the position of the black-hole and also the diffraction pattern from the Hartmann plate.

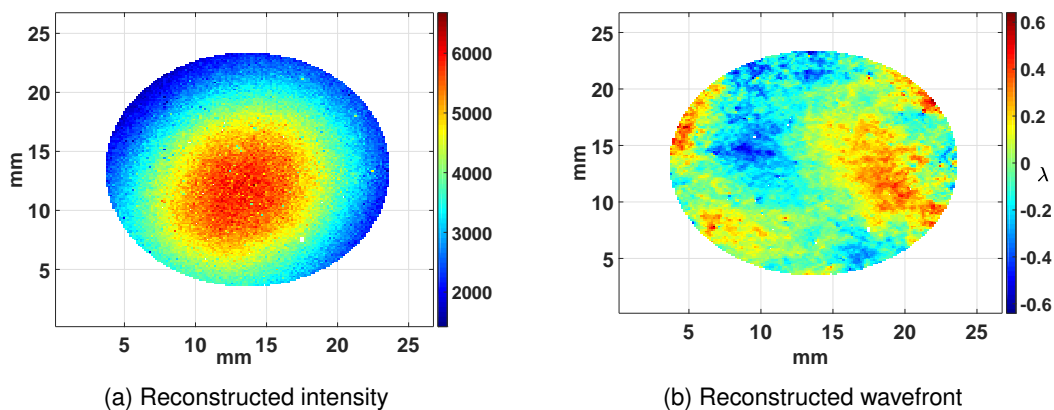


Figure 3.15: Reconstructed intensity and wavefront of the spatially filtered XUV beam used for high-NA XUV WFS calibration.

From the analysis, a calibration file for the high-NA XUV WFS was produced and it was used in the HASO software from Imagine Optic to reconstruct the wavefront and intensity of the calibration beam.

Figure 3.15a and 3.15b shows the reconstructed intensity and wavefront of the beam respectively.

Analysis using the HASO software with the calibration file gives a wavefront accuracy of  $\lambda/6$  RMS for the calibrated high-NA XUV WFS, assuming a central wavelength of  $\lambda = 32$  nm for the XUV beam. Further the acquired images were analyzed and the RMS wavefront error obtained is plotted in figure 3.16 and it shows the repeatability of the high-NA XUV WFS. The wavefront calibration measurements gives a repeatability of  $\frac{1}{30} \lambda/6$  RMS to  $\frac{1}{40} \lambda/6$  RMS for the high-NA XUV WFS.

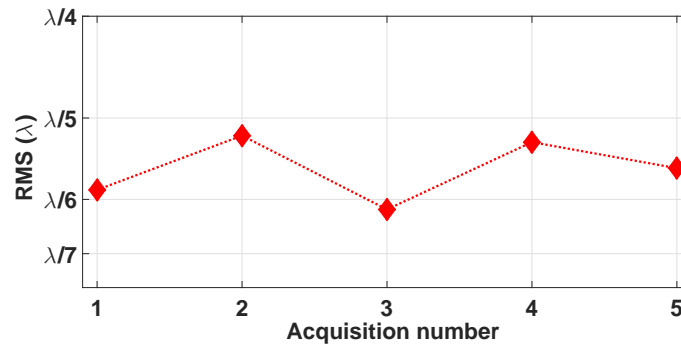


Figure 3.16: The RMS wavefront of the different calibration images acquired for the high-NA XUV WFS calibration.

Although the wavefront accuracy of the calibrated high-NA XUV WFS was low, it was enough to be used in applications such as measuring the wavefront of high-NA XUV optics such as the toroidal mirror used for focusing the XUV pulses onto the pinholes in the calibration setup, multilayer mirrors and highly diverging XUV sources such as HHG in solids.

### 3.3 Experimental results on wavefront characterization of XUV optics

The achieved wavefront accuracy for the high-NA XUV WFS is not the ultimate high accuracy that can be achieved using the iterative procedure for calibration. However, the current wavefront accuracy is sufficient for characterizing the wavefront of XUV multilayer mirrors and high-NA XUV optics such as the toroidal mirror used for focusing the XUV pulses onto the pinholes in the calibration setup. The spatial characterization of XUV optics using the high-NA XUV WFS was performed at Salle, Corail, LOA. Experimental results on characterization of the wavefront errors introduced by three multilayer mirrors are presented. Additionally, the characterization of the wavefront of an XUV beam after a toroidal mirror focus and preliminary optimization of the toroidal mirror focus are presented.

#### 3.3.1 Multilayer mirror calibration

Multilayer mirrors (discussed in section 3.1.1) are important for using in applications in which the wavelength specificity is needed. For XUV beams, multilayer mirrors are used to focus or reflect the selected spectral region of the XUV pulse spectrum for applications in imaging and probing. In these applications, it is important to know the kind of wavefront aberrations these multilayer mirrors introduce

in the beam wavefront after reflection since this can affect the spatial quality of the XUV beam. The multilayer mirrors are calibrated using the high-NA XUV WFS(3.2.2.2). The use of high-NA XUV WFS was preferred because of its in-vacuum maneuverability and the multilayer mirrors are used at an angle of  $15^\circ$  to the incident beam. Further, the use of the high-NA XUV WFS will be useful in characterizing a larger part of the mirror because of its higher aperture.

Three multilayer mirrors with central wavelengths at 53 eV (23.4 nm), 37 eV (33.5 nm) and 28 eV (44.3 nm) with a narrow bandwidth of 2 eV and with a manufacturer specified reflectivity of 20%, 15% and 11% at  $15^\circ$  to normal incidence were purchased from UltraFast Innovations GmbH, Germany and characterized in wavefront. The mirrors are 2 inch in size on a fused silica substrate with multilayer of coatings and the materials of the coating is a trade secret of the company, UltraFast Innovations GmbH.

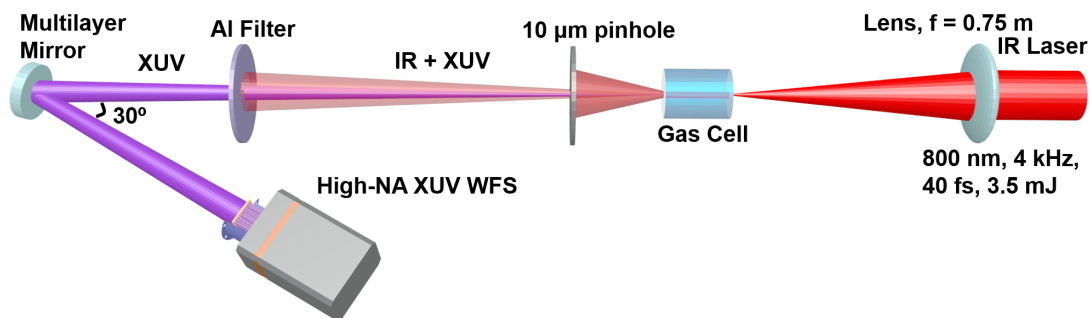


Figure 3.17: Schematics of multilayer mirror calibration

The experiment was carried out at the HH beamline, Salle Corail, LOA (2.2.2.2). Figure 3.17 shows the schematic of the experimental setup for multilayer mirror calibration with the high-NA XUV WFS. In the experimental setup, the first part is the XUV source and its spatial filtering. The XUV source used was HHG from argon. The high-intensity laser (2.2.2.2) was focused on to a 20 mm long gas cell filled with argon gas at 30 mbar using a plano-convex lens of focal length, 750 mm. A  $10\ \mu\text{m}$  ceramic pinhole was placed on a 3-axis stage at 15 cm from the pinhole to spatially filter the HH beam. The pinhole also reduces the transmission of the residual IR laser. After the pinhole two aluminum filters of thicknesses 150 nm and 300 nm were used to filter out the residual IR laser. The spatially filtered XUV beam is then reflected from the multilayer mirror to measure its wavefront.

The transmission through the pinhole was optimized using the 3-axis stage. The XUV beam diffracted at the pinhole was recorded using an X-ray PI-MTE 2048 B in-vacuum CCD at a distance of 150 cm from the pinhole and it is shown in figure 3.18. The beam was elliptical with a FWHM of 5.3 mm and 5.9 mm along the horizontal and vertical direction of the beam at CCD.

The multilayer mirror was placed at a distance of 231.5 cm from the pinhole position with an angle of  $15^\circ$  to the incident XUV beam. The high NA XUV WFS was placed at a distance of 32.5 cm from the multilayer mirror to capture the XUV beam reflected from the multilayer mirror with a deviation of  $30^\circ$  to incident XUV beam. Figure 3.19 shows a picture of the experimental setup for multilayer mirror calibration. From the measured size of the spatially filtered beam, the beam size at the multilayer mirror was estimated to have a minimum FWHM of  $\sim 12$  mm in the smaller diameter. Thus, we can characterize completely an area at the center of the multilayer mirrors with a diameter of 12 mm in the wavefront.

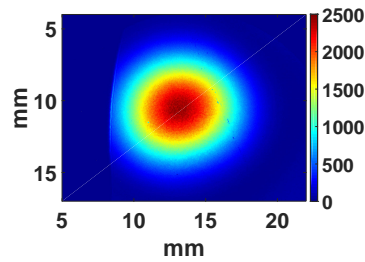


Figure 3.18: Spatially filtered XUV beam from a 10  $\mu\text{m}$  pinhole. The cut in the intensity pattern at the left side of the figure is due to the clipping of XUV beam by an aluminum filter holder placed before the X-ray CCD.

Before measuring the wavefront, the WFS was aligned perpendicular to the XUV beam by looking at the black-hole as described in the previous section (3.2.1.2).

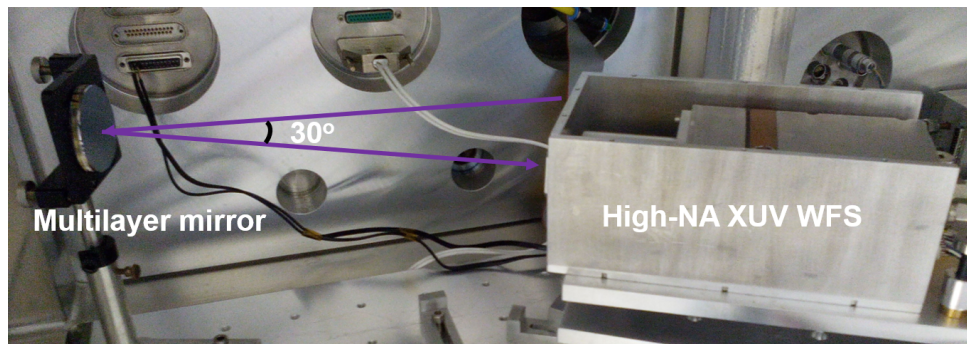
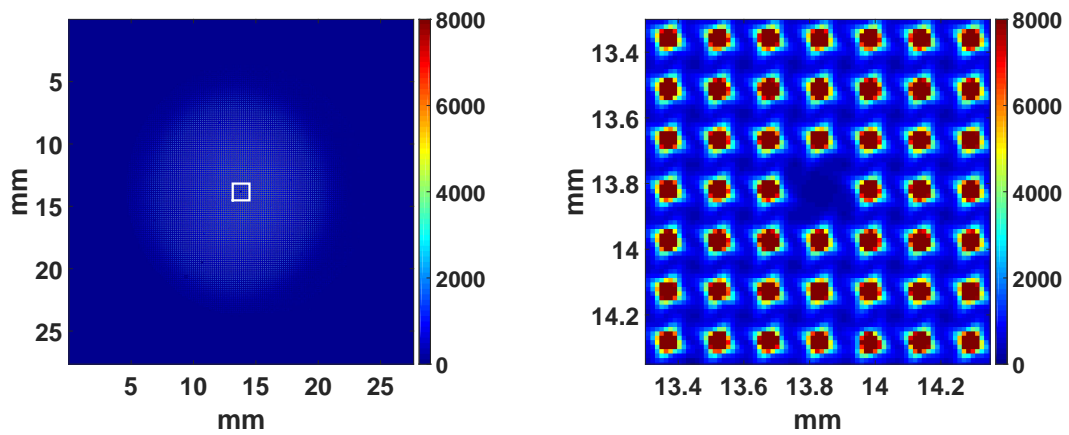


Figure 3.19: Experimental setup for multilayer mirror calibration

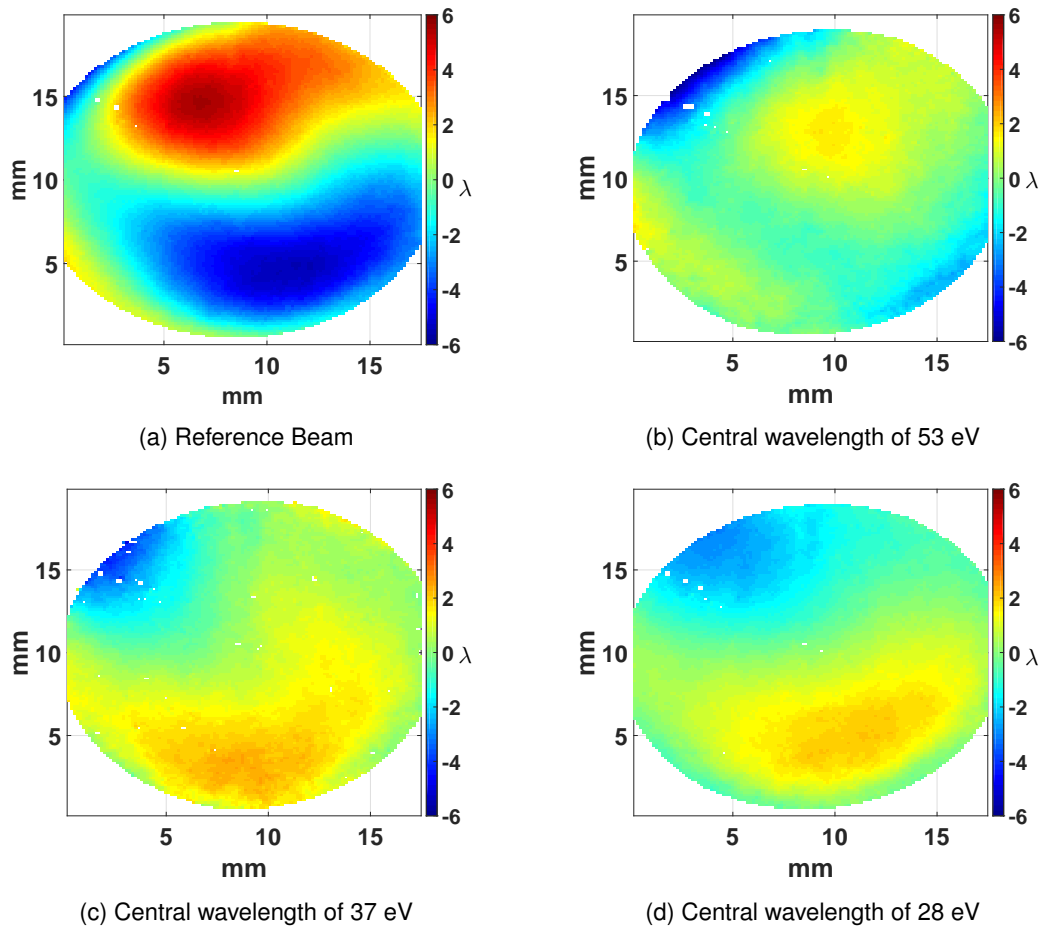
The wavefront from the multilayer mirrors reflecting at three different central wavelengths were measured using the high-NA XUV WFS. For calibration of the wavefront errors introduced by the multilayer mirrors, a reference wavefront was recorded without the multilayer mirror by placing the high-NA XUV WFS directly in front of the spatially filtered XUV beam at a distance of 218 cm from the pinhole. The figure 3.20a shows the raw wavefront sensor image with a white square showing the center part with the black-hole. Figure 3.20b shows the zoom of the part marked in figure 3.20a and here we can clearly see the position of the black-hole and also the diffraction pattern from the Hartmann plate.

The wavefront aberrations were obtained after analysis in HASO for the direct and reflected wavefronts from the three multilayer mirrors. For each multilayer mirror, the wavefront errors were estimated at their particular wavelength and for the reference wavefront the wavelength of 32 nm is used. For obtaining the wavefront error introduced by each multilayer mirror, the reconstructed intensity of the beams was fitted to a Gaussian and then the beam size was limited to  $3\sigma$  ( $\sigma$  is the standard deviation of the Gaussian fit). The centroid the reconstructed intensity map was estimated from the Gaussian fit and these centroids were used as the center point for the reconstructed wavefronts. The absolute wavefront errors of each multilayer mirror are obtained by subtracting the wavefront errors of the reference wavefront from the measured multilayer wavefront. The reference wavefront and absolute multilayer mirror wavefronts are shown in figure 3.21. Since the spatially filtered beam was elliptical, the pattern on the WFS also has an elliptical beam distribution. The major wavefront aberration coefficients for the reference



(a) False color map of the raw image from the WFS (b) Zoomed central part shown in white square in (a).

Figure 3.20: Raw image of spatially filtered XUV signal recorded on the high-NA XUV Hartmann WFS.



(a) Reference Beam

(b) Central wavelength of 53 eV

(c) Central wavelength of 37 eV

(d) Central wavelength of 28 eV

Figure 3.21: Reconstructed wavefront of (a) reference beam and (b,c,d) calibrated wavefronts of multilayer mirrors (with different central wavelengths).

wavefront and the multilayer mirrors are listed in table 3.1. The wavefront errors are estimated in  $\lambda$

Multilayer mirror	RMS	PV	Astg. 0°	Astg. 45°	Coma 0°	Coma 90°	Spheri- cal
@ wavelength	( $\lambda$ )						
Reference @ 32 nm	0.652	4.409	0.002	0.073	0.239	0.003	0.015
MLM - 53 eV @ 24.4 nm	1.015	6.321	0.105	0.013	0.435	0.002	0.005
MLM - 37 eV @ 33.5 nm	0.404	2.1	0.184	-0.008	0.046	-0.002	-0.012
MLM - 28 eV @ 44.3 nm	0.423	2.758	0.041	0.017	0.183	0.003	-0.015

Table 3.1: The value of major aberrations for the reference wavefront and multilayer mirror (MLM - eV) with different central wavelengths.

considering the central wavelengths for different multilayer mirrors. The wavefront errors introduced by the multilayer mirrors alone can be obtained by comparing them to the reference wavefront. On comparison with the reference wavefront, we can see that the wavefront errors introduced by the multilayer mirrors are close to or less than the XUV wavelengths which the mirrors reflect.

Three multilayer mirrors reflecting at different central wavelengths were calibrated in wavefront aberrations introduced on reflection. These mirrors can be now used to reflect XUV sources for applications. These multilayer mirrors will be used to reflect a single harmonic order from the HHs generated from solids to characterize the wavefront of the individual harmonic orders.

### 3.3.2 Toroidal mirror wavefront optimization using high-NA XUV WFS

The wavefront of the toroidal mirror used to focus the XUV pulses was measured. The XUV pulse after the focus of the toroidal mirror is highly diverging and hence the high-NA XUV WFS was used to measure the wavefront and optimize the focus.

A toroidal mirror is combination of two curved focusing surfaces, one in a plane parallel to the beam (sagittal plane) and one in a plane perpendicular to the beam (tangential plane) with two different radii of curvature. The mirror equation in the tangential plane is given by

$$\frac{1}{u} + \frac{1}{v} = \frac{2}{R \sin(\alpha)} = \frac{1}{f_{tan}} \quad (3.10)$$

and in sagittal plane it is given by,

$$\frac{1}{u} + \frac{1}{v} = \frac{2 \sin(\alpha)}{r} = \frac{1}{f_{sag}} \quad (3.11)$$

where  $u$  is the distance of object from the mirror,  $v$  is the distance of image from the mirror,  $\alpha$  is the grazing incidence angle,  $R$  and  $r$  are the tangential and sagittal radius of curvatures of the toroidal mirror respectively.  $f_{tan}$  and  $f_{sag}$  are the tangential and sagittal focuses. Toroidal mirror in grazing incidence is often used to focus XUV beams [116, 52], but the focal spot of toroidal mirror is associated with aberrations [116, 52]. Thus, to get a better spatial quality at the focus, it is necessary to optimize the focal

spot. We performed a preliminary optimization of the focal spot of a toroidal mirror using the high-NA XUV WFS.

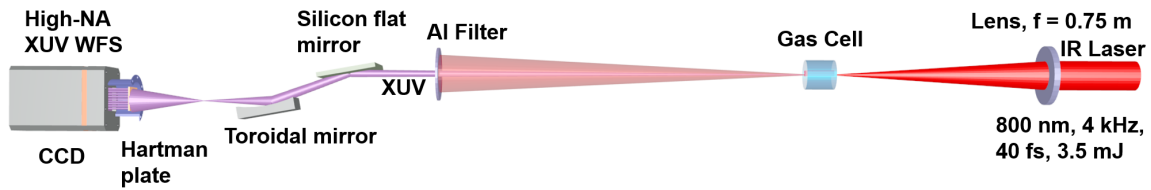


Figure 3.22: Schematic of the experimental setup for optimization of toroidal mirror focus using high-NA XUV WFS.

For calibration of high-NA XUV WFS, a toroidal mirror was used to focus the XUV beam onto the pinholes (section 3.2.2.2). The gold coated toroidal mirror had a tangential radius of curvature,  $R = 1500$  mm and its dimensions are  $100$  mm  $\times$   $30$  mm. It was used at a grazing angle of  $10^\circ$  with the incident beam. The theoretical focal length can be estimated using the equation 3.10 and it is  $13$  mm. The calibrated high-NA XUV WFS is used to measure the WFS from the toroidal mirror without the pinhole and further to optimize its focus. Figure 3.22 shows the schematics of the experimental setup for toroidal mirror focus optimization. The experimental setup consists of XUV source which is HHG from argon, aluminum filters of thicknesses  $150$  nm,  $300$  nm used to filter out residual IR laser beam and then the XUV beam is steered into the toroidal mirror using a silicon flat mirror which is placed at  $10^\circ$  incidence. The toroidal mirror was placed on 5-axis stage at a grazing incidence of  $10^\circ$ . The toroidal mirror was placed at a distance of  $201.8$  cm from the gas cell. Using the equation 3.10, the effective focal length can be estimated as  $13.92$  mm. In the experiment, the WFS was placed after the focal spot to measure the wavefront of the toroidal mirror.

The first step of the experiment was to pre-align the toroidal mirror using a He-Ne laser and a visible CCD (Thorlabs CCD - DCC1645C). The visible CCD was placed at the estimated focal position in a 3-axis stage. The toroidal mirror was moved in different axis with respect to the incident beam to finally optimize the focal spot. The optimization was done by increasing the intensity at the central spot as shown in figure 3.23 and reduce the intensity along the scattered spots. The visible CCD was moved

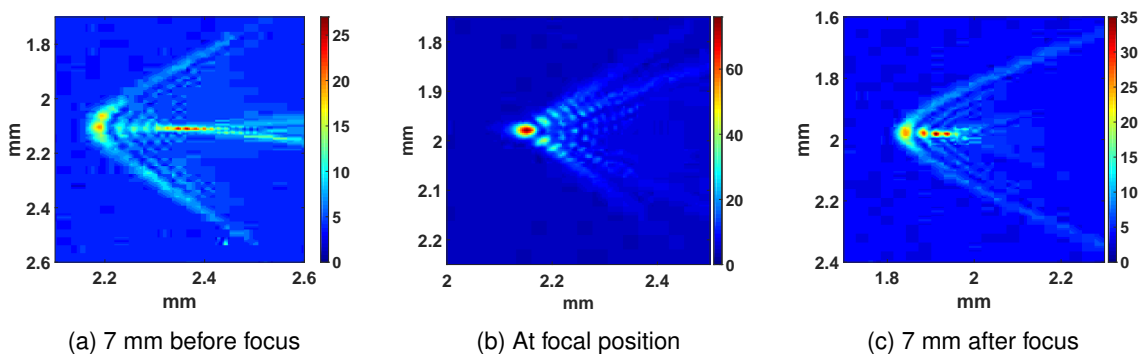


Figure 3.23: Image of focal spot at different distances from the focus of a toroidal mirror illuminated by a He-Ne laser and recorded using a visible CCD. In (b) the high intense spot size is  $25$   $\mu$ m  $\times$   $32$   $\mu$ m.

along the focus to find the best focus position. Figure 3.23 shows the images acquired by the CCD

at different distances along the direction of the focus and also at the best focal position. Figure 3.23a shows the image 7 mm before the focal spot and figure 3.23c shows the image the 7 mm after the focal spot. Figure 3.23b shows the image at the focal spot and the focal spot pattern recorded is similar to the one obtained for ray tracing calculations of the toroidal mirror at grazing incidence in literature [116]. The central bright spot at the focal spot was elliptical and its FWHM along horizontal and vertical was estimated at  $32\ \mu\text{m} \times 25\ \mu\text{m}$ .

For optimization of the toroidal mirror focus in the XUV, the WFS was kept at a distance of 17 cm from the toroidal mirror focus position. The WFS was placed away from the toroidal mirror focus to have bigger beam size to have a higher sampling of the beam for the WFS. Figure 3.24 shows a picture of the experimental setup for optimization of the toroidal mirror. The WFS was placed in a multi-axis stage as explained in the high-NA XUV WFS calibration (3.2.2.2). The WFS was aligned perpendicular to the

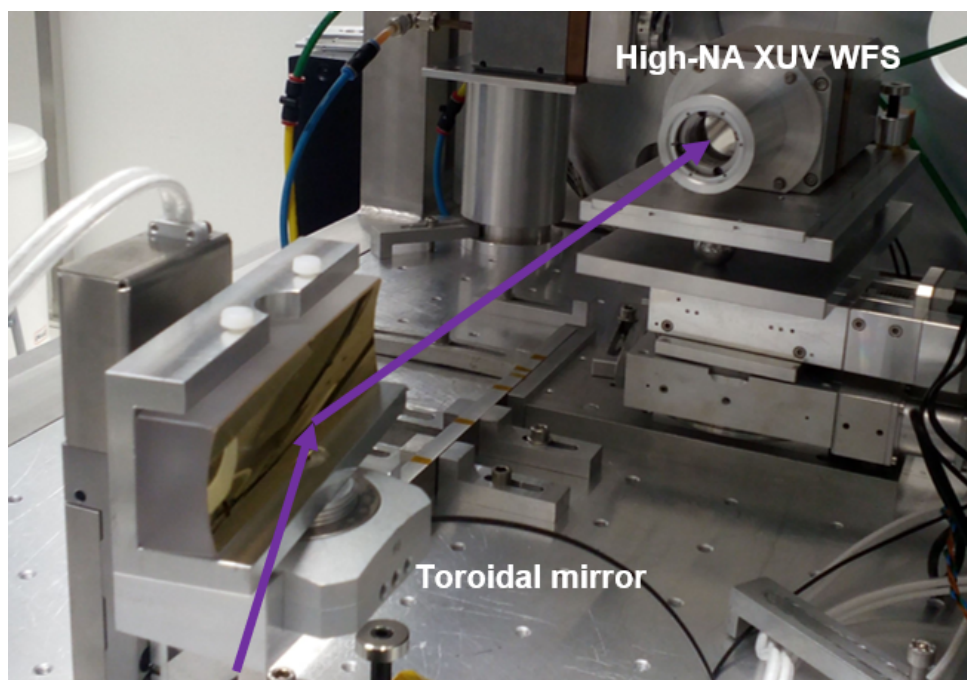
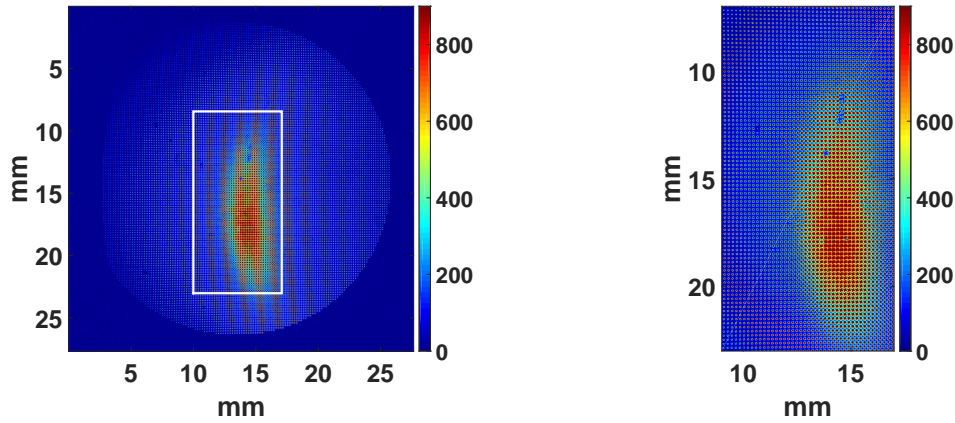


Figure 3.24: Experimental setup for optimization of toroidal mirror focus showing the orientation of the toroidal mirror with respect to the WFS. The violet line shows the direction of XUV beam.

incident beam.

The wavefront of the XUV beam from the toroidal mirror was recorded and the wavefront errors are optimized by adjusting the toroidal mirror position with respect to the incident beam. This was done by moving the toroidal mirror in the 5-axis stage on which it was placed. The figure 3.25a shows the raw WFS image with a white rectangle showing the beam from the toroidal mirror. Figure 3.25b shows the zoom of the part highlighted in figure 3.25a.

For measuring the wavefront the beam dimension was limited to  $1/e^2$  of the maximum intensity. Figures 3.26a and 3.26b shows the reconstructed intensity and wavefront respectively of the XUV beam from toroidal mirror before optimization. The wavefront error measured before optimization was  $34.72\ \lambda$  RMS and  $181.96\ \lambda$  peak to valley (PV) considering a central wavelength of  $\lambda = 32\ \text{nm}$  for harmonics. The major aberration in the wavefront before optimization was astigmatism  $0^\circ$  along the horizontal plane of the



(a) False color map of the raw image from the WFS

(b) White rectangle highlighted in (a).

Figure 3.25: Raw image of XUV beam after the focus of the toroidal mirror recorded on the high-NA XUV Hartmann WFS.

toroidal mirror as expected. For optimization, the value of astigmatism  $0^\circ$  and the RMS wavefront error were reduced. The optimization resulted in reduction of the wavefront error to  $25.49 \lambda$  RMS and  $152.46 \lambda$  PV. The astigmatism  $0^\circ$  was reduced from  $17.37 \lambda$  to  $2.6 \lambda$ . But at the same time the astigmatism  $45^\circ$  and other wavefront errors increased although the RMS wavefront error decreased. The major aberration values from the toroidal mirror wavefront before and after optimization are listed in table 3.2. Figures 3.26c and 3.26d shows the reconstructed intensity and wavefront of the XUV beam respectively after optimization.

Wavefront aberrations	RMS ( $\lambda$ )	PV ( $\lambda$ )	Astg. $0^\circ$ ( $\lambda$ )	Astg. $45^\circ$ ( $\lambda$ )	Coma $0^\circ$ ( $\lambda$ )	Coma $90^\circ$ ( $\lambda$ )	Spheri- cal ( $\lambda$ )
Before optimization	34.92	183.78	23.17	-0.44	-0.14	3.73	-1.62
After optimization	25.49	152.54	3.95	15.68	-0.52	-1.13	-0.75

Table 3.2: The value of major aberrations for the wavefront from toroidal mirror measured at 17 cm from the focus.

From the maximum size of the beam and the distance between focal spot position and the WFS, the NA of the toroidal mirror, in this case, was estimated to be in the order of 0.04. So it would have been difficult to optimize the toroidal mirror focus using currently available XUV WFS since their NA is in the order of 0.01 [129, 128]. Geometrical back propagation in HASO software was used to check the focal spot dimension before and after optimization. Since the focal spot was astigmatic, the radius of the second moment of the intensity distribution was used to measure the focal spot dimension. Further, we restricted beam dimension to  $1 \sigma$  (where  $\sigma$  is the standard deviation of the horizontal or vertical intensity distribution) of the maximum intensity since we wanted to observe an increase in the peak intensity at the focal spot. The radius of the second moment of the intensity distribution was  $49.5 \mu\text{m}$  before optimization and it was reduced to  $41.4 \mu\text{m}$ . This corresponds to  $\sim 20\%$  reduction in focal spot and this corresponds to  $\sim 40\%$  increase in the peak intensity at the toroidal mirror focus considering only the central part of

the toroidal mirror focus.

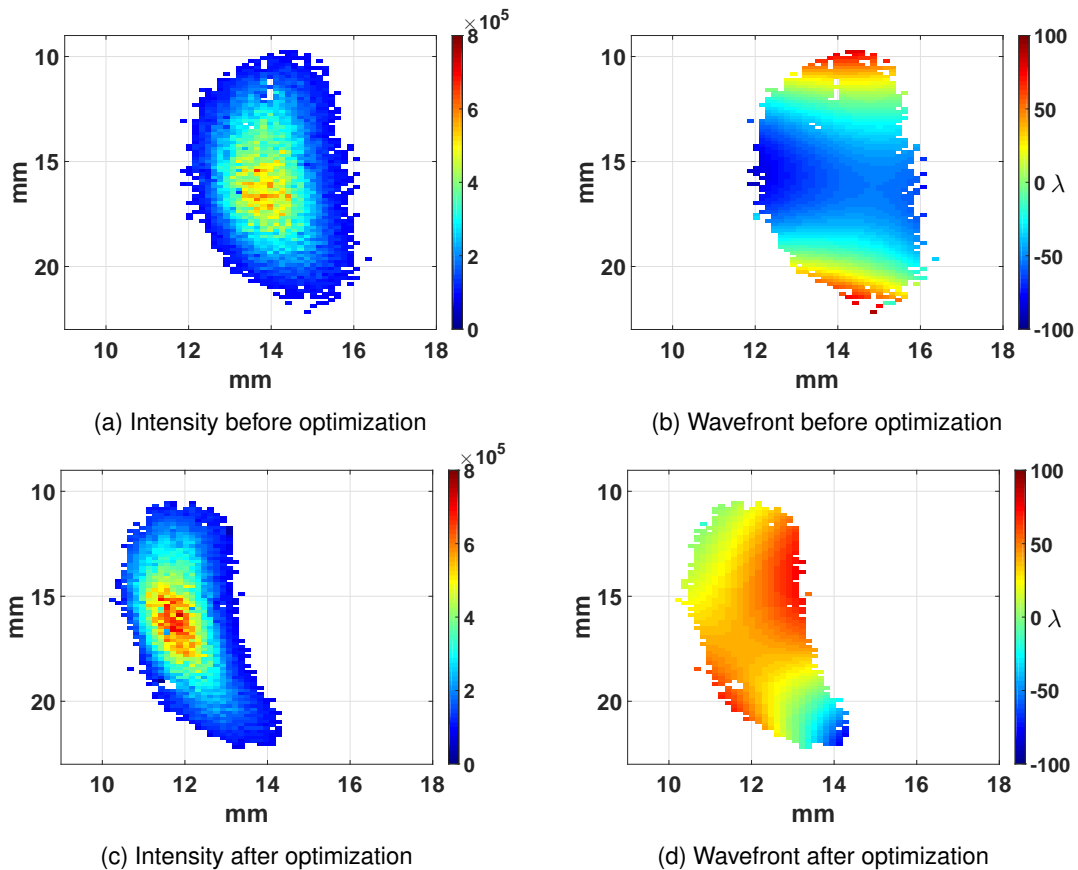


Figure 3.26: Reconstructed Intensity and wavefront from the toroidal mirror before (a, b) and after (c, d) optimization, measured at 17 cm from the toroidal mirror focus.

### 3.4 Experimental results on wavefront characterization of HHG

The wavefront characterization of XUV pulses from HHG in gases and solids was performed using the XUV Hartmann WFS. The motivation for this wavefront characterization is to optimize the XUV source wavefront. The results are presented in this section.

#### 3.4.1 Wavefront characterization of high harmonics from gases

The wavefront characterization of HH from gases was performed at different HHG conditions. The XUV pulse wavefront was measured for HHG using high repetition rate short pulse laser system at Salle Corail, LOA and also a long pulse, single shot laser system at L2I, IST. The two different measurements were carried out using two different wavefront sensors working on the Hartmann principle of wavefront sensing.

##### 3.4.1.1 Wavefront measurement performed at Salle Corail, LOA, France

The wavefront characterization of XUV pulses generated from HHG in argon was carried out at Salle Corail, LOA. From the typically used conditions for HHG at Salle Corail, it was observed that HHG in

argon generated brightest XUV photons and for applications, it was necessary to spatially characterize the XUV pulses from HHG in argon. The WFS used for this experiment is a low-NA Hartmann type wavefront sensor from Imagine Optic. The sensor consists of a Hartmann plate fixed at a distance of 211 mm from a detector. The detector used is a back-illuminated X-ray CCD, PIXIS-XO 1024B from Princeton instruments having  $1024 \times 1024$  pixels with a size of  $13 \mu\text{m} \times 13 \mu\text{m}$ . The Hartmann plate is made of nickel with a thickness of  $100 \mu\text{m}$  and has  $32 \times 32$  square holes with a hole size of  $110 \mu\text{m}^2$  and distance of  $387 \mu\text{m}$  between them. As in other XUV WFS from Imagine Optic, the holes in the Hartmann plate are rotated by  $25^\circ$  to avoid the interference between adjacent holes [126]. From the earlier calibration measurements carried out at LOA, the wavefront accuracy of this XUV WFS was estimated as  $\lambda/50$  RMS, considering a wavelength of 32 nm. The estimated maximum numerical aperture of this XUV WFS is in the order of 0.01. Figure 3.27a shows the XUV WFS and figure 3.27b shows the Hartmann plate inside the XUV WFS.

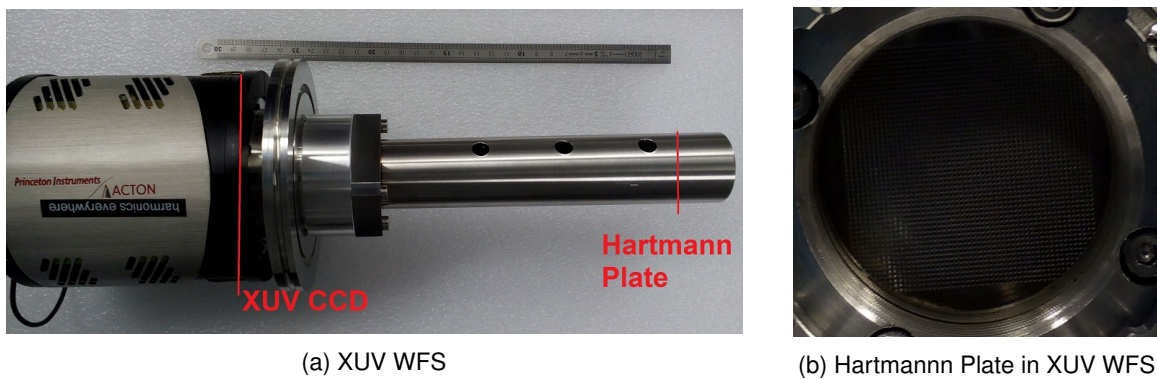


Figure 3.27: XUV Hartmann wavefront sensor.

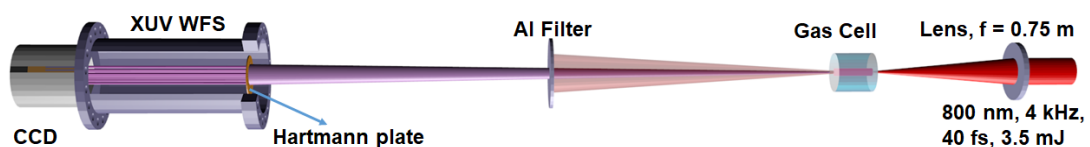


Figure 3.28: Schematic of experimental setup for wavefront characterization of high harmonics generated from gases.

The figure 3.28 shows the schematic of the experimental setup for wavefront characterization. The short pulse IR laser in Salle Corail, LOA (2.2.2.2) is focused onto a gas cell of length 15 mm with argon gas using a plano-convex lens of focal length 750 mm. Aluminum filters of thicknesses 150 nm, 300 nm and 150 nm were used to filter out the residual IR laser. The filtered XUV beam is recorded by the XUV WFS. The WFS used is the one which goes on a flange on a vacuum chamber. Figure 3.29 shows the XUV WFS attached to a flange at the end of the experimental chamber in the HH beamline at Salle Corail, LOA.

The wavefront of the direct harmonic beam was measured using the XUV WFS at different argon gas pressures. The figure 3.30a shows the raw wavefront sensor image with a white square showing the center part with black-hole. Figure 3.30b shows the zoom of the part marked in figure 3.20a.

For the analysis,  $\lambda = 32 \text{ nm}$  is considered as the harmonic central wavelength. The reconstructed

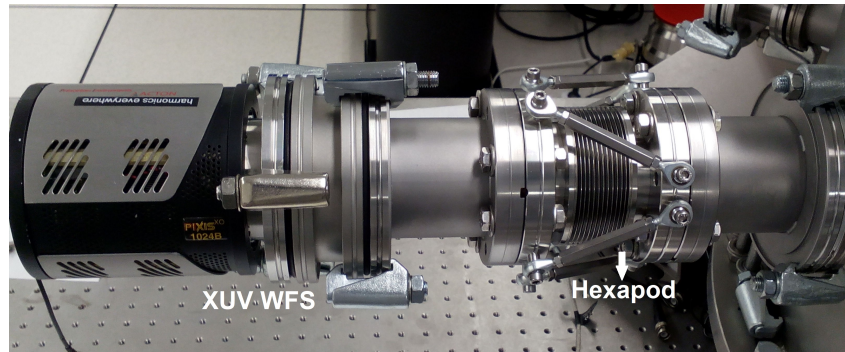
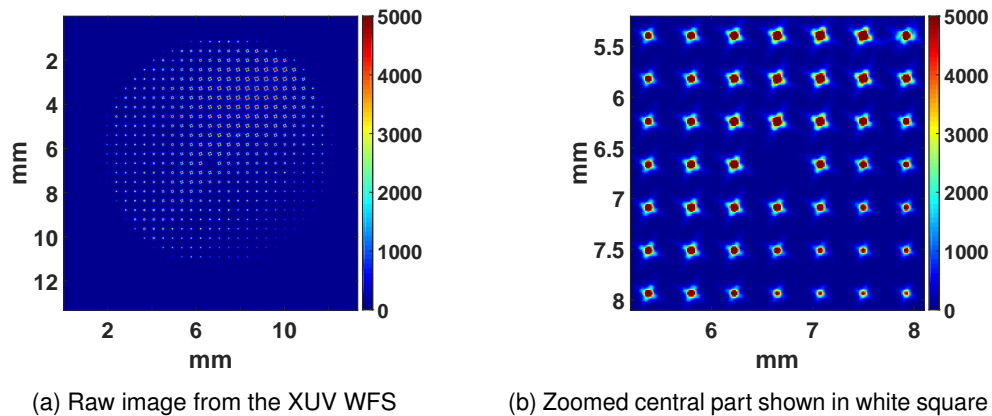


Figure 3.29: XUV WFS attached to the vacuum chamber for wavefront characterization of high harmonics generated from gases.



(a) Raw image from the XUV WFS

(b) Zoomed central part shown in white square in (a).

Figure 3.30: Raw image of spatially filtered XUV signal recorded on an XUV Hartmann WFS.

XUV beam wavefront from argon at different gas pressures is in figure 3.31 and the value of major aberrations estimated are listed in table 3.3.

Figure 3.31f shows the variation of RMS and PV wavefront errors at different pressures for HHG from argon for conditions at Salle Corail, LOA. From this plot we can see that the both RMS and PV wavefront errors are lower at 65 mbar in the measurements. Further the wavefront errors for HHG in argon at 65 mbar was analyzed and the major wavefront aberration coefficients and RMS and PV wavefront errors are plotted in figures 3.31g and 3.31h respectively. The wavefront of harmonics at pressures higher than 65 mbar was not measured because it was difficult to maintain the vacuum at higher gas pressures.

The wavefront analysis of HHG in argon using the short pulse laser system at LOA gives an RMS wavefront error less than  $\lambda/10$  considering a central wavelength of 32 nm for harmonics for all the gas pressures. RMS wavefront error optimized with a value  $< \lambda/16$  for HHG from argon at a pressure of 65 mbar. It was already shown that the harmonic output is optimized when the RMS wavefront error was minimized [50]. The XUV source with optimized RMS wavefront error and HH output can be used for applications such as imaging and XUV WFS calibration.

### 3.4.1.2 Wavefront measurement performed at L2I, IPFN, IST Lisbon, Portugal

The wavefront measurement of XUV beam generated by HHG in argon using the in-house built diode pumped long pulse laser was carried out at L2I, IST (explained in section 2.2.2.1). The wavefront

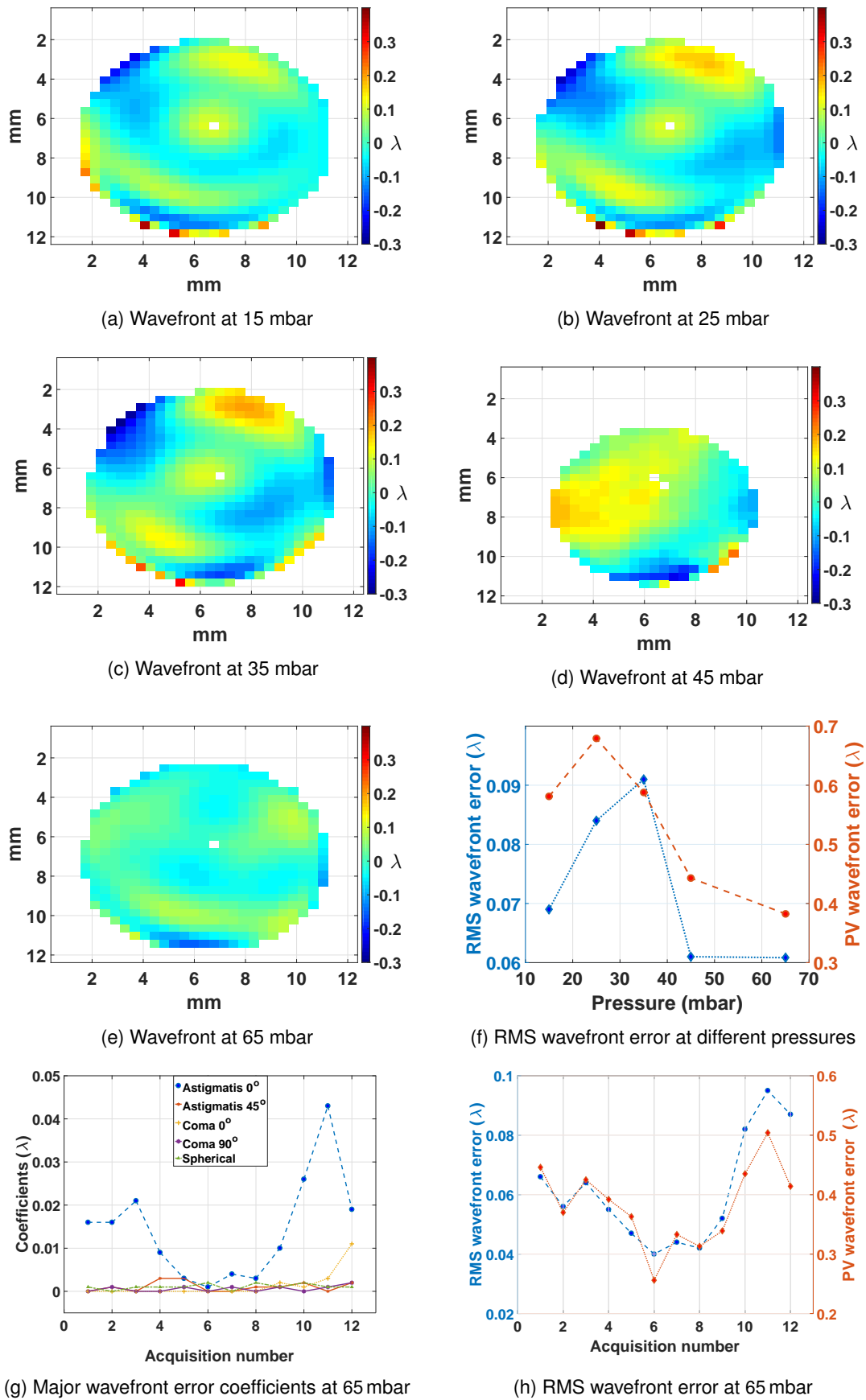


Figure 3.31: The measured wavefront of high harmonics at different gas pressures. (g) and (h) The optimized wavefront errors at 65 mbar.

Wavefront errors	RMS	PV	Astg. 0°	Astg. 45°	Coma 0°	Coma 90°	Spherical
mbar	$\lambda$						
15	0.069	0.581	0.001	0.007	0.001	0.001	0.001
25	0.084	0.679	0.005	0.015	0	0	0.001
35	0.091	0.588	0.004	0.016	0.002	0	0
45	0.061	0.443	0.003	0.006	0.002	0.003	0.001
65	0.061	0.383	0.014	0.001	0.001	0.001	0.001

Table 3.3: The value of major wavefront aberrations for high harmonic beam measured at different gas pressures

sensor used was the XUV Hartmann WFS jointly developed by Laser-Laboratorium Göttingen e.V. (LLG) and Deutsches elektronen-synchrotron (DESY) [127, 115]. Figure 3.32a shows the XUV Hartmann WFS from DESY fixed with the translation and tip / tilt stage. This XUV WFS works for a wavelength range of 4

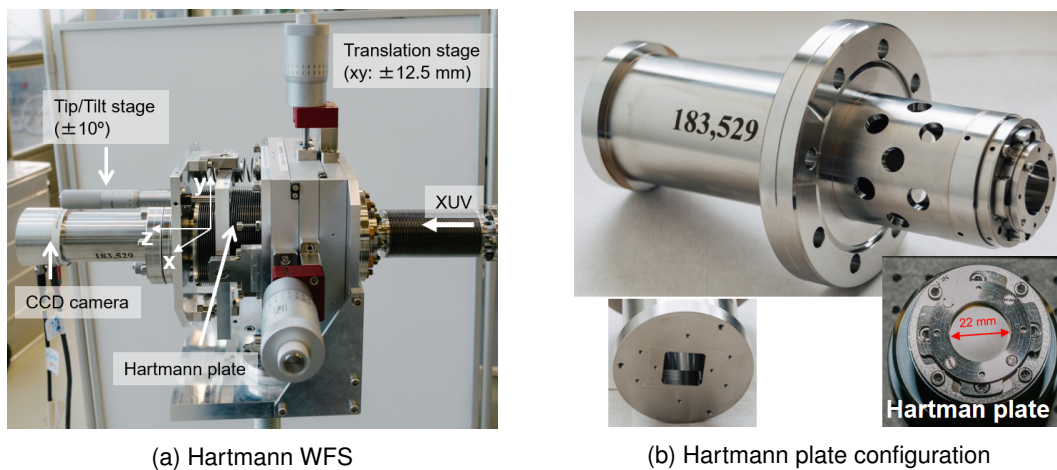


Figure 3.32: XUV Hartmann WFS from DESY, Germany

- 40 nm. The detector used in this WFS is a visible CCD, MR4021MU from XIMEA with a dynamic range of 14 bits. It has  $2048 \times 2048$  pixels with pixel size of  $7.4 \mu\text{m} \times 7.4 \mu\text{m}$  giving a field of view of  $15.2 \text{ mm} \times 15.2 \text{ mm}$ . The CCD was coated with an XUV to visible converter P43 ( $\text{Gd}_2\text{O}_2\text{S:Pr, Ce}$ ). The Hartmann plate is made of  $10 \mu\text{m}$  thick nickel foil with circular holes of diameter  $75 \mu\text{m}$  and a separation of  $250 \mu\text{m}$  between them with a total of  $59 \times 59$  holes in an area of diameter 22 mm. The Hartmann plate was fixed at distance of 199.953 mm from the CCD. The Hartmann plate and detector system were mounted with a translation stage which can move in X and Y within a range of  $\pm 12.5 \text{ mm}$  and also a tip/tilt stage which has a range of  $\pm 10^\circ$ . Figure 3.32b shows the Hartmann plate and holder on which it is attached. The holder has a length of 183.529 mm. From the earlier calibration measurements carried out at FLASH FEL - DESY, the RMS wavefront accuracy of this XUV WFS was estimated as 1.1 nm. This wavefront sensor is also estimated to have NA in the order of 0.01.

The schematic of the experimental setup for wavefront characterization is shown in figure 3.33. The IR laser is steered to the vacuum chamber using dielectric mirrors. A plano-convex lens fixed on a motorized stage inside the vacuum chamber is used to focus the laser onto a gas cell of length 10 mm

filled with argon gas at a pressure of 65 mbar. The residual IR after HHG was filtered out using an aluminum filter of thickness 300 nm without a mesh and it has a theoretical transmission of 49% [92]. The mesh-less filter was used to avoid diffraction, which disturbs the wavefront measurement. The XUV WFS was placed after the filters.

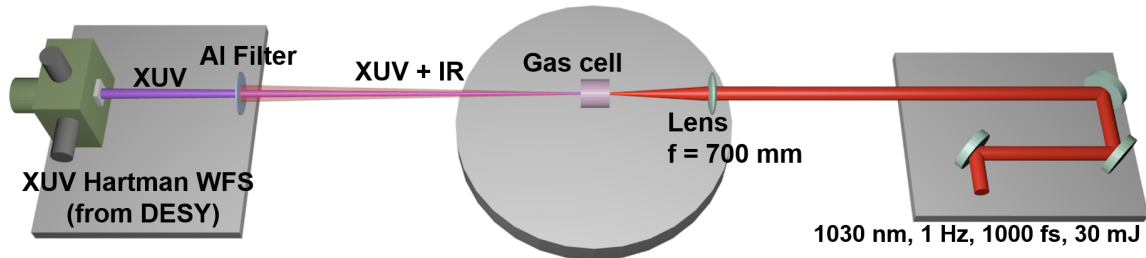


Figure 3.33: Schematic of the experimental setup for HH wavefront measurement at L2I

Figure 3.34 shows a picture of XUV WFS from DESY attached to the HH beamline after the aluminum filter.

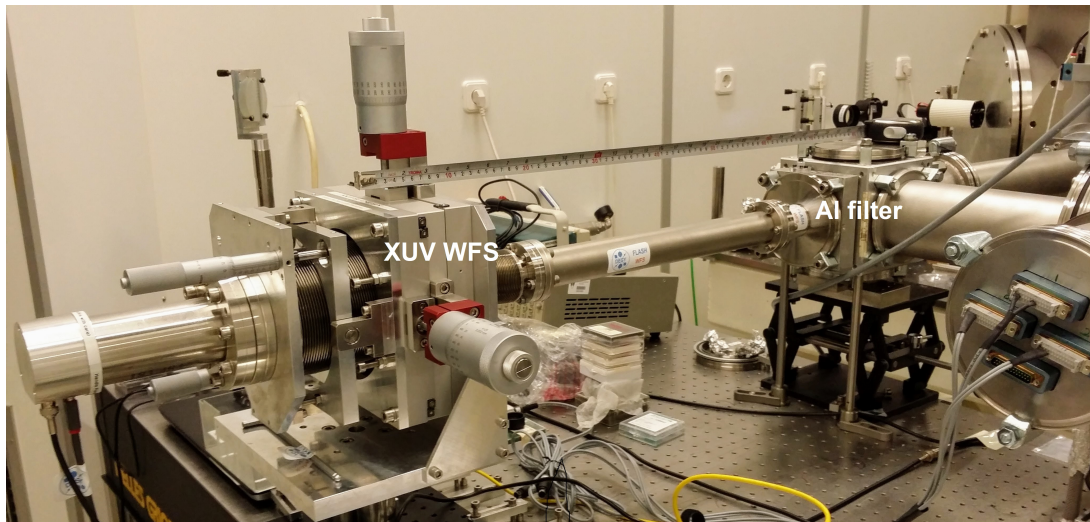


Figure 3.34: Experimental setup showing the XUV WFS attached to the HHG beamline at L2I.

For wavefront measurement, the WFS was aligned perpendicular to the beam by aligning the black-hole to the center of the CCD. Wavefront measurements were carried out for HHG in argon with the same optimized generation conditions as listed in table 2.1, except the pressure was increased to 65 mbar. This was done to reduce the ellipticity of the beam while still maintaining the photon counts. The wavefront data was acquired by integrating the HH signal for 20 seconds. In a previous study it was shown that the integration of wavefronts of multiple shots will not change the RMS wavefront error [50].

The wavefronts recorded were analyzed using the software MrBeam [129]. The full width half maximum (FWHM) of the HH beam diameter is about  $2\text{ mm} \times 3\text{ mm}$  at the CCD of the WFS. In total 13 consecutive HH wavefronts were recorded in the same conditions for HHG and compared to estimate the stability of the wavefront. Prior to wavefront reconstruction a dark image was subtracted and hot pixels were removed for each measurement. Hot pixels arose due to the long exposure time,  $\sim 40\text{ s}$ . For the reconstruction a rectangle of  $32 \times 23$  apertures was selected and centered on recorded HH intensity,

which covers full aperture of the beam. In figure 3.35 an example for a recorded wavefront is shown. For each measurement the RMS wavefront error, astigmatism and coma were calculated. Additionally, the mean values and their standard deviation were calculated. Figure 3.36 shows the evolution of the RMS wavefront error, astigmatism and coma for the different acquisitions and in table 3.4 the mean values are summarized. These results were published in early 2017 [137].

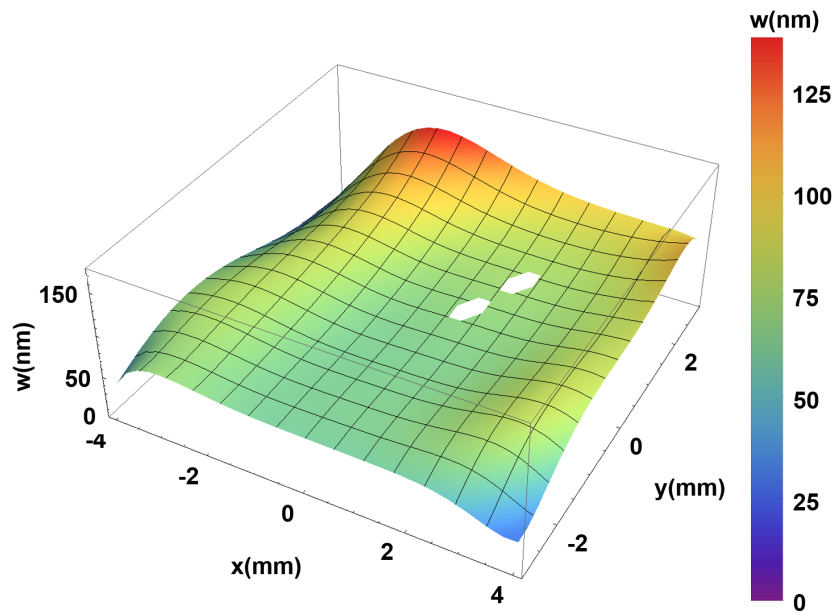


Figure 3.35: An example of a reconstructed high harmonic wavefront (acquisition 1) measured with the Hartmann type XUV wavefront sensor.

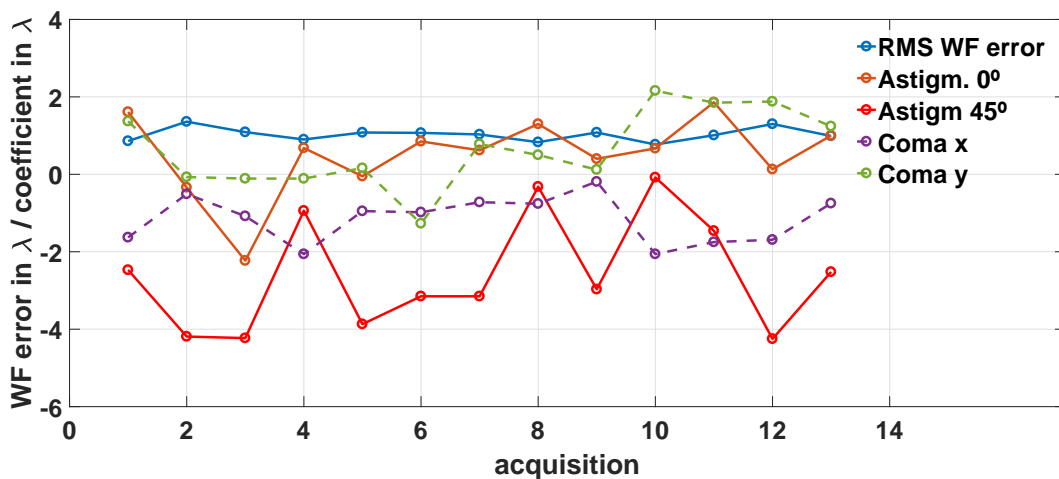


Figure 3.36: The evolution of the RMS wavefront error and the Zernike coefficients of the main aberrations.

### 3.4.2 Wavefront characterization of high harmonics from solids

The HHG in solids generally gives higher XUV photon count as compared to HHG in gases. Hence, it is important to characterize HHs from solids in wavefront to use it in applications. Further, knowing

Parameter	RMS	Astg. 0°	Astg. 45°	Coma 0°	Coma 90°	RMS Slope
Units	$\lambda$	$\lambda$	$\lambda$	$\lambda$	$\lambda$	mrad
Mean	1.06	0.5	0.164	-2.58	-1.16	0.6
Standard Deviation	0.17	1.03	1.47	0.608	1.122	0.01

Table 3.4: Mean values for the RMS wavefront error and the Zernike coefficients over 13 acquisitions.

the aberrations of the HH wavefront gives an idea on how well it can be focused to a small spot which has application in lithography. Also, from the measured wavefront the XUV source, i.e the plasma state can be studied by back-propagating to the source. The HHs from solids are more divergent compared to HHs from gases [75] and also the emission of harmonics in the specular direction makes it difficult to use a low-NA XUV WFS for the wavefront characterization. Although the wavefront of solid HHs has been measured before using ptychography [138], it was never measured in a single shot. This prevents using HHs from solids as a probe for ultrafast phenomena in the XUV. Here the calibrated high-NA XUV WFS was used for measuring the wavefront of HHs from solids. The HHs were measured after a wavefront characterized multilayer mirror to select certain wavelengths among the HHs and also to reduce the residual IR laser and debris produced during HHG from solids.

The wavefront characterization of HH from solids was carried out at JETI200, Helmholtz Institute, Jena, Germany for the first time. The JETI200 laser facility and HHG from solids are discussed in sections 2.3.2.1 and 2.3.2.2. The HH wavefront was measured under the two different mechanisms of HHG from solids, CWE and ROM at conditions similar to the ones described in section 2.3.2.2 except the laser energy used was only 460 mJ. The conditions for solid HHG under CWE and ROM mechanism was tested with lower energies before measuring the wavefront.

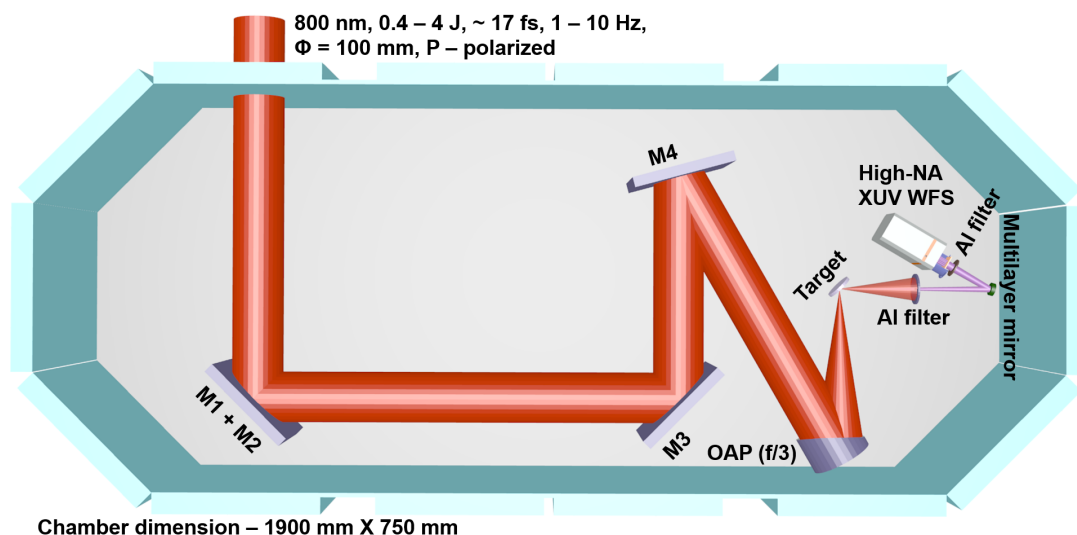


Figure 3.37: Schematic of the experimental setup for wavefront characterization at Helmholtz Institute, Jena, Germany

The experimental setup for wavefront measurement for HH from solids at JETI200 is shown in figure 3.37. The experimental setup until HHG is similar as explained in section 2.3.2.2. After the target,

along with the specular direction, the filter wheel is replaced by an aluminum filter of thickness 340 nm. A multilayer mirror was placed downstream to the filter and it reflects the only certain spectral range in the HH generated. The multilayer mirror was placed at a distance of 350 mm from the target at an angle of  $15^\circ$  with respect to the incident radiation. The XUV beam reflected off the multilayer mirror is detected using the high-NA XUV in-vacuum WFS placed at a distance of 17 cm from the multilayer mirror. A second aluminum filter thickness 150 nm was also placed before the high-NA XUV WFS to further filter out the residual IR and other lower order harmonics.

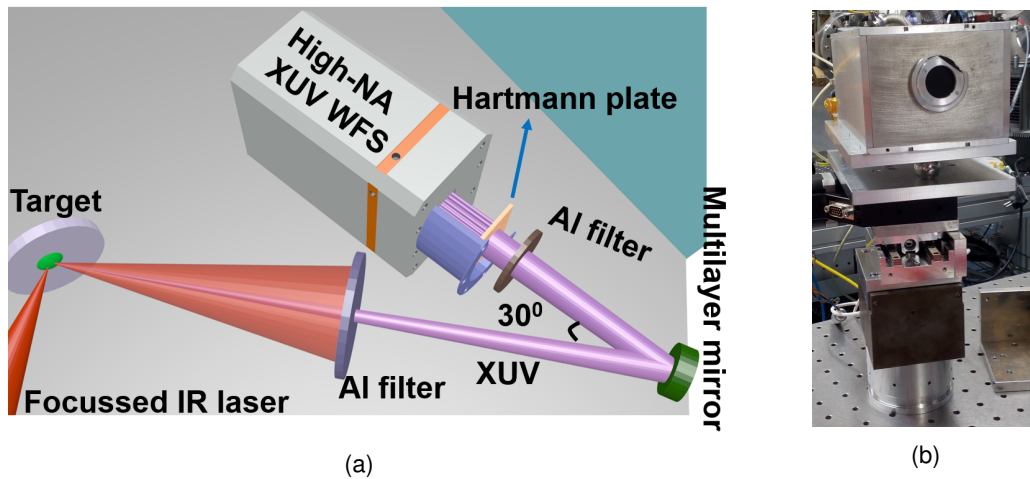


Figure 3.38: Schematic of the experimental setup of high-NA XUV WFS inside the target chamber for measuring the wavefront of HH from solids (a) and a picture of the high-NA XUV WFS inside a protective aluminum box on a multi-axis stage (b).

Figure 3.38a shows the zoomed part of the high-NA XUV WFS setup inside the target chamber. Figure 3.38b shows the high-NA XUV WFS in a multi-axis stage which can translate horizontally and vertically, rotate and also can adjust the tilt of the WFS with respect to the incident beam. The XUV WFS is also covered in an aluminum box to further protect it from the scattered residual IR and other higher order harmonics.

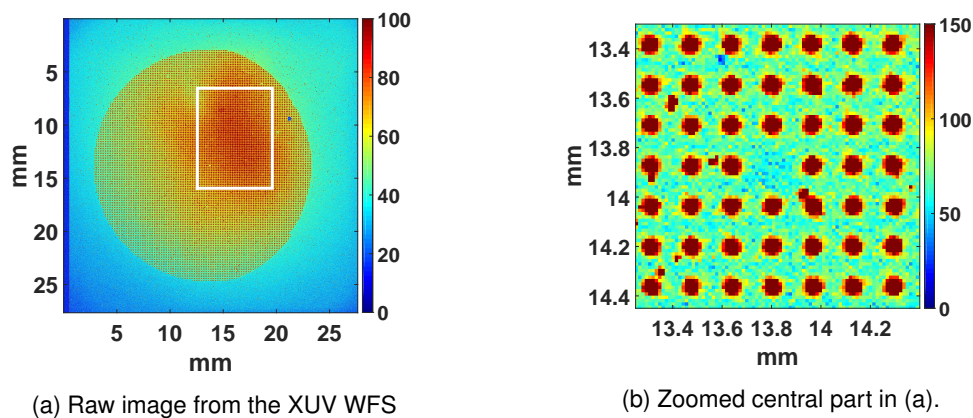


Figure 3.39: Raw image of spatially filtered XUV signal recorded on an XUV Hartmann WFS.

The wavefront was measured for HHG from solids under CWE and ROM mechanisms. Figure 3.39a shows the raw image recorded by the high-NA XUV WFS for solid HHG by CWE mechanism. The

high intense part of the beam is highlighted in a white box. Figure 3.39b shows the zoomed central part. From the raw images, it is clear that the background in these measurements is high (signal to noise  $\sim 2$ ) and the beam is not in the center but on the upper right quadrant of the WFS. The high background noise arises mainly from the scattering of the incident laser pulses at the target and also from the scattering of lower harmonic orders generated.

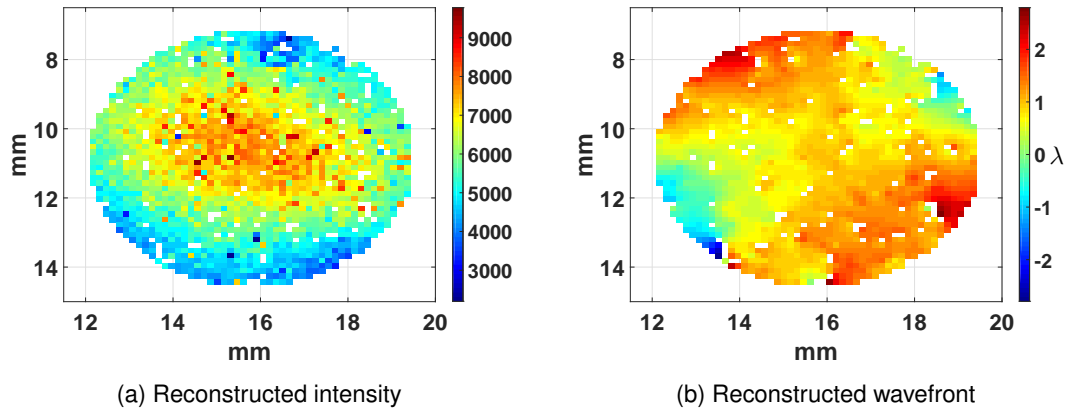


Figure 3.40: Reconstructed intensity and the wavefront of HHG in solids under the CWE mechanism.

The wavefront measurement for CWE mechanism was carried out with a multilayer mirror which reflects at a central wavelength of 28 eV (44.3 nm). For the analysis, the wavefront errors are calculated in the units of wavelength ( $\lambda$ ) considering the central wavelength of the multilayer mirror used in the experiment as the wavelength reflected. Figures 3.40a and 3.40b shows the reconstructed intensity and wavefront for solid HHG under CWE mechanism. The major wavefront aberrations measured are listed in table 3.5.

The solid HHs generated under the ROM mechanism was also measured with a multilayer mirror which reflects at a central wavelength of 37 eV (33.5 nm). Figures 3.41a and 3.41b shows the reconstructed intensity and wavefront of this measurement. The major wavefront aberration measured for solid HHG by ROM mechanism are listed in table 3.5.

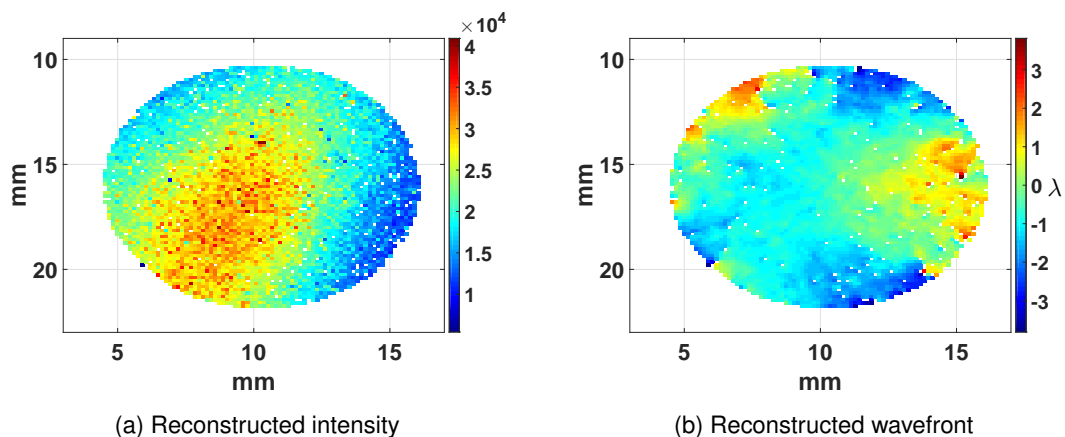


Figure 3.41: Reconstructed intensity and wavefront of HHG in solids under the ROM mechanism.

Since the signal to noise ratio in the measurement is low ( $\sim 2$ ), the analysis was done by

HHG Mechanism	Multilayer mirror central wavelength	RMS $\lambda$	PV $\lambda$	Astg. 0° $\lambda$	Astg. 45° $\lambda$
CWE	28 eV (44.4 nm)	0.581	5.583	0.024	0.159
ROM	37 eV (33.5 nm)	0.89	6.589	0.07	0.031

Table 3.5: The value of major wavefront aberrations for solid HHG under different mechanisms.

considering a circle around the intense part of the beam recorded on the WFS. Although the analysis was done with a circular aperture, the fitting with Zernike polynomial in modal reconstruction was not working properly, meaning the RMS wavefront error in modal and zonal reconstruction was not the same. This might be due to the low signal to noise ratio. The major wavefront aberration hence measured was using zonal reconstruction, which limits the measurement to only RMS, PV and astigmatism wavefront errors. Also, the wavefronts were not corrected for the wavefront errors introduced by the multilayer mirror used to reflect the XUV pulses generated. This is because it was observed in the wavefront sensor data that the beam pointing was changing in each shot and this means that the harmonics are not necessarily reflecting off the center of the multilayer mirror always. Since the calibration of the mirror was only around  $\sim 10$  mm area at the center of the multilayer mirror, it is not correct to subtract the wavefront errors comparing to the wavefront errors introduced by the multilayer mirror. Also, the multilayer mirrors used in the experiment were characterized with a RMS wavefront errors  $> 0.1 \lambda$ , which is less than the wavefront errors measured for HHs from solids. Hence, the effect of the wavefront errors from the multilayer mirrors used, on the solid HH wavefront is negligible.

The wavefront measurement of HHs from solids by reflecting the HHs from different multilayer mirrors under different conditions were successfully carried out. But in most of the cases, only a part of the beam was recorded by the WFS despite the fact that the WFS was aligned at the right angle and height. The results presented above are from the measurements where most parts of the HH beam was on the WFS. The wavefront measurement of solid HHG was carried out under the conditions obtained before the wavefront measurement was taken, but still, the wavefront measurement was having difficulty with a signal to noise ratio, stability in terms of energy and pointing and repeatability. Further, experiments with more stable solid HH is necessary to fully characterize the wavefront.

### 3.4.3 A comparison between wavefront of HHG from gases and solids

The measured of XUV wavefront from HHG in gases and solids are compared here. The major wavefront errors for HHG in gases measured at L2I and LOA, HHG in solids with CWE and ROM mechanisms measured at JETI 200 are listed in table 3.6.

The XUV wavefront measured for HHG in argon at 65 mbar at L2I and LOA differ in wavefront errors mainly because of the different generation conditions at the two labs. The wavefront aberrations were optimized in both the beamlines. The wavefront of characterized HHG in argon can be used in XUV imaging. The wavefront of XUV source at LOA has low RMS wavefront error and this source was used for calibrating the XUV wavefront sensors which requires a XUV source with a good quality wavefront.

Lab	HHG	RMS	PV	Astg. 0°	Astg. 45°
	Mechanism	$\lambda$	$\lambda$	$\lambda$	$\lambda$
LOA	Gas (Argon @ 65 mbar) (32 nm)	0.061	0.383	0.014	0.001
L2I	Gas (Argon @ 65 mbar) (32 nm)	1.06		0.5	0.164
JETI 200	Solid (CWE) with MLM - 28 eV (44.3 nm)	0.581	5.583	0.024	0.159
JETI 200	Solid (ROM) with MLM - 37 eV (33.5 nm)	0.89	6.589	0.07	0.031

Table 3.6: The value of major wavefront errors for HHG from solids and gases (MLM -multilayer mirror).

The wavefront of XUV source at L2I has comparatively higher wavefront error. However, the single shot XUV pulse energy at L2I is higher compared to that of LOA. The wavefront characterized XUV source at L2I can be used to probe laser-produced plasma [137]. The wavefront measurement of HHG in gases using long pulse lasers like in L2I is important as some large laser facilities use long pulse lasers for HHG. Hence, characterizing and optimizing wavefront of such XUV sources will help in improving the quality of results in plasma probing using XUV pulses [76].

The wavefront of solid harmonics was measured for the first time at JETI 200. The XUV wavefront measured for HHG in solids shows wavefront aberrations with higher peak to valley fluctuations although the RMS is lower. This shows a promise for future use in applications such as imaging and probing. However, the wavefront measurements were not having enough signal to noise ratio to fully characterize in terms of Zernike coefficients, wavefront errors. Also, it was observed that the pointing of the solid HH pulses were changing in each shot. Since the HHG process is different under CWE and ROM mechanisms, they are expected to have different wavefront parameters and ROM harmonics are expected to have higher divergent beams compared to CWE harmonics [75, 104]. However, the measured wavefront data does not show a significant difference between the wavefront of harmonics under CWE and ROM mechanisms. This may be due to the presence of ROM harmonics in the CWE spectrum and maybe we are only measuring the wavefront of ROM harmonics.

Solid HH wavefront measurement is promising but, not yet conclusive in terms of wavefront errors and wavefront stability. The solid HH wavefront measurements requires further experiments and analysis to have the knowledge and control on the wavefront, and this will allow it to be used as an XUV source for applications. Also it can be used to study the plasma properties during solid HHG.

## Chapter 4

# Temporal metrology of XUV pulses

### 4.1 Introduction

The advent of pulsed lasers started a new era for time-resolved studies of various physical phenomena. Some of these time-resolved studies include spectroscopy, pump-probe experiments and time-resolved dynamics of electron motion. These applications require temporally well characterized pulses.

The optical lasers can deliver pulses with duration ranging from nanoseconds to femtoseconds. For lasers which work in the visible and infrared, there are different temporal characterization methods currently available [139]. For pulse duration below few picoseconds, the electronic detectors are not fast enough to characterize the pulses. Optical sampling techniques [140] can be used to further lower the limit for electronics to characterize the short optical pulses. In cases where there is no reference pulses available, the short pulse can be used to characterize itself. Such a method is called an autocorrelation [141]. In an autocorrelator, the pulse to be measured is split into two and overlapped in an instantaneously responding nonlinear medium. The response of the medium at different temporal delay between the split pulses can be written as the autocorrelation function of the pulse. The intensity of autocorrelation signal can be written as

$$I_{AC}(\tau) = \int I(t)I(t + \tau) \quad (4.1)$$

where  $I(t)$  is the intensity of the pulse to be measured and  $I(t + \tau)$  is the time delayed replica of the pulse. The pulse duration can be obtained from the width of the autocorrelation ( $W_{AC}$ ) by assuming the pulse to be a Gaussian or  $\text{sech}^2$  function. In case of a Gaussian autocorrelation signal, the pulse duration ( $\Delta t_{pulse}$ ) can be written as [142]

$$\Delta t_{pulse} = W_{AC}/\sqrt{2} \quad (4.2)$$

Depending on the nonlinearity used and geometry, there are different varieties of autocorrelators. In general, the autocorrelators have a drawback that they cannot measure the spectral phase of the pulse.

To fully characterize the temporal profile of a pulse, the knowledge of spectral phase and intensity of the pulse is essential. The spectral phase is a complex phase term for the spectral components in the

pulse and it can be described as how different spectral components are related at a point in time. For ultrashort pulses ( $< 100$  fs) this becomes quite important as the spectral phase can cause changes in the temporal shape of the pulse. For optical pulses, the major methods, which measure the spectral phase and temporal duration are based on frequency-resolved optical gating (FROG) [143] and spectral phase interferometry for direct electric field reconstruction (SPIDER) [59]. FROG is essentially an autocorrelation measurement with spectrally resolved signal. The setup is similar to an autocorrelator with a spectrometer in place of a CCD or a photo-diode. The pulse duration is obtained using an iterative phase retrieval algorithm called principal component generalized projections algorithm, which starts with an initial guess considering the pulse duration, central wavelength and spectral bandwidth [144]. The algorithm compares the traces obtained with the guess to the actual trace obtained in the experiment and continues until it converges. This creates an analytical equation between the simulation and the experimental trace. This is a robust method, which is less affected by noise. Depending on the nonlinearity used and the geometry, there are different variety of FROG available for ultrashort pulse measurement [145]. One of the main problem with FROG is that the algorithm may take more time to converge. Single shot FROG measurement called GRENOUILLE is also available for pulse measurement method [146].

SPIDER involves spectral interference between the pulse to be measured and its spectrally sheared and temporally delayed replica. The pulse duration in this case can be retrieved using a phase retrieval algorithm [147, 59]. The algorithm gives the pulse duration without any iterative method. There are different kinds of SPIDER based on the geometry and the use of temporal or spatial separation between the pulse and its spectrally sheared replica [148].

A near IR laser with a central wavelength around 800 nm can have a pulse duration as short as 2.67 fs, if we could isolate a single cycle of the pulse, which is an experimentally difficult process. Also, even with this pulse duration, this laser cannot be used for volumetric probing of plasma states as they are reflected from the plasma surface. One way to solve these problems is to employ radiation with shorter in wavelength such as ultrashort pulse sources in the XUV spectral region. The major XUV sources are free electron lasers (FEL), synchrotrons, x-ray lasers (XRL) and HHG. Among these sources, only FEL [21, 149, 24] and HHG [150, 57] provide XUV pulses with ultrashort pulse duration in the XUV or x-rays. HHG inherently generates the XUV pulses with few femtoseconds up tens of attoseconds [32, 77]. There are different pulse characterization techniques for ultrashort pulses in the XUV. This chapter presents the XUV temporal metrology with major focus on "all-optical" pulse characterization techniques for pulses in the XUV spectral region. Sections 4.2 and 4.3 presents all-optical temporal characterization method of XUV pulses from HHG and FEL respectively.

#### 4.1.1 Temporal characterization techniques for XUV pulses

The main pulse characterization techniques for the XUV pulses from HHG and XUV FEL are presented here. For XUV pulses from HHG the energy of the pulses varies from nanojoules to few microjoules, the spectrum can be broad and pulse duration ranges from few tens of femtoseconds down to few tens of attoseconds [32]. For XUV pulses from FEL, the energy varies from few microjoules to hundreds of microjoules, the spectrum is usually narrow compared to XUV pulse from HHG and the pulse

duration ranges from few hundreds of femtoseconds to few femtoseconds. The temporal characterization method for the XUV source hence depends on the characteristics of the source. The most common XUV pulse characterization techniques for XUV pulses from HHG and FEL are briefly described below.

#### 4.1.1.1 XUV pulses from HHG

The XUV pulses from HHG can have single pulse or a pulse train with pulse duration from femtoseconds to attoseconds depending on the process of HHG [77]. The methods of pulse characterization vary slightly for a single pulse or for a train of pulses. The pulse characterization techniques follows its roots from the visible and IR temporal characterization methods such as autocorrelation, FROG and SPIDER. The different temporal characterization techniques in the XUV pulses from HHG can be broadly categorized into two: indirect detection of XUV pulses also called **ex-situ measurements techniques** and direct detection of XUV pulses, also called **in-situ measurement techniques** [77]. Both type of measurement techniques are briefly discussed in this section.

#### Ex-situ temporal characterization techniques:

The ex-situ pulse characterization of XUV pulses involves manipulation of XUV pulses after it is generated and indirect detection. In most ex-situ pulse measurement methods, the interaction of XUV pulses with gases is used as the nonlinear interaction. The interaction includes processes like above-threshold ionization and two-photon absorption, which are modeled under different conditions and the pulse duration is deduced from the model [78]. Since the XUV radiation is not directly detected, these methods are also called indirect methods [77].

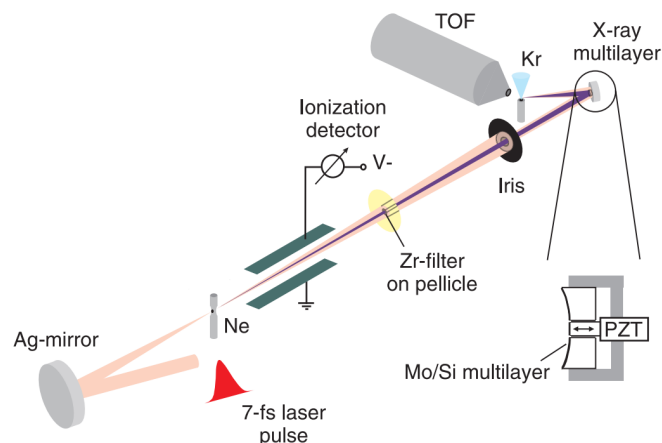


Figure 4.1: Schematic of an experimental setup for cross-correlation method. The XUV pulses generated by HHG in neon gas. The photoelectrons generated by the XUV pulses in krypton gas in presence of the IR laser is recorded using a time of flight (TOF) electron spectrometer. Figure taken from [150].

The pulse duration of XUV pulses from HHG was first measured by Drescher et al. [150] using a cross-correlation method. The method involved generation of photoelectrons by the XUV pulse in krypton gas in presence of the IR driving laser and detection using an electron spectrometer. The delay between the IR laser and XUV generated is controlled and a cross-correlation signal obtained resulted in a pulse

duration of 1.8 fs which is lower than the single cycle pulse duration of the driving IR laser. Figure 4.1 shows the schematic of the experimental setup for cross-correlation method.

The cross-correlation method was later used to detect sub-femtosecond XUV pulse duration [57]. Sub-femtosecond XUV pulses were detected using two-color two-photon ionization using the IR and XUV field. The method is called reconstruction of attosecond harmonic burst by interference in two-photon transition (RABITT) [151, 152]. In RABITT, the driving IR laser present during photo-ionization of argon gas by the XUV pulses modulates the energy of the electrons produced and generates sidebands in the photoelectron spectrum. The delay between the IR and XUV was changed and the corresponding sideband formation was recorded. From this information, the temporal amplitude was reconstructed in the RABITT technique. Figure 4.2 shows the schematic of the experimental setup for RABITT.

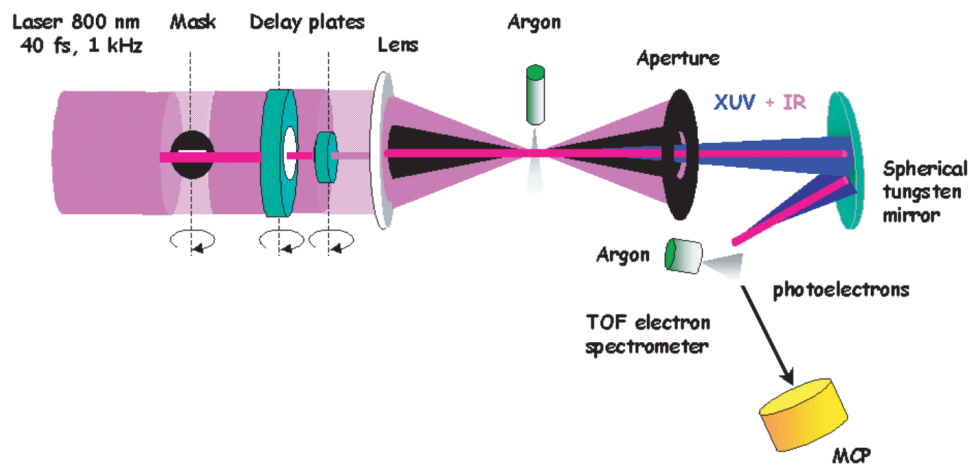


Figure 4.2: Schematic of an experimental setup for RABITT. XUV pulses from HHG ionizes argon gas in presence of the IR laser and the electron generated are detected using a TOF electron spectrometer. Taken from [151].

Photo-ionization of gases by XUV pulses in the presence of IR laser pulses can also affect the angular distribution and energy of the electrons produced. Depending on when the electrons are produced with respect to the IR laser field the photoelectron spectrum distribution changes. From these changes the pulse duration of the XUV can be retrieved and the method is called attosecond streaking [58, 153, 154]. Figure 4.3 shows the schematic of an experimental setup for attosecond streaking.

In intensity autocorrelation method for XUV, the two pulses are created by either by splitting the driving laser [155] or the XUV is split into two using a split mirror [156] and then in both cases the XUV pulses interact with helium gas jet and the photoelectrons generated during the interaction are detected by an electron spectrometer. The delay between the two pulses are related with the photoelectron spectrum and by comparing the two-photon ionization of XUV pulses in helium gas with the delay, the pulse duration of the XUV pulses can be retrieved [156].

The methods like cross-correlation or X - FROG for the XUV pulses [157] uses two-photon ionization in gases with XUV pulses in presence of IR laser field and the photoelectrons generated were detected using an electron spectrometer to create a spectrogram, also called FROG trace. The FROG iterative reconstruction algorithm is used to retrieve the pulse duration. Figure 4.4 shows the schematic of a typical experimental setup for FROG in the XUV. Single color FROG was also later achieved in the XUV using the

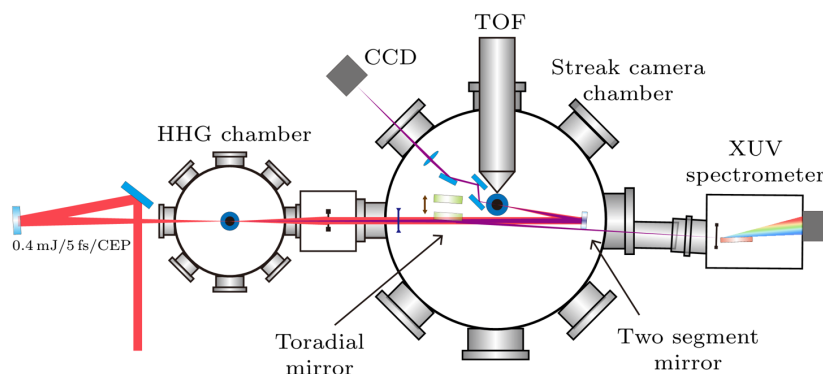


Figure 4.3: Schematic of an experimental setup for streaking. The electrons ionized by the XUV pulses are streaked by the IR laser field present and detected using a TOF electron spectrometer. Figure taken from [154].

same method [158] and measured sub-femtosecond XUV pulses. A combination of attosecond streaking and FROG retrieval method has been used to characterize XUV pulse as short as 80 attoseconds [31].

More robust pulse duration measurement like frequency-resolved optical gating for complete reconstruction of attosecond bursts (FROG-CRAB) was also later introduced to measure the attosecond XUV pulses. FROG CRAB is similar to FROG and it also includes some aspects of RABITT as well [159]. The FROG-CRAB method has been used to measure XUV pulse durations  $< 200$  as [160].

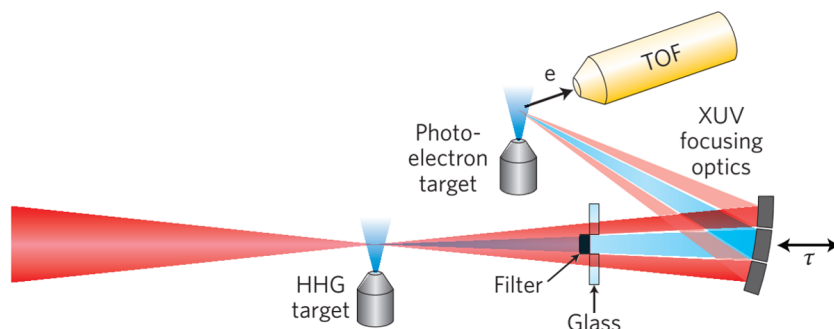


Figure 4.4: Schematic of a typical experimental setup for FROG. Photoelectron spectrum generated by the XUV in presence of IR is recorded with respect to the delay between XUV and IR to generate the FROG trace. Figure taken from [56].

Broader XUV pulses with shorter pulse duration can also be characterized by the method called phase retrieval by omega oscillation filtering (PROOF) [161]. PROOF uses a similar experimental setup as FROG-CRAB and it works with much lower energy of near IR driving field. In PROOF the spectral distribution of the photoelectrons modified by the near IR laser field is recorded by the photoelectron spectrometer at different delay between the IR and XUV fields. The presence of the driving laser field results in oscillations in the electron spectrum at a constant energy and the spectral phase can be retrieved by finding the spectral phase corresponding to the sinusoidal oscillations [161]. The PROOF method has been used to measure XUV pulses as short as 67 as [32]. There is also an improved version of PROOF called iPROOF for XUV pulse characterization [162]. Methods like attosecond spectral shearing interferometry which involves a combination of SPIDER with photoelectron spectroscopy [163] and single shot autocorrelator [164] for XUV pulse characterization has been proposed.

### In-situ temporal characterization techniques:

The in-situ temporal measurement techniques for XUV pulses from HHG mainly depends on the HHG method. In-situ methods mostly involve all-optical setup and direct detection of XUV pulses. The in-situ method using double color was introduced by Dudovich et al. It involves the generation of XUV pulses in presence of driving IR laser and its weak SH field [165]. The presence of SH field causes breaking the symmetry and generates odd and even HHs. In this method, the detector is an XUV spectrometer and the intensity of even harmonics generated is observed with respect to the phase difference between the IR and its second harmonic. From this, the pulse duration can be deduced by relating the delay between the two pulse fields and the corresponding even harmonic intensity. Figure 4.5 shows the schematic of an experimental setup for a double color in-situ method. Later this technique was used along with RABITT to characterize attosecond pulse train [166].

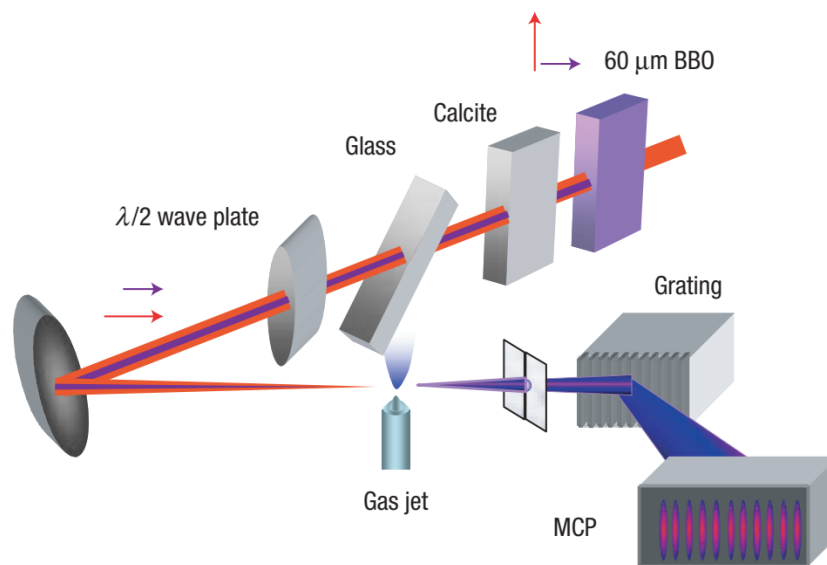


Figure 4.5: Schematic of an experimental setup for a double color in-situ method. IR laser and its SH generate HHs and the modulation in the HH spectrum is recorded using an XUV spectrometer. Figure modified from [165].

A spatially encoded in-situ measurement was later demonstrated called space-time reconstruction of attosecond pulses (STRAP) [56, 167]. In STRAP the weak second harmonic field is introduced at a small angle along with the IR pulse for HHG. The second harmonic field perturbs the XUV wavefront in the near-field and hence the far-field pattern as well [167]. The delay between the IR and second harmonic is recorded as the modulations in the spatially resolved XUV spectra in the far-field. From the spectrogram using the principal component generalized projection algorithm [144] and parametric fitting procedure, the XUV pulse structure can be reconstructed. The temporal information is obtained from the phase modulation of the XUV wavefront and its dependence on the XUV emission time [167]. Figure 4.5 shows the schematic of an experimental setup for STRAP.

One of the techniques, in which XUV generation is manipulated for temporal measurement with an all-optical setup, is called SPIDER in XUV [61, 62]. This method is analogous to the SPIDER for IR laser pulses [168].

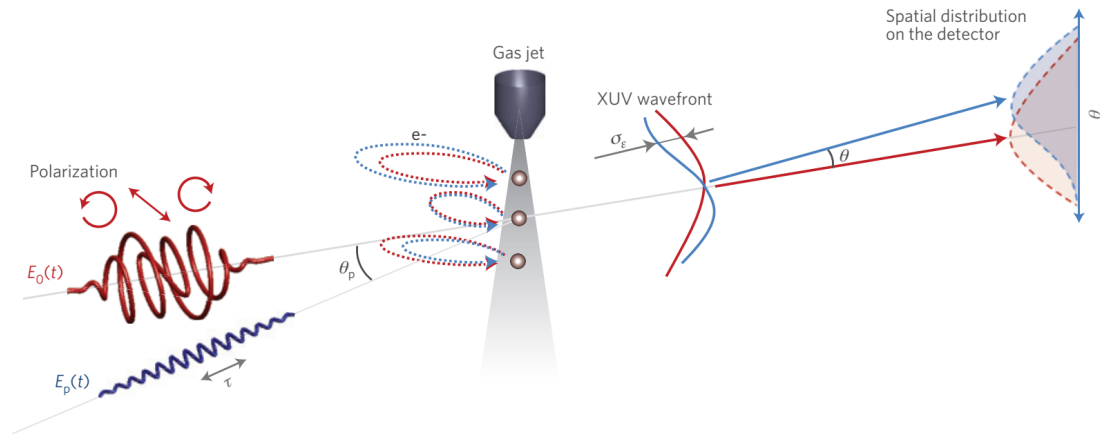


Figure 4.6: Schematic of an experimental setup for STRAP. Polarized IR laser and its weak second harmonic interact at angle in a gas jet and a spatial modulation is introduced in the XUV intensity distribution. Figure taken from [167].

#### 4.1.1.2 XUV FEL

The temporal metrology of XUV FEL is also a challenging task mainly because the pulses are in the XUV spectral range and also because of the high shot to shot instability of the FEL in general. However, seeded FELs have less shot to shot instability. Since the XUV FELs have higher pulse energy compared to HHG, less efficient nonlinear process in different materials can be used for pulse characterization methods [169, 170, 171, 172]. Similar to HHG, there are direct detection and indirect detection methods for XUV FEL pulses [173].

The indirect methods for XUV FEL pulse characterization are similar to that of XUV pulses from HHG. The autocorrelator method for pulse duration measurement of XUV pulses from FEL uses wavefront splitting of the pulse to create the two pulses and photo-ionization in a gas (helium / nitrogen) medium as the nonlinear process. This photo-ionization is used as a nonlinear process for the pulse duration measurement. The ions generated by the interaction between the XUV pulse and the gas is recorded by an ion spectrometer and the autocorrelation signal is obtained by comparing the ionization yield to the delay between the pulses. Terahertz streaking methods are also used to measure the pulse duration of XUV FEL pulses. Similar to the streaking experimental setup for XUV pulses from HHG, in streaking for XUV FEL, the XUV pulses ionizes a sample and the electrons produced are streaked in the field of an optical laser and the pulse duration is retrieved from the variations in the electron spectrum recorded [174]. In cross-correlation method for XUV FEL, the XUV pulse ionizes a sample in presence of an IR laser pulse and pulse duration is obtained by comparing the formation of side-bands in the recorded spectrum of electrons generated to the delay between the XUV and IR pulses [175].

Direct measurement methods of XUV FEL pulse duration involves detection of either the XUV pulse or an optical pulse generated in a nonlinear process due to the XUV pulse. Cross-correlation method involves the change in transient reflectivity of a sample in presence of XUV FEL pulses [176, 175] to measure the XUV pulse duration. A spectral correlation method for XUV FEL pulse characterization involves measuring the spectrum of the pulses and deducing the pulse duration by statistical analysis [177]. Spectral shearing interferometric methods are also available for XUV FEL pulse characterization.

Three-wave mixing is used as the nonlinear process for pulse characterization [178]. Another spectral interferometry based method called SPIDER was also proposed for characterization of XUV FEL pulses [179].

## 4.2 All optical temporal metrology of XUV pulses from HHG

The XUV pulses from HHG with pulse duration ranging from femtoseconds to attoseconds needs pulse duration measurement which is reliable, fast and direct. Single shot pulse measurement methods are better to avoid shot to shot fluctuations associated with the laser, gas pressure or other properties. The methods described in the section 4.1.1.1 includes direct and indirect methods. In indirect methods the photoelectrons generated by the XUV in different conditions are detected and then the pulse duration is obtained by modeling the interaction of XUV pulses with the gases. Albeit indirect method is the most used pulse duration measurement for XUV pulses from HHG, it is not the best option as the pulse duration mostly depends on how good the modeling of ionization by XUV pulses is done and also the operation of complex electron spectrometers makes the pulse characterization an experiment in itself. Using all-optical temporal characterization methods with direct detection is a better option to avoid these problems. Among the different direct detection methods explained in section 4.1.1.1, for the methods involving the use of second harmonic field along with IR field for generation of HHG requires very short IR pulse with carry envelope phase stabilization and highly precise control of polarization and delay between the IR and second harmonic. These two conditions are difficult to achieve. The other direct methods are based on SPIDER. SPIDER relies on spectral interference and it requires spectrally sheared pulses delayed in time or separated in space. Although SPIDER is experimentally difficult to realize for XUV pulses, it can be tested within the capabilities of a laser laboratory. Also, SPIDER can work in single shot and the pulse duration can be retrieved without using an iterative algorithm.

In this section, we discuss the about the temporal metrology of XUV pulses from HHG with an all-optical direct measurement based on SPIDER. The numerical simulation on SPIDER and spatially encoded arrangement for SPIDER (SEA-SPIDER) and the experimental progress towards realization of SEA SPIDER in the XUV are presented.

### 4.2.1 Introduction to SPIDER and SEA-SPIDER

The full temporal characterization of an optical pulse requires the knowledge of intensity and phase of the pulse. An electromagnetic pulse can be represented by its electric field for non-relativistic cases. The electric field consists of a real part and a complex imaginary part and it can be represented analytically in the temporal domain as

$$E(t) = |E(t)| \exp(i[\psi_0 + \psi(t) - \omega_0 t]) \quad (4.3)$$

where  $|E(t)|$  is the time dependent envelope of the electric field,  $\omega_0$  is the carrier frequency,  $\psi(t)$  is the time dependent phase and  $\psi_0$  is a constant called carrier envelope offset phase. The time dependent intensity is given by the square of the electric field,  $I(t) = E(t)^2$ . The electric field in the frequency domain

can be obtained by the Fourier transform of equation 4.3 and it is given by

$$E(\omega) = \mathcal{F}(E(t) e^{i\omega t}) = |E(\omega)| e^{i\phi(\omega)} \quad (4.4)$$

where  $|E(\omega)|$  is the spectral amplitude and  $\phi(\omega)$  is the spectral phase. The spectral intensity is given by  $I(\omega) = |E(\omega)|^2$ . The spectral phase describes the relative phase between the different optical frequencies in the pulse. The spectral phase of the pulse determines if the pulse duration can be transform limited or not, since the derivative of the spectral phase, which is group delay determines how different spectral components arrive in time around the central frequency of the pulse. The spectral phase can be expanded in terms of the central frequency as a Taylor series as follows [180]

$$\phi(\omega) = \sum_{j=0}^{\infty} \frac{\phi^{(j)}(\omega_0)}{j!} (\omega - \omega_0)^j \text{ with } \phi^{(j)}(\omega_0) = \left. \frac{\partial^j \phi(\omega)}{\partial \omega^j} \right|_{\omega_0} \quad (4.5)$$

$$\phi(\omega) = \phi(\omega_0) + \frac{1}{1!} \phi'(\omega_0)(\omega - \omega_0) + \frac{1}{2!} \phi''(\omega_0)(\omega - \omega_0)^2 + \frac{1}{3!} \phi'''(\omega_0)(\omega - \omega_0)^3 + \dots \quad (4.6)$$

where  $\omega_0$  is the central frequency and  $j$  is the index for all the frequencies available in the pulse spectrum. The zeroth order  $\phi(\omega_0)$  describes the absolute phase of the pulse. The first order term,  $\phi'(\omega_0)$  leads to a temporal shift of the pulse in the time domain. The second order term  $\phi''(\omega_0)$  corresponds to a quadratic phase of the pulse and it relates to the velocity of the different frequency components in the pulse when it travels through a medium. It is also called group delay dispersion (GDD). GDD causes a pulse to stretch in time and increases the pulse duration. The third order term  $\phi'''(\omega_0)$  is called third order dispersion (TOD) also contributes to the stretching of a pulse when it travels through a medium. The temporal structure of electric field of a pulse can be fully reconstructed if the spectrum of the pulse and its spectral phase are known and this can be done by taking the inverse FT of equation 4.4. For XUV pulses with short pulse duration and high bandwidth, different available methods are limited to certain pulse duration or certain spectrum. The indirect methods have more limitations as the modeling changes for pulse duration change from femtoseconds to attoseconds. The direct detection methods are more flexible as they can be used for different pulse durations. Among the direct detection methods, spectral interferometry is one of the most viable option. There are different spectral interferometry techniques available for the characterization of short pulse IR lasers. For the XUV because of its short pulse nature, the self referencing spectral interferometry method is the best option since the pulse itself is the shortest probe available and also in spectral interferometry the spectral phase information can be measured using a slow detector like a spectrometer. The self referencing spectral interferometry which is used in this work is SPIDER and a variation of it called SEA-SPIDER.

#### 4.2.1.1 SPIDER : Spectral phase interferometry by direct electric field reconstruction

Spectral phase interferometry for electric field reconstruction (SPIDER) is an interferometric all optical pulse characterization method introduced for ultrashort pulse near IR lasers [181, 59]. Different variations of SPIDER have been developed and used for characterization short pulse near IR lasers

[168, 182].

In SPIDER, the pulse to be measured interferes with its spectrally sheared and temporally delayed replica in a spectrometer. The spectral interference between the pulse and its sheared replica enables to have mapping between the spectral phase at a frequency and spectral phase at frequency shifted by the spectral shear. The electric field of the pulse to be measured can be represented in spectral domain as

$$E(\omega) = |E(\omega)| e^{i\phi(\omega)} \quad (4.7)$$

where  $\omega$  is the central frequency of the pulse spectrum and  $\phi(\omega)$  is the spectral phase. The electric field of the spectrally sheared or shifted replica with a spectral shear of  $\Omega$  can be written as

$$E(\omega - \Omega) = |E(\omega - \Omega)| e^{i\phi(\omega - \Omega)} \quad (4.8)$$

For the two pulses to spectrally interfere one of the pulse should be temporally delayed with respect to the other by a time,  $\tau$ . This will impart fringes of frequency  $2\pi/\tau$  in the spectrum. The interference with no spectral shear between the pulses ( $\Omega = 0$ ), known as a spectrogram  $S(\omega)$  can be written as

$$S(\omega)_C = (E(\omega) + E(\omega))^2 \quad (4.9)$$

$$S(\omega)_C = E(\omega)^2 + E(\omega)^2 + 2|E(\omega)||E(\omega)| \cos(\omega\tau) \quad (4.10)$$

$$S(\omega)_C = 2I(\omega) + 2\sqrt{I(\omega)I(\omega)} \cos(\omega\tau) \quad (4.11)$$

This spectrogram is also called a calibration spectrogram as it is the spectrogram without the shear and it is used to calibrate the temporal delay. Here the spectral modulation is in the  $\cos(\omega\tau)$  term and this gives a fixed fringe separation. When a spectral shear is introduced in one of the pulses, this will change the nominal fringe spacing in the interference pattern and it is called the SPIDER spectrogram and it can be written as

$$S(\omega) = E(\omega)^2 + E(\omega - \Omega)^2 + 2|E(\omega)||E(\omega - \Omega)| \cos(\phi(\omega) - \phi(\omega - \Omega) + \omega\tau) \quad (4.12)$$

$$S(\omega) = I(\omega) + I(\omega - \Omega) + 2\sqrt{I(\omega)I(\omega - \Omega)} \cos(\phi(\omega) - \phi(\omega - \Omega) + \omega\tau) \quad (4.13)$$

This spectrogram has the intensity term given by  $I(\omega) + I(\omega - \Omega)$  and also the oscillation term given by  $\cos(\phi(\omega) - \phi(\omega - \Omega) + \omega\tau)$ , which contains the phase term. The spectral phase can be recovered by using the phase retrieval procedure by Takeda et al. [147]. This involves mainly four steps: Fourier transform (FT) of the spectrogram, filtering one of the phase part which is separated from the central intensity part by the time delay, inverse FT of the filtered part and then concatenate to get the phase along the pulse spectrum. A flow chart of the spectral phase retrieval procedure is shown in figure 4.7. The FT of the SPIDER spectrogram can be written as [62]

$$S(\tilde{t}) = \mathcal{F}(S(\omega)) \quad (4.14)$$

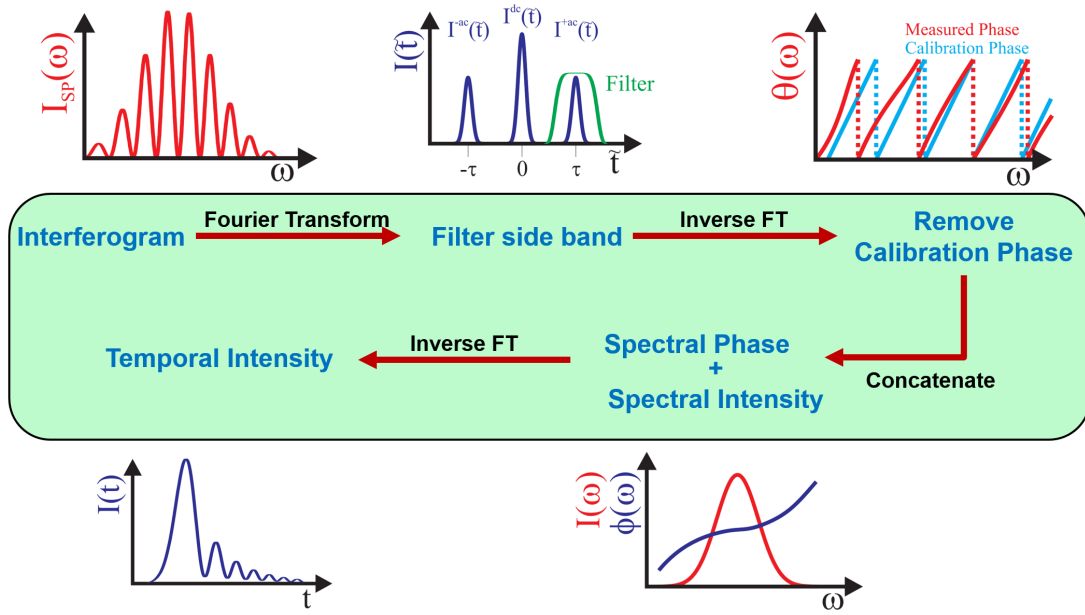


Figure 4.7: A flow chart of SPIDER Algorithm. Modified from [62].

$$S(\tilde{t}) = I_{dc}(\tilde{t}) + I_{ac}(\tilde{t} + \tau) + I_{ac}(\tilde{t} - \tau) \quad (4.15)$$

One of the side bands ( $I_{ac}(\tilde{t} + \tau)$  or  $I_{ac}(\tilde{t} - \tau)$ ) can be filtered using a super Gaussian filter. The inverse FT of the filtered phase part gives the spectral phase difference between the pulse and its sheared replica with the constant delay phase term and it can be written as [62]

$$\tilde{\theta}(\omega) = \mathcal{F}^{-1}(I_{ac}(\tilde{t} + \tau)) = \tilde{\phi}(\omega) - \tilde{\phi}(\omega - \Omega) + \omega\tau \quad (4.16)$$

The constant delay phase term  $\omega\tau$  can be removed by subtracting the phase difference term obtained for the calibration spectrogram using the same procedure described above. Considering a small shear, equation 4.16 can be written as the spectral phase gradient [62]

$$\tilde{\theta}(\omega) = \Omega \frac{\tilde{\phi}(\omega) - \tilde{\phi}(\omega - \Omega)}{\Omega} \simeq \Omega \frac{\partial \tilde{\phi}(\omega)}{\partial \omega} \quad (4.17)$$

The spectral phase of the pulse can be retrieved by integration or concatenation of the spectral phase difference ( given in equation 4.17) between the pulse and its sheared replica. Figure 4.8 shows the idea of phase retrieval through integration or concatenation [62]. In the integration method, the integration of scaled phase difference  $\frac{\tilde{\theta}(\omega)}{\Omega}$  gives the spectral phase with a polynomial accuracy depending on the integration method. Trapezoidal integration method can be used to reconstruct the spectral phase until 3<sup>rd</sup> order polynomial [62]. By concatenation method, the spectral phase at a frequency  $\omega_0 + \Omega$  can be calculated according to the following equation, [62]

$$\tilde{\phi}(\omega_0 + \Omega) = \tilde{\phi}(\omega_0) + [\tilde{\phi}(\omega_0 + \Omega) - \tilde{\phi}(\omega_0)] = \tilde{\phi}(\omega_0) + \tilde{\theta}(\omega_0 + \Omega) \quad (4.18)$$

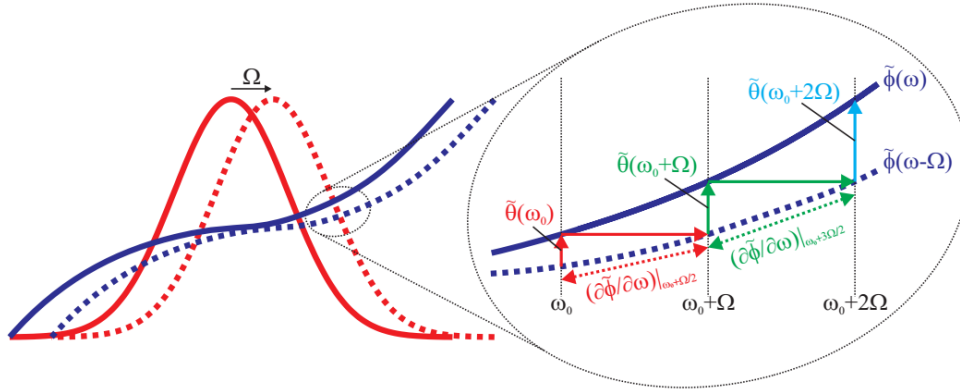


Figure 4.8: Concept of integration or concatenation of the phase difference extracted from a SPIDER spectrogram. Taken from [62].

This equation can be generalized for the whole spectrum of the pulse and it can be written as [59, 62]

$$\tilde{\phi}(\omega_0 + N\Omega) = \tilde{\phi}(\omega_0) + \begin{cases} \sum_{n=1}^N \tilde{\theta}(\omega_0 + n\Omega) & \text{if } N \geq 1 \\ 0 & \text{if } N = 0 \\ \sum_{n=0}^{|N|-1} \tilde{\theta}(\omega_0 - n\Omega) & \text{if } N \leq -1 \end{cases} \quad (4.19)$$

where  $N$  is the number of samples in the pulse spectrum. The retrieved spectral phase values with concatenation or integration are separated by the spectral shear  $\Omega$ . According to Nyquist–Shannon sampling theorem, for pulse with a temporal width of  $T$ , it can be reconstructed completely if the sampling frequency is less than  $2\pi/T$ . This gives us the relation between the pulse duration and the spectral shear as

$$\Omega \leq \frac{2\pi}{T} \quad (4.20)$$

Using the spectrum of the pulse and retrieved spectral phase we can reconstruct the electric field of the pulse by a Fourier transform as shown here,

$$E(t) = \mathcal{F} \left[ \sqrt{I(\omega)} e^{i\tilde{\phi}(\omega)} \right] \quad (4.21)$$

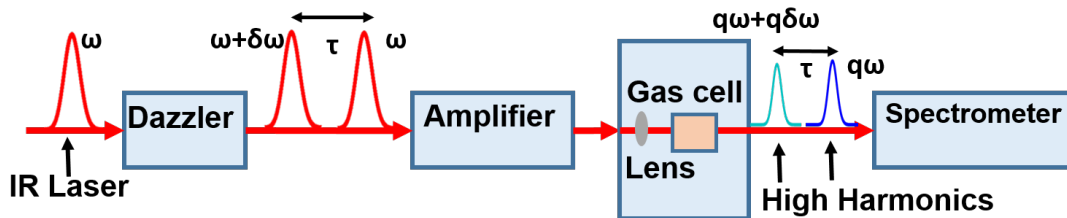


Figure 4.9: Schematic of experimental setup for SPIDER. Modified from [60].

The major difficulty in the implementation of XUV SPIDER is creating the spectrally sheared and time delayed replica of the pulse. A SPIDER setup has been already realized for measuring the

XUV pulses and was able to measure an XUV pulse with duration up to 13 fs [61]. Figure 4.9 shows a schematic of the SPIDER. Here the driving IR pulse is split into two and one is spectrally shifted and delayed in time with respect to the other with the use of a Dazzler [183] and both the beams are focused onto the gas cell to generate harmonics. The XUV pulses generated from both beams interfere spectrally on an XUV spectrometer.

#### 4.2.1.2 SEA-SPIDER : Spatially encoded arrangement for SPIDER

The major difficulty of an XUV SPIDER is that it requires a high resolution XUV spectrometer since it involves resolving fringes in the spectral direction. Another difficulty appears due to co-linear geometry, which results perturbations of the second driving laser pulse due to the ionization of the gas by the first pulse and this has to be avoided. Indeed, the two pulses have to be exactly the same with only a shift in wavelength. A time delay less than few hundreds of femtoseconds can affect the quality of the second XUV pulses and a time delay greater than this demands very high resolution for the spectrometer. Both of these difficulties can be avoided by creating spatial separation between the pulse and its spectrally sheared replica instead of a temporal delay. This method is called spatially encoded arrangement for SPIDER (SEA-SPIDER) [182, 60, 62]. SEA-SPIDER for XUV was introduced by Cormier et al., [60]. In SEA-SPIDER the spectral phase information is encoded in the spectrally resolved spatial interference pattern. This technique relaxes requirements on using a high resolution XUV spectrometer [182, 60]. SEA-SPIDER has been used for measuring pulse duration of visible and IR pulses but not for XUV pulses [60, 62] yet.

The SEA-SPIDER can be analytically described as follows. The spectral interference between the pulse to be measured and its replica with zero spectral shear with respect to the pulse, called the calibration SEA-SPIDER spectrogram is given by

$$S(\omega, x)_{SEA-C} = E(\omega, x)^2 + E(\omega, x)^2 + 2 |E(\omega, x)| |E(\omega, x)| \cos(\mathbf{K}x) \quad (4.22)$$

$$S(\omega, x)_{SEA-C} = I(\omega, x) + I(\omega, x) + 2 \sqrt{I(\omega, x)I(\omega, x)} \cos(\mathbf{K}x) \quad (4.23)$$

where  $\mathbf{K}$  is the difference between the wave-vectors of the pulse and its replica and  $x$  is the spatial separation between the pulses. The SEA-SPIDER spectrogram with a spectral shear of  $\Omega$  between the pulse and its spectrally sheared replica is given by

$$S(\omega, x)_{SEA} = E(\omega, x)^2 + E(\omega - \Omega, x)^2 + 2 |E(\omega, x)| |E(\omega - \Omega, x)| \cos(\phi(\omega) - \phi(\omega - \Omega) + \mathbf{K}x) \quad (4.24)$$

$$S(\omega, x)_{SEA} = I(\omega, x) + I(\omega - \Omega, x) + 2 \sqrt{I(\omega, x)I(\omega - \Omega, x)} \cos(\phi(\omega) - \phi(\omega - \Omega) + \mathbf{K}x) \quad (4.25)$$

The term inside the cosine function in the above equations is the tilt between the two pulses.

$$\mathbf{K}x = (\mathbf{k}_1 - \mathbf{k}_2) \cdot x \quad (4.26)$$

where  $\mathbf{k}_1$  and  $\mathbf{k}_2$  are the wave vectors of the pulse and its replica respectively. The wave-vector differences

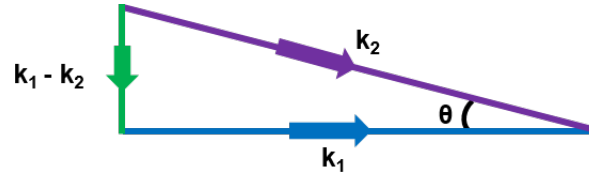


Figure 4.10: Pictorial representation of wave-vector difference ( $\mathbf{k}_1 - \mathbf{k}_2$ ).

between the pulse and its replica is shown pictorially in figure 4.10, considering that the replica is making angle of  $\theta$  on the pulse. Now the difference between the two wave-vectors can be written in terms of the angle between them. The equation 4.26 can be rewritten as

$$Kx = x k_1 \sin(\theta) \quad (4.27)$$

Using equation 4.27 we can rewrite equations 4.23 and 4.25 as follows

$$S(\omega, x)_{SEA-C} = I(\omega, x) + I(\omega, x) + 2 \sqrt{I(\omega, x)I(\omega, x)} \cos(k_1 x \sin(\theta)) \quad (4.28)$$

$$S(\omega, x)_{SEA} = I(\omega, x) + I(\omega - \Omega, x) + 2 \sqrt{I(\omega)I(\omega - \Omega)} \cos(\phi(\omega) - \phi(\omega - \Omega) + k_1 x \sin(\theta)) \quad (4.29)$$

SEA-SPIDER gives a 2-D spectrogram and the phase can be retrieved from it in two ways [62]. One can proceed with a 2-D FFT of the 2-D spectrogram along the spatial and the spectral direction or a 1-D FFT of the 2-D spectrogram only along the spatial direction. Both methods will yield the same result [62]. Here the 1-D FFT of the 2-D spectrogram along the spatial direction is followed. After the FT the methods are the same as for SPIDER. The spectral phase difference obtained is concatenated or integrated to reconstruct the spectral phase. Similar to SPIDER, in SEA-SPIDER the pulse structure can be reconstructed by knowing the pulse spectrum and spectral phase.

For the experimental realization of SEA-SPIDER in the XUV, two spatially separated sources of XUV pulses are required. Figure 4.11 shows the schematics of SEA-SPIDER proposed in the XUV [60]. Here two driving laser pulses are separated by a distance of  $\Delta x$  and they are focused onto a gas cell generating the harmonics. The harmonics generated interfere in the far-field on an XUV spectrometer. The spectrometer shown in figure 4.11 consists of a reflective grating focusing the XUV pulse and its sheared replica on an XUV sensitive CCD.

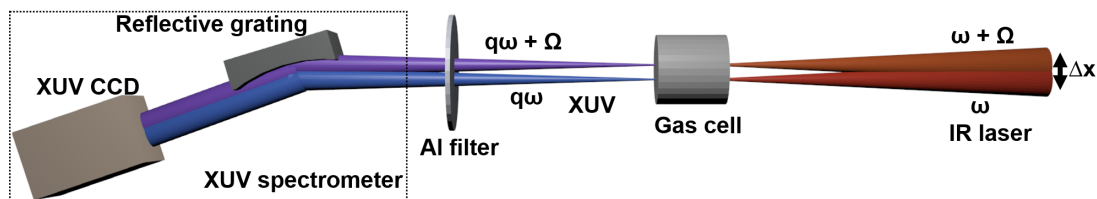


Figure 4.11: Schematic of a basic setup for SEA-SPIDER in XUV.

### 4.2.1.3 Methods of introducing spectral shear

One of the major difficulty in realizing a SPIDER or SEA-SPIDER in XUV is the complication in generating a spectrally sheared replica of the pulse to be measured. In a SPIDER or a SEA-SPIDER for IR lasers, this problem is solved by using nonlinear materials. The lack of efficient nonlinear materials in the XUV makes it difficult to generate the spectrally sheared replica in the XUV. One option is to introduce the spectral shear in the IR driving laser and then generate XUV pulses with the IR laser and the sheared replica. There are different ways to introduce shear in the driving laser pulse [62]. One of the methods is to use the commercially available pulse shaper, Dazzler [183], based on an acousto-optic filter. It can be used to create a spectrally sheared replica of the pulse delayed in time. This method has been already used for the first SPIDER measurement in the XUV [61]. The pulse shapers are limited by the bandwidth and energy of the pulse used. Also, a pulse shaper is an expensive device, which is not easily available in most of the laboratories. Another method is to use amplitude shaping by spectrally clipping the pulse to generate another pulse spectrally shifted with respect to the other. The amplitude shaping can be done by clipping the pulse inside a compressor. Amplitude shaping is a difficult procedure and the precision in clipping the frequencies in the pulse spectrum is important to have the required shear for SPIDER or SEA-SPIDER.

Another way of introducing shear is using nonlinear mixing of the driving IR laser. In this method, the IR laser is split into two and second harmonic (SH) pulses are generated by this split IR pulses. By carefully tuning the phase matching angle of the SHG, the central wavelength of the SH can be tuned [179]. A schematic of a possible experimental setup to generate a pulse and its spectrally sheared replica of the pulse based on SHG is shown in figure 4.12. In the experimental setup, the driving IR laser is split

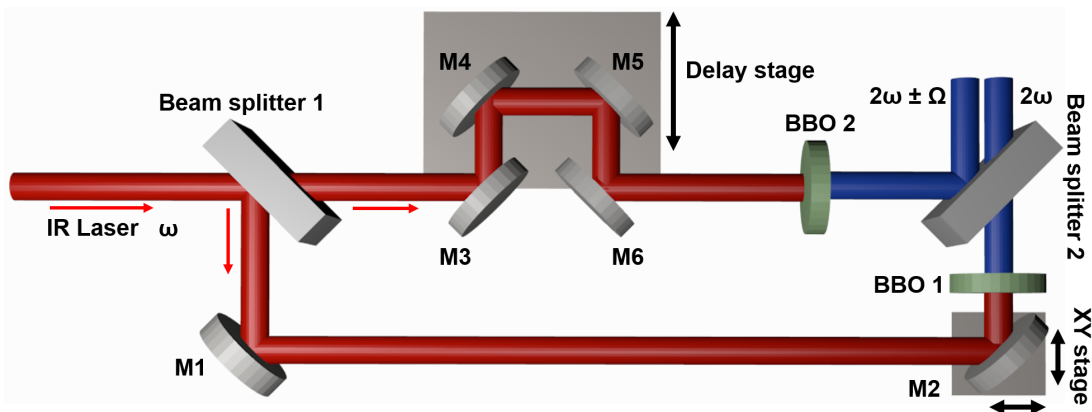


Figure 4.12: Schematic of experimental for generating a pulse and its spectrally sheared replica.

into two with beam splitter 1. The laser beam which passes through the beam splitter 1 is steered through a delay line with mirrors M3 to M6 until BBO 2. The SH is generated at BBO 2 and it is reflected by the beam splitter 2. The beam which is reflected by the beam splitter 1 is steered by the mirrors M1 and M2 to the BBO 1. The SH generated in BBO 1 is transmitted through the beam splitter 2. The delay stage in the setup can be adjusted to control the temporal delay between the two pulses. The XY stage on which M2 is placed can be adjusted to control the spatial separation between the two SH pulses. The SHG in

one of the arms, for example the one with XY stage can be detuned from the optimum position to shift its SH central frequency from  $2\omega$  to  $2\omega \pm \Omega$  and this generates the spectral shear required for the SPIDER or SEA-SPIDER experiment. With a delay line in one of the arms, this method can be used to generate spectrally sheared pulses with temporal delay for using it in SPIDER configuration. The spatial separation between the second harmonic and its sheared replica can be done by adjusting the XY stage. Further the pulse and its sheared replica can be focused onto a gas cell to generate HH and its spectrally sheared replica with a time delay or spatial separation. In this way, this method of tuning the second harmonic generation for generating sheared replica is a suitable method for SPIDER or SEA-SPIDER in the XUV.

## 4.2.2 Numerical simulations for SPIDER and SEA-SPIDER

For realizing the SEA-SPIDER experimental setup in the XUV experimental parameters like source separation and spectral shear required needs to be calculated. For retrieving the pulse duration, a retrieval algorithm is required. Considering this, a reconstruction algorithm for SPIDER was developed [59, 62, 147]. The algorithm was used to numerically simulate and test the parameters that are feasible for experiments. Numerical simulations was carried out first for a SPIDER experimental configuration for the SH pulses and later for the XUV pulses. Further, the SPIDER reconstruction algorithm was modified for SEA-SPIDER and then numerical simulations were carried out for a SEA-SPIDER experimental configuration. The effect of probable noise during the experiment was also simulated for both SPIDER and SEA-SPIDER. The results of this numerical study is presented in this section.

### 4.2.2.1 SPIDER algorithm for SH pulses

The SPIDER algorithm was used to obtain the pulse duration and reconstruct its electric field of numerically simulated of SH pulses. Figure 4.13 shows the result of the numerical simulations. The input spectrum has a central wavelength of 400 nm with a pulse duration  $\sim 30$  fs. With a second order phase of  $500 \text{ fs}^2$ , the pulse duration becomes  $\sim 54.5$  fs. The numerically simulated input pulse, spectrally sheared replica and their corresponding spectral phase are shown in figure 4.13a. The numerically simulated spectral interference with a time delay of 200 fs is shown in figure 4.13b. The delay of 200 fs was chosen for the simulations to be able to use a spectrometer available in the lab for the experiments. Simulated interferogram was used as the input for the SPIDER algorithm. The phase part was filtered from the interference pattern after doing a FT and it is shown in figure 4.13c. The inverse FFT of the filtered phase term gives the measured phase of the spectral interference with spectrally sheared SH pulses. Similarly, the calibration phase can be retrieved from the calibration interferogram generated by interference between SH pulse and its replica. The measured phase and calibration phase are shown in figure 4.13d. The phase difference between measured and calibration phase is obtained and it is concatenated to retrieve the spectral phase of the SH pulse. Figure 4.13e shows the input and retrieved spectral phase and they are in good agreement over a range of 2 times the FWHM of the spectrum. Figure 4.14f shows the input and retrieved spectral phase with the input pulse spectrum. Further, the retrieved spectral phase was used to reconstruct the electric field of the SH pulses and it is shown in figure 4.13g. Figure 4.13h shows the reconstructed SH pulse in the time domain with a Gaussian fitting.

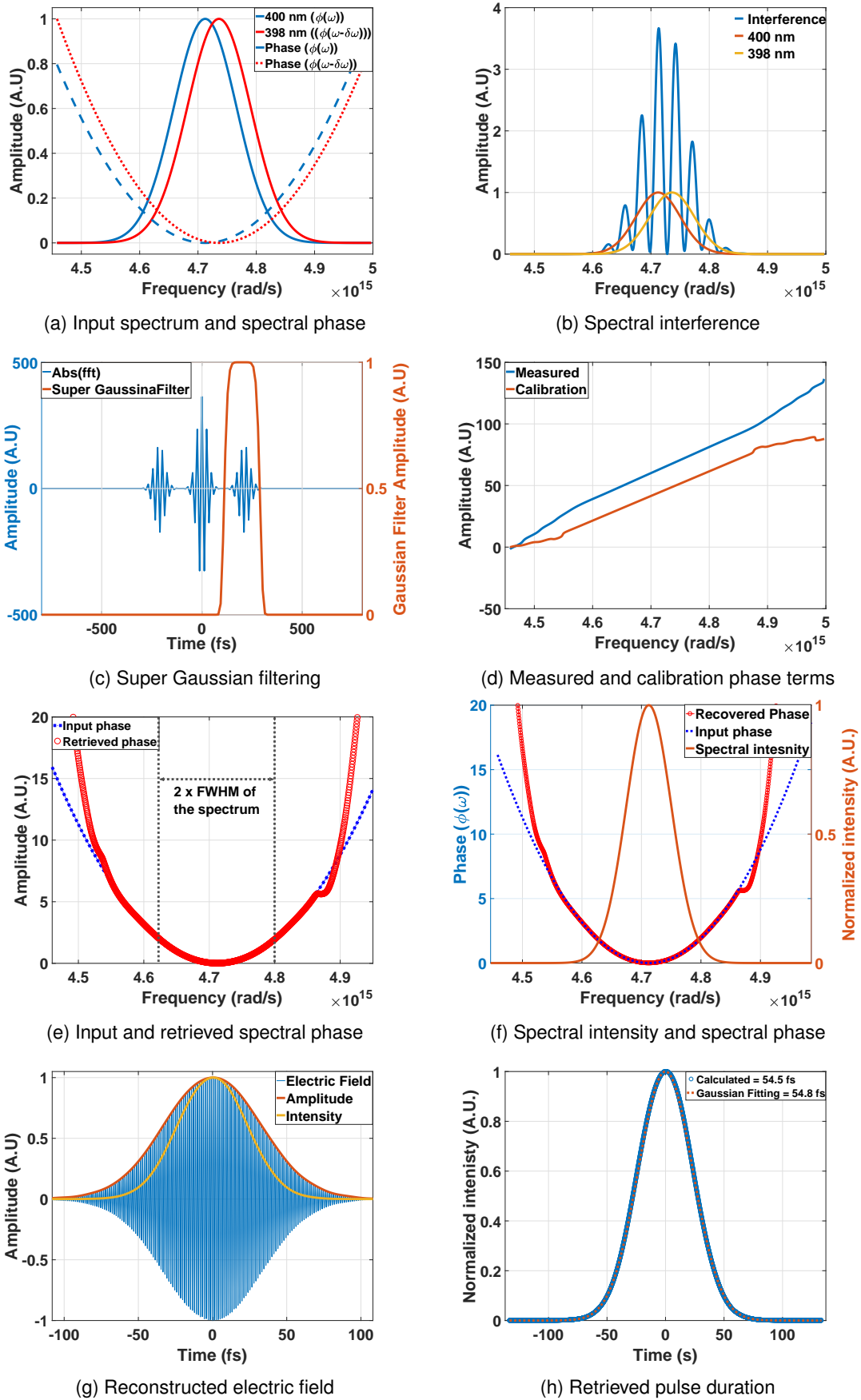


Figure 4.13: Results from the SPIDER algorithm for SH pulses.

The FWHM of the Gaussian fit gives a pulse duration of 54.8 fs which is in good agreement with the theoretically calculated pulse duration of 54.5 fs.

The SPIDER algorithm can be used for measuring the pulse duration of SH pulses using experimental setups similar to the one explained in section 4.2.1.3.

#### 4.2.2.2 SPIDER algorithm for XUV pulses

The SPIDER algorithm was used to test the experimental conditions possible for the XUV pulses generated by HHG in gases. The pulse duration was measured and the electric field was reconstructed for XUV pulses from the numerically simulated spectral interferogram using the SPIDER reconstruction algorithm based on the flow chart shown in figure 4.14. The input for the numerical simulation was a pulse with a central wavelength of 30.77 nm (13<sup>th</sup> harmonic of 400 nm) and its sheared replica with a central wavelength of 30.92 nm. Both pulse and sheared replica were assumed to have a bandwidth of 0.5 nm which corresponds to a FTL pulse duration of 2.8 fs and with a chirp (GDD) of 5 fs<sup>2</sup>, this pulse broadens to 5.71 fs. Figure 4.14a shows the spectrum and spectral phase of the input. Figure 4.14b shows spectral interference simulated for the given input with a temporal delay of 100 fs between them. The SPIDER reconstruction algorithm was used to reconstruct the electric field of the input pulse. The positive phase part of the FFT of the spectral interference was filtered using a super-Gaussian filter and it is shown in figure 4.14c and an inverse FFT was done to get the measured spectral phase. A calibration spectrogram was also simulated without a spectral shear between the pulse and its replica. The positive phase part from this was also filtered out in the same way as before and an inverse FFT was done to get the calibration phase. Both calibration phase and measured phase are plotted in figure 4.14d. Further, the difference between the two phase values was taken and integrated using trapezoidal integration method to retrieve the spectral phase of the pulse to be measured. The retrieved and input spectral phase is plotted in figure 4.14e. The input and retrieved spectral phase match quite well. Figure 4.14f shows the input and retrieved spectral phase plotted along with the input pulse spectrum. The FFT of the retrieved spectral phase with the input pulse spectrum gives the electric field of the pulse and it is plotted in figure 4.14g. The square of the electric field was taken to get the temporal intensity of the pulse and it was fitted with a Gaussian fit. The FWHM of the Gaussian fit was 5.7 fs and it matches well with the theoretically estimated pulse duration of 5.71 fs. The intensity profile of the pulse and the Gaussian fit are plotted in figure 4.14h.

In the experiment mostly two parameters can change with time, the shear between the pulses due to laser fluctuation and the delay between the pulses due to the vibration of optical table, chambers and laser stability. Thus considering the experimental scenario, the reconstruction capability of the SPIDER code was tested by adding random noise in delay and shear between the two pulses. The delay was modeled as a random noise with a mean of 100 fs (same as the earlier case) giving a standard deviation of 5 fs for 100 shots. The shear used was with a random noise giving a mean shear of 2 nm and a standard deviation of 0.1 nm for 100 shots. Figures 4.15a and 4.15b show the plot of simulated noise in delay and shear over hundred shots.

The SPIDER spectrogram was generated for 100 shots with the noise in delay and shear and all

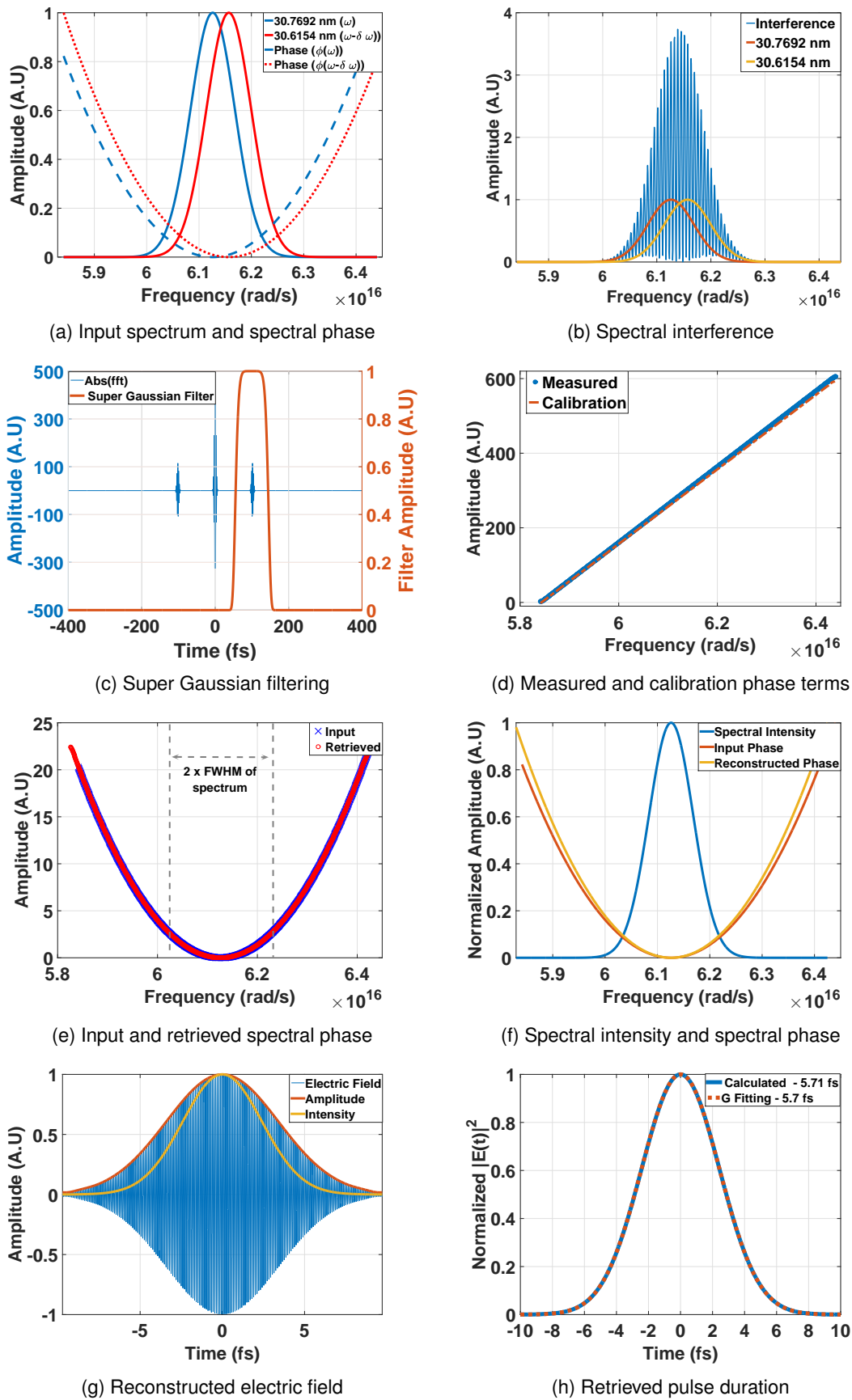


Figure 4.14: Results from the SPIDER algorithm for XUV pulses.

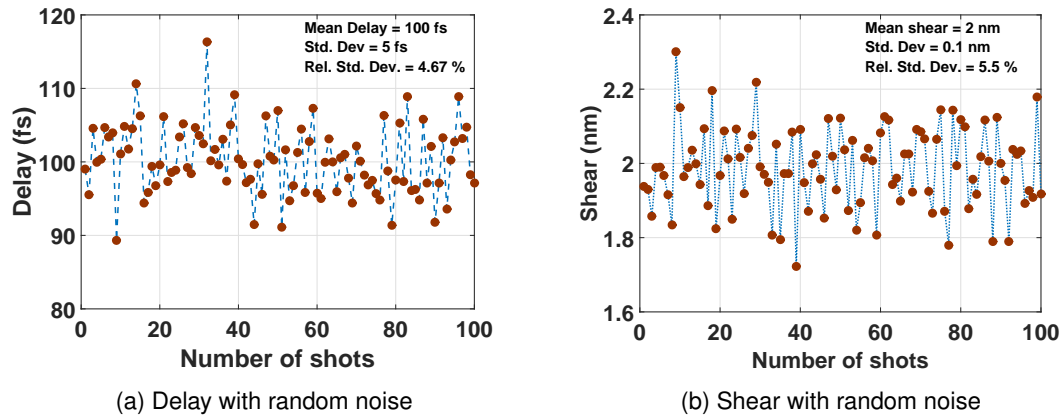


Figure 4.15: Delay and shear with noise for SPIDER.

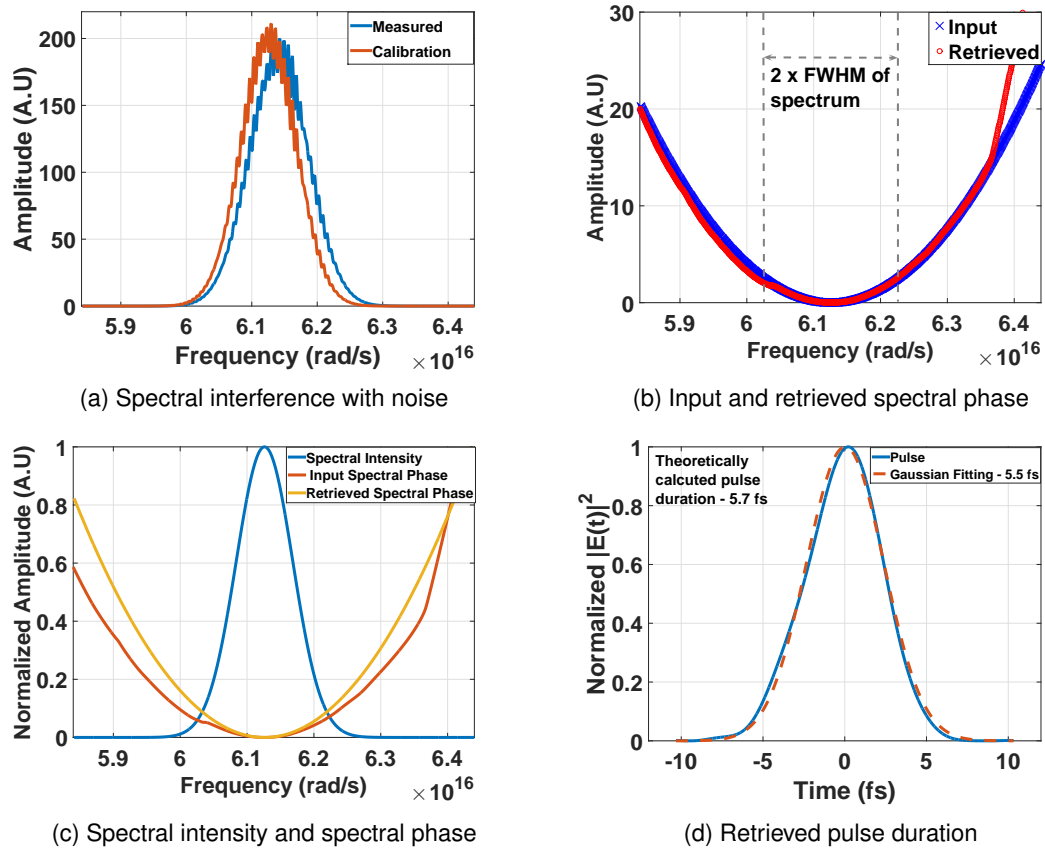


Figure 4.16: Results from SPIDER algorithm with noise added.

of them were added together to form a spectrogram with random noise. This was done also to test the effect of data integrated in time. Figure 4.16a shows the measured and calibration interferogram with noise. Using the phase retrieval algorithm developed, the spectral phase of the pulse was retrieved and it is plotted in figure 4.16a. The input and retrieved spectral phase match quite well in  $2 \times$  FWHM of the pulse spectrum and it is shown in figure 4.16b. Figure 4.16c shows the input and retrieved spectral phase plotted along with the input pulse spectrum. The temporal intensity of the pulse was reconstructed and fitted with a Gaussian fit to get the pulse duration. The FWHM of the Gaussian fit gives a pulse duration of 5.5 fs which is close to the theoretically calculated pulse duration of 5.71 fs. The pulse and the Gaussian fit are plotted in figure 4.16d. The algorithm developed is working well and is able to retrieve the pulse duration even under noisy conditions.

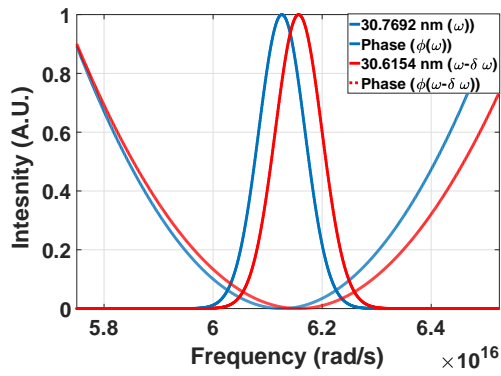
#### 4.2.2.3 SEA-SPIDER algorithm

The SPIDER algorithm was modified for SEA-SPIDER. The input used are exactly same as that of the SPIDER except instead of a temporal delay between the pulse and its spectrally sheared replica, a spatial separation of 1 mm was introduced to generate the 2-D spectrogram. This separation was used after checking the spectrogram produced and the possible spectral resolution required. The measured SEA-SPIDER spectrogram is shown in figure 4.17b. Figure 4.17c shows the calibration spectrogram without any spectral shear between the pulse and its replica. The fringes in the measured spectrogram and the calibration spectrogram have a difference in orientation. In the measured spectrogram, the fringes are tilted to one side, because of the second order phase added in the input. In this way, the SEA-SPIDER spectrogram will give a hint of the presence of any second-order phase in the pulse.

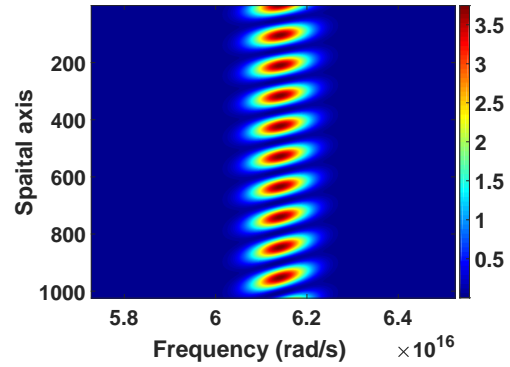
The SEA-SPIDER reconstruction is carried out by taking a 1-D FFT of the 2-D spectrogram along the spatial axis. After this, the positive part in the FFT was filtered and summed to phase part from the spectrogram. Using the same procedure the calibration phase term was also extracted from the calibration spectrogram. Both measured and calibration phase is plotted in figure 4.17e. After removing the calibration spectral phase from the measured one, it is integrated with trapezoidal integration method to retrieve the spectral phase of the input pulse. The input and measured spectral phase are plotted in figure 4.17f.

Although the input and retrieved spectral phase agree quite well, there is a small difference between them and it is plotted in figure 4.17g over  $2 \times$  FWHM of the pulse spectrum. Figure 4.17h shows the input and retrieved spectral phase plotted along with the spectral intensity of the pulse. Taking the FFT of the given spectral intensity of the pulse and retrieved spectral phase, the electric field of the pulse is reconstructed and it is plotted in figure 4.17i. The temporal intensity is calculated from the electric field and it is fitted with a Gaussian fit to get the pulse duration. The Gaussian fit gives a FWHM pulse duration of 5.7 fs and it is same as the theoretically calculated pulse duration of 5.7 fs considering the second order phase (same as in SPIDER) was added to the input pulse. The temporal intensity of the pulse and the Gaussian fit are plotted in figure 4.17j.

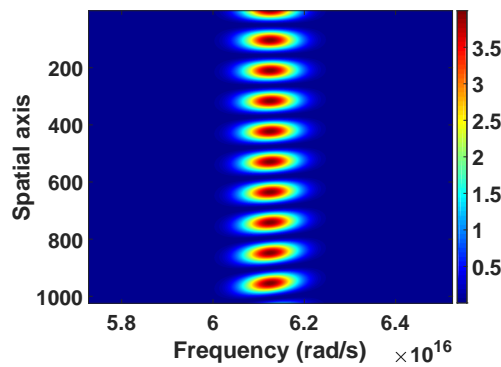
For a SEA-SPIDER experimental scenario in which the contrast of the spectrogram may be low due to noise, low signal, and signal integration. This was tested numerically. A noise with a Gaussian profile



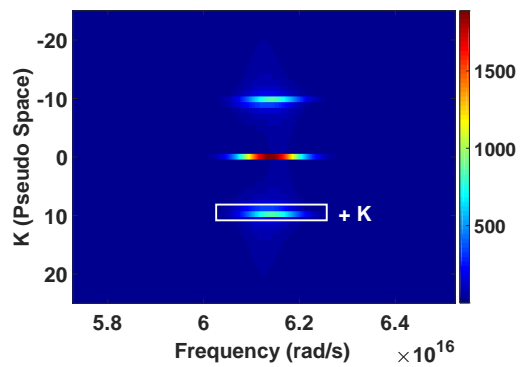
(a) Input spectrum and spectral phase



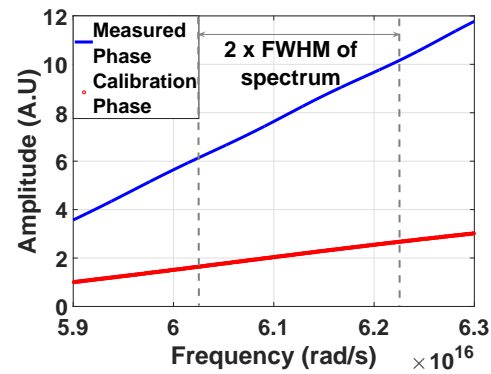
(b) 2D spectrogram



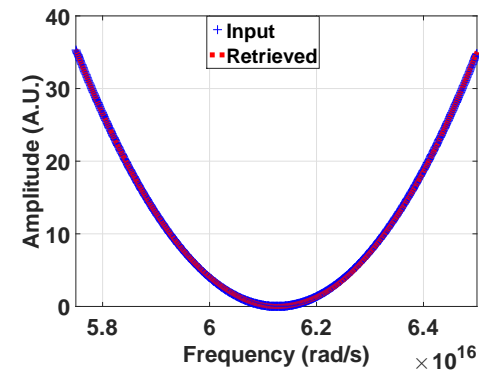
(c) Calibration spectrogram



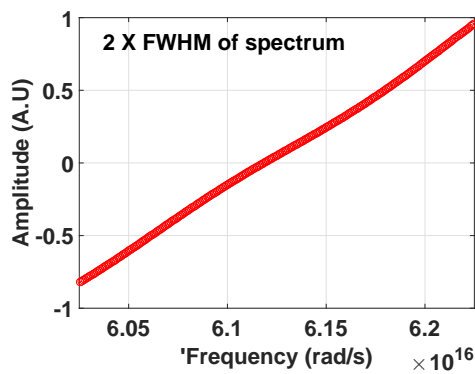
(d) FFT of Spectrogram



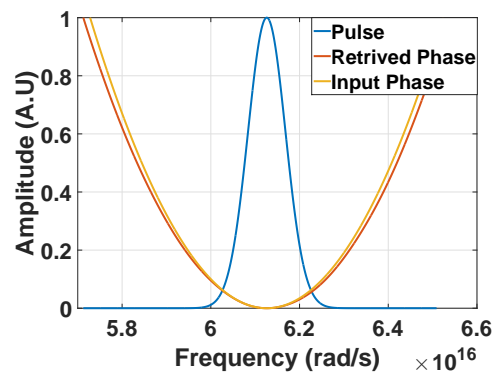
(e) Measured and calibration phase terms



(f) Input and retrieved spectral phase



(g) Difference of input and retrieved spectral phase



(h) Spectral intensity and spectral phase

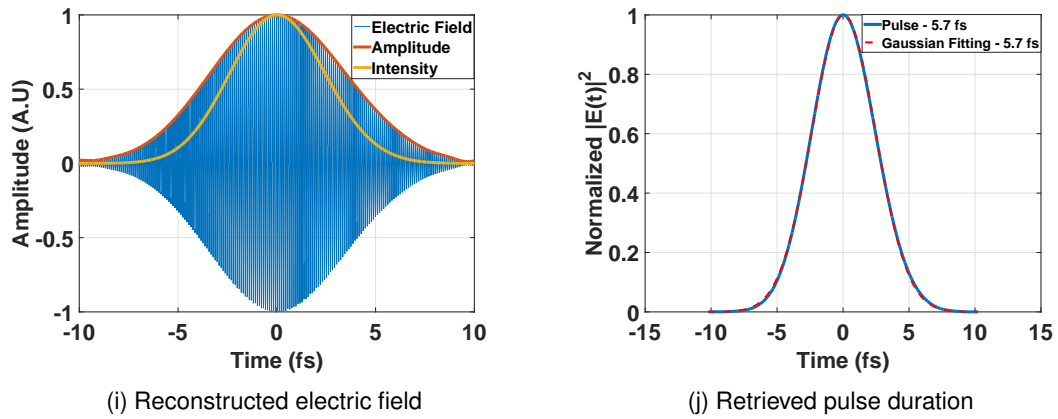


Figure 4.17: Results from the SEA-SPIDER algorithm.

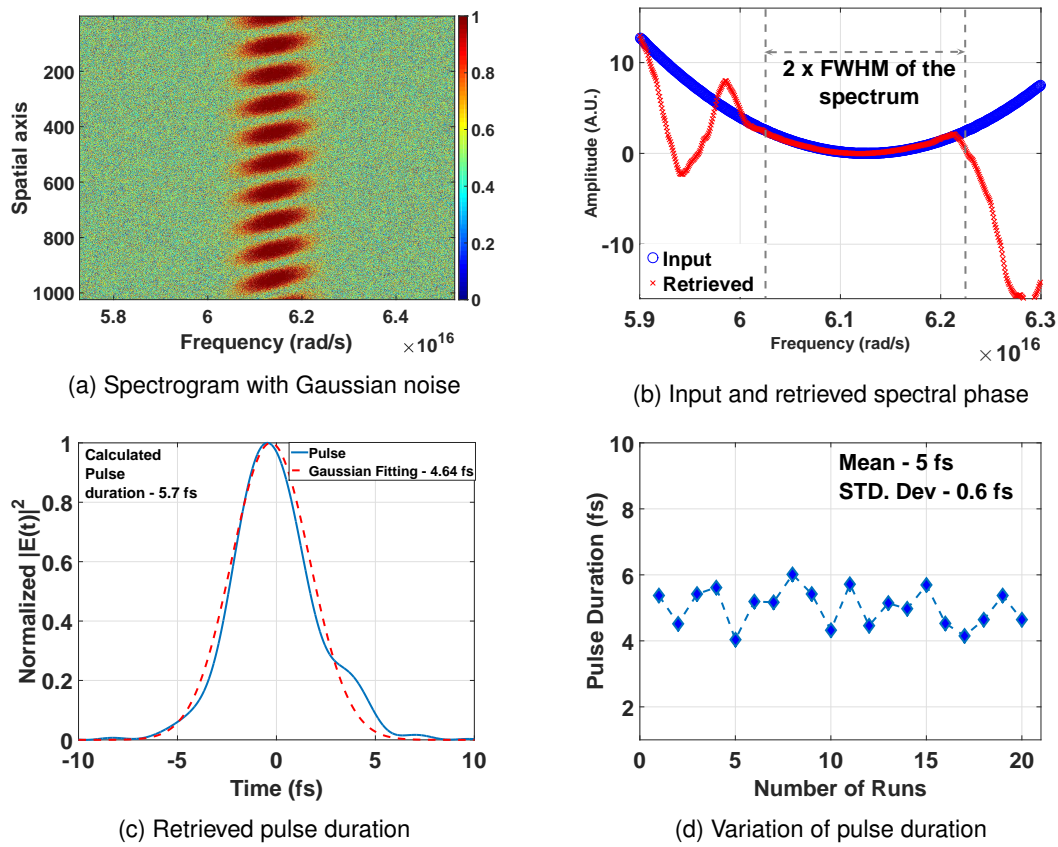


Figure 4.18: Results from the SEA-SPIDER algorithm with Gaussian noise.

having intensity 0.5 times the normalized intensity of the actual spectrogram at all the frequencies with a standard deviation of 0.05 is added to the actual spectrogram. It is plotted in figure 4.18a. The same was done for the calibration spectrogram. Using the reconstruction algorithm following the same methods as discussed above, the spectral phase was retrieved and it is plotted along with the input spectral phase in figure 4.18b. Over a range of  $2 \times$  FWHM of the input pulse spectrum, the input and retrieved spectral phase agree well. The pulse duration retrieved using this spectral phase is plotted in figure 4.18c. The Gaussian fit gives FWHM is 4.64 fs. The simulation was carried out with random noise for 20 times and the pulse duration obtained from the runs are plotted in figure 4.18d. From these simulations, the mean pulse duration obtained was 5 fs with a standard deviation of 0.6 fs. This corresponds to  $\sim 0.9$  times the FTL pulse duration of 5.7 fs. This shows that the algorithm is robust against noise and is able to retrieve the pulse duration.

#### 4.2.2.4 Generation of spectral shear

The creation of a spectrally sheared replica of pulses is crucial for the SEA-SPIDER experiment setup. As discussed already in the section 4.2.1.3, one of the possible ways of introducing spectral shear is by tuning phase matching angle for SHG. The amount of change in the phase matching angle to shift the central frequency of the SH is calculated in the following section.

From the simulations it can be seen that the spectral shear needed is  $\sim 2$  nm. In the experiment BBO crystals with a thickness of 200  $\mu\text{m}$ , cut for type - I phase matching at a central wavelength of 800 nm is used. BBO is a negative uniaxial nonlinear crystal, which means that the extraordinary refractive index ( $n_e$ ) is lower than the ordinary refractive index ( $n_o$ ). In a negative uniaxial crystal, the fundamental wave travels as an ordinary wave and the second harmonic wave travels as an extraordinary wave for birefringence of the material to compensate for dispersion [63]. The phase matching condition for a negative uniaxial crystal with type - I phase matching, the wave-vector mismatch ( $\Delta k$ ) should be zero and it is written as [63],

$$\Delta k = k_{2\omega} - 2k_{\omega} = 0 \quad (4.30)$$

where  $k_{2\omega}$  is the wave-vector for second harmonic beam and  $k_{\omega}$  is the wave-vector for the fundamental beam. For phase matching with angular tuning, i.e, controlling the orientation of the crystal with respect to the propagation direction of the incident beam, the phase matching condition can be written as [63],

$$\Delta k = k_{2\omega} - 2k_{\omega} = \frac{4\pi}{\lambda}(n_{e,2\omega}(\theta) - n_{o,\omega}) \quad (4.31)$$

where  $\theta$  is the angle between the propagation vector and the angle of the crystal,  $n_{e,2\omega}(\theta)$  is the angle-dependent extraordinary refractive index of the second harmonic beam and  $n_{o,\omega}$  is the ordinary refractive index of the fundamental beam. Here the subscripts,  $o$  and  $e$  are used to represent ordinary and extraordinary beams respectively.  $\theta$  is the phase matching angle. The value of  $n_{e,2\omega}(\theta)$  can be obtained from the dispersion relation for SHG and is given by [63],

$$\frac{\sin^2 \theta}{n_{e,2\omega}(\theta)} + \frac{\cos^2 \theta}{n_{o,2\omega}} = \frac{1}{n_{o,\omega}} \quad (4.32)$$

where  $n_{o,2\omega}$  is the ordinary refractive index of the second harmonic beam. The second harmonic intensity for type-I phase matching in BBO nonlinear crystal is given by [63]

$$I_{2\omega}(L, \theta) = \frac{2 \omega^2 d_{eff}^2 L^2}{n_{e,2\omega}(\theta) n_{o,\omega}^2 c^2 \epsilon_0} \left[ \frac{\sin\left(\frac{\Delta k L}{2}\right)}{\frac{\Delta k L}{2}} \right]^2 I_{\omega}^2 \quad (4.33)$$

where  $L$  is the length of the nonlinear medium (here the thickness of the BBO crystal),  $d_{eff}$  is the effective nonlinear susceptibility of the nonlinear medium,  $c$  is the speed of light and  $\epsilon_0$  is the vacuum permittivity.

The phase matching angle for SHG of a fundamental laser with a central wavelength of 800 nm can be calculated using equation 4.33 and it is at  $29.02^\circ$  for type-I phase matching in BBO. The spectral shear required in the second harmonic central wavelength for the SEA-SPIDER as per simulations is 2 nm. Numerical calculation was done using equation 4.33 to calculate the phase matching angle required to shift the central frequency of second harmonic by 2 nm for a Ti:Sa laser with central wavelength of 800 nm and pulse duration of 33 fs and the results are plotted in figure 4.19. From figure 4.19 we can see that the central frequency of second harmonic can be shifted to 398 nm and 402 nm from 400 nm by changing  $\theta$  to  $29.4^\circ$  and  $28.63^\circ$  respectively. Here we can also see that the detuning of phase matching angle for spectrally shifting the central wavelength also leads to decrease in second harmonic intensity compared to the best phase matched case (for  $\theta = 29.02^\circ$ ).

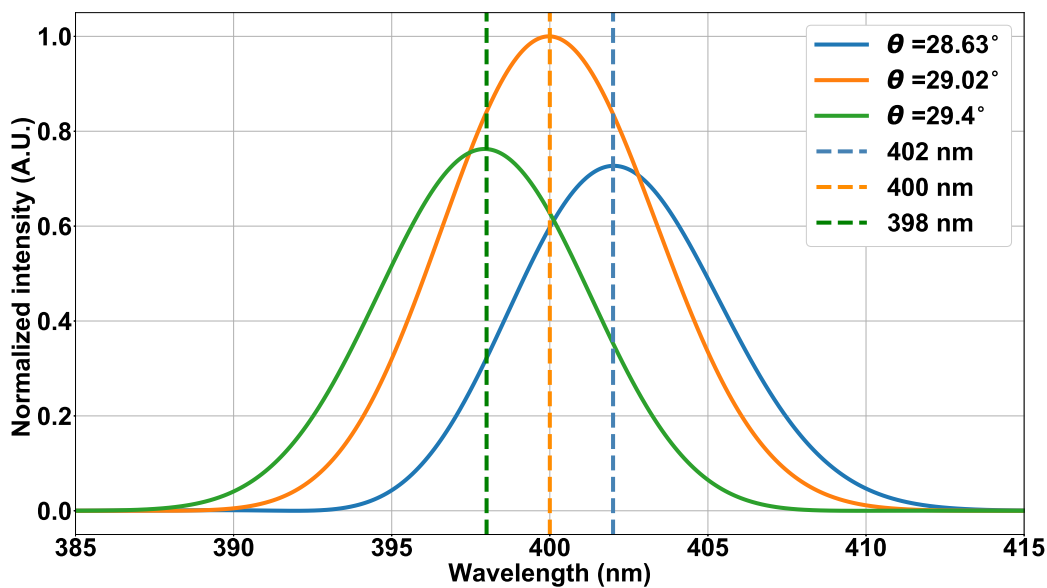


Figure 4.19: The SH intensity at different  $\theta$  are normalized to the SH intensity at  $\theta = 29.02^\circ$ . The dotted lines shows the central wavelength of the SH intensity spectrum at different  $\theta$ .

### 4.2.3 Experimental progress for SEA-SPIDER

Different experimental setups were tested for realizing a SEA-SPIDER in the XUV. HHG from gases was used as the XUV source. Tuning SHG was used as the method to generate shear between HH pulses that is being created from SH pulses [179]. The motivation behind all the SEA-SPIDER experimental setups were to have a setup, which is non-invasive to other experiments. The experimental setups were



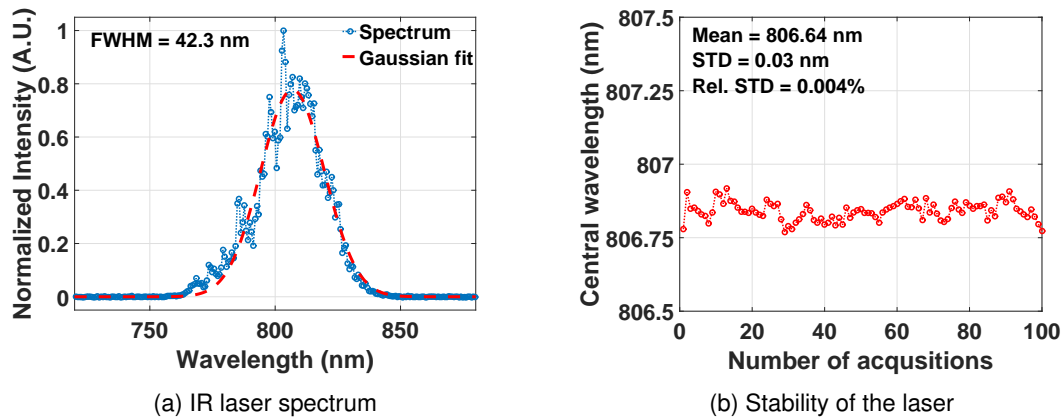


Figure 4.21: Spectrum and spectral stability of the IR laser measured before the BBO.

low due to low BBO efficiency coupled with multiple focal spots due to the presence of focused IR and SH beams. The energy before the beam splitter in IR was nearly 2 mJ and after the dichroic mirrors, the energy was less than 0.15 mJ in each beamline. With this energy per pulse and assuming  $\sim 100 \mu\text{m}$  diameter focal spot at the gas cell, the peak intensity at the focal spot is  $< 10^{14} \text{ W/cm}^2$  which is at the limit for generating HH in argon and xenon.

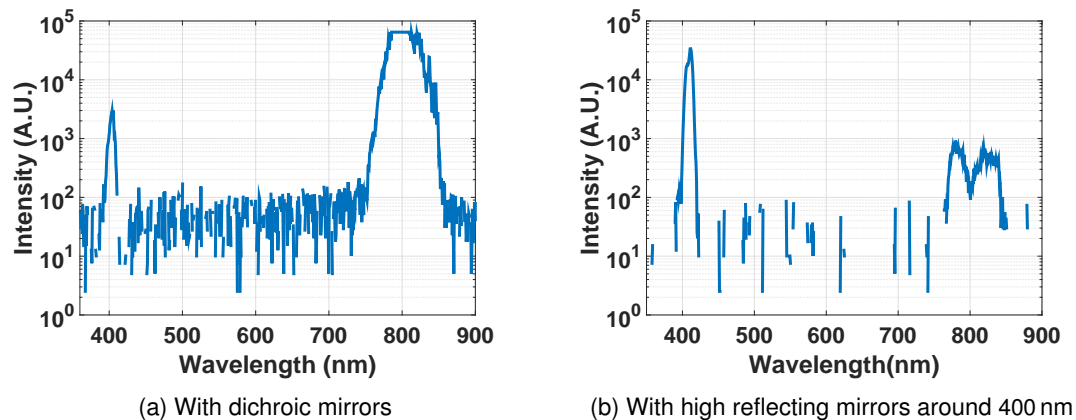


Figure 4.22: Spectrum showing the contrast in intensity between IR and SH using dichroic mirrors and high reflecting laser line mirrors.

The experimental setup was modified using a lens with a shorter focal length of 500 mm to decrease the focal spot size, which in turn increases the peak intensity. The dichroic mirrors were replaced with high reflecting mirrors at SH wavelength to increase the contrast between IR and SH. The thickness of the BBOs used was increased to  $500 \mu\text{m}$  for higher SH conversion efficiency and further moved the experimental setup in-vacuum. The in-vacuum setup was to reduce the effect of the focused beam on the vacuum window and also to contain the stray reflections of the IR and SH. Figure 4.23 shows a picture of the experimental setup in-vacuum. One of the high reflecting SH mirror in the fixed beamline was motorized in tip/tilt for adjusting the pointing of the HH beam in-vacuum. Further, the spectra of the SH in the in-vacuum setup was measured. Figure 4.22b shows the intensity contrast between the IR and SH spectrum. Here the SH intensity is 2 orders of magnitude higher than that of IR laser beam. After the use of two highly reflecting mirrors at the SH wavelength, the IR was successfully filtered. The SH was

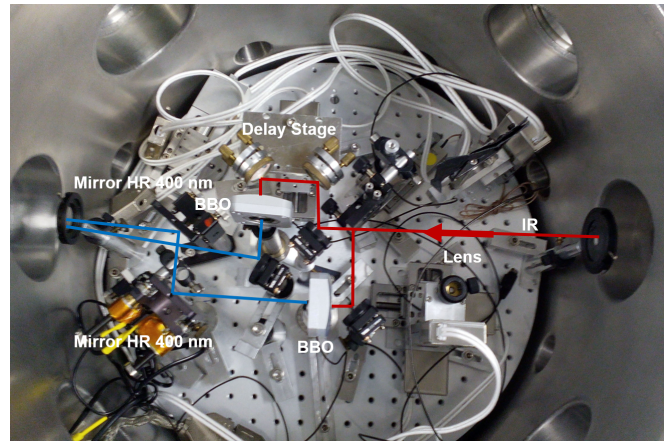


Figure 4.23: Experimental setup for generating spectrally sheared HH sources at Salle Corail, LOA

optimized in intensity and with a thicker crystal, the efficiency increased to  $> 20\%$ . The SH spectrum and spectral stability were measured after the high reflecting mirrors. Figure 4.24a shows the SH spectrum with a central wavelength of 404.12 nm and FWHM of 8 nm. Figure 4.24b shows the spectral stability with a standard deviation of central wavelength in the order of 0.01 nm over 100 acquisitions. The spectrometer used was having a resolution of 0.14 nm and the standard deviation value obtained is statistical. It also shows the laser and SH spectrum are quite stable.

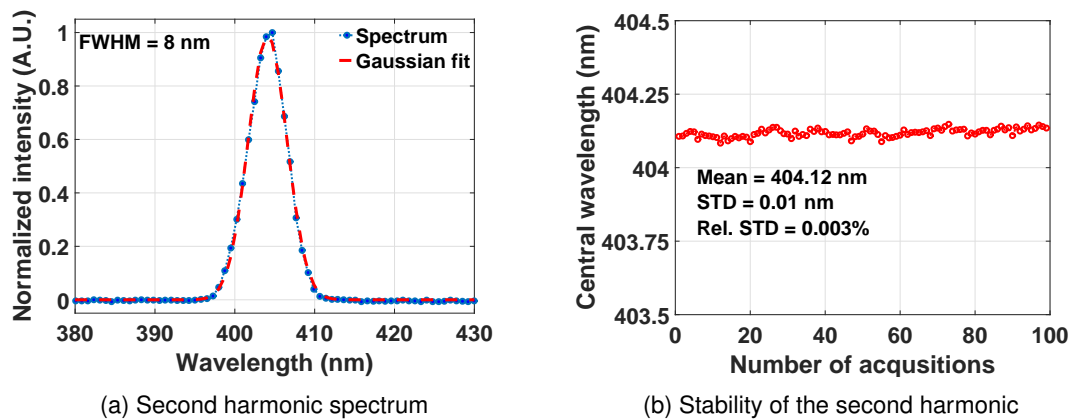


Figure 4.24: Spectrum and spectral stability of the second harmonic measured after BBO.

HHG was tested with the in-vacuum configuration and no XUV photons were detected by the CCD. One of the reasons for this may be the stretching of the laser pulse duration due to GDD and TOD introduced by the dielectric coating of the IR beam splitter. The IR beam splitter is 8 mm thick and made of BK7 anti-reflection coating for near IR spectral region. This was tested by changing the intensity beam splitter with wavefront beam splitter. A rectangular metallic mirror was used as the wavefront beam splitter and the beam was split with the upper part going through the delay line and lower part reflected to the fixed beamline. At first, the HHG in argon was tested with the reflected beamline. Figure 4.25a shows the footprint of HH recorded by the PI-MTE X-ray CCD in the experimental chamber. Further, the HHG from the two beamlines was tested with the wavefront splitting geometry. Figure 4.25b shows the HHG with two SH beams. However, it was not possible to move the two XUV beams close enough to overlap. The

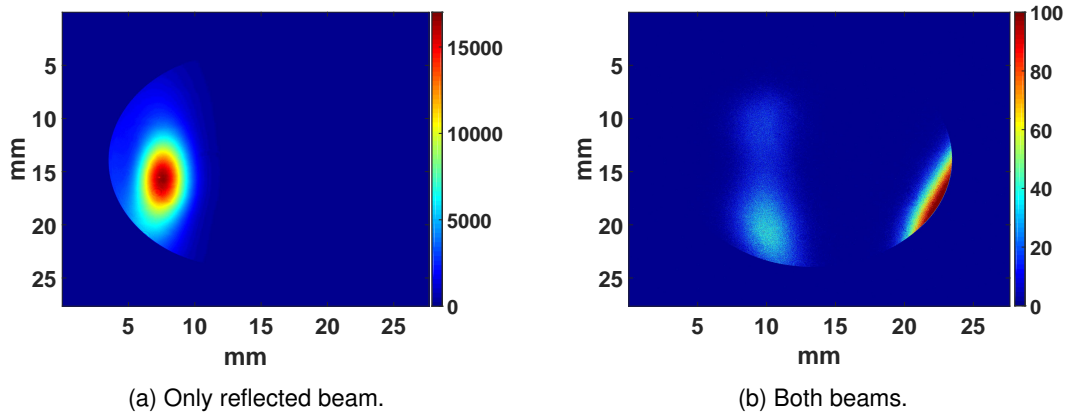


Figure 4.25: Footprint of HHG with wavefront splitting configuration of the tested SEA-SPIDER experimental setup.

20 mm diameter Al filter used before the CCD to block the IR clipped most part of the XUV beam from the delay line. In presence of the XUV beam from the delay line the intensity of the XUV beam from the fixed line was also low. This might be due to refraction of XUV beams by the gas in presence of two SH beams.

The HHG with two SH pulses was optimized in a way to see the two HH pulses on the CCD, however, no overlap was observed. This might be due to the design of experimental setup, which was too tight to make movements and it was difficult to get a spatial separation of 1 mm between the two HH beams at the source generation position using the tested geometries. Also, the energy of the laser was a limiting factor when splitting the beam into two.

#### 4.2.3.2 Experimental setup tested at VOXEL Lab, IST

The SEA-SPIDER experiment at VOXEL lab in IST was designed for nearly collinear propagation for the two SH pulses. Figure 4.26 shows the schematic of the implemented SEA-SPIDER experimental setup at the VOXEL lab, IST.

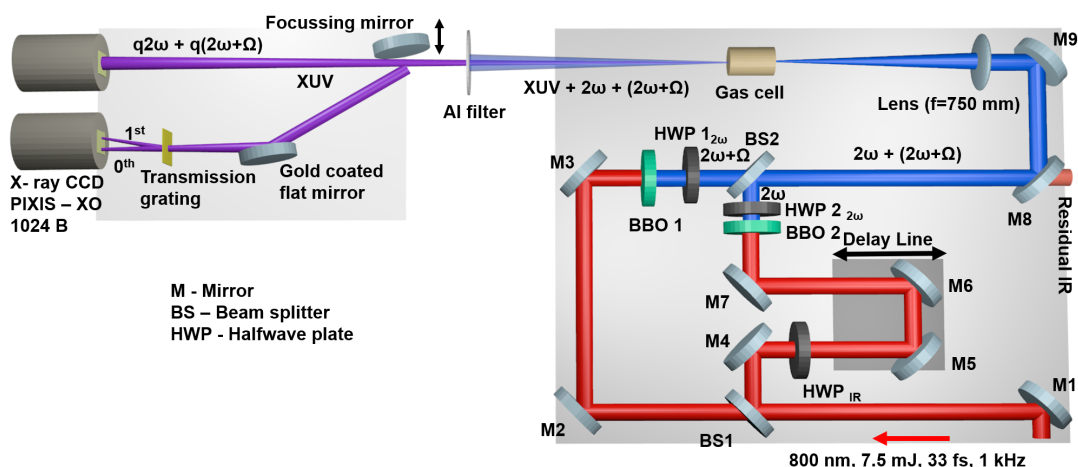


Figure 4.26: Schematic of the SEA-SPIDER experimental setup at VOXEL Lab, IST.

The experimental setup uses two identical BBOs with a thickness of 200  $\mu\text{m}$  and an aperture of 10 mm. The IR laser at the VOXEL lab (2.2.2.3) is split into two replicas (delay beamline and fixed

beamline) in intensity with a non-polarizing 50 : 50 beam splitter, BS1. The transmitted IR laser in the fixed beamline is steered onto BBO 1 using mirrors M2 and M3 which are broadband dielectric mirrors coated for high reflectivity at a central wavelength around 800 nm. After the BBO 1, a half wave plate (HWP  $1_{2\omega}$ ) is used to optimize the polarization of the SH pulses generated. The IR laser reflected from the IR beam splitter, BS1 goes to the delay beamline and it passes through an IR HWP and then through a delay stage followed by the BBO 2 and HWP  $2_{2\omega}$ . HWP  $2_{2\omega}$  has anti-reflection coating for the SH. All high reflectivity coatings for the mirrors in the IR are centered around 800 nm and the SH mirrors are centered around 400 nm. The split beams from the delay beamline and fixed beamline are recombined with the beam splitter BS2. The two SH beams after this beam splitter are aligned co-linearly and steered onto the lens using two highly reflecting dielectric mirrors for the SH, M8 and M9. A lens of focal length of 750 mm is used to focus the two SH beam onto the gas cell of length 15 mm. Figure 4.27 shows a

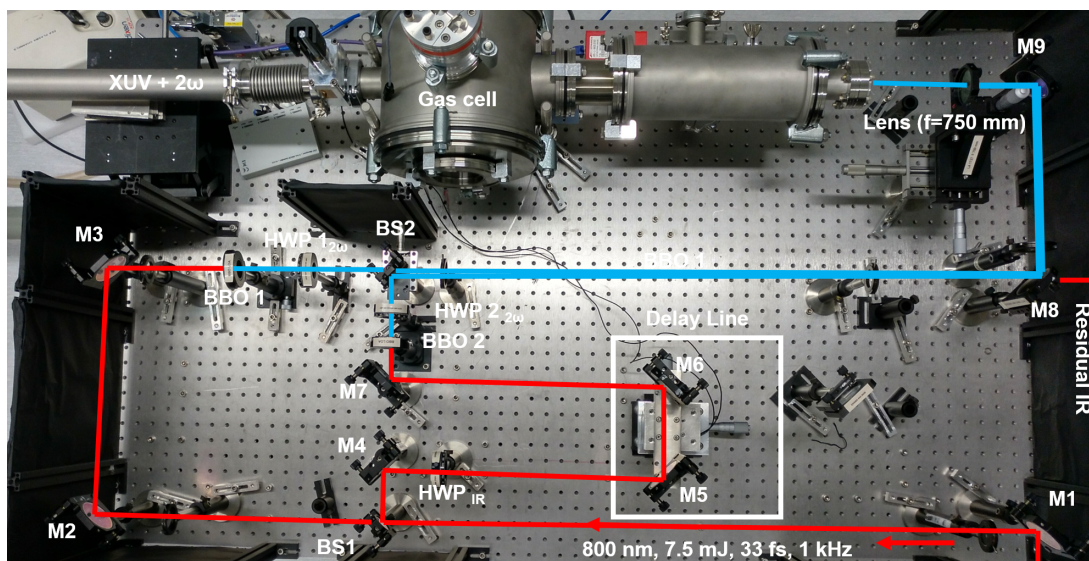


Figure 4.27: Experimental setup for generating the SH and its spectrally sheared replica at the VOXEL lab, IST

picture of the experimental setup for generating the SH and its spectrally sheared replica. After the gas cell, the XUV generated is filtered from the SH using an Al filter of thickness 150 nm. The filtered XUV is optimized by looking at the footprint using an XUV sensitive CCD. After optimization, the HH spectrum is measured using an XUV spectrometer. The XUV spectrometer consists of a focusing mirror (ROC -10 m) at a grazing incidence of  $10^\circ$  followed by a gold-coated flat mirror at a grazing incidence of  $10^\circ$ , a transmission grating (1000 lines/ mm) and an X-ray CCD. The focusing mirror can be moved in and out allowing the observation of the direct footprint of the two XUV pulses generated.

The IR laser spectrum and stability in spectrum was measured using an Ocean Optics HR 2000+ spectrometer, which has a spectral resolution of 1.4 nm. Figure 4.28a shows the IR spectrum of the laser with a FWHM of 43.6 nm at a central wavelength of 799.9 nm. The stability of the spectrum is plotted in figure 4.28b and the laser central wavelength has standard deviation of 0.032 nm over the measured 100 acquisitions. The standard deviation calculated statistically is an order lower than the resolution of the spectrometer.

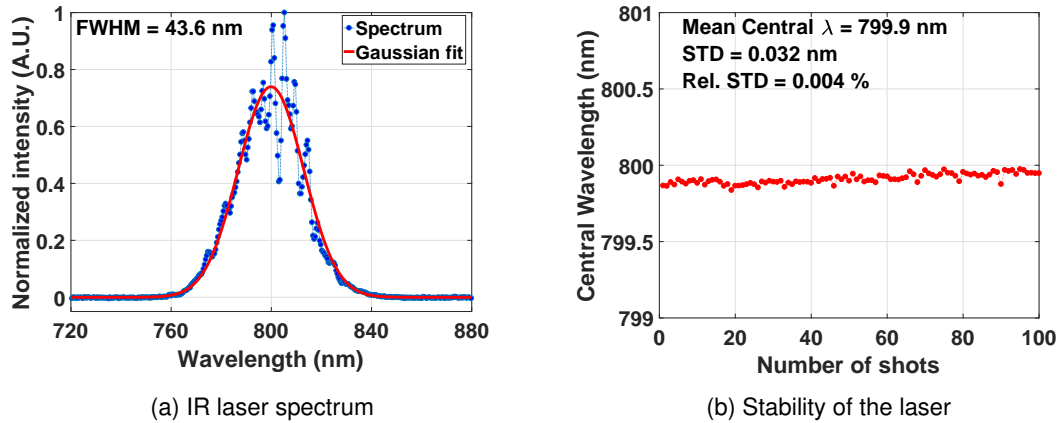


Figure 4.28: Spectrum and stability of the IR laser measured before BBO.

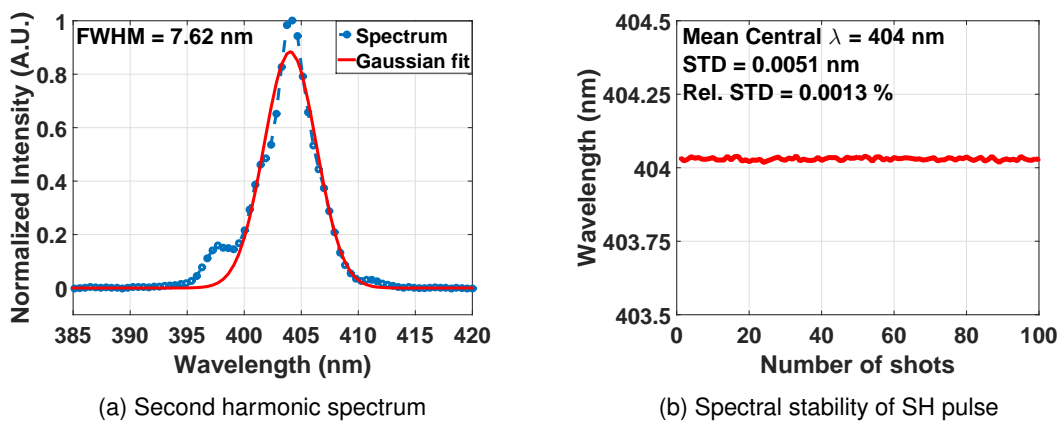


Figure 4.29: Spectrum and stability of the second harmonic measured after BBO.

First the SH with 200  $\mu\text{m}$  thick BBO was optimized with an efficiency of  $\sim 20\%$ . The optimized spectrum of the SH is shown in figure 4.29a and it has a bandwidth of 7.62 nm with a central wavelength of 404 nm. The spectral stability of SH is plotted in figure 4.29b.

Further the detuning of the BBOs phase matching angle to generate the spectrally sheared SH was characterized. The figure 4.30a shows the variation of the central wavelength of the SH with respect to the tuning of phase matching angle.  $0^\circ$  is the experimentally optimized phase matching angle for maximum SH conversion efficiency. A phase matching angle change of  $> 1^\circ$  was required to spectrally shift the central wavelength of SH from the optimum phase matched position of  $\sim 404$  nm to  $\sim 403$  nm. This change required in the phase matching angle is higher compared to the calculated values shown in figure 4.19. Also, the intensity of the SH reduces with the detuning of the phase matching angle. Figure 4.30b shows the variation of intensity with respect to the tuning of phase matching angle.

After optimization of SHG, the experimental setup was aligned as shown in figure 4.26 without the gas cell and XUV spectrometer. The SH beams were focused and the diverging beams were detected using the XUV sensitive CCD at the end of the experimental chamber. The SH beams were separated in height by adjusting the BS2 in the experimental setup and it resulted in generation of spatial interference pattern. The separation was  $\sim 1$  mm at the focal spot between the SH beams before the adjustment. With this source separation and a source to detector (here the screen) distance of 3.36 m, the interference

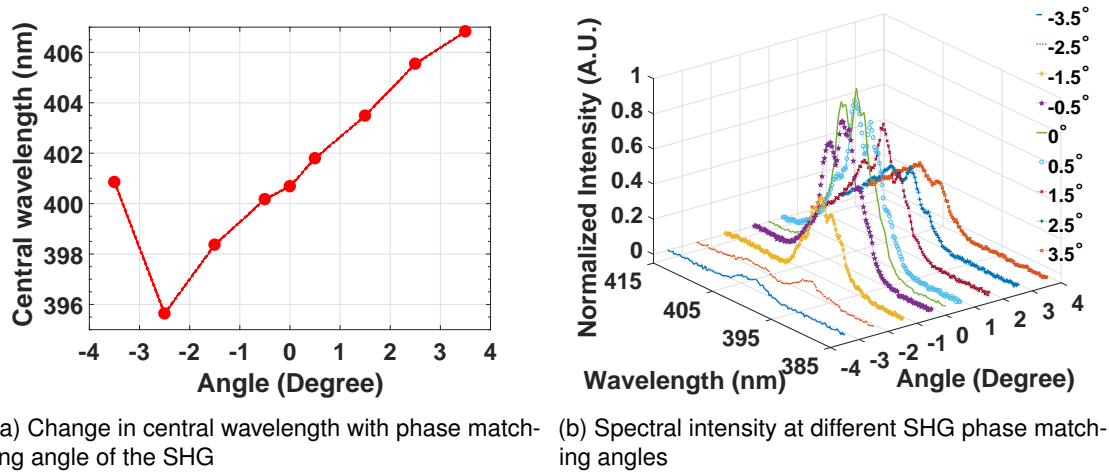


Figure 4.30: Experimentally measured SH spectrum of the phase matching angle scan for SHG in a BBO crystal.

fringe separation for the SH wavelength of 400 nm can be calculated theoretically using the equation [12],

$$\Delta x = \frac{\lambda L}{d} \quad (4.34)$$

where  $\lambda$  is the wavelength of the incident beam,  $L$  is the distance between the source and detector and  $d$  is the separation between the two source position. The fringe separation hence calculated is 1.34 mm. Figures 4.31a and 4.31b show the interference pattern and its line-out along the horizontal direction, of the recorded spatial interference, respectively. The interference pattern was recorded using the XUV

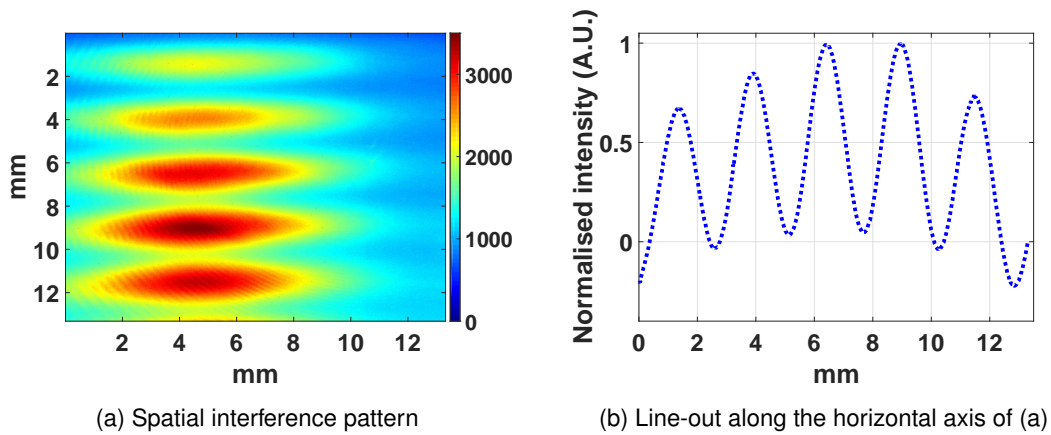


Figure 4.31: Spatial interference obtained between SH and its spectrally sheared replica.

sensitive CCD. From the recorded image, the fringe separation was calculated as 2.5 mm. The longer fringe separation observed in the SH corresponds to shorter source separation. The change in source separation to a lower value might be due the final adjustments made to generate the spectral interference. Using the equation 4.34, the source separation for the experimentally observed fringe separation is calculated as  $\sim 0.54$  mm. The generation of the interference pattern with good contrast confirms that the two SH pulses are at zero delay. These SH pulses were used to generate the HHs.

HHs were generated in argon at 15 mbar using the SH pulses from the delay beamline and the

fixed beamline with a separation of 0.54 mm between the two sources in a gas cell of length 15 mm. The footprint of the HHs generated were recorded using an XUV sensitive CCD. The footprint of HH pulses from the delay beamline and fixed beamline are shown in figure 4.32a and 4.32b, respectively. Both beam were optimized at the same generation conditions and the images obtained were acquired over 400 ms.

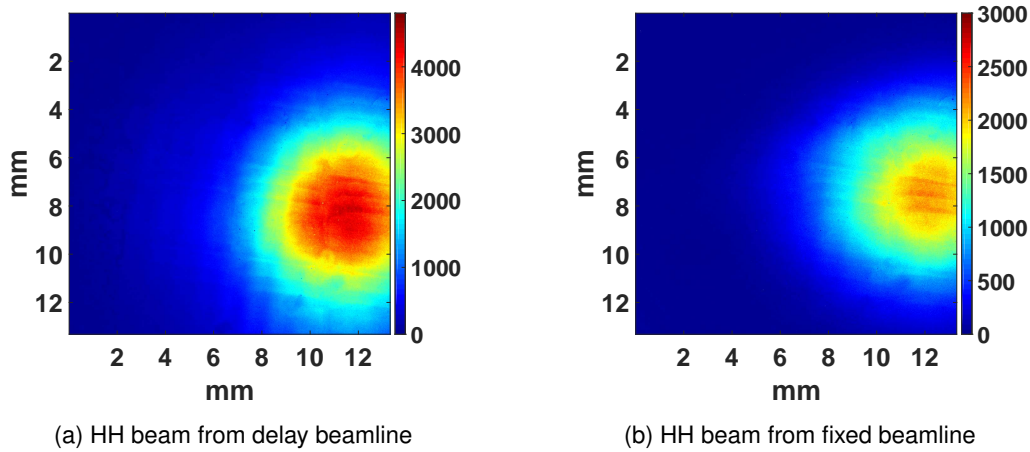


Figure 4.32: Footprint of HH beams from the two beamlines.

The next step of the experiment is to observe the interference between the two spectrally sheared XUV beams and further measure the SEA-SPIDER signal. This requires measurement and optimization of spectral shear between the two HH pulses. Further experiments are required to optimize the HHG, measure the XUV spectrum of the pulse and its replica, and measure the spectral interference to finally retrieve the pulse duration of XUV pulses from HHG.

#### 4.2.3.3 Experimental realization of SPIDER for SH pulses

The temporal characterization of pulses in the blue-violet region of the electromagnetic spectrum using methods such as autocorrelation is challenging since there are no nonlinear crystals with enough phase matching bandwidth for this spectral region [184]. There are methods like FROG [143], non-collinear autocorrelation using two-photon absorption in GaN photo-diodes [185] and cross-correlation methods [184] available for blue-violet pulse characterization. However, among the above mentioned methods only FROG can measure the spectral phase of the pulses and, it relies on iterative algorithms and requires multiple shots. Here we introduce a SPIDER for the blue-violet region of the electromagnetic spectrum. The spectral phase and pulse duration can be retrieved using the SPIDER algorithm without iterative processes. Also, it can work in single shot operation.

The configuration of the experimental setup for SEA-SPIDER is shown in figure 4.26 was modified to a SPIDER experimental setup for SH pulses. This was done by changing the spatial separation to a temporal delay and using a spectrometer for the visible spectral region to measure the spectral interference of the SH pulses. The SPIDER algorithm discussed in section 4.2.2.1 was used to retrieve the SH pulse duration.

In the experimental setup, shown in figure 4.26, the SH and spectrally sheared replica were generated. Figure 4.33a shows the spectrum of the pulse and its replica without any spectral shear

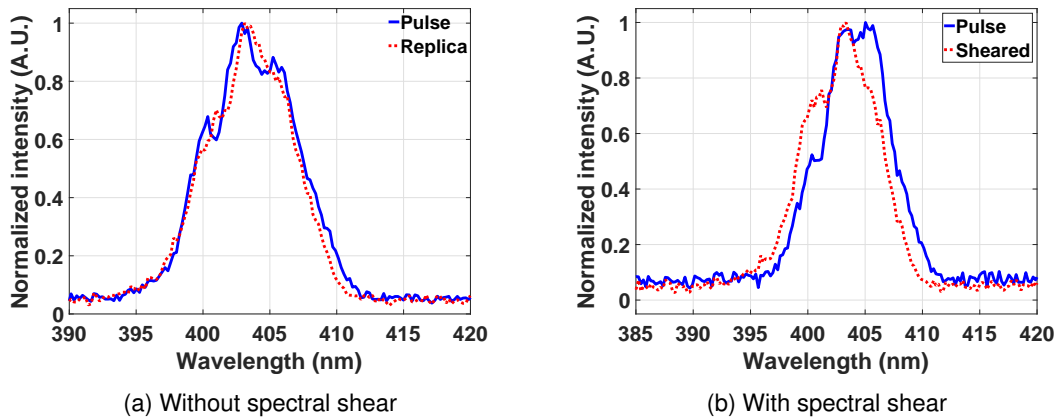


Figure 4.33: Spectrum of the SH pulse and its replica.

between them. The pulse from the delay line in the experimental setup is considered as the main pulse and the one from the fixed line is considered as the replica. The spectrometer used is USB4000 from Ocean optics with an estimated spectral resolution of 1.1 nm. However, the measurements using this spectrometer give  $\sim 4$  points per nm. The central wavelength and the FWHM is calculated from these measurements. The pulse and replica have a central wavelength of  $\sim 403.8 \pm 1.1$  nm and a FWHM of  $\sim 7.5 \pm 1.1$  nm. From the FWHM, the FTL pulse duration of the SH pulse can be estimated as  $\sim 32 \pm 5$  fs. The spectrum of the replica of the pulse was spectrally shifted by  $\sim 1$  nm by detuning the phase matching angle of the BBO. Figure 4.33b shows the spectrum of the pulse and its replica with a spectral shear of  $\sim 1$  nm.

The spectral interference between the pulse and the replica was recorded without the spectral shear between them for calibrating the delay and measuring the calibration phase. Further, the spectral interference is recorded between the pulse and replica with a spectral shear. Figure 4.34a shows the spectral interference recorded. The FT of the spectral interference is shown in figure 4.34b and frequencies at  $\sim 170$  fs and  $\sim 300$  can be seen. The delay between the pulses was estimated comparing the interference peaks to numerically simulated spectral interference with delays of 170 fs and 300 fs. In comparison, the delay was estimated to be  $\sim 170$  fs. The frequencies at  $\sim 300$  fs is may be due to scattering of the pulses inside the spectrometer since the size of the beam was larger than the entrance of the spectrometer. Figure 4.34c shows the phase part of the sheared and calibration spectral interference. The spectral phase retrieved using the SPIDER algorithm is plotted in figure 4.34d along with the spectral intensity. The spectral phase and the spectral intensity are used to reconstruct the electric field of the pulse and the temporal intensity and are shown in figure 4.34e and figure 4.34f respectively. The Gaussian fitting of the temporal intensity of the pulse gives a FWHM pulse duration of  $\sim 39 \pm 5$  fs.

The measured pulse duration of the SH pulses is  $\sim 1.2$  times the FTL pulse duration. However, the SH pulse and its replica travel in different paths in the experimental setup, i.e, the pulse is reflected by a beam-splitter with multilayer mirror coating for wavelength around 400 nm and the replica is transmitted through the same beam splitter. This might affect the pulse duration of the SH pulses. Further careful analysis of the optics used and, the separate characterization of SH pulses from delay line and the fixed

line using other methods of pulse characterization in this spectral region [184, 143, 185] is required to verify whether the measured pulse duration is the real pulse duration.

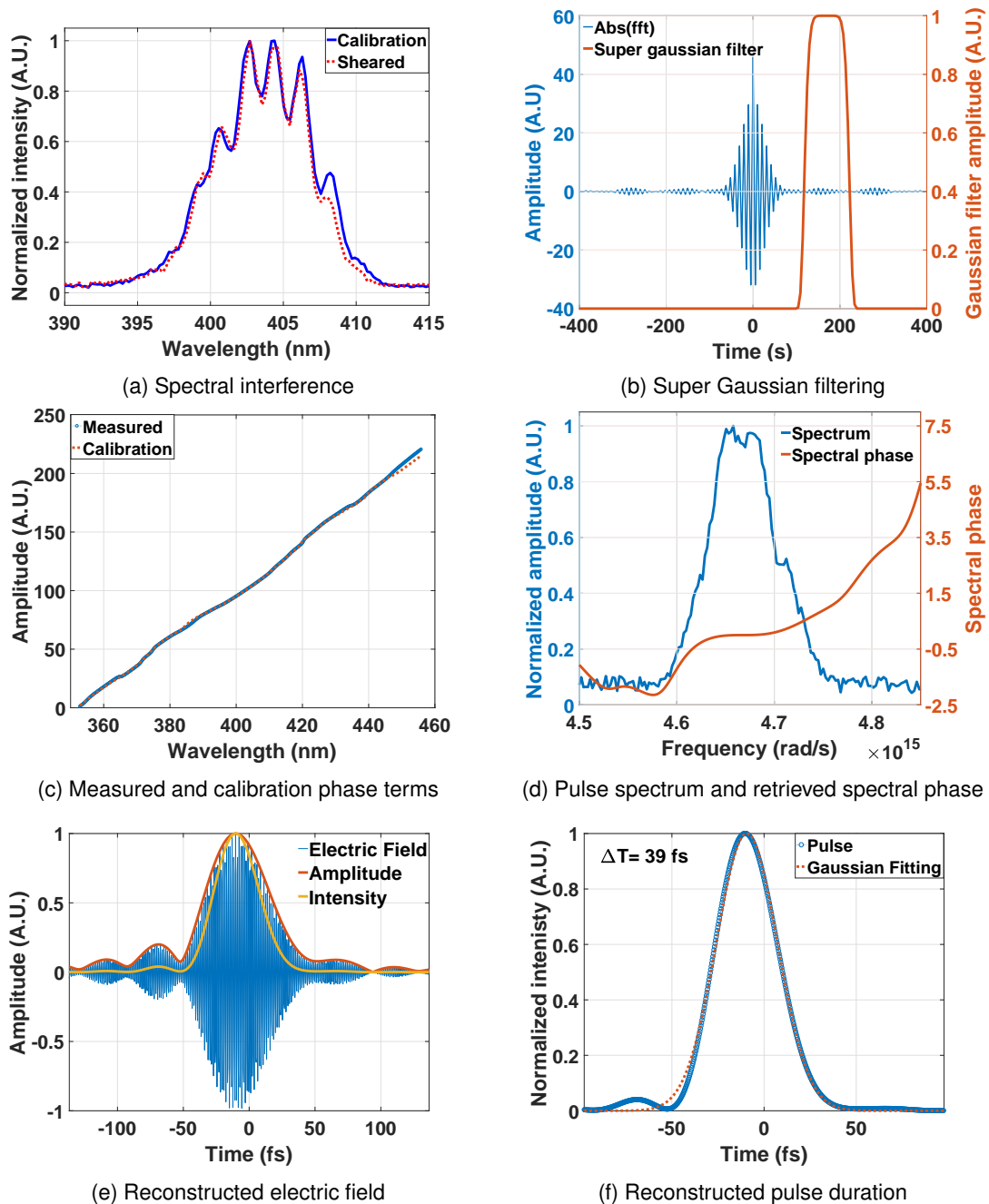


Figure 4.34: Reconstruction of the electric field of SH pulses using the SPIDER algorithm.

#### 4.2.3.4 Modification and improvements required for experimental realization of a SEA-SPIDER for XUV pulses from HHG at VOXEL lab, IST

The SEA-SPIDER experimental setup for XUV pulses from HHG was designed for HH beamlines at Salle Corail, LOA and VOXEL lab, IST. The experiment at LOA was not completely successful. However, the results from experiments at LOA helped to understand the necessity for nearly collinear geometry for the pulse and its spectrally sheared replica. Further, the experiment was carried out at the VOXEL lab,

IST. The SHG and phase matching was tested. Also, a SPIDER measurement for SH pulses was carried out. However, experiment on optimizing HHG using SH pulses and measuring the spectral interference between the XUV pulses are yet to be carried out.

Further testing, optimization, and modification for the experimental setup are necessary for successfully completing the SEA-SPIDER experiment at the VOXEL lab. First, the SHG needs to be optimized in the fixed and delay beamlines. The optimization involves tuning the phase matching of the BBO and further verifying the spectrum of SH pulses with a spectrometer with sub-nanometer resolution. The analysis of the SH spectrum from the two beamlines showed that even after two highly reflecting mirrors for the SH pulses, the spectrum from the fixed beamline has a significantly high intensity of the IR spectral components. Figure 4.35 shows the SH spectrum from the two beamlines in the SEA-SPIDER experimental setup shown in figure 4.26. The presence of IR and SH pulses for HHG will result in the

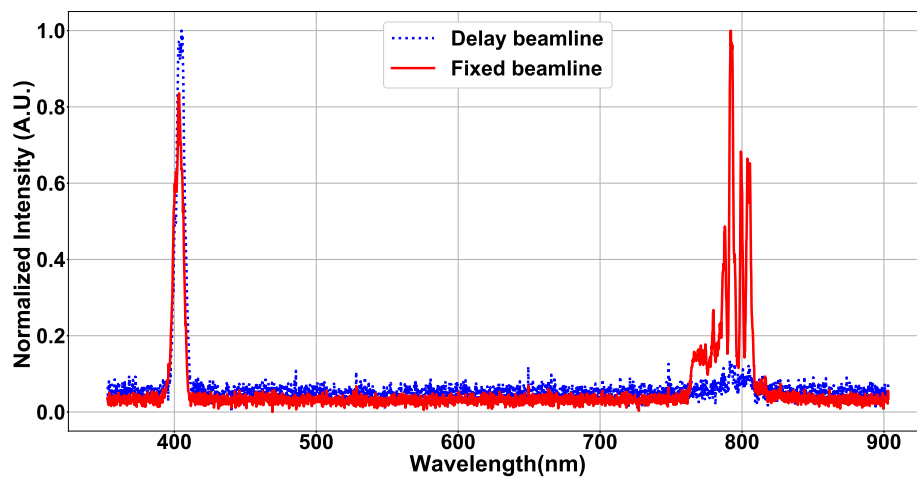


Figure 4.35: The spectrum of SH pulses from the SEA-SPIDER experimental setup.

generation of odd-even harmonics [90]. Also, the orthogonal polarization between the IR and the SH can result in the generation of HH with some elliptical polarization [186, 187]. The HHs generated from the fixed beamline can have elliptical polarization and compare to the HHs from delay beamline. This can result in a condition where no interference can be observed since the two XUV pulses are not of the same polarization [188]. To avoid this scenario, further optimization of the SHG in the fixed beamline needs to be done and also more high reflecting mirrors for SH pulses needs to be placed in the experimental setup to completely filter out the IR. Since the SH pulses from the delay beamline and the fixed beamline pass in different optical paths, their pulse duration may be different. Hence, the pulse duration of SH pulses needs to be measured individually by using a cross-correlator or a FROG setup [184, 143]. Further, the SHG needs to be optimized to have nearly same pulse duration for the two SH pulses to ensure the same generating conditions for the two XUV pulses. Also, the fine-tuning the separation between the SH pulse and its replica at the focus needs to be done with better accuracy and control. The separation can be verified by analyzing the spatial interference between the SH pulses.

After the optimization and verification of SHG, we should be able to generate the XUV pulse and its spectrally sheared replica. However, generating the two XUV pulses with a separation of  $\leq 1$  mm and

maintaining the same alignment as that of the SH pulses is a difficult task. The spatial overlap between the XUV pulses can be checked by looking at the footprint of the two XUV pulses on the XUV CCD before moving to the XUV spectrometer setup. With a vertical separation of  $\leq 1$  mm between the two XUV pulses at the focus of the SH pulses, the fringe separation can be estimated as  $\geq 100 \mu\text{m}$  and this corresponds to  $\sim 8$  pixels in the XUV CCD in the experimental setup. With careful optimization of SHG, HHG and XUV beam alignment, the SEA-SPIDER for XUV pulses from HHG in gases can be realized at VOXEL lab, IST.

### 4.3 All optical temporal metrology of XUV free-electron laser

An all-optical temporal metrology for XUV pulses from a free electron laser (FEL) was carried out at the FERMI FEL in the Elettra Synchrotron Facility in Trieste, Italy [24]. The all-optical temporal metrology was based on an autocorrelation of the XUV pulses from the FEL using four-wave mixing (FWM) in the XUV [63, 189] as the nonlinear process. The principle of FEL operation, FWM, and the experiment results are presented in this section.

#### 4.3.1 Introduction to Free electron laser

FELs are XUV source similar to HHG except it gives a higher number of photons [21, 149]. Unlike HHG, the FELs are not tabletop devices. FELs are generally large facilities with high maintenance cost. A FEL consists of a source of relativistic electrons and an undulating magnetic field. The electrons accelerated to relativistic velocities passes through periodically aligned magnets with alternating polarity known as an undulator. This results in a sinusoidal oscillatory motion of the electrons. In the laboratory frame, the undulator has a period of  $\lambda_u$  and for the relativistic electrons, this period is given by  $\lambda^* = \lambda_u/\gamma$ , where  $\gamma$  is the Lorentz factor. The electrons oscillating in the magnetic field emit radiation like an oscillating dipole with a frequency of  $\omega^* = 2\pi c/\lambda^*$  [190]. In the laboratory frame, one sees a strongly blue-shifted wavelength for this radiation because of the Doppler effect and it is given by

$$\lambda_L \approx \frac{\lambda^*}{2\gamma} \approx \frac{\lambda_u}{2\gamma^2} \quad (4.35)$$

Further, the radiation emitted by the undulator can contain the higher order harmonics of  $\lambda_L$  and thus the wavelength of the radiation from the undulator can be expressed as

$$\lambda_m = \frac{\lambda_L}{m}, m = 1, 2, 3, \dots \quad (4.36)$$

The radiation emitted from the undulator adds up incoherently and thus the output power increases linearly with the number of electrons added along the length of the undulator. A coherent addition of the undulator radiation is made possible by the modulating the electrons in the undulator with an electric field to form microbunches. The microbunching of electrons will result in a quadratic increase of the output intensity with the number of electrons [190]. In case of the FEL with the emission of radiation in the XUV, the amplification of radiation occurs in a single pass through the undulator. Figure 4.36 shows the

schematic of the undulator operation. There are two main single pass FEL configurations. The first is

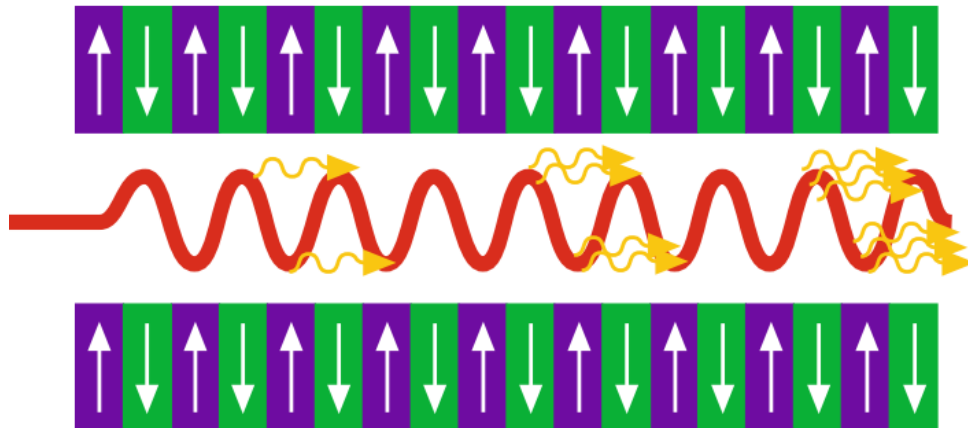


Figure 4.36: Schematic of oscillatory motion of an electron in an undulator [190, 86]

based on self-amplified spontaneous emission (SASE) [190, 191]. In a SASE FEL, the radiation emitted by the electrons along the undulator itself acts as the modulating field for creating the microbunches. Self-amplifying SASE FELs have the disadvantage of fluctuations in energy and spectrum. The second type of FELs are called the seeded FELs and are based on seeding the electron beam with a coherent external optical source and the higher order harmonics of external seed is generated by the process of high gain harmonic generation (HGHG) [190]. In a seeded FEL the accelerated electrons first pass through an undulator called the modulator where the electron beam is seeded with an external coherent source. The electrons traveling in a sinusoidal trajectory are modulated in energy with the field of the external source and the modulator magnets are adjusted to be in resonance with the external seed wavelength. The electron beam then goes through a dispersive element which results in the microbunching of the slow and fast electrons. After the dispersive element, the electron beam goes through an undulator called radiator where the magnets are placed with a period which corresponds to the FEL output frequency. The FEL pulse emitted after the radiator has higher order harmonics of the seed frequency [190]. Figure 4.37 shows the schematic of a seeded FEL [192].

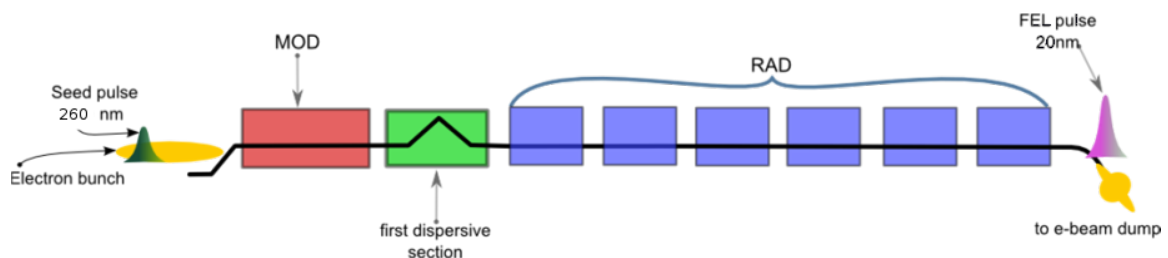


Figure 4.37: Schematic of a seeded FEL [192]

#### 4.3.1.1 FERMI FEL at Elettra Synchrotron, Trieste, Italy

The Free Electron laser Radiation for Multidisciplinary Investigations (FERMI) FEL is a part of the Elettra synchrotron facility in Trieste, Italy. The FERMI FEL is a seeded FEL and works on the principle of

high gain harmonic generation with an external seed [193, 194, 195]. It can work in two configurations, a single cascade configuration called the FERMI FEL 1 [194] and a double cascade configuration called the FERMI FEL 2 [195]. The FEL 1 is seeded by an optical laser with a central wavelength of  $\sim 260$  nm (3rd harmonic of Ti:Sa laser with central wavelength around 800 nm) and a pulse duration of  $\sim 140$  fs [175, 196]. FEL 1 generates the harmonics of seed laser frequency by the process of HGHG and the generated harmonic wavelength is given by

$$\lambda_{FEL1} = \frac{\lambda_{seed}}{h_1} \quad (4.37)$$

where  $\lambda_{seed}$  is the seed laser wavelength and  $h_1$  is the harmonic order in FEL 1. Figure 4.37 shows the schematic of the FERMI FEL 1. The bandwidth of FEL 1 under standard operating conditions is given by [197]

$$\Delta\omega_{FEL1} = h_1^{1/3} \Delta\omega_{seed} \quad (4.38)$$

where  $\Delta\omega_{seed}$  is the seed laser bandwidth. Under normal operating conditions of the seeded FEL 1, the FEL pulse duration can be estimated from the seed pulse duration ( $\Delta t_{seed}$ ) with the formula [175],

$$\Delta t_{FEL1} = \frac{\Delta t_{seed}}{\sqrt{h_1}} \quad (4.39)$$

When the FEL is optimized for the maximum output energy called the saturated condition, the pulse duration of the seeded FEL 1 can be estimated from the seed pulse duration ( $\Delta t_{seed}$ ) with the formula [197]

$$\Delta t_{FEL1} = \Delta t_{seed} h_1^{-1/3} \quad (4.40)$$

The major output parameters of the FEL 1 are listed in table 4.1 [194]. The FEL 2 works on the basis of double stage cascaded system with a double harmonic conversion. In the double stage cascade the FEL 2 is self seeded with the output of the first stage [198, 195], the FEL 1. The output of FEL 1 is tuned and adjusted to be seeded for the FEL 2. The FEL 1 output, relativistic electron beam and the XUV pulses goes through a second modulator where the modulator magnets are adjusted to be in resonance with the XUV pulse and the electron beam is modulated in energy with the electric field of the XUV pulse. After this the electron beam passes through the second dispersive section after which it achieves micro-bunching. The micro-bunches then goes through a second radiator where the harmonics of the XUV pulses (FEL 1 output) are generated [195]. The wavelength of the FEL 2 output wavelength is given by

$$\lambda_{FEL2} = \frac{\lambda_{seed}}{h_1 \times h_2} \quad (4.41)$$

where  $h_2$  is the harmonic order in FEL 2. The bandwidth of FEL 2 under standard operating conditions is given by [197]

$$\Delta\omega_{FEL2} = (h_1 \times h_2)^{1/3} \Delta\omega_{seed} \quad (4.42)$$

Under normal operating conditions of the seeded FEL 2, the pulse duration can be estimated from the seed pulse duration ( $\Delta t_{seed}$ ) with the formula [175],

$$\Delta t_{FEL1} = \frac{\Delta t_{seed}}{\sqrt{h_1 \times h_2}} \quad (4.43)$$

In saturation condition, the pulse duration can be estimated from the seed pulse duration ( $\Delta t_{seed}$ ) with the formula [197]

$$\Delta t_{FEL2} = \Delta t_{seed} (h_1 \times h_2)^{-1/3} \quad (4.44)$$

The figure 4.38 shows the schematic of the FERMI FEL 2. The major parameters of the FERMI FEL 2 is listed in table 4.1.

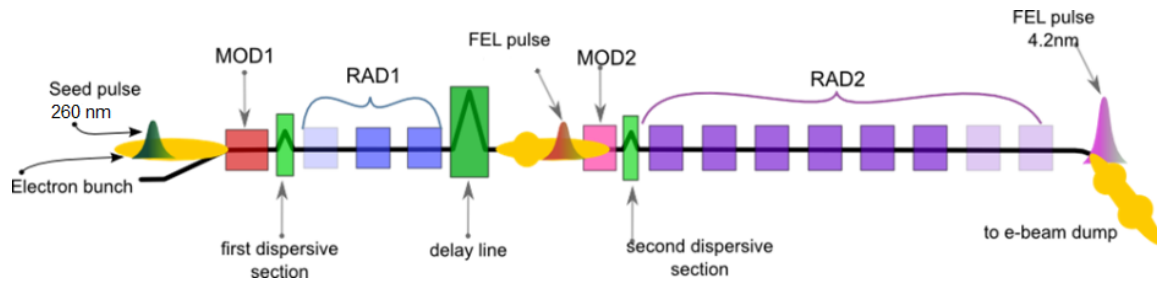


Figure 4.38: Schematic of the two stage seeded FERMI FEL, Trieste [192]

Parameters	FEL 1 (Single stage)	FEL 2 (Double stage)
Wavelength (nm)	100 - 20	20 - 4
Energy per pulse ( $\mu\text{J}$ )	20 - 100	$\leq 10$
Energy Stability (RMS)	20 %	50 %
Output power (GW)	$> 2$	$> 1$
Estimated pulse duration (fs)	$< 100$	40 - 100
Repetition rate (Hz)	10	10

Table 4.1: Principle parameters for FERMI FEL [194, 193, 196]

### 4.3.2 Overview of four-wave mixing

FWM is a third order nonlinear effect [199, 63]. It is the lowest order nonlinear effect which does not depend on the inversion symmetry of the medium. FWM involves interaction between three coherent electromagnetic fields in a material to generate a fourth coherent electromagnetic field. FWM is observed when highly coherent and intense laser beams interact with nonlinear materials. The intense laser fields incident on the material at an angle  $\theta$ , interferes and creates a spatially dependent intensity or polarization distribution on the material which changes its optical properties (refractive index and absorption). This changes in the optical properties create grating like structures [199, 200]. The incident fields are diffracted in the induced intensity gratings and the FWM signal generated at different positions are directed to a certain direction depending on the phase matching condition of the incident beams [200]. The three

incident beams in FWM process can be of the same frequency (called degenerate FWM) or of different frequencies (non-degenerate FWM). The FWM can be described in terms of the change in polarization induced by the high intense fields on the material. The induced polarization  $\vec{P}$  can be written as [63, 199]

$$\vec{P} = \chi^{(1)}\vec{E}_1 + \chi^{(2)}\vec{E}_2 + \chi^{(3)}\vec{E}_3 + \dots = \vec{P}^{(1)} + \vec{P}^{(2)} + \vec{P}^{(3)} + \dots, \quad (4.45)$$

where  $\vec{E}$  is the electric field and  $\chi$  is the nonlinear susceptibility.  $\vec{P}^{(1)}$  represents the linear part of polarization and the  $\vec{P}^{(2)}$  and  $\vec{P}^{(3)}$  represents the nonlinear part with contribution from higher orders. In the case of the FWM process, it is represented by  $\vec{P}^{(3)}$  as it describes the interaction between the three fields. It is given by [199, 171]

$$\vec{P}^{(3)}(\vec{r}) = \chi^{(3)}\vec{E}^3 = \chi^{(3)}\vec{E}_1(\omega_1, \vec{k}_1)\vec{E}_2(\omega_2, \vec{k}_2)\vec{E}_3(\omega_3, \vec{k}_3)\exp[i\vec{k}_4\cdot\vec{r} - i\omega_4 t] \quad (4.46)$$

where  $\vec{E}_1(\omega_1, \vec{k}_1)$ ,  $\vec{E}_2(\omega_2, \vec{k}_2)$  and  $\vec{E}_3(\omega_3, \vec{k}_3)$  are the three input electric fields with their corresponding frequencies  $\omega$  and wave vectors  $\vec{k}$ .  $\vec{k}_4 = \pm\vec{k}_1 \pm \vec{k}_2 \pm \vec{k}_3$  is the wave vector for the fourth electric field  $\vec{E}_4(\omega_4, \vec{k}_4)$  generated in the FWM process. For phase matching, the difference between the wave vectors  $\Delta\vec{k}$  should be equal to zero. Figure 4.39a shows a possible FWM setup where two laser pulses with frequencies  $\omega_1$  and  $\omega_2$ , create the intensity grating in the presence of a third pulse with frequency  $\omega_3$ , generates the FWM signal at a fourth frequency  $\omega_4$ .  $2\theta$  is the angle between  $\omega_1$  and  $\omega_2$ .  $\theta_B$  is the angle from the optic axis to  $\omega_3$ . Figure 4.39b shows the  $\vec{k}$  diagram for the setup in figure 4.39a. The phase

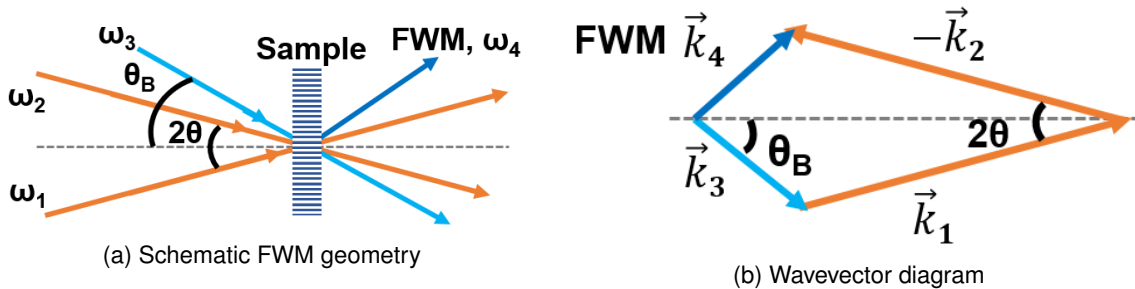


Figure 4.39: Schematic of a possible FWM geometry [189]

matching condition for the FWM setup in figure 4.39a is given by [189]

$$\vec{k}_4 = \vec{k}_1 - \vec{k}_2 + \vec{k}_3 \quad (4.47)$$

Ultrashort laser pulses focused on a nonlinear material generates transient grating structures, which are either standing or moving. They disappear in the absence of these short laser pulses. These structures can be probed with another beam and the resulting FWM signal can be used to probe dynamics of processes which occur on ultrashort time scales [200, 171].

#### 4.3.2.1 Four-wave mixing in the XUV

The study of FWM or in general nonlinear processes like second harmonic generation in the XUV is limited because of the unavailability of high intensity sources in the XUV. After the advent of FELs with

high intensities in the XUV [21, 22, 24], it is now possible to study the nonlinear process with XUV pulses [169]. The FERMI seeded FEL with high intensity and highly stable coherent XUV radiation [194, 189] enabled the study of FWM in XUV [189]. The schematic of the experimental setup for FWM in the XUV carried out at FERMI FEL is shown in figure 4.40.

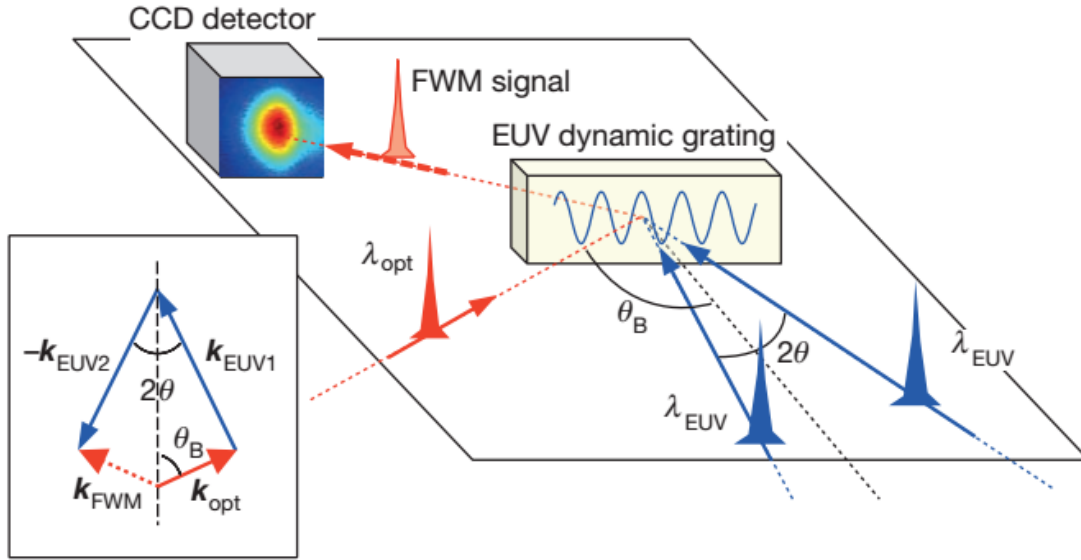


Figure 4.40: Schematic of transient grating generation in XUV at FERMI FEL (Inset:  $\vec{k}$  diagram) [189]

In this experiment the FWM signal was generated by focusing two XUV pulses from the FEL and an optical pulse which is the second harmonic of a Ti:Sa laser on a glass ( $\text{SiO}_2$ ) sample. The FEL pulses subtend an angle of  $2\theta = 6.16$  deg on the glass sample which was kept perpendicular to the bisector of the angle between the FEL pulses. The transient gratings generated by the FEL pulses are probed with an optical pulse. The optical pulse incident onto the sample at an angle of  $\theta_B = 49.9$  deg with respect to the bisector of the angle between the FEL pulses. All the three pulses were in the same plane. The value of the FEL wavelength, optical laser wavelength and the angles subtended by the pulses at the samples were calculated based on the phase matching condition and it is given by [189]

$$\lambda_{EUV} \sin(\theta_B) = \lambda_{opt} \sin(\theta) \quad (4.48)$$

The direction of propagation of the FWM signal is given by

$$\vec{k}_{FWM} = \vec{k}_{EUV1} - \vec{k}_{EUV2} + \vec{k}_{opt} \quad (4.49)$$

where  $\vec{k}_{FWM}$ ,  $\vec{k}_{EUV1}$ ,  $\vec{k}_{EUV2}$ ,  $\vec{k}_{opt}$  are the wavevectors of the FWM signal, EUV1, EUV2 and the optical pulse respectively. Here EUV represents extreme ultraviolet radiation from the FEL.

#### 4.3.2.2 Autocorrelation using transient gratings

The generation of transient gratings in a nonlinear medium by coherent laser pulses can be used to measure the pulse duration of the laser pulses [201]. The variation of the transient grating efficiency

can be measured with respect to the delay between the coherent laser pulses using a probe pulse and the transmitted intensity of the probe pulse can be modeled as the autocorrelation between the two laser pulses. The pulse duration can be then deduced from the FWHM of the intensity of autocorrelation assuming a Gaussian or  $\text{sech}^2$  according to the pulse shape of the laser pulses. With transient gratings, for pulses whose coherence time  $\tau_c$  is nearly equal to the Fourier transform limited laser pulse duration  $\tau_p$ , i.e.,  $\tau_c \approx \tau_p$ , the autocorrelation yields the pulse duration as per equations 4.1 and 4.2 [201]. The coherence time  $\tau_c$  is given by [12]

$$\tau_c = \frac{\sqrt{2 \ln 2 / \pi}}{\Delta\nu} \quad (4.50)$$

where  $\Delta\nu$  is the spectral bandwidth in Hz. The autocorrelation function in equation 4.1 can be rewritten considering the effect of the coherence of the pulses as [201]

$$I_{AC}(\tau) = \int I(t)I(t + \tau_d)dt + |\Gamma^{(2)}(\tau_d)|^2 \quad (4.51)$$

where  $\Gamma^{(2)}$  is the second-order coherence function and  $\tau_d$  is the delay between the pulses in the autocorrelation. When the laser pulse duration is not at the FTL, i.e.,  $\tau_c \ll \tau_p$ , the equation for the intensity autocorrelation using the transient gratings method can be written as [201]

$$I_{AC}(\tau) = \frac{\tau_c}{\tau_p} \int I(t)I(t + \tau) + |\Gamma^{(2)}(\tau_d)|^2 \quad (4.52)$$

The autocorrelation function is lower in this case by a factor of  $\tau_c/\tau_p$ . This can result in sharp spikes in the intensity autocorrelation curve [201]. In this case, the autocorrelation measurement gives not the pulse duration but the coherence time of the pulse [201].

### 4.3.3 Experimental results

The goal of the experiment was to measure the pulse duration of FERMI FEL 2 using an all-optical method. Previous measurements were done mainly using indirect methods which are based on electron spectrometers and modeling [202, 175]. The all-optical methods have the advantage that it is direct and requires no modeling. The all-optical method used is based on transient gratings based autocorrelation [201, 139] between the XUV pulses from the FEL.

For the autocorrelation, based on the generation of transient gratings, between the XUV pulses from the FEL, the nonlinear process involved is four-wave mixing (refer section 4.3.2.1) [189]. Here the delay between the FEL pulses is scanned in presence of the optical laser and the corresponding FWM signal is recorded as the autocorrelation signal.

#### 4.3.3.1 Description of the experimental setup

The autocorrelation measurement was carried out at the DiProl (Diffraction and Projection Imaging) beamline at the FERMI FEL [203] which is mainly used for coherent diffraction imaging. The schematic of the experimental setup for pulse duration measurement is shown in figure 4.40. A picture of the DiProl beamline is shown in figure 4.41. The FEL beam entering the beamline is first focused by the K-B optics

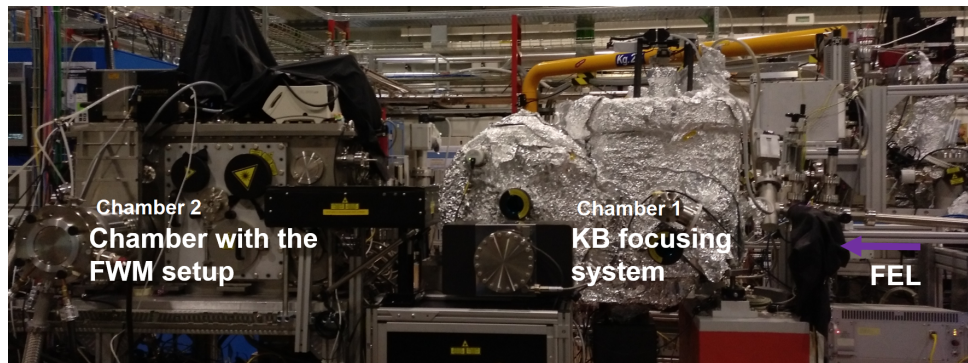


Figure 4.41: Experimental setup at MiniTIMER delay line, DiPROL, FERMI FEL [204]

[117] focusing setup in chamber 1 onto the sample position in the chamber 2, DiProl chamber. The DiProl chamber has the MiniTIMER [204], a compact split and delay line placed before the sample position.

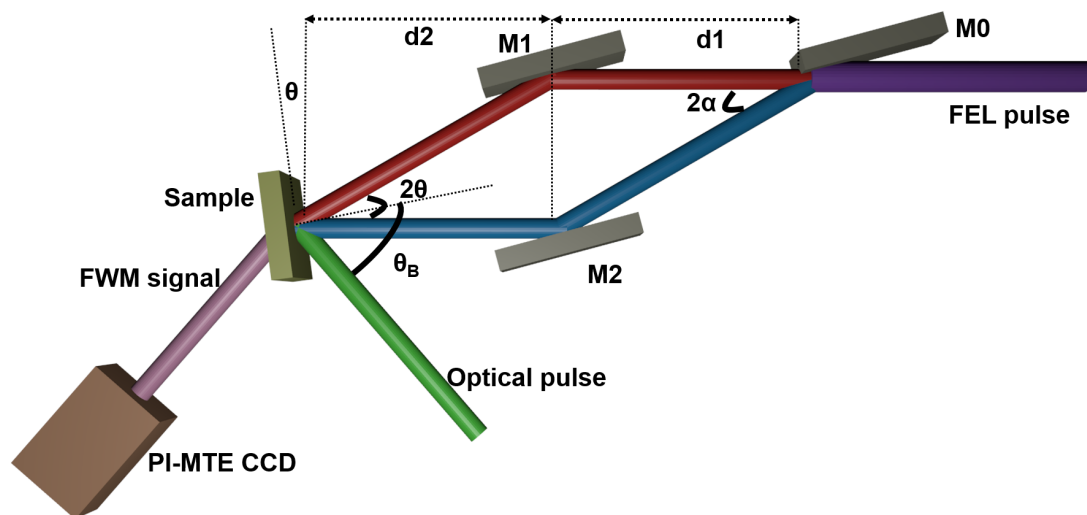


Figure 4.42: Schematic of the experimental setup at the MiniTIMER delay line, DiPROL, FERMI FEL.

The schematic of the FWM experimental setup with the MiniTIMER split and delay line is shown in figure 4.42 [189]. The setup consists of three carbon coated mirrors  $M_0$ ,  $M_1$  and  $M_2$  with a length of 70 mm each. The mirror  $M_0$  which is positioned in grazing incidence splits the incoming FEL beam in the wavefront and the downstream mirrors,  $M_1$  and  $M_2$  control the spatial and temporal separation between the split beams on the sample [189]. The design of positions of mirrors  $M_0$ ,  $M_1$ ,  $M_2$  and sample corresponds to a parallelogram geometry with beam splitting angle ( $2\alpha$ ) equal to the beam crossing angle ( $2\theta$ ) at the sample. The designed distances of the split delay setup is  $d_1 = d_2 = 125$  mm and  $2\alpha = 2\theta = 6^\circ$ , which corresponds to a zero delay between the split FEL beams. The MiniTIMER setup can scan up to a delay of  $\pm 500$  fs and also the angle  $2\alpha$  can be changed in the range of  $3^\circ - 9^\circ$ . All the components in the experimental setup are fixed on motorized multi-axis stages and can be moved in vacuum during the experiment.

The third beam in the FWM, the optical pulse interacts with the sample at an angle of  $\theta_B$  with respect to the normal of the sample. The optical pulse used is generated by SHG in a BBO crystal with a fraction of the Ti:Sapphire laser that is used to seed the FERMI FEL. Since both the seed pulse

and optical pulse in the experiment have the same origin, the jitter between the FEL pulses and the optical pulse can be optimized to  $< 10$  fs, which is much shorter than the expected FEL pulse duration. Hence, we can assume jitter free operation between FEL pulses and optical pulse. The SH has a central wavelength of 392.8 nm and it is coplanar to the FEL pulses. The optical pulse is focused on the target at a point where both FEL pulses interfere using a 700 mm plano-convex lens. The angle  $\theta_B$  can be manipulated in the range of  $47^\circ - 51^\circ$ . The delay between the FEL and optical pulse can be tuned from  $-10$  to 300 ps. All the experimental setup is pre-aligned using a Ti-Sa laser before using the FEL. The spatio-temporal overlap of the FEL and optical pulses is obtained by a cross-correlation method based on the transient reflectivity of the FEL beams on a solid  $\text{Si}_3\text{N}_4$  reference sample [189]. Figure 4.43a shows

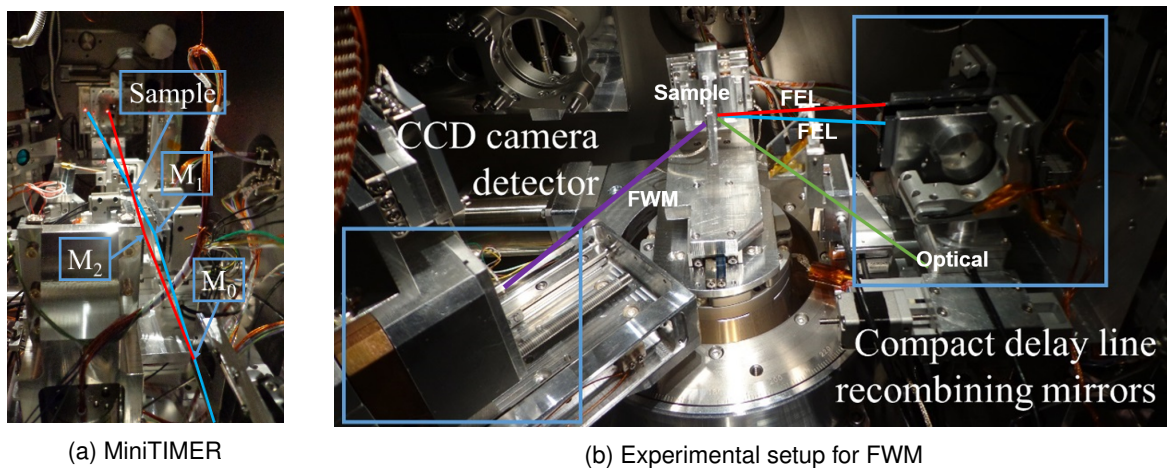


Figure 4.43: Experimental setup at DiPROI, FERMI FEL [204]

a picture of the split and delay system in the MiniTIMER beamline. Figure 4.43b shows the picture of experimental setup for FWM inside the DiProI chamber with the MiniTIMER. The FWM signal generated is recorded by an X-ray PI-MTE 2048B CCD.

#### 4.3.3.2 Results

The pulse duration of the FERMI FEL 2 was measured using an all optical autocorrelation method based on transient gratings. The transient gratings were generated by two XUV pulses from the FEL 2 on a solid  $\text{Si}_3\text{N}_4$  sample in a process called FWM.

The FEL was operating under saturated conditions. The averaged spectrum of FERMI FEL 2 measured over 50 acquisitions is shown in figure 4.44. The central wavelength of the FEL 2 was  $\sim 16.49$  nm which corresponds to the 16<sup>th</sup> harmonic of the seed laser. Since it is the FEL 2, the 16<sup>th</sup> harmonic is combination of 4<sup>th</sup> harmonic of the seed laser generated by the FEL 1 and further the 4<sup>th</sup> harmonic of the FEL 1 generated by the FEL 2 [196]. The spectrum has a bandwidth of  $\sim 0.02$  nm.

The autocorrelation measurement of the FEL 2 pulse duration was carried out by changing the delay between the two FEL pulses using the MiniTIMER split and delay system and recording the corresponding FWM signal. Figure 4.45 shows the plot of autocorrelation signal.

The two XUV pulses from FEL 2 are assumed to have a Gaussian pulse distribution and hence the autocorrelation signal is also assumed to have a Gaussian distribution. However, the autocorrelation

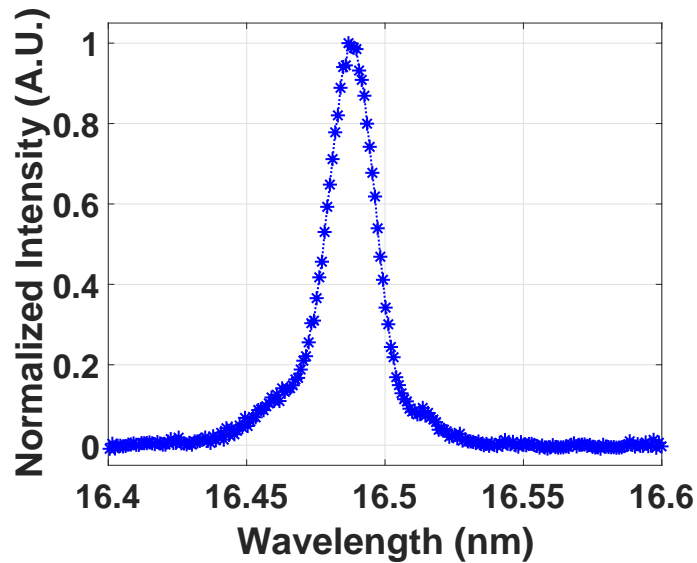


Figure 4.44: The averaged spectrum of FERMI FEL 2 measured over 50 acquisitions.

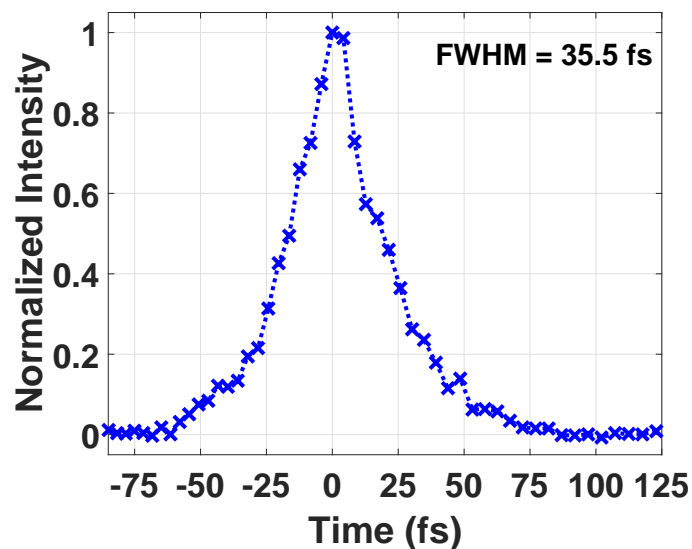


Figure 4.45: The transient grating based autocorrelation signal measured for FERMI FEL 2.

signal obtained in this experiment using the transient grating method is not a Gaussian. From the section 4.3.2.2, it can be inferred that the autocorrelation signal deviates from a Gaussian when the  $\tau_c < \tau_p$  and only the peak of the signal remains [201]. In our experiment our dynamic range of the measurement is only good enough to record the peak and not the complete autocorrelation signal. Hence, the autocorrelation signal is shown figure 4.45 is only the peak of the signal and does not give the pulse duration of the XUV pulses from FEL 2.

However, Trebino et al., have shown that the autocorrelation method based on transient gratings can also be used to measure the coherence time of the ultrashort laser pulses when the coherence time is lower than the pulse duration [201]. From the current transient grating based autocorrelation measurement shown in figure 4.45, the coherence time of FEL 2 can be estimated as 35.5 fs. The theoretical value of

coherence time for the FEL 2 is calculated using the equation 4.50 where,  $\Delta\nu_{FEL2}$  is obtained from the FEL 2 spectrum. The theoretically calculated  $\tau_c$  is 30.11 fs. The measured coherence time for FEL 2 is  $\sim 1.2$  times the calculated coherence time.

The all-optical transient grating based autocorrelation method for pulse duration measurement of the FERMI FEL 2 was carried out. Although we successfully measured transient four-wave mixing in the XUV, the autocorrelation signal did not measure the pulse duration. Instead, the coherence time of the FEL 2 pulses was measured. To measure the pulse duration of the FEL 2 using the transient grating based autocorrelation method requires the pulses to be near FTL. Compressors designed for XUV can be used to compress the FEL 2 pulses to near FTL and the transient grating based autocorrelation method can be used to measure the temporal duration of these pulses.



# Chapter 5

## Conclusions and perspectives

This thesis includes work performed on the generation and spatio-temporal characterization of XUV sources. Most of the work was carried out with HHG as the source of XUV pulses. The major part of the thesis is experimental work supported by numerical calculation for the experiments. The experiments were carried out in collaboration with the following research institutes: LOA - France, Queens University Belfast - UK, Helmholtz Institute Jena - Germany, FERMI FEL - Italy, DESY - Germany and Imagine Optic - France, a company specialized in optical metrology and its applications.

The major conclusions, achievements for the work done in this thesis along with future perspectives are presented in this chapter.

### 5.1 Conclusions

The major conclusions obtained during this thesis work are listed below.

The XUV source generation:

- ❖ HHG was optimized in energy and photon counts in different laboratories using different laser systems. The optimization conditions and the XUV beam parameters obtained are compared and are listed in table 2.5.
- ❖ The HHs generated were also characterized in the spectrum and spatial intensity distribution.
- ❖ An experiment of HHG in solid was performed at JETI200, Helmholtz Institute, Jena, Germany. The solid HHG conditions were optimized to generate HH under CWE and ROM mechanisms.

Spatial metrology of XUV optics and sources:

- ❖ An XUV Hartmann WFS was calibrated in collaboration with Imagine Optics with a wavefront accuracy of  $\sim \lambda/29$  RMS considering a central wavelength of  $\lambda = 32$  nm for the XUV source.
- ❖ A novel high-NA XUV Hartmann WFS was calibrated for the first time with a wavefront accuracy of  $\sim \lambda/6$  RMS considering a central wavelength of  $\lambda = 32$  nm for the XUV source.

- ❖ Multilayer mirrors with three different central wavelengths were calibrated in wavefront using the high-NA XUV WFS. The results are listed in table 3.1. The wavefront of a toroidal mirror at grazing incidence was measured using the high-NA XUV WFS and preliminary optimization was carried out with a  $\sim 40\%$  enhancement of intensity at the focus.
- ❖ The wavefront of XUV sources from HHG in gases was optimized using XUV WFSs in at LOA and L2I. The wavefront of HH from solids was measured using the calibrated high-NA XUV WFS for the first time. The major wavefront errors for the wavefront characterized XUV sources are listed in table 3.6.

Temporal metrology of XUV sources:

- ❖ An all-optical method using SEA-SPIDER for temporal metrology of XUV pulses from HHG in gases was proposed. A SPIDER algorithm was developed and numerical simulations were carried out using this algorithm to determine the experimental parameters required. Experiments for SEA-SPIDER was carried out at Salle Corail, LOA and VOXEL lab, IST.
- ❖ A pulse characterization method based on SPIDER was introduced for the blue-violet spectral region. Numerical simulations were carried-out for pulse with spectrum around 400 nm using a SPIDER algorithm developed. First experiments on SPIDER in the blue-violet spectral region was carried-out at the VOXEL lab, IST and the results are presented.
- ❖ An all-optical temporal metrology method based on autocorrelation using FWM in the XUV was implemented at the seeded FERMI FEL 2. This method was used to measure the coherence time of the XUV pulses from FEL 2 and the measured coherence time was  $\sim 1.2$  times the calculated coherence time.

### 5.1.1 Achievements

The major accomplishments of this thesis work are listed below.

- ❖ HHG was first tested and optimized in energy using the in-house built diode-pumped Yb:CaF<sub>2</sub> / Yb:YAG laser. The wavefront of HH generated by the long pulse laser was also measured and optimized in collaboration with DESY, Germany. The wavefront measurement of HHG using long pulse lasers was done for the first time to our knowledge. These results were published in early 2017 [137].
- ❖ HHG at the HH beamline in the newly built Salle Corail, LOA was successfully carried out. Further, the energy, spectrum and wavefront of HHG from gases was measured.
- ❖ A HH beamline was successfully established at the VOXEL lab, IST. The optimized XUV pulses from HHG in gases was characterized in energy and spectrum. A SEA-SPIDER experimental setup for XUV pulses was deployed with spectral shearing in the SH pulses. A SPIDER measurement was carried out for the SH pulses using the same setup and a publication is being written on this.

- ❖ An XUV WFS was calibrated in collaboration with Imagine Optics, France with a wavefront accuracy of  $\sim \lambda/29$  RMS, which is now used at the HHG beamline, ELI beamlines, Prague, Czech Republic.
- ❖ A high-NA XUV Hartmann WFS was calibrated in collaboration with Imagine Optics, France and Centre for plasma physics, Queen's University Belfast, UK with a wavefront accuracy of  $\sim \lambda/6$  RMS at the Salle Corail HH beamline, LOA. A publication is being written on this work.
- ❖ The wavefront of HHG from solids was measured under different generation conditions for the first time to our knowledge at JETI200, Helmholtz Institute, Jena, Germany in collaboration with LOA, Imagine Optics, and Centre for plasma physics, Queen's University Belfast.
- ❖ The coherence time XUV pulses from the FEL 2 was measured using an autocorrelation method based on transient gratings.

## 5.2 Perspectives

In this section, the possible applications based on the results of this thesis are discussed. The major future perspectives of the current thesis work are as follows:

- ❖ The optimized XUV beam from HHG in gases at L2I using the diode-pumped Yb:CaF<sub>2</sub> / Yb:YAG laser system provides ways to probe the plasma created by the same laser system with higher pulse energies. The wavefront characterization of this optimized XUV source also can be used to measure the refractive index of plasma created by laser.
- ❖ The calibrated high-NA XUV WFS can be now used for full optimization of toroidal mirror focus. A Schwarzschild objective [134] can be used to create a tight focus which in turn gives a highly divergent beam and this can be used to test the high-NA XUV WFS.
- ❖ The high-NA XUV WFS can be used to further measure and optimize the wavefront of HHG from solids. The measured solid HH wavefront can be used along with the reconstructed intensity to backpropagate to the HH source to study the changes at the plasma source.
- ❖ The spatio-temporal characterization of attosecond lighthouses can be performed by using the high-NA in-vacuum XUV WFS. Multiple high-NA in-vacuum XUV WFS can be used for simultaneously characterizing the wavefront of the isolated attosecond pulses.
- ❖ The all-optical temporal metrology method based on SEA-SPIDER can be effectively implemented by carefully choosing the optics and introducing a spectral shear in the replica of driving laser. Further a HH beamline with high stability in terms of pointing and energy is required.
- ❖ The SEA-SPIDER experimental setup can be modified with a visible spectrometer to measure the pulse duration of the SH.
- ❖ The transient grating based autocorrelation method can be used to measure the pulse duration of the XUV pulses from the FERMI FEL 2 after compressing the pulses using an XUV compressor, to near FTL.

The possibility of plasma probing with XUV radiation based on optimized HHG at L2I and a holographic imaging technique with wavefront correction are presented.

### 5.2.1 Plasma diagnostics with XUV radiation

The change of the state of matter from solid to plasma is a topic of great interest as it involves the transition through states of matter with densities close to solids which is present in the interior of large planets [18, 17, 16]. The sub-picosecond time scale of the transitions near-solid density makes it difficult to study these transient states of matter. Transmission diagnostics for solid density plasma are complex and difficult to set up due to probes requiring to be in the X-ray spectrum [205, 206].

The critical density of solids for ultrashort optical lasers is in the order of  $10^{22}\text{cm}^{-3}$  and hence they are not an option to probe a volume of near solid densities. For this reason, short wavelengths have to be used [3, 20]. The wavelengths which can pass through near-solid densities are in the XUV or X-ray spectral range. The critical density for a pulse with a central wavelength of 32 nm is in the order of  $10^{24}\text{cm}^{-3}$ . The ultrashort probes available in the spectral range are FEL, HHG, and XRL. The use of XUV pulses from HHG as a probe for plasmas is attractive since it is comparatively compact and easy to set up in small laboratories.

XUV pulses have already been used in probing plasma states using methods like XUV interferometry [207], deflectometry [122], and spectroscopy [16]. Another technique to measure the refractive index of plasma across the whole plasma region is using a wavefront sensor [38, 208]. Here we describe the possibility of measuring the refractive index of a plasma created by the laser at L2I and probing it using XUV pulses from HHG, generated by the same laser and detecting with an XUV WFS [137].

#### 5.2.1.1 XUV wavefront studies for plasma characterization

The XUV WFS is based on the Hartmann technique has been proposed for measuring the change in electron density [208] and refractive index [38] of high energy density plasma with XUV probes. The use XUV WFS has the advantage over XUV interferometry [207] or deflectometry [122] that it can be used over a wide wavelength range and it is experimentally simple to set up. Moreover, the XUV WFS measures the changes in the wavefront perpendicular to the direction of the beam and it gives a 2-D map of the deflection introduced by the plasma on the probe beam [208]. Also, the XUV WFS measures the shift in the diffracted spot of the XUV probe by the Hartmann plate with respect to the same by a plain perfect wavefront and hence it is not affected by the ambiguous  $2\pi$  phase shift problems in interferometry or deflectometry [208, 38].

A schematic of the proposed experimental setup is shown in figure 5.1. In the setup, the high energy density plasma state is created by focusing an IR pump laser onto a thin film target. This plasma state is probed with an XUV probe beam and it is detected using an XUV WFS. The WFS detects the changes in the wavefront due to the changes in the plasma created in the presence of a laser. The XUV wavefront with and without the pump beam are compared to get the actual changes or deflection in the probe beam introduced by the high energy density plasma state.

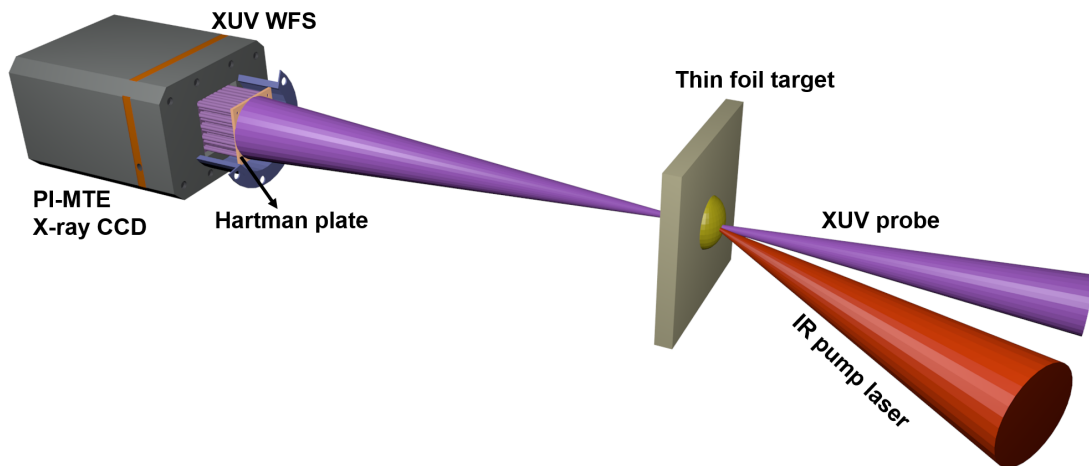


Figure 5.1: Schematic of basic experimental arrangement used for wavefront sensing of high-density targets.

The HHs optimized and characterized in wavefront in L2I, IST (see section 3.4.1.2) can be used as an XUV probe for measuring changes in plasma refractive index. The HHG in xenon gives harmonics with stability in terms of pointing, energy, and spectrum with a 1.44 nJ per shot. Using the possibility of having a high energy optically synchronized pump laser from the in-house built diode laser gives the possibility of measuring the plasma created by this laser probed with the optimized XUV pulse. In [38] values for the absorption and deflection of an XUV probe pulse in aluminum heated to warm-dense conditions are estimated. The referenced values result from heating aluminum with a FEL, however, WDM can also be produced with optical lasers as shown in [206, 209, 76]. At a temperature of 10 eV an absorption coefficient of  $\alpha \approx 4.5 \times 10^6$  is estimated for photons with an energy of 30 eV ( $\sim 41$  nm), which leads to an absorption of  $\sim 75\%$  in a 300 nm thick foil. For lower photon energies more absorption is expected. In xenon, the HH order 23 with a wavelength of 44.7 nm has an energy of 13% of the whole spectrum which corresponds to  $\sim 0.18$  nJ. This corresponds to  $\sim 2 \times 10^6$  counts in the XUV CCD camera used in the experiment. For an area of  $100 \times 100$  pixels on the CCD, this relates to 200 counts per pixel, which is sufficient to be recorded in a single-shot acquisition. The deflection  $\phi(x)$  of a beam in a plasma is given by the gradient of the refractive index  $\nabla n$  and the length of the plasma  $L$  by

$$\phi(x) = \int_0^L \nabla n(x, z) dz \quad (5.1)$$

where  $x$  is the transverse direction to the plasma and  $z$  the perpendicular direction. Following [38], the biggest deflection of a HH probe beam, bigger than the created plasma at WDM conditions, is between the cold Al foil and warmest part of the solid plasma at 10 eV temperature. For a plasma with a diameter of  $20 \mu\text{m}$ , a maximum beam deflection of 0.93 mrad is expected under these conditions. The measured mean slope of the characterized HH source is 0.6 mrad with a standard deviation of  $10 \mu\text{rad}$ , (see table 3.4) which is smaller than the expected beam deflections. Therefore, the plasma induced deflections are more significant than the fluctuations of the probe beam.

## 5.2.2 XUV imaging with wavefront correction

The development of coherent sources in the XUV and X-ray region such as Synchrotron's, FEL, X-ray lasers, HHG has resulted in the development of imaging techniques at short wavelengths. The interest in XUV imaging techniques is largely driven by achieving better resolution than optical light and extending XUV photon energies to the water window and beyond for biological imaging applications in laboratory scale setups. To use XUV pulses in imaging systems, it requires focusing optics in the XUV. Because of the optical properties of materials in the XUV spectral range most of the focusing optics used are reflective optics at grazing incidence discussed in section 3.1.1 or diffractive optics such as zone plates. The use of these optics often results in a beam with aberration like in the case of KB optics [117] or toroidal mirrors. Hence, the use of lens-less imaging methods is advantageous when using XUV beams.

One of the most common lens-less imaging methods is called coherent diffraction imaging (CDI) [2, 34]. Although it is mainly performed in FEL's for imaging of biological samples [2, 11], single shot CDI experiments are possible with HHs [34]. In CDI, the object to be imaged is illuminated with coherent XUV radiation and the resulting diffraction pattern produced is recorded. From the diffraction pattern, the image can be reconstructed by using the Fresnel-Huygens equation [2]. Since the only intensity of the diffraction pattern can be recorded, the phase information is retrieved from the intensity pattern using iterative phase retrieval algorithms [2]. The phase information retrieved, along with the intensity recorded is used to reconstruct the image of the object [2]. Since CDI typically only uses a single reflective optic to concentrate photons onto the object and aberrations can be minimal, theoretically, there is no limit on the resolution except the limit on the wavelength of the coherent light source.

Another lensless imaging technique in the XUV is Fourier transform holography (FTH) [42, 79]. In FTH, the diffraction of coherent radiation by an object along with the radiation from a reference is recorded in the far-field. The reference aperture, usually circular and the object are assumed to be in the same plane. The far-field diffraction, also known as Fraunhofer diffraction pattern in FTH contains the information regarding the object and the reference. The object can be reconstructed by taking the Fourier transform of the far-field diffraction pattern. Unlike CDI, FTH method does not depend on iterative algorithm. One of the problems with FTH is that the resolution is also dependent on the reference hole size and its position compared to the object. A lens-less method similar to FTH is in-line holography. Unlike FTH, in-line holography does not require a reference beam and also no optics to focus the beam on to the sample. In in-line holography, the sample is illuminated with a coherent beam and the interference of light diffracted by the sample and the light which is transmitted around the sample is recorded by a detector and the object is reconstructed from this intensity pattern [39, 210].

The use of lens-less imaging techniques in the XUV avoids the aberrations due to complicated optical setups but the intrinsic aberration of the source reduces the resolution that can be achieved with these techniques. To further improve the imaging quality it is necessary to improve the wavefront aberrations of the imaging source [46]. In cases where the wavefront aberrations cannot be further optimized, another option is to numerically correct for the wavefront aberration during reconstruction.

In this section the possibility of in-line holography with wavefront correction for the XUV spectral region is presented.

### 5.2.2.1 Wavefront correction for in-line holography

In-line holography is a simple realization of a holographic imaging technique. This method was proposed by D. Gabor [211]. This is a lens-less imaging method and it does not involve the use of any reference beams. In in-line holography, a plane or spherical wave is incident on the sample and the hologram is created by the interference of light diffracted from the sample and the light transmitted without interacting with the sample. This means that the sample and the reference waves travel in the same axis, unlike FTH. This method has the advantage that it only requires the coherent source, object and the detector. Since it does not involve any iterative algorithm, the image reconstruction is faster. Also, the sample to be imaged does not need any special sample preparation such as the inclusion of reference pinholes.

Figure 5.2 shows a scheme of the in-line holography setup with a coherent spherical beam. The setup shows a diverging spherical beam illuminating the sample as it passes through and around the sample and the hologram are recorded by the CCD. From the hologram, the image can be reconstructed [212, 213].

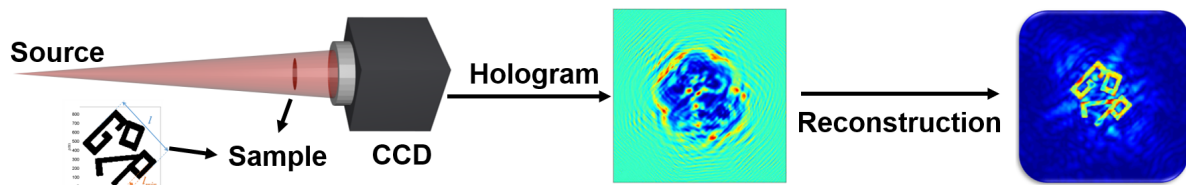


Figure 5.2: Schematic of in-line holography imaging. Modified from [213]

In classical imaging, the resolution of the object depends on how well the different features of the object can be resolved. Hence, it mainly depends on the detector resolution. In FTH or in-line holography, the resolution of the imaging depends on how well the interference fringes formed by the reference and object waves can be resolved. The theoretical lateral resolution is given by [210, 212, 213]

$$\delta_{lat} = \frac{\lambda}{2NA} \quad (5.2)$$

where  $NA$  is the numerical aperture of the beam and it is given by  $NA = D/L$  where  $D$  is the beam diameter and  $L$  is the source to detector distance. From equation 5.2, it can be seen that, for a higher resolution, beams lower wavelength and higher  $NA$  is required.

In-line holography has been mathematically treated in earlier publications [212, 213]. The wavefront correction for in-line holography has been numerically studied by Duarte, et al., [213, 214]. From the numerical simulations it can be seen that by correcting the wavefront aberrations in the beam, the reconstruction is better [213]. Figure 5.3a shows the object used in simulations for in-line holography. Simulation was carried out for generating hologram of this object by in-line holography using a beam with a known astigmatism. In the simulation, a source to object distance of 5 cm and an object to detector

distance of 20 cm were considered. The wavefront aberration, i.e, the astigmatism simulated for the beam is shown in figure 5.3b. The hologram obtained with astigmatic beam is used to reconstruct the object [213]. Figure 5.3c shows the reconstructed image of the object without wavefront correction and figure 5.3d shows the reconstructed object by correcting the reconstruction with the known wavefront aberration. From the two figures, it is clear that wavefront correction improves the quality of the image reconstructed in in-line holography.

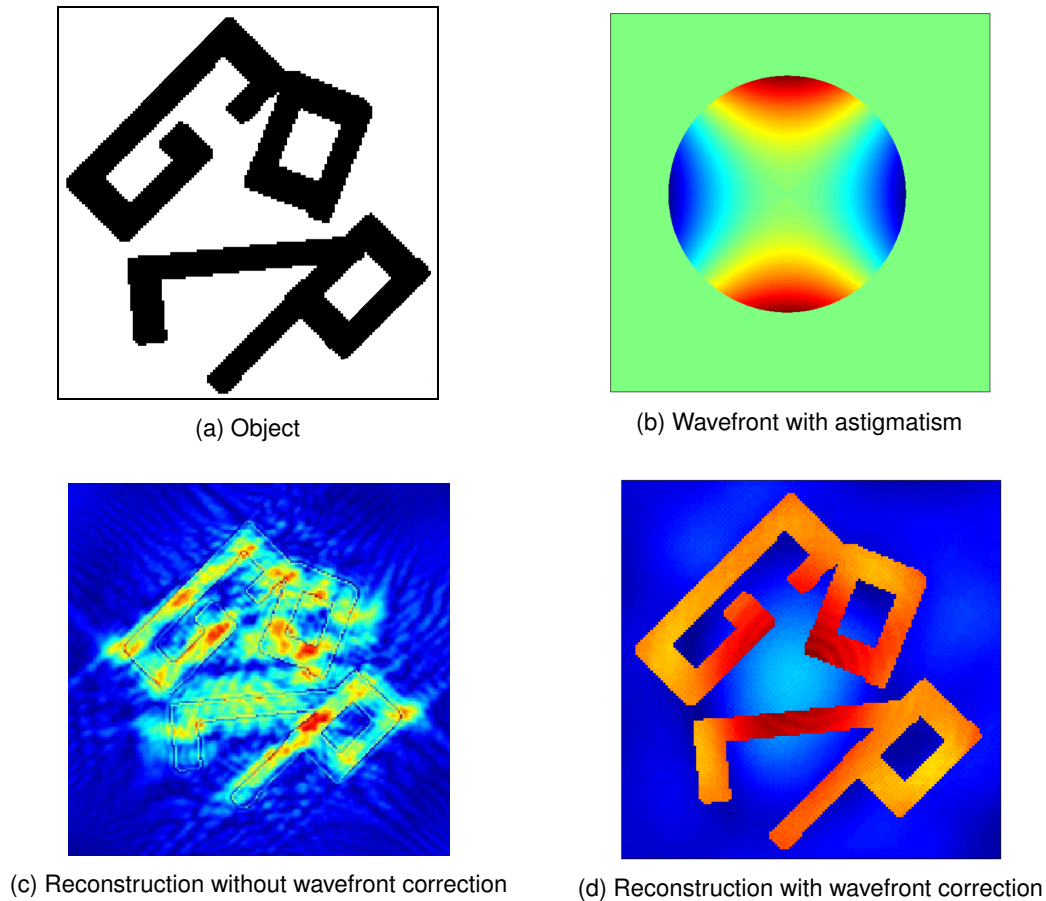
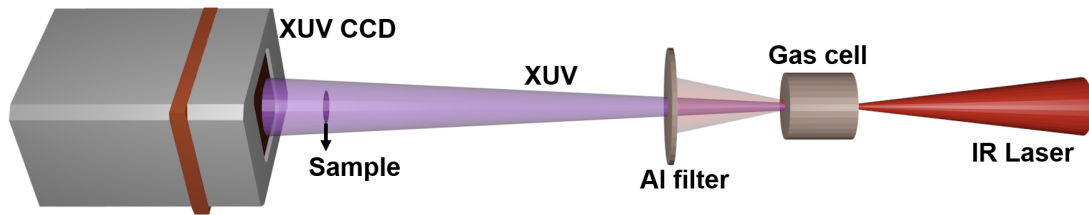


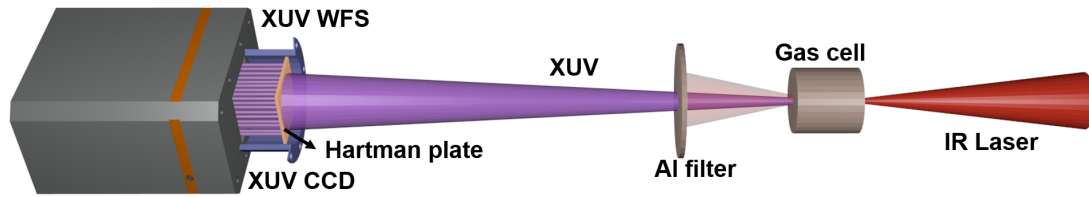
Figure 5.3: Numerical simulations for in-line holography with wavefront correction. Taken from [213]

In-line holography has been already realized using XUV pulses [39] and it has been shown that for a sub-micron resolution at an XUV wavelength of 30 nm, the NA of the source has to be  $> 0.015$  [39]. Higher NA focusing optics can be used with the low divergent HHs to increase the resolution. However, for wavefront correction, the currently available low-NA XUV WFS [128, 115] cannot be used. The recently calibrated high-NA XUV WFS ( $NA \approx 0.1$ ) can be used to perform the wavefront correction for in-line holography using the XUV pulses. The availability of high-NA XUV WFS makes it easier for measuring the wavefront of the high-NA XUV source and later use it in the reconstruction. A schematic of a possible experimental setup for wavefront correction in in-line holography in the XUV is shown in figure 5.4. The XUV is generated through HHG by focusing the IR laser onto a gas cell. The sample is placed after a filter, which filters the residual IR. After recording the hologram using an XUV sensitive CCD, the sample can be removed from the beam and the XUV WFS can be placed to measure the wavefront of the XUV beam used to create the hologram. Figure 5.4b shows the schematic of the XUV wavefront measurement

setup. The sample can be reconstructed with the wavefront correction using the same method used for simulations.



(a) Schematic of experimental setup for in-line holography using XUV beams.



(b) Schematic of experimental setup for wavefront measurement of the XUV beam used for in-line holography using the high-NA XUV WFS.

Figure 5.4: Schematic of the concept of wavefront correction in in-line holography using XUV beams.

## 5.3 Scientific contributions

This work resulted in a number of peer-reviewed articles in international journals and also conference/workshop proceedings.

### Journal Publications

1. **Jayanath. C. P. Koliyadu**, Lu Li, Hannah Donnelly, Hugo Dacasa, Guillaume Dovillaire, Swen Künzel, Gonçalo Figueira, Marta Fajardo, Brenden Dromey, Matt Zepf, Philippe Zeitoun, *"High numerical aperture Hartmann wavefront sensor calibration for the XUV spectral range"*, *In preparation*.
2. Joana Duarte, Gareth Williams, Swen Künzel, **Jayanath Koliyadu**, Hugo Dacasa, Benoît Mahieu, Hamed Merdji, Philippe Zeitoun, Marta Fajardo, *"Digital in-line holography corrected from aberrations by resorting to wavefront sensor measurements"*, *In preparation*.
3. **Jayanath C. P. Koliyadu**, Swen Künzel, Thomas Wodzinski, Barbara Keitel, Joana Duarte, Gareth O. Williams, Celso P. João, Hugo Pires, Victor Hariton, Mario Galletti, Nuno Gomes, Gonçalo Figueira, João Mendanha Dias, Nelson Lopes, Philippe Zeitoun, Elke Plönjes and Marta Fajardo. *"Optimization and Characterization of High-Harmonic Generation for Probing Solid Density Plasmas"*, *Photonics*, 4, 25, 2017.
4. Gonçalo Figueira, Joana Alves, João Mendanha Dias, Marta Fajardo, Nuno Gomes, Victor Harrington, Imran Tayyab, Celso João, **Jayanath Koliyadu**, Swen Künzel, Nelson Lopes, Hugo Piers, Filipe Ruao, Gareth Williams, *"Ultrashort pulse capability at the L2I high intensity laser facility"*, *High Power Laser Science and Engineering*, 5, e2, 2017.

### Oral Presentations @ Conferences, Meetings and Workshops

1. **Jayanath Koliyadu**, Lu Li, Hannah Donnelly, Hugo Dacasa, Guillaume Dovillaire, Swen Künzel, Gonçalo Figueira, Marta Fajardo, Brenden Dromey, Matt Zepf, Philippe Zeitoun, *"Calibration of XUV Optics and high NA Hartmann wavefront sensor"*, Laserlab users meeting, Vilnius, Lithuania (27 - 29 August 2017).
2. **Jayanath Koliyadu**, Hugo Dacasa, Marta Fajardo, Philippe Zeitoun, *"VOXEL Metrology Station @ LOA"*, VOXEL Meeting, Amsterdam, Netherlands (15 - 16 June 2016).

### Conferences / Workshops - Posters / Publications

1. Krishna Chaitanya, Li Lu, Ross McHugh, **Jayanath Koliyadu**, Alexander Saevert, Christian Roedel, Brenden Dromey, Matthew Zepf, Philippe Zeitoun, *"Study of 200 TW laser-driven surface high order harmonics with a high NA Hartmann wavefront sensor"*, Winter College on Extreme Non-linear Optics, Attosecond Science and High-field Physics, ICTP, Trieste, Italy (5 - 16 February 2018).

2. **Jayanath. C. P. Koliyadu**, Lu Li, Hannah Donnelly, Hugo Dacasa, Guillaume Dovillaire, Swen Künzel, Gonçalo Figueira, Marta Fajardo, Brenden Dromey, Matt Zepf, Philippe Zeitoun, *"High numerical aperture Hartmann wavefront sensor calibration for the XUV spectral range"*, CIENCIA 17, Lisbon, Portugal (3 - 5 September 2017).
3. **Jayanath. C. P. Koliyadu**, Lu Li, Hannah Donnelly, Hugo Dacasa, Guillaume Dovillaire, Swen Künzel, Gonçalo Figueira, Marta Fajardo, Brenden Dromey, Matt Zepf, Philippe Zeitoun, *"High numerical aperture Hartmann wavefront sensor calibration for the XUV spectral range"*, 44<sup>th</sup> EPS Conference on Plasma Physics, Belfast, U K (26 - 30 June 2017).
4. Joana Duarte, Gareth Williams, Swen Künzel, **Jayanath Koliyadu**, Hugo Dacasa, Benoît Mahieu, Hamed Merdji, Philippe Zeitoun, Marta Fajardo, *"Digital in-line holography corrected from aberrations by resorting to wavefront measurements"*, COST MP1203 meeting "X-ray optics metrology", Athens, Greece (19<sup>th</sup> - 21<sup>st</sup> September 2016).
5. **Jayanath Koliyadu**, Swen Künzel, Celso João, Gonçalo Figueira, Marta Fajardo, *"High-Harmonic generation with diode-pumped Yb:CaF<sub>2</sub> / Yb:YAG laser"*, PhD open day, IST, Lisbon, Portugal 2015.
6. **Jayanath Koliyadu**, Swen Künzel, Celso João, Gonçalo Figueira, Marta Fajardo, *"High-Harmonic generation with diode-pumped Yb:CaF<sub>2</sub> / Yb:YAG laser"*, ELI beamlines and HILASE summer school, Prague, Czech Republic, 2015.
7. Hugo Dacasa, Davide Bleiner, Guillaume Dovillaire, Joana Duarte, Marta Fajardo, **Jayanath Koliyadu**, et al., *"EUV wavefront measurements of a Schwarzschild microscope objective"*, COST (MP1203) workshop, Milan, Italy, 2015.



# Bibliography

- [1] D. Attwood. *Soft x-rays and extreme ultraviolet radiation : principles and applications*. Cambridge University Press, 2007.
- [2] H. N. Chapman and K. A. Nugent. Coherent lensless X-ray imaging. *Nature Photonics*, 4(12): 833–839, Dec. 2010.
- [3] S. Dobosz, G. Doumy, H. Stabile, P. D'Oliveira, P. Monot, F. Réau, S. Hüller, and P. Martin. Probing hot and dense laser-induced plasmas with ultrafast xuv pulses. *Phys. Rev. Lett.*, 95:025001, Jul 2005.
- [4] B. Wu and A. Kumar. Extreme ultraviolet lithography: a review. *Journal of Vacuum Science & Technology B: Microelectronics and Nanometer Structures Processing, Measurement, and Phenomena*, 25(6):1743–1761, 2007.
- [5] Z. Tao, C. Chen, T. Szilvási, M. Keller, M. Mavrikakis, H. Kapteyn, and M. Murnane. Direct time-domain observation of attosecond final-state lifetimes in photoemission from solids. *Science*, 353 (6294):62–67, 2016.
- [6] S. Haessler, J. Caillat, W. Boutu, C. Giovanetti-Teixeira, T. Ruchon, T. Auguste, Z. Diveki, P. Breger, A. Maquet, B. Carré, et al. Attosecond imaging of molecular electronic wavepackets. *Nature Physics*, 6(3):200, 2010.
- [7] J. Itatani, J. Levesque, D. Zeidler, H. Niikura, H. Pépin, J.-C. Kieffer, P. B. Corkum, and D. M. Villeneuve. Tomographic imaging of molecular orbitals. *Nature*, 432(7019):867, 2004.
- [8] F. Calegari, G. Sansone, S. Stagira, C. Vozzi, and M. Nisoli. Advances in attosecond science. *Journal of Physics B: Atomic, Molecular and Optical Physics*, 49(6):062001, 2016.
- [9] P. Bolognesi, L. Bañares, and M. Alcamí. Xuv/x-ray light and fast ions for ultrafast chemistry. *Physical Chemistry Chemical Physics*, 19(30):19533–19535, 2017.
- [10] H. N. Chapman, A. Barty, S. Marchesini, A. Noy, S. P. Hau-Riege, C. Cui, M. R. Howells, R. Rosen, H. He, J. C. Spence, et al. High-resolution ab initio three-dimensional x-ray diffraction microscopy. *JOSA A*, 23(5):1179–1200, 2006.
- [11] O. Miyashita and Y. Joti. X-ray free electron laser single-particle analysis for biological systems. *Current Opinion in Structural Biology*, 2017.

- [12] B. E. Saleh, M. C. Teich, and B. E. Saleh. *Fundamentals of photonics*, volume 22. Wiley New York, 1991.
- [13] S. W. Hell and J. Wichmann. Breaking the diffraction resolution limit by stimulated emission: stimulated-emission-depletion fluorescence microscopy. *Optics letters*, 19(11):780–782, 1994.
- [14] U. Durig, D. Pohl, and F. Rohner. Near-field optical scanning microscopy with tunnel-distance regulation. *IBM journal of research and development*, 30(5):478–483, 1986.
- [15] R. Lee, H. Baldis, R. Cauble, O. Landen, J. Wark, A. Ng, S. Rose, C. Lewis, D. Riley, J.-C. Gauthier, et al. Plasma-based studies with intense x-ray and particle beam sources. *Laser and Particle Beams*, 20(3):527–536, 2002.
- [16] U. Zastra. *Innovative XUV and X-ray Plasma Spectroscopy to explore Warm Dense Matter*. PhD thesis, Friedrich-Schiller-Universität Jena, 2010.
- [17] J. D. Lindl, P. Amendt, R. L. Berger, S. G. Glendinning, S. H. Glenzer, S. W. Haan, R. L. Kauffman, O. L. Landen, and L. J. Suter. The physics basis for ignition using indirect-drive targets on the national ignition facility. *Physics of Plasmas*, 11(2):339–491, 2004.
- [18] D. Saumon, G. Chabrier, D. Wagner, and X. Xie. Modeling pressure-ionization of hydrogen in the context of astrophysics. *International Journal of High Pressure Research*, 16(5-6):331–343, 2000.
- [19] J. Metzkes, K. Zeil, S. Kraft, M. Rehwald, T. Cowan, and U. Schramm. Reflective optical probing of laser-driven plasmas at the rear surface of solid targets. *Plasma Physics and Controlled Fusion*, 58(3):034012, 2016.
- [20] N. Medvedev, U. Zastra, E. Förster, D. O. Gericke, and B. Rethfeld. Short-time electron dynamics in aluminum excited by femtosecond extreme ultraviolet radiation. *Physical review letters*, 107(16):165003, 2011.
- [21] P. Emma, R. Akre, J. Arthur, R. Bionta, C. Bostedt, J. Bozek, A. Brachmann, P. Bucksbaum, R. Coffee, F.-J. Decker, et al. First lasing and operation of an ångstrom-wavelength free-electron laser. *nature photonics*, 4(9):641–647, 2010.
- [22] FLASH, the Free-Electron LASer in Hamburg, DESY, Germany. <https://flash.desy.de/>. Accessed: 2018-03-05.
- [23] SACLA - SPring-8 Angstrom Compact free electron LASer, Japan. <http://xfel.riken.jp/eng/>. Accessed: 2018-03-05.
- [24] FERMI FEL, Elettra Sinchrotrone, Trieste, Italy. <http://www.elettra.eu/lightsources/fermi/machine.html>. Accessed: 2018-03-05.
- [25] J. L. Krause, K. J. Schafer, and K. C. Kulander. High-order harmonic generation from atoms and ions in the high intensity regime. *Phys. Rev. Lett.*, 68:3535–3538, Jun 1992. doi: 10.1103/PhysRevLett.68.3535.

- [26] A. L'Huillier and P. Balcou. High-order harmonic generation in rare gases with a 1-ps 1053-nm laser. *Physical Review Letters*, 70(6):774, 1993.
- [27] M. C. Kohler, T. Pfeifer, K. Z. Hatsagortsyan, and C. H. Keitel. 4 frontiers of atomic high-harmonic generation. *Advances in Atomic Molecular and Optical Physics*, 61:159, 2012.
- [28] P. Zeitoun, G. Faivre, S. Sebban, T. Mocek, et al. A high-intensity highly coherent soft x-ray femtosecond laser seeded by a high harmonic beam. *Nature*, 431(7007):426, 2004.
- [29] A. Depresseux, E. Oliva, J. Gautier, F. Tissandier, J. Nejd, M. Kozlova, G. Maynard, J. Goddet, A. Tafzi, A. Lifschitz, et al. Table-top femtosecond soft x-ray laser by collisional ionization gating. *Nature Photonics*, 9(12):817–821, 2015.
- [30] P. Salieres, A. L'huillier, P. Antoine, and M. Lewenstein. Study of the spatial and temporal coherence of high order harmonics. *arXiv preprint quant-ph/9710060*, 1997.
- [31] E. Goulielmakis, M. Schultze, M. Hofstetter, V. S. Yakovlev, J. Gagnon, M. Uiberacker, A. L. Aquila, E. Gullikson, D. T. Attwood, R. Kienberger, et al. Single-cycle nonlinear optics. *Science*, 320(5883):1614–1617, 2008.
- [32] K. Zhao, Q. Zhang, M. Chini, Y. Wu, X. Wang, and Z. Chang. Tailoring a 67 attosecond pulse through advantageous phase-mismatch. *Opt. Lett.*, 37(18):3891–3893, Sep 2012.
- [33] T. Gaumnitz, A. Jain, Y. Pertot, M. Huppert, I. Jordan, F. Ardana-Lamas, and H. J. Wörner. Streaking of 43-attosecond soft-x-ray pulses generated by a passively cep-stable mid-infrared driver. *Optics Express*, 25(22):27506–27518, 2017.
- [34] A. Ravasio, D. Gauthier, F. R. N. C. Maia, M. Billon, J.-P. Caumes, D. Garzella, M. Géléoc, O. Gobert, J.-F. Hergott, A.-M. Pena, H. Perez, B. Carré, E. Bourhis, J. Gierak, A. Madouri, D. Mailly, B. Schiedt, M. Fajardo, J. Gautier, P. Zeitoun, P. H. Bucksbaum, J. Hajdu, and H. Merdji. Single-shot diffractive imaging with a table-top femtosecond soft x-ray laser-harmonics source. *Phys. Rev. Lett.*, 103:028104, Jul 2009.
- [35] O. Guilbaud, F. Tissandier, J.-P. Goddet, M. Ribière, S. Sebban, J. Gautier, D. Joyeux, D. Ros, K. Cassou, S. Kazamias, et al. Fourier-limited seeded soft x-ray laser pulse. *Optics letters*, 35(9):1326–1328, 2010.
- [36] E. Oliva, M. Fajardo, L. Li, S. Sebban, D. Ros, and P. Zeitoun. Soft x-ray plasma-based seeded multistage amplification chain. *Optics letters*, 37(20):4341–4343, 2012.
- [37] S. Sebban, A. Depresseux, E. Oliva, J. Gautier, F. Tissandier, J. Nejd, M. Kozlova, G. Maynard, J. Goddet, A. Tafzi, et al. Toward compact and ultra-intense laser-based soft x-ray lasers. *Plasma Physics and Controlled Fusion*, 60(1):014030, 2017.
- [38] G. Williams, H.-K. Chung, S. Vinko, S. Künzel, A. Sardinha, P. Zeitoun, and M. Fajardo. Method of time resolved refractive index measurements of x-ray laser heated solids. *Physics of Plasmas*, 20(4):042701, 2013.

- [39] A.-S. Morlens, J. Gautier, G. Rey, P. Zeitoun, J.-P. Caumes, M. Kos-Rosset, H. Merdji, S. Kazamias, K. Cassou, and M. Fajardo. Submicrometer digital in-line holographic microscopy at 32 nm with high-order harmonics. *Optics letters*, 31(21):3095–3097, 2006.
- [40] A. McPherson, G. Gibson, H. Jara, U. Johann, T. S. Luk, I. McIntyre, K. Boyer, and C. K. Rhodes. Studies of multiphoton production of vacuum-ultraviolet radiation in the rare gases. *JOSA B*, 4(4): 595–601, 1987.
- [41] B. Chen, R. A. Dilanian, S. Teichmann, B. Abbey, A. G. Peele, G. J. Williams, P. Hannaford, L. Van Dao, H. M. Quiney, and K. A. Nugent. Multiple wavelength diffractive imaging. *Phys. Rev. A*, 79:023809, Feb 2009.
- [42] D. Gauthier, M. Guizar-Sicairos, X. Ge, W. Boutu, B. Carré, J. Fienup, and H. Merdji. Single-shot femtosecond x-ray holography using extended references. *Physical review letters*, 105(9):093901, 2010.
- [43] J.-F. Hergott. *XUV Interferometry Using High Order Harmonics: Application to Plasma Diagnostics*. Springer US, Boston, MA, 2001. ISBN 978-1-4615-1351-3.
- [44] B. Vodungbo, J. Gautier, G. Lambert, A. B. Sardinha, M. Lozano, S. Sebban, M. Ducouso, W. Boutu, K. Li, B. Tudu, M. Tortarolo, R. Hawaldar, R. Delaunay, V. López-Flores, J. Arabski, C. Boeglin, H. Merdji, P. Zeitoun, and J. Lüning. Laser-induced ultrafast demagnetization in the presence of a nanoscale magnetic domain network. *Nature Communications*, 3:999, Aug. 2012. ISSN 2041-1723.
- [45] A. Schiffrin, T. Paasch-Colberg, N. Karpowicz, V. Apalkov, D. Gerster, S. Mühlbrandt, M. Korbman, J. Reichert, M. Schultze, S. Holzner, J. V. Barth, R. Kienberger, R. Ernstorfer, V. S. Yakovlev, M. I. Stockman, and F. Krausz. Optical-field-induced current in dielectrics. *Nature*, 493(7430):70–74, Dec. 2012.
- [46] X. Ge, W. Boutu, D. Gauthier, F. Wang, A. Borta, B. Barbrel, M. Ducouso, A. Gonzalez, B. Carré, D. Guillaumet, et al. Impact of wave front and coherence optimization in coherent diffractive imaging. *Optics express*, 21(9):11441–11447, 2013.
- [47] E. Constant, D. Garzella, P. Breger, E. Mével, C. Dorrer, C. Le Blanc, F. Salin, and P. Agostini. Optimizing high harmonic generation in absorbing gases: Model and experiment. *Physical Review Letters*, 82(8):1668, 1999.
- [48] C. V. Vuong, K. B. Dinh, P. Hannaford, and L. V. Dao. Phase-matched high-order harmonic generation in a semi-infinite gas cell with absorbing gaseous media. *Journal of Nonlinear Optical Physics & Materials*, 24(03):1550031, 2015.
- [49] J. Gautier, P. Zeitoun, C. Hauri, A.-S. Morlens, G. Rey, C. Valentin, E. Papalarazou, J.-P. Goddet, S. Sebban, F. Burgy, et al. Optimization of the wave front of high order harmonics. *The European Physical Journal D*, 48(3):459–463, 2008.

- [50] S. Künzel, G. Williams, W. Boutu, E. Galtier, B. Barbrel, H. Lee, B. Nagler, U. Zastra, G. Dovillaire, R. Lee, et al. Shot-to-shot intensity and wavefront stability of high-harmonic generation. *Applied optics*, 54(15):4745–4749, 2015.
- [51] S. Kazamias, D. Douillet, F. Weihe, C. Valentin, A. Rousse, S. Sebban, G. Grillon, F. Augé, D. Hulin, and P. Balcou. Global optimization of high harmonic generation. *Physical review letters*, 90(19):193901, 2003.
- [52] H. Coudert-Alteirac, H. Dacasa, F. Campi, E. Kueny, B. Farkas, F. Brunner, S. Maclot, B. Manschwetus, H. Wikmark, J. Lahl, et al. Micro-focusing of broadband high-order harmonic radiation by a double toroidal mirror. *Applied Sciences*, 7(11):1159, 2017.
- [53] S. Le Pape, P. Zeitoun, M. Idir, P. Dhez, J. Rocca, and M. François. Electromagnetic-field distribution measurements in the soft x-ray range: full characterization of a soft x-ray laser beam. *Physical review letters*, 88(18):183901, 2002.
- [54] P. Mercère, P. Zeitoun, M. Idir, S. L. Pape, D. Douillet, X. Levecq, G. Dovillaire, S. Bucourt, K. A. Goldberg, P. P. Naulleau, and S. Rekawa. Hartmann wave-front measurement at 13.4 nm with  $\lambda_{EUV}/120$  accuracy. *Opt. Lett.*, 28(17):1534–1536, Sep 2003.
- [55] D. Lee, J. Park, J. Sung, and C. Nam. Wave-front phase measurements of high-order harmonic beams by use of point-diffraction interferometry. *Optics letters*, 28(6):480–482, 2003.
- [56] K. T. Kim, D. M. Villeneuve, and P. B. Corkum. Manipulating quantum paths for novel attosecond measurement methods. *Nature Photonics*, 8(3):187–194, Feb. 2014. ISSN 1749-4885, 1749-4893. doi: 10.1038/nphoton.2014.26.
- [57] M. Hentschel, R. Kienberger, C. Spielmann, G. A. Reider, N. Milosevic, T. Brabec, P. Corkum, U. Heinzmann, M. Drescher, and F. Krausz. Attosecond metrology. *Nature*, 414(6863):509–513, nov 2001.
- [58] J. Itatani, F. Quéré, G. L. Yudin, M. Y. Ivanov, F. Krausz, and P. B. Corkum. Attosecond streak camera. *Physical Review Letters*, 88(17):173903, 2002.
- [59] C. Iaconis and I. A. Walmsley. Self-referencing spectral interferometry for measuring ultrashort optical pulses. *IEEE Journal of Quantum Electronics*, 35(4):501–509, Apr 1999.
- [60] E. Cormier, I. A. Walmsley, E. M. Kosik, A. S. Wyatt, L. Corner, and L. F. DiMauro. Self-referencing, spectrally, or spatially encoded spectral interferometry for the complete characterization of attosecond electromagnetic pulses. *Physical review letters*, 94(3):033905, 2005.
- [61] Y. Mairesse, O. Gobert, P. Breger, H. Merdji, P. Meynadier, P. Monchicourt, M. Perdrix, P. Salières, and B. Carré. High harmonic xuv spectral phase interferometry for direct electric-field reconstruction. *Physical review letters*, 94(17):173903, 2005.
- [62] A. S. Wyatt. *Spectral interferometry for the complete characterisation of near infrared femtosecond and extreme ultraviolet attosecond pulses*. PhD thesis, University of Oxford, 2007.

- [63] R. W. Boyd. *Nonlinear optics*. Academic press, 2003.
- [64] A. L. Lytle. *Phase matching and coherence of high-order harmonic generation in hollow waveguides*. PhD thesis, University of Colorado at Boulder, 2008.
- [65] R. Carman, C. Rhodes, and R. Benjamin. Observation of harmonics in the visible and ultraviolet created in co<sub>2</sub>-laser-produced plasmas. *Physical Review A*, 24(5):2649, 1981.
- [66] D. von der Linde, T. Engers, G. Jenke, P. Agostini, G. Grillon, E. Nibbering, A. Mysyrowicz, and A. Antonetti. Generation of high-order harmonics from solid surfaces by intense femtosecond laser pulses. *Phys. Rev. A*, 52:R25–R27, Jul 1995.
- [67] B. Wolter, M. Pullen, A.-T. Le, M. Baudisch, K. Doblhoff-Dier, A. Senftleben, M. Hemmer, C. D. Schröter, J. Ullrich, T. Pfeifer, et al. Ultrafast electron diffraction imaging of bond breaking in di-ionized acetylene. *Science*, 354(6310):308–312, 2016.
- [68] P. B. Corkum and F. Krausz. Attosecond science. *Nature physics*, 3(6):381, 2007.
- [69] T. Popmintchev, M.-C. Chen, D. Popmintchev, P. Arpin, S. Brown, S. Ališauskas, G. Andriukaitis, T. Balčiunas, O. D. Mücke, A. Pugzlys, et al. Bright coherent ultrahigh harmonics in the keV x-ray regime from mid-infrared femtosecond lasers. *science*, 336(6086):1287–1291, 2012.
- [70] M. Zepf, B. Dromey, S. Kar, C. Bellei, D. Carroll, R. Clarke, J. Green, S. Kneip, K. Markey, S. Nagel, et al. High harmonics from relativistically oscillating plasma surfaces—a high brightness attosecond source at keV photon energies. *Plasma Physics and Controlled Fusion*, 49(12B):B149, 2007.
- [71] A. L. Cavalieri, N. Müller, T. Uphues, V. S. Yakovlev, A. Baltuška, B. Horvath, B. Schmidt, L. Blümel, R. Holzwarth, S. Hendel, et al. Attosecond spectroscopy in condensed matter. *Nature*, 449(7165):1029, 2007.
- [72] M. Schultze, E. M. Bothschafter, A. Sommer, S. Holzner, W. Schweinberger, M. Fiess, M. Hofstetter, R. Kienberger, V. Apalkov, V. S. Yakovlev, et al. Controlling dielectrics with the electric field of light. *Nature*, 493(7430):75, 2013.
- [73] M. Uiberacker, T. Uphues, M. Schultze, A. J. Verhoef, V. Yakovlev, M. F. Kling, J. Rauschenberger, N. M. Kabachnik, H. Schröder, M. Lezius, et al. Attosecond real-time observation of electron tunnelling in atoms. *Nature*, 446(7136):627, 2007.
- [74] F. Quéré, C. Thauray, P. Monot, S. Dobosz, P. Martin, J.-P. Geindre, and P. Audebert. Coherent wake emission of high-order harmonics from overdense plasmas. *Physical review letters*, 96(12):125004, 2006.
- [75] M. Yeung, B. Dromey, D. Adams, S. Cousens, R. Hörlein, Y. Nomura, G. D. Tsakiris, and M. Zepf. Beaming of high-order harmonics generated from laser-plasma interactions. *Physical review letters*, 110(16):165002, 2013.

- [76] B. Kettle, T. Dzelzainis, S. White, L. Li, B. Dromey, M. Zepf, C. Lewis, G. Williams, S. Künzel, M. Fajardo, et al. Experimental measurements of the collisional absorption of xuv radiation in warm dense aluminium. *Physical Review E*, 94(2):023203, 2016.
- [77] M. Chini, K. Zhao, and Z. Chang. The generation, characterization and applications of broadband isolated attosecond pulses. *Nature Photonics*, 8(3):178–186, feb 2014. doi: 10.1038/nphoton.2013.362.
- [78] F. Krausz and M. Ivanov. Attosecond physics. *Reviews of Modern Physics*, 81(1):163, 2009.
- [79] G. O. Williams, A. Gonzalez, S. Künzel, L. Li, M. Lozano, E. Oliva, B. Iwan, S. Daboussi, W. Boutu, H. Merdji, et al. Fourier transform holography with high harmonic spectra for attosecond imaging applications. *Optics Letters*, 40(13):3205–3208, 2015.
- [80] J. Li, X. Ren, Y. Yin, Y. Cheng, E. Cunningham, Y. Wu, and Z. Chang. Polarization gating of high harmonic generation in the water window. *Applied Physics Letters*, 108(23):231102, 2016.
- [81] G. J. Stein, P. D. Keathley, P. Krogen, H. Liang, J. P. Siqueira, C.-L. Chang, C.-J. Lai, K.-H. Hong, G. M. Laurent, and F. X. Kärtner. Water-window soft x-ray high-harmonic generation up to the nitrogen k-edge driven by a khz, 2.1  $\mu\text{m}$  opcpa source. *Journal of Physics B: Atomic, Molecular and Optical Physics*, 49(15):155601, 2016.
- [82] P. B. Corkum. Plasma perspective on strong field multiphoton ionization. *Physical Review Letters*, 71(13):1994, 1993.
- [83] M. Lewenstein, P. Balcou, M. Y. Ivanov, A. L’huillier, and P. B. Corkum. Theory of high-harmonic generation by low-frequency laser fields. *Physical Review A*, 49(3):2117, 1994.
- [84] L. Keldysh et al. Ionization in the field of a strong electromagnetic wave. *Sov. Phys. JETP*, 20(5):1307–1314, 1965.
- [85] M. Ammosov, N. Delone, V. Krainov, A. Perelomov, V. Popov, M. Terent’ev, G. L. Yudin, and M. Y. Ivanov. Tunnel ionization of complex atoms and of atomic ions in an alternating electric field. *Sov. Phys. JETP*, 64:1191, 1986.
- [86] S. Künzel. *Characterization, optimization and applications of coherent XUV sources*. PhD thesis, University of Lisbon, 2017.
- [87] M. B. Gaarde, F. Salin, E. Constant, P. Balcou, K. Schafer, K. Kulander, and A. L’Huillier. Spatiotemporal separation of high harmonic radiation into two quantum path components. *Physical Review A*, 59(2):1367, 1999.
- [88] C. João, H. Pires, and G. Figueira. Hybrid diode-pumped yb: Caf<sub>2</sub>/yag laser system delivers 20 mj pulses at 1050 nm for nd: glass amplifier seeding. In *Advanced Solid State Lasers*, pages AM5A–45. Optical Society of America, 2014.

- [89] I. J. Kim, C. M. Kim, H. T. Kim, G. H. Lee, Y. S. Lee, J. Y. Park, D. J. Cho, and C. H. Nam. Highly efficient high-harmonic generation in an orthogonally polarized two-color laser field. *Physical Review Letters*, 94(24):243901, 2005.
- [90] G. Lambert, J. Gautier, C. Hauri, P. Zeitoun, C. Valentin, T. Marchenko, F. Tissandier, J. P. Goddet, M. Ribière, G. Rey, et al. An optimized khz two-colour high harmonic source for seeding free-electron lasers and plasma-based soft x-ray lasers. *New Journal of Physics*, 11(8):083033, 2009.
- [91] A. Mitrofanov and D. Tokarchuk. Fabrication of multilayer thin film filters on support screens and their properties. *Nuclear Instruments and Methods in Physics Research Section A: Accelerators, Spectrometers, Detectors and Associated Equipment*, 282(2-3):546–550, 1989.
- [92] CXRO. [www.cxro.lbl.gov](http://www.cxro.lbl.gov). Accessed: 2018-03-05.
- [93] VOXEL. <http://www.ipfn.ist.utl.pt/voxel>. Accessed: 2018-03-05.
- [94] P. Gibbon. Harmonic generation by femtosecond laser-solid interaction: A coherent “water-window” light source? *Phys. Rev. Lett.*, 76:50–53, Jan 1996.
- [95] G. D. Tsakiris, K. Eidmann, J. M. ter Vehn, and F. Krausz. Route to intense single attosecond pulses. *New Journal of Physics*, 8(1):19, 2006.
- [96] S. Gordienko, A. Pukhov, O. Shorokhov, and T. Baeva. Relativistic doppler effect: Universal spectra and zeptosecond pulses. *Physical review letters*, 93(11):115002, 2004.
- [97] P. Gibbon. *Short pulse laser interactions with matter An Introduction*. Imperial College Press, 2005.
- [98] U. Teubner and P. Gibbon. High-order harmonics from laser-irradiated plasma surfaces. *Reviews of Modern Physics*, 81(2):445, 2009.
- [99] P. Gibbon. High-order harmonic generation in plasmas. *IEEE Journal of Quantum Electronics*, 33(11):1915–1924, 1997.
- [100] R. Lichters, J. Meyer-ter Vehn, and A. Pukhov. Short-pulse laser harmonics from oscillating plasma surfaces driven at relativistic intensity. *Physics of Plasmas*, 3(9):3425–3437, 1996.
- [101] M. Zepf, G. Tsakiris, G. Pretzler, I. Watts, D. Chambers, P. Norreys, U. Andiel, A. Dangor, K. Eidmann, C. Gahn, et al. Role of the plasma scale length in the harmonic generation from solid targets. *Physical Review E*, 58(5):R5253, 1998.
- [102] S. V. Bulanov, N. Naumova, and F. Pegoraro. Interaction of an ultrashort, relativistically strong laser pulse with an overdense plasma. *Physics of Plasmas*, 1(3):745–757, 1994.
- [103] F. Brunel. Not-so-resonant, resonant absorption. *Physical Review Letters*, 59(1):52, 1987.
- [104] C. Thaury, F. Quéré, J.-P. Geindre, A. Levy, T. Ceccotti, P. Monot, M. Bougeard, F. Réau, P. d’Oliveira, P. Audebert, et al. Plasma mirrors for ultrahigh-intensity optics. *Nature Physics*, 3(6):424, 2007.

- [105] JETI200, Helmholtz Institute, Jena, Germany. [https://www.hi-jena.de/en/helmholtz\\_institute\\_jena/about-the-helmholtz-institute-jena/experimental\\_facilities/local/jeti200-laser-kopie/](https://www.hi-jena.de/en/helmholtz_institute_jena/about-the-helmholtz-institute-jena/experimental_facilities/local/jeti200-laser-kopie/). Accessed: 2018-03-05.
- [106] G. Doumy, F. Quéré, O. Gobert, M. Perdrix, P. Martin, P. Audebert, J. Gauthier, J.-P. Geindre, and T. Wittmann. Complete characterization of a plasma mirror for the production of high-contrast ultraintense laser pulses. *Physical Review E*, 69(2):026402, 2004.
- [107] J. Jasny, U. Teubner, W. Theobald, C. Wülker, J. Bergmann, and F. P. Schäfer. A single-shot spectrograph for the soft x-ray region. *Review of Scientific Instruments*, 65(5):1631–1635, 1994.
- [108] Andor XUV CCD. <http://www.andor.com/scientific-cameras/high-energy-detection>. Accessed: 2018-03-05.
- [109] S. Fuchs, C. Rödel, M. Krebs, S. Hädrich, J. Bierbach, A. Paz, S. Kuschel, M. Wünsche, V. Hilbert, U. Zastra, et al. Sensitivity calibration of an imaging extreme ultraviolet spectrometer-detector system for determining the efficiency of broadband extreme ultraviolet sources. *Review of Scientific Instruments*, 84(2):023101, 2013.
- [110] S. Kahaly, S. Monchocé, H. Vincenti, T. Dzelzainis, B. Dromey, M. Zepf, P. Martin, and F. Quéré. Direct observation of density-gradient effects in harmonic generation from plasma mirrors. *Physical review letters*, 110(17):175001, 2013.
- [111] PIXIS-XO Soft X-Ray Cameras. <https://www.princetoninstruments.com/products/PIXIS-XO-XRay>. Accessed: 2018-03-05.
- [112] C. Valentin, D. Douillet, S. Kazamias, T. Lefrou, G. Grillon, F. Augé, G. Mullet, P. Balcou, P. Mercère, and P. Zeitoun. Imaging and quality assessment of high-harmonic focal spots. *Optics letters*, 28(12):1049–1051, 2003.
- [113] H. Mashiko, A. Suda, and K. Midorikawa. Focusing coherent soft-x-ray radiation to a micrometer spot size with an intensity of  $10^{14}$  w/cm<sup>2</sup>. *Optics letters*, 29(16):1927–1929, 2004.
- [114] P. P. Naulleau, K. A. Goldberg, S. H. Lee, C. Chang, C. Bresloff, D. Attwood, and J. Bokor. The euV phase-shifting point-diffraction interferometer: a sub-angstrom reference-wave accuracy wavefront metrology tool. *Applied Optics*, 38(LBNL-43179), 1999.
- [115] B. Flöter, P. Juranić, S. Kapitzki, B. Keitel, K. Mann, E. Plönjes, B. Schäfer, and K. Tiedtke. EUV hartmann sensor for wavefront measurements at the free-electron LASer in hamburg. *New Journal of Physics*, 12(8):083015, 2010.
- [116] C. Bourassin-Bouchet, M. M. Mang, F. Delmotte, P. Chavel, and S. De Rossi. How to focus an attosecond pulse. *Optics express*, 21(2):2506–2520, 2013.
- [117] P. Kirkpatrick and A. V. Baez. Formation of optical images by x-rays. *J. Opt. Soc. Am.*, 38(9):766–774, Sep 1948.

- [118] J. Hartmann. Bemerkungen über den bau und die justirung von spektrographen. *Zeitschrift für Instrumentenkunde*. Berlin: Julins Springer, pages 17–27, 1900.
- [119] *Hartmann Wavefront Analyzer Tutorial*. Spiricon Laser beam diagnostics, 2004.
- [120] J. Wang and D. E. Silva. Wave-front interpretation with zernike polynomials. *Applied optics*, 19(9): 1510–1518, 1980.
- [121] W. H. Southwell. Wave-front estimation from wave-front slope measurements. *JOSA*, 70(8): 998–1006, 1980.
- [122] J. Nejd, M. Kozlová, T. Mocek, and B. Rus. Measuring the electron density gradients of dense plasmas by deflectometry using short-wavelength probe. *Physics of Plasmas*, 17(12):122705, 2010.
- [123] Imagine Optics. <https://www.imagine-optic.com/>. Accessed: 2018-03-05.
- [124] Le laboratoire d'optique appliquée (loa). <http://loa.ensta-paristech.fr/>. Accessed: 2018-03-05.
- [125] Synchrotron soleil. <https://www.synchrotron-soleil.fr/en/about-us>. Accessed: 2018-03-05.
- [126] Imagine optic patent. PCT/FR02/02495, 2002.
- [127] Laser-laboratorium göttingen e.v. (llg). <http://www.llg-ev.de/willkommen/index.html>. Accessed: 2018-03-05.
- [128] HASO EUV. <https://www.imagine-optic.com/product/haso-euv/>. Accessed: 2018-03-05.
- [129] B. Keitel, E. Plönjes, S. Kreis, M. Kuhlmann, K. Tiedtke, T. Mey, B. Schäfer, and K. Mann. Hartmann wavefront sensors and their application at flash. *Journal of synchrotron radiation*, 23(1):43–49, 2016.
- [130] V. Banine and R. Moors. Plasma sources for euv lithography exposure tools. *Journal of Physics D: Applied Physics*, 37(23):3207, 2004.
- [131] P. Takman, H. Stollberg, G. A. Johansson, A. Holmberg, M. Lindblom, and H. M. Hertz. High-resolution compact x-ray microscopy. *Journal of microscopy*, 226(2):175–181, 2007.
- [132] T. Harada, M. Nakasuji, T. Kimura, T. Watanabe, H. Kinoshita, and Y. Nagata. Imaging of extreme-ultraviolet mask patterns using coherent extreme-ultraviolet scatterometry microscope based on coherent diffraction imaging. *Journal of Vacuum Science & Technology B, Nanotechnology and Microelectronics: Materials, Processing, Measurement, and Phenomena*, 29(6):06F503, 2011.
- [133] K. A. Goldberg. *Extreeme ultraviolet interferometry*. PhD thesis, University of California, 1996.
- [134] H. Dacasa. *Spatial and temporal metrology of coherent ultrashort pulses in the extreme-ultraviolet domain*. PhD thesis, University of Paris-Saclay, 2017.

- [135] H. F. Talbot. Lxxvi. facts relating to optical science. no. iv. *The London and Edinburgh Philosophical Magazine and Journal of Science*, 9(56):401–407, 1836.
- [136] J. Wen, Y. Zhang, and M. Xiao. The talbot effect: recent advances in classical optics, nonlinear optics, and quantum optics. *Advances in Optics and Photonics*, 5(1):83–130, 2013.
- [137] J. C. P. Koliyadu, S. Künzel, T. Wodzinski, B. Keitel, J. Duarte, G. O. Williams, C. P. João, H. Pires, V. Hariton, M. Galletti, et al. Optimization and characterization of high-harmonic generation for probing solid density plasmas. *Photonics*, 4(2):25, 2017.
- [138] A. Leblanc, S. Monchocé, H. Vincenti, S. Kahaly, J.-L. Vay, and F. Quéré. Spatial properties of high-order harmonic beams from plasma mirrors: A ptychographic study. *Physical review letters*, 119(15):155001, 2017.
- [139] M. Wollenhaupt, A. Assion, and T. Baumert. *Femtosecond Laser Pulses: Linear Properties, Manipulation, Generation and Measurement*, pages 937–983. Springer New York, New York, NY, 2007. ISBN 978-0-387-30420-5.
- [140] C. Schmidt-Langhorst and H.-G. Weber. Optical sampling techniques. In *Ultrahigh-Speed Optical Transmission Technology*, pages 453–481. Springer, 2005.
- [141] K. Sala, G. Kenney-Wallace, and G. Hall. Cw autocorrelation measurements of picosecond laser pulses. *IEEE Journal of Quantum Electronics*, 16(9):990–996, 1980.
- [142] J.-C. Diels and W. Rudolph. *Ultrashort laser pulse phenomena*. Academic press, 2006.
- [143] D. J. Kane and R. Trebino. Characterization of arbitrary femtosecond pulses using frequency-resolved optical gating. *IEEE Journal of Quantum Electronics*, 29(2):571–579, 1993.
- [144] D. J. Kane. Recent progress toward real-time measurement of ultrashort laser pulses. *IEEE Journal of Quantum Electronics*, 35(4):421–431, 1999.
- [145] R. Trebino, K. W. DeLong, D. N. Fittinghoff, J. N. Sweetser, M. A. Krumbügel, B. A. Richman, and D. J. Kane. Measuring ultrashort laser pulses in the time-frequency domain using frequency-resolved optical gating. *Review of Scientific Instruments*, 68(9):3277–3295, 1997.
- [146] P. O’shea, M. Kimmel, X. Gu, and R. Trebino. Highly simplified device for ultrashort-pulse measurement. *Optics Letters*, 26(12):932–934, 2001.
- [147] M. Takeda, H. Ina, and S. Kobayashi. Fourier-transform method of fringe-pattern analysis for computer-based topography and interferometry. *J. Opt. Soc. Am.*, 72(1):156–160, Jan 1982.
- [148] I. A. Walmsley and C. Dorrer. Characterization of ultrashort electromagnetic pulses. *Advances in Optics and Photonics*, 1(2):308–437, 2009.
- [149] European XFEL. <https://www.xfel.eu/>. Accessed: 2018-03-05.

- [150] M. Drescher, M. Hentschel, R. Kienberger, G. Tempea, C. Spielmann, G. A. Reider, P. B. Corkum, and F. Krausz. X-ray pulses approaching the attosecond frontier. *Science*, 291(5510):1923–1927, 2001.
- [151] P. . M. Paul, E. Toma, P. Breger, G. Mullot, F. Augé, P. Balcou, H. Muller, and P. Agostini. Observation of a train of attosecond pulses from high harmonic generation. *Science*, 292(5522):1689–1692, 2001.
- [152] H. . G. Muller. Reconstruction of attosecond harmonic beating by interference of two-photon transitions. *Applied Physics B: Lasers and Optics*, 74:s17–s21, 2002.
- [153] R. Kienberger, E. Goulielmakis, M. Uiberacker, A. Baltuska, V. Yakovlev, F. Bammer, A. Scrinzi, T. Westerwalbesloh, U. Kleineberg, U. Heinzmann, et al. Atomic transient recorder. *Nature*, 427(6977):817–821, 2004.
- [154] Z. Min-Jie, Y. Peng, T. Hao, H. Xin-Kui, Z. Wei, Z. Shi-Yang, W. Li-Feng, Y. Chen-Xia, and W. Zhi-Yi. Generation and measurement of isolated 160-attosecond xuv laser pulses at 82 ev. *Chinese Physics Letters*, 30(9):093201, 2013.
- [155] T. Sekikawa, A. Kosuge, T. Kanai, and S. Watanabe. Nonlinear optics in the extreme ultraviolet. *Nature*, 432(7017):605–609, 2004.
- [156] P. Tzallas, D. Charalambidis, N. Papadogiannis, K. Witte, and G. D. Tsakiris. Direct observation of attosecond light bunching. *Nature*, 426(6964):267–271, 2003.
- [157] T. Sekikawa, T. Kanai, and S. Watanabe. Frequency-resolved optical gating of femtosecond pulses in the extreme ultraviolet. *Physical review letters*, 91(10):103902, 2003.
- [158] A. Kosuge, T. Sekikawa, X. Zhou, T. Kanai, S. Adachi, and S. Watanabe. Frequency-resolved optical gating of isolated attosecond pulses in the extreme ultraviolet. *Physical review letters*, 97(26):263901, 2006.
- [159] Y. Mairesse and F. Quéré. Frequency-resolved optical gating for complete reconstruction of attosecond bursts. *Physical Review A*, 71(1):011401, 2005.
- [160] F. Ferrari, F. Calegari, M. Lucchini, C. Vozzi, S. Stagira, G. Sansone, and M. Nisoli. High-energy isolated attosecond pulses generated by above-saturation few-cycle fields. *Nature Photonics*, 4(12):875–879, 2010.
- [161] M. Chini, S. Gilbertson, S. D. Khan, and Z. Chang. Characterizing ultrabroadband attosecond lasers. *Optics express*, 18(12):13006–13016, 2010.
- [162] G. Laurent, W. Cao, I. Ben-Itzhak, and C. L. Cocke. Attosecond pulse characterization. *Optics express*, 21(14):16914–16927, 2013.
- [163] F. Quéré, J. Itatani, G. Yudin, and P. Corkum. Attosecond spectral shearing interferometry. *Physical review letters*, 90(7):073902, 2003.

- [164] G. Kolliopoulos, P. Tzallas, B. Bergues, P. Carpeggiani, P. Heissler, H. Schröder, L. Veisz, D. Charalambidis, and G. D. Tsakiris. Single-shot autocorrelator for extreme-ultraviolet radiation. *JOSA B*, 31(5):926–938, 2014.
- [165] N. Dudovich, O. Smirnova, J. Levesque, Y. Mairesse, M. Y. Ivanov, D. Villeneuve, and P. B. Corkum. Measuring and controlling the birth of attosecond xuv pulses. *Nature physics*, 2(11):781–786, 2006.
- [166] J. Dahlström, T. Fordell, E. Mansten, T. Ruchon, M. Swoboda, K. Klünder, M. Gisselbrecht, A. L’Huillier, and J. Mauritsson. Atomic and macroscopic measurements of attosecond pulse trains. *Physical Review A*, 80(3):033836, 2009.
- [167] K. T. Kim, C. Zhang, A. D. Shiner, S. E. Kirkwood, E. Frumker, G. Gariepy, A. Naumov, D. Villeneuve, and P. Corkum. Manipulation of quantum paths for space-time characterization of attosecond pulses. *Nature Physics*, 9(3):159, 2013.
- [168] M. Anderson, A. Monmayrant, S.-P. Gorza, P. Wasylczyk, and I. A. Walmsley. Spider: A decade of measuring ultrashort pulses. *Laser Physics Letters*, 5(4):259, 2008.
- [169] T. E. Glover, D. M. Fritz, M. Cammarata, T. K. Allison, S. Coh, J. M. Feldkamp, H. Lemke, D. Zhu, Y. Feng, R. N. Coffee, M. Fuchs, S. Ghimire, J. Chen, S. Schwartz, D. A. Reis, S. E. Harris, and J. B. Hastings. X-ray and optical wave mixing. *Nature*, 488(7413):603–608, aug 2012. doi: 10.1038/nature11340.
- [170] F. Bencivenga and C. Masciovecchio. Fel-based transient grating spectroscopy to investigate nanoscale dynamics. *Nuclear Instruments and Methods in Physics Research Section A: Accelerators, Spectrometers, Detectors and Associated Equipment*, 606(3):785–789, 2009.
- [171] F. Bencivenga, S. Baroni, C. Carbone, M. Chergui, M. Danailov, G. De Ninno, M. Kiskinova, L. Raimondi, C. Svetina, and C. Masciovecchio. Nanoscale dynamics by short-wavelength four wave mixing experiments. *New Journal of Physics*, 15(12):123023, 2013.
- [172] L. Misoguti, I. Christov, S. Backus, M. Murnane, and H. Kapteyn. Nonlinear wave-mixing processes in the extreme ultraviolet. *Physical Review A*, 72(6):063803, 2005.
- [173] W. Helml, I. Grguraš, P. N. Juranić, S. Düsterer, T. Mazza, A. R. Maier, N. Hartmann, M. Ilchen, G. Hartmann, L. Patthey, et al. Ultrashort free-electron laser x-ray pulses. *Applied Sciences*, 7(9): 915, 2017.
- [174] I. Grguraš, A. R. Maier, C. Behrens, T. Mazza, T. Kelly, P. Radcliffe, S. Düsterer, A. Kazansky, N. Kabachnik, T. Tschentscher, et al. Ultrafast x-ray pulse characterization at free-electron lasers. *Nature Photonics*, 6(12):852–857, 2012.
- [175] P. Finetti, H. Höppner, E. Allaria, C. Callegari, F. Capotondi, P. Cinquegrana, M. Coreno, R. Cucini, M. B. Danailov, A. Demidovich, et al. Pulse duration of seeded free-electron lasers. *Physical Review X*, 7(2):021043, 2017.

- [176] R. Riedel, A. Al-Shemmary, M. Gensch, T. Golz, M. Harmand, N. Medvedev, M. Prandolini, K. Sokolowski-Tinten, S. Toilekis, U. Wegner, et al. Single-shot pulse duration monitor for extreme ultraviolet and x-ray free-electron lasers. *Nature communications*, 4:ncomms2754, 2013.
- [177] A. Lutman, Y. Ding, Y. Feng, Z. Huang, M. Messerschmidt, J. Wu, and J. Krzywinski. Femtosecond x-ray free electron laser pulse duration measurement from spectral correlation function. *Physical Review Special Topics-Accelerators and Beams*, 15(3):030705, 2012.
- [178] S. Yudovich and S. Shwartz. X-ray-pulse characterization by spectral shearing interferometry using three-wave mixing. *Physical Review A*, 90(3):033805, 2014.
- [179] B. Mahieu, D. Gauthier, G. D. Ninno, H. Dacasa, M. Lozano, J.-P. Rousseau, P. Zeitoun, D. Garzella, and H. Merdji. Spectral-phase interferometry for direct electric-field reconstruction applied to seeded extreme-ultraviolet free-electron lasers. *Opt. Express*, 23(14):17665–17674, Jul 2015.
- [180] F. Träger. *Springer handbook of lasers and optics*. Springer Science & Business Media, 2012.
- [181] C. Iaconis and I. A. Walmsley. Spectral phase interferometry for direct electric-field reconstruction of ultrashort optical pulses. *Optics letters*, 23(10):792–794, 1998.
- [182] E. Kosik, L. Corner, A. Wyatt, E. Cormier, I. Walmsley, and L. Dimauro. Complete characterization of attosecond pulses. *Journal of Modern Optics*, 52(2-3):361–378, 2005.
- [183] H. Seiler, B. Walsh, S. Palato, A. Thai, V. Crozatier, N. Forget, and P. Kambhampati. Kilohertz generation of high contrast polarization states for visible femtosecond pulses via phase-locked acousto-optic pulse shapers. *Journal of Applied Physics*, 118(10):103110, 2015.
- [184] A. Fürbach, T. Le, C. Spielmann, and F. Krausz. Generation of 8-fs pulses at 390 nm. *Applied Physics B*, 70(1):S37–S40, 2000.
- [185] A. M. Streltsov, K. Moll, A. L. Gaeta, P. Kung, D. Walker, and M. Razeghi. Pulse autocorrelation measurements based on two-and three-photon conductivity in a gan photodiode. *Applied Physics Letters*, 75(24):3778–3780, 1999.
- [186] G. Lambert, B. Vodungbo, J. Gautier, B. Mahieu, V. Malka, S. Sebban, P. Zeitoun, J. Luning, J. Perron, A. Andreev, et al. Towards enabling femtosecond helicity-dependent spectroscopy with high-harmonic sources. *Nature communications*, 6:6167, 2015.
- [187] B. Mahieu, S. Stremoukhov, D. Gauthier, C. Spezzani, C. Alves, B. Vodungbo, P. Zeitoun, V. Malka, G. De Ninno, and G. Lambert. Control of ellipticity in high-order harmonic generation driven by two linearly polarized fields. *Physical Review A*, 97(4):043857, 2018.
- [188] M. Born and E. Wolf. *Principles of optics*, 1975.
- [189] F. Bencivenga, R. Cucini, F. Capotondi, A. Battistoni, R. Mincigrucci, E. Giangrisostomi, A. Gessini, M. Manfredda, I. Nikolov, E. Pedersoli, et al. Four wave mixing experiments with extreme ultraviolet transient gratings. *Nature*, 520(7546):205, 2015.

- [190] P. Schmuser, M. Dohlus, J. Rossbach, and C. Behrens. Free-electron lasers in the ultraviolet and x-ray regime physical principles, experimental results, technical realization. *SPRINGER TRACTS IN MODERN PHYSICS*, 258(1):ALL–ALL, 2014.
- [191] B. W. McNeil and N. R. Thompson. X-ray free-electron lasers. *Nature photonics*, 4(12):814–821, 2010.
- [192] E. Allaria, A. Battistoni, F. Bencivenga, R. Borghes, C. Callegari, F. Capotondi, D. Castronovo, P. Cinquegrana, D. Cocco, M. Coreno, et al. Tunability experiments at the fermi@ elettra free-electron laser. *New Journal of Physics*, 14(11):113009, 2012.
- [193] C. Bocchetta, D. Bulfone, P. Craievich, M. Danailov, G. D’Auria, G. DeNinno, S. Di Mitri, B. Diviacco, M. Ferianis, A. Gomezel, et al. Facility updates: Fermi@ elettra: A free electron laser for euv and soft x-ray radiation. *Synchrotron Radiation News*, 18(6):30–35, 2005.
- [194] E. Allaria, R. Appio, L. Badano, W. Barletta, S. Bassanese, S. Biedron, A. Borga, E. Busetto, D. Castronovo, P. Cinquegrana, et al. Highly coherent and stable pulses from the fermi seeded free-electron laser in the extreme ultraviolet. *Nature Photonics*, 6(10):699–704, 2012.
- [195] E. Allaria, D. Castronovo, P. Cinquegrana, P. Craievich, M. Dal Forno, M. Danailov, G. D’Auria, A. Demidovich, G. De Ninno, S. Di Mitri, et al. Two-stage seeded soft-x-ray free-electron laser. *Nature Photonics*, 7(11):913–918, 2013.
- [196] Photon Beam Parameters, FERMI FEL, Elettra Sinchrotrone, Trieste, Italy. <https://www.elettra.trieste.it/lightsources/fermi/beam-parameters-copy.html?showall=>. Accessed: 2018-03-05.
- [197] G. Stupakov. Effect of finite pulse length and laser frequency chirp on hghg and eehg seeding. Technical report, SLAC National Accelerator Laboratory, Stanford University, 2011.
- [198] G. Geloni, V. Kocharyan, and E. Saldin. A novel self-seeding scheme for hard x-ray fels. *Journal of Modern Optics*, 58(16):1391–1403, 2011.
- [199] Y.-R. Shen. The principles of nonlinear optics. *New York, Wiley-Interscience, 1984, 575 p.*, 1984.
- [200] H. J. Eichler, P. Günter, and D. W. Pohl. *Laser-induced dynamic gratings*, volume 50. Springer-Verlag Berlin Heidelberg, 1986.
- [201] R. Trebino, E. K. Gustafson, and A. E. Siegman. Fourth-order partial-coherence effects in the formation of integrated-intensity gratings with pulsed light sources. *JOSA B*, 3(10):1295–1304, 1986.
- [202] D. Gauthier, E. Allaria, M. Coreno, I. Cudin, H. Dacasa, M. B. Danailov, A. Demidovich, S. Di Mitri, B. Diviacco, E. Ferrari, et al. Chirped pulse amplification in an extreme-ultraviolet free-electron laser. *Nature communications*, 7, 2016.

- [203] DiProl, FERMI Free Electron Laser, Elettra Sinchrotrone, Trieste, Italy. <http://www.elettra.eu/lightsources/fermi/fermi-beamlines/diproi/diproihome/>. Accessed: 2018-03-05.
- [204] MiniTIMER deay line, DiProl, FERMI Free Electron Laser, Elettra Sinchrotrone, Trieste, Italy. <http://www.elettra.eu/lightsources/fermi/fermi-beamlines/diproi/diproihome/page-3.html?showall=>. Accessed: 2018-03-05.
- [205] E. G. Saiz, G. Gregori, D. O. Gericke, J. Vorberger, B. Barbrel, R. Clarke, R. R. Freeman, S. Glenzer, F. Khattak, M. Koenig, et al. Probing warm dense lithium by inelastic x-ray scattering. *Nature Physics*, 4(12):940–944, 2008.
- [206] L. Gartside, G. Tallents, A. Rossall, E. Wagenaars, D. Whittaker, M. Kozlová, J. Nejdí, M. Sawicka, J. Polan, M. Kalal, et al. Extreme ultraviolet interferometry of warm dense matter in laser plasmas. *Optics letters*, 35(22):3820–3822, 2010.
- [207] R. Smith, J. Dunn, J. Nilsen, V. Shlyaptsev, S. Moon, J. Filevich, J. Rocca, M. Marconi, J. Hunter, and T. Barbee Jr. Picosecond x-ray laser interferometry of dense plasmas. *Physical review letters*, 89(6):065004, 2002.
- [208] K. Baker, J. Brase, M. Kartz, S. Olivier, B. Sawvel, and J. Tucker. Electron density characterization by use of a broadband x-ray-compatible wave-front sensor. *Optics letters*, 28(3):149–151, 2003.
- [209] Y. Ping, A. Correa, T. Ogitsu, E. Draeger, E. Schwegler, T. Ao, K. Widmann, D. Price, E. Lee, H. Tam, et al. Warm dense matter created by isochoric laser heating. *High Energy Density Physics*, 6(2):246–257, 2010.
- [210] J. Garcia-Sucerquia, W. Xu, S. K. Jericho, P. Klages, M. H. Jericho, and H. J. Kreuzer. Digital in-line holographic microscopy. *Applied optics*, 45(5):836–850, 2006.
- [211] D. Gabor et al. A new microscopic principle. *Nature*, 161(4098):777–778, 1948.
- [212] T. Latychevskaia and H.-W. Fink. Practical algorithms for simulation and reconstruction of digital in-line holograms. *Applied optics*, 54(9):2424–2434, 2015.
- [213] J. Duarte. Coherent xuv imaging. Master’s thesis, Instituto Superior Tecnico, Lisbon, Portugal, 2015.
- [214] J. Duarte, G. O. Williams, S. Kunzel, J. Koliyadu, J. D. Rodrigues, H. Dacasa, B. Mahieu, P. Zeitoun, H. Merdji, and M. Fajardo. Digital in-line holography corrected from aberrations by resorting to wavefront sensor measurements. *In preparation*, 2018.